UNSTEADY BUFFETING FORCES AND GUST RESPONSE OF BRIDGES WITH PROPER ORTHOGONAL DECOMPOSITION APPLICATIONS

POD 解析を用いた橋梁の変動空気力及びガスト応答に関する研究

THAI-HOA LE

2007

Abstract

The unsteady buffeting forces and the gust response prediction of bridges in the atmospheric turbulent flows is recently attracted more attention due to uncertainties in both experiment and analytical theory. The correction functions such as the aerodynamic admittance function and the spatial coherence function have been supplemented to cope with limitations of the quasi-steady theory and strip one so far. Concretely, so-called single-variate quasi-steady aerodynamic admittance functions as the transfer functions between the wind turbulence and induced buffeting forces, as well as coherence of wind turbulence has been widely applied for the gust response prediction. Recent literatures, however, pointed out that the coherence of force exhibits higher than that of turbulence. These correction functions, in the other words, contain their uncertainties which are required to be more understanding.

Proper orthogonal decomposition (POD), known as the Karhunen-Loeve decomposition has been applied popularly in many engineering fields. Main advantage of the POD is that the multi-variate correlated random fields/processes can be decomposed and described in such simplified way as a combination of limited number of orthogonally low-order dominant eigenvectors (or turbulent modes) which is convenient and applicable for order-reduced representation, simulation of the random fields/processes such as the turbulent fields, turbulent-induced force fields and stochastic response prediction as well. The POD and its proper transformations based on either zero-time-lag covariance matrix or cross spectral one of random fields/processes have been branched by either the covariance proper transformation (CPT) in the time domain or the spectral proper transformation (SPT) in the frequency domain. So far, the covariance matrix-based POD and its covariance proper transformation in the time domain has been used almost in the wind engineering topics due to its simplification in computation and interpretation.

In this research, the unsteady buffeting forces and the gust response prediction of bridges with

emphasis on the POD applications have been discussed. Investigations on the admittance function of turbulent-induced buffeting forces and the coherence one of the surface pressure as well as the spatial distribution and correlation of the unsteady pressure fields around some typically rectangular cylinders in the different unsteady flows have been carried out thanks to physical measurements in the wind tunnel. This research indicated effect of the bluff body flow and the wind-structure interaction on the higher coherence of buffeting forces than the coherence of turbulence, thus this effect should be accounted and undated for recent empirical formulae of the coherence function of the unsteady buffeting forces. Especially, the multi-variate nonlinear aerodynamic admittance function has been proposed in this research, as well as the temporo-spectral structure of the coherence functions of the wind turbulence and the buffeting forces has been firstly here using the wavelet transform-based coherence in order to detect intermittent characteristics and temporal correspondence of these coherence functions. In POD applications, three potential topics in the wind engineering field have been discussed in the research: (i) analysis and identification, modeling of unsteady pressure fields around model sections; (ii) representation and simulation of multi-variate correlated turbulent fields and (iii) stochastic response prediction of structures and bridges. Especially, both POD branches and their proper transformations in the time domain and the frequency one have been used in these applications. It found from these studies that only few low-order orthogonal dominant modes are enough accuracy for representing, modeling, simulating the correlated random fields (turbulence and unsteady surface pressure, unsteady buffeting forces), as well as predicting stochastic response of bridges in the time and frequency domains. The gust response prediction of bridges has been formulated in the time domain at the first time in this research using the covariance matrix-based POD and its covariance proper transformation which is very promising to solve the problems of the nonlinear and unsteady aerodynamics. Furthermore, the physical linkage between these low-order modes and physical causes occurring on physical models has been interpreted in some investigated cases.

Contents

List of figures

List of tables

Preface

The research presented here has been carried out as the partial fulfillment of the requirements of my International Doctoral Program in Engineering at the Bridge and Wind Engineering Laboratory, the Department of Civil and Earth Resources Engineering of the Kyoto University, Japan between October 2004 and September 2007.

It backs to my memory about my initial interest in the wind engineering and long-span bridge aerodynamics dated back to my days and my duties during I worked for the Institute of Transport Science and Technology (ITST), the Ministry of Transport Vietnam and I studied the graduate course at the Graduate Center for Engineering Mechanics, the Vietnam National University at Hanoi. It seems to be new topics of the bridge aerodynamics at Vietnam, where various long-span bridges were under construction and planed to be constructed. I found myself my aspiration and motivation to focus my studies in this topic. I received many supports and encouragements from many persons, to whom I would like to express my grateful thanks.

It is my great pleasure to avail this opportunity to express my sincere gratitude to all respective persons who helped and contributed to make my research in reality and possibility. Firstly, I would like to express my sincere gratitude to my academic supervisor Prof. MASARU MATSUMOTO for his reception, guidance, support and encouragements to my pursuit and fulfillment of my doctoral research at his Laboratory. He has taught me first lessons on the importance and essentials of the bluff body flow aerodynamics and its relationship to mechanism and fundamentals of the aerodynamic and aeroelastic phenomena with usage of the physical experiments and the wind tunnel tools.

I would like to express the special thanks Ass. Prof. Hiromichi SHIRATO at the Bridge and Wind Engineering Laboratory for his enthusiastic helps, advices and continuous guidance in the buffeting research group and in my individual as well. The many thanks would be expressed to Assi. Prof. Tomomi YAGI for his daily helps, caring and administrative management concerning to me, and keeping track on my application procedures as well. The advices and helps from Prof.

Junichi MORI, the Chief of Center for Foreign Students and person-in-charge with Foreign Cooperation and Relations, Kyoto University and from Ms. Toshiko OHASHI, person-in-charge with Foreign Students in the International Doctoral Programs in Engineering, Graduate School of Engineering, Kyoto University for my daily life, campus life and Japanese culture would be acknowledged. I also would acknowledge Prof. Dong-Anh NGUYEN, President of Scientific Committee, Institute of Mechanics （IMech）, Vietnamese Academy for Science and Technology (VAST) for his personal communication, academic assistance and scientific information.

The examining committee of my doctoral dissertation was composed of Prof. Masaru MATSUMOTO, Prof. Hiromasa KOWAI (Disaster Prevention Research Institute- DPRI, Kyoto University), Prof. Hiromichi SHIRATO. I would like to express my thanks to them and their significant suggestions, revisions and helps would be acknowledged.

Let me save this chance to express my grateful thanks to the International Doctoral Program in Engineering at Kyoto University, the Japanese Government' s Mobukagakusho Scholarship Program for the financial support. Special thank also would be expressed to the Japanese Government's Japanese International Cooperation Agency (JICA), who invited me to participate the three-month training course in Osaka, Japan and gave me a precious chance to contact and visit the Bridge and Wind Engineering Laboratory, Kyoto University.

I was also grateful for the friendship, hospitality, helps and contributions of the graduate students in my research laboratory during the three-year period when I have been studied, who I can not present all their names here, including the individuals in my research groups: Messrs Tetsuro MIZUNO, Kenji YAMANE, Takuro FURUKAWA, Yuya SUMIKURA and VanBao NGUYEN.

Last but not least, I would delicate this research to my Parent, my Wife and two little Sons.

Kyoto University, July 2007.

Chapter 1

General Introduction

1.1 Long-span bridges and wind effects

It is generally agreed that only last two decades of the 20th century, many large-scale bridges have been successfully built around over the world. Long-span bridges typically imply for cable-supported bridges, consisting of suspension bridges (SB) and cable-stayed ones (CSB). Recently, the Akashi-Kaikyo bridge (SB,1991m,Japan) and the Tatara bridge (CSB,890m,Japan), in which information inside brackets denotes to type of bridge, main span length and construction countries, are holding the world longest span records, besides number of other typical long-span cable-supported bridges around the world should be mentioned as Minami Bisan-Seto bridge (SB,1723m,Japan), Great Belt bridge (SB,1623m,Denmark), Tsing Ma bridge (SB,1377m,Hong Kong), Normandy bridge (CSB,856m,France), Yangpu bridge (CSB,602m,China), Meiko bridge (CBS,590m,Japan), Tsurumi Tsubasa bridge (CBS,510m,Japan), Ikuchi bridge (CSB,490m,Japan), Oresund bridge (CSB,490m,Denmark) and many others. It can be seen some typically super-span cable-supported bridge projects are under construction or being soon started in different parts of the world such as Stonecutter bridge (CSB,1018m,Hong Kong), Messina Strait bridge (SB,3300m,Italy), Gibralta Strait bridge (SB,8400m,Spain-Morocco), SuThong bridge (CSB,1088m,China) and others, are going to hold the new world records in their main span length of the bridge types after completion. Furthermore, many super long-span bridges across the seas have been proposed in the feasibility studies in many counties like Japan, Korea, China and other. In Japan, some huge overseas bridge projects have been scheduled for discussion and consideration. Apart from three overseas bridge routs linking main Honshu and Shikoku islands are now under traffic service that are holding the world longest spans of their types, some other Ho-yo, Kitan and Tsugaru strait-crossing bridge projects are under the consideration and the pre-feasibility studies that many exciting problems concerning to design and analysis will be exhibited. Undoubtedly, the long-span bridges gain more advantageous to build new sea-crossing or strait-crossing routines to compare with another structural alternatives such as

underground tunnel, floating tunnel. It seems that the longer spans, the more slender structures and the higher strength materials are still hinged tendency on the world bridge engineering in the few coming decades.

The design and analysis of the long-span bridges or super long-span bridges emerge some critical engineering problems as follows:

(1) Dynamic behaviors of bridges due to the traffic live loads, the earthquake and the atmospheric wind flows play very important role and more concerns in the design and analysis.

(2) New structural design, new technologies in fabrication and construction as well as new high strength materials are favorable to be applied, thus many new engineering problems are accordingly faced, especially in the aspect of natural hazardous reduction and mitigation.

It is strongly agreed that the long-span bridges are prone to the wind effects, the wind-induced vibrations and the aeroelastic instability problem as well. In the past lesson, the complete collapse of the Tacoma Narrow bridge (SB,980m,USA) in 1940 at USA reminded civil engineers and scientists to be much aware of the important role of the aerodynamic phenomena and the wind-induced vibrations, see Figure 1.1.

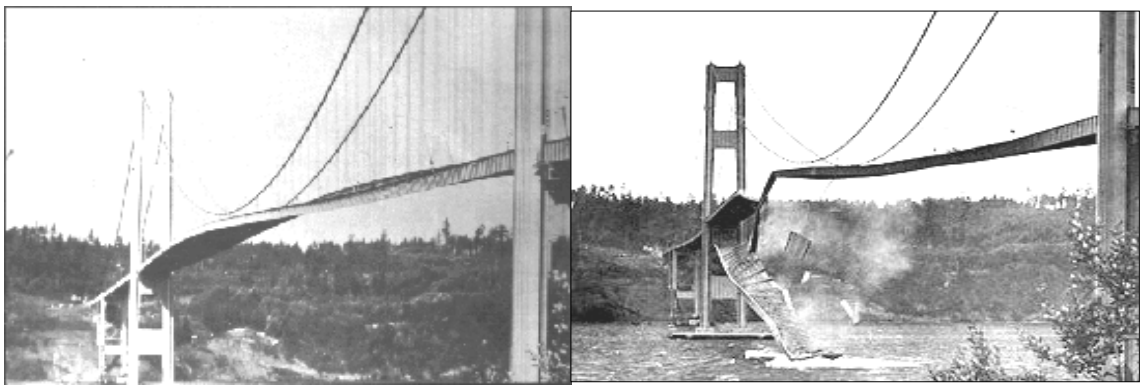

Fig. 1.1 Extreme amplitude vibration and collapse of Tacoma Narrow bridge in USA, 1940

Evaluation of the wind-induced vibrations or the wind resistance design has become the more and more concern for design and analysis of the long-span bridges, especially the problems relate to the aeroelastic instability and the random response due to the turbulent wind.

1.2 Bridge aerodynamics and classification

Bridge structures under the atmospheric wind flows can exhibit to one of the aerodynamic phenomena, of the wind-induced vibrations, or many as the aerodynamic interference and coupling to be occurred. Their classification of the aerodynamic phenomena can be based on some ways. Typically, it can be classified based on the fundamental bluff-body aerodynamics, the fluid dynamics and characteristics of around-body flow that cored in the wind-structure interaction as formation of flow separation and reattachment, local separation bubble, vortex-shedding, one or two shear layers on structure surface (Matsumoto 2000). He also discussed that (1) simultaneous modification of approaching flow and around-structure flow by structure's shape, scale, movement and wind's velocity, relative attack angle and; (2) local pressure distribution at leading edge zone of structure surface played very important role to explain in generation mechanisms of aerodynamic phenomena and wind-induced vibrations.

As simpler approach and practical application, however classification of bridge aerodynamics can be based on their characteristics on amplitude of response and effects. Bridge responses subjected to the wind loading can be divided into two main categories: limited-amplitude and divergent-amplitude wind-induced vibrations. The former comprises the vortex-induced vibrations, buffeting, wake-induced vibrations and rain-wind-induced vibrations with their effects of dynamic fatigue and serviceable discomfort, whereas the later consist of flutter, galloping and wake instability with their structural instability and catastrophe, see Figure 1.2.

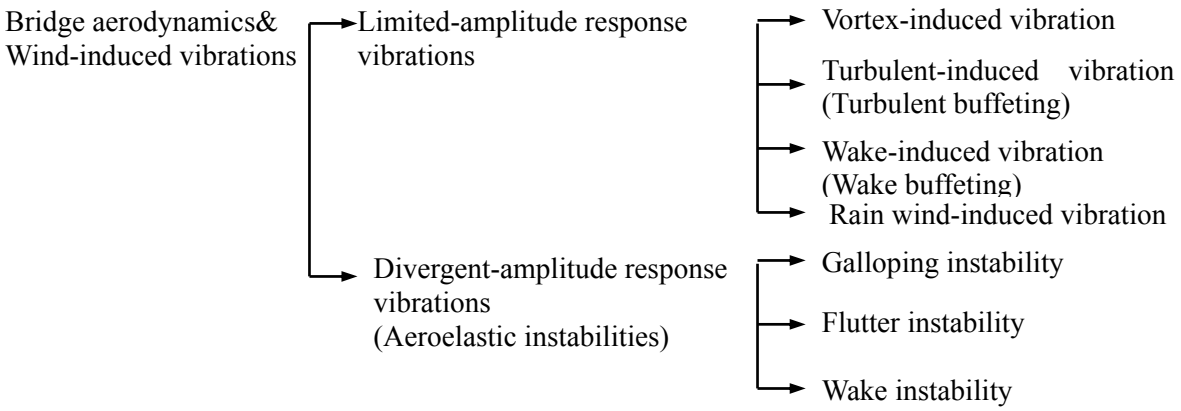

Fig.1.2 Classification of bridge aerodynamics and aeroelastics

Basing on amplitude of response depending on the nondimensional reduced wind velocity ($U_{re} = U/nB$; where U: mean wind velocity, n: frequency, B: deck width), it can be generalized that the vortex-induced phenomena usually occur at low velocity range, the buffeting phenomena is significant at medium velocity range up to high velocity range, whereas the

aeroelastic phenomena occur at high velocity range, see Figure 1.3.

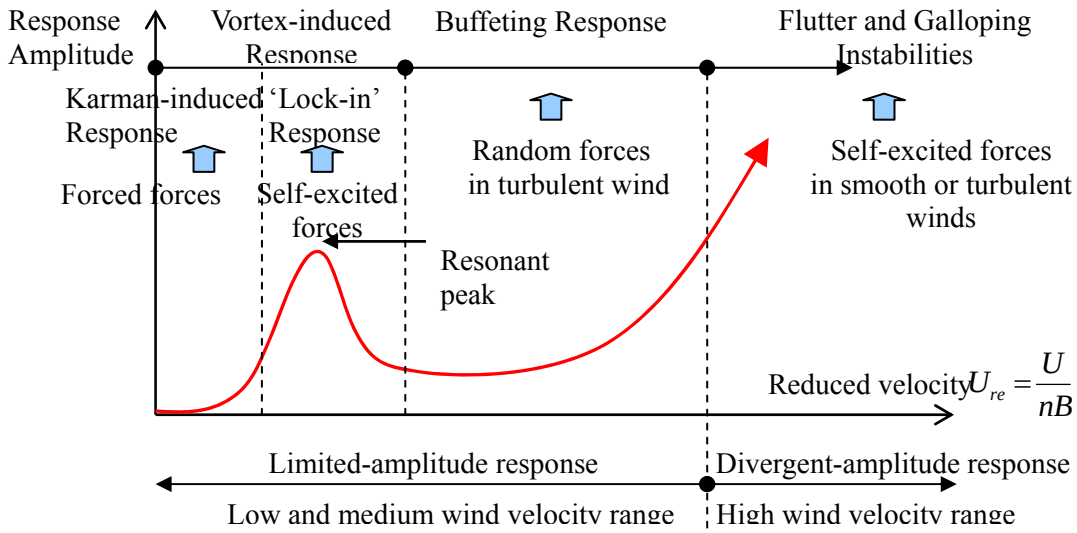

Fig. 1.3 Response amplitude of wind-induced vibrations versus reduced wind velocity

Some main points of the above-mentioned bridge aerodynamics will be briefly presented hereinafter.

(1) The vortex-induced vibrations are the limited-amplitude aerodynamic oscillation induced by either the typical Karman vortex shedding at the wake of structure or another vortex shedding on the surface and wake of structure. Vortex shedding is generated by characteristics of the ongoing wind flows, structural geometry and motion of structure. It is paid much attention on the vortex-induced vibration of bridges due to large response amplitude at resonant state that well-known as frequency 'lock-in' phenomenon and happened at low critical velocity range. Vibrational amplitude, however, is decayed due to structural damping and wind velocity come out of the critical velocity range. In the resonant state, moreover, vortex-induced forces have no longer forced but non-linear motion-induced ones. For bridge design, the critical velocity range and maximum response are purposed to investigate on vortex-induced vibration through means of wind tunnel experiments and theoretical analyses. Some studies indicated that streamlined sections usually exhibit larger response due to the vortex-induced vibration than bluffer sections as stiffen truss girders or Π-shaped girders.

(2) The buffeting phenomenon is defined as the random aerodynamic vibration in the turbulent wind flows due to unsteady wind forces or unsteady buffeting forces generated by the fluctuating velocity components or wind turbulence. Gust response is classified

into the limited-amplitude phenomena due to effect of structural damping. Maximum gust response of bridges in the turbulent wind must be required for the buffeting evaluation and random aerodynamic response. The gust response is predicted via experimental and analytical investigation in either the frequency domain or the time domain. However, some assumptions and limitation of the unsteady buffeting forces due to approximation and simplification of the quasi-steady theory and the strip theory which are still used so far. Correction functions such as the aerodynamic admittance function, the coherence function are supplemented in account for frequency dependence and spatial correlation of the unsteady buffeting forces. Assumptions and usage of the correction functions bring uncertainties in the buffeting response evaluation. Analytical method in the frequency domain proposed by Davenport (1962) still validates and is applied so far.

(3) The wind-induced dry-state vibration and the rain-wind-induced vibration observed at inclined stayed cables of cable-stayed bridges in the windy and stormy days can respond excessive amplitude. Mechanism of the wind-induced dry-state and rain-wind-induced vibrations relates to formation of upper water rivulet and axial shear flow, three-dimensional Karman vortex shedding on surface, along and in wake of the inclined cables (Matsumoto et al. 1997, Matsumoto 2000, Matsumoto et al. 2005).

(4) The galloping instability was firstly observed by excessive response amplitude of the iced electric transmission lines under the strong wind and is classified into type of the divergent-amplitude vibration that associated with mechanism of negative slope of aerodynamic coefficients against relative attack angle (based on the well-known Den Hartog's criterion). Analytical models carried out under linear and nonlinear behavior for non-circular sections (Matsumoto 2000).

(5) The flutter instability also belongs to the divergent-amplitude self-controlled vibration generated by the wind-structure interaction and negative aerodynamic damping mechanism. Flutter instability is one of the most critical concerns to bridge aerodynamics and aeroelastics at the high velocity range due to its catastrophic behavior. Critical wind velocity at which the flutter instability occurring can be determined by either the numerical analytical methods or the experimental tools.

(6) The wake-induced vibrations and wake instability can be generated when bridges or their structural components are located on the wake of upstream adjacent structures. Wake-induced vibrations also are known as interference and proximity phenomena, moreover, only can be investigated under the means of experiments or full-scale measurements.

1.3 Background and objectives of study

Among above-mentioned bridge aerodynamic and aeroelastic phenomena, the stochastic gust response due to the random buffeting forces in the atmospheric turbulent wind and the flutter instability due to the self-excited aerolastic forces and the wind-structure interaction are usually required more concerns and interests. These phenomena and their effects must be considered carefully in the design and construction stages, especially for the long-span bridges constructed in coastal and stormy, windy areas which are high risks from the aerodynamic and aeroelastic effects. It is generally agreed that the aeroelastic instability is only favorable to occur in the cases of the high velocity range, the bluff girder sections with low torsional stiffness, however these conditions are seldom met with the modern girder sections of streamlining and high torsional stiffness. Therefore, critical wind velocity which the flutter instability occurs usually exhibits much higher than natural wind velocity at the bridge sites. Additionally, experimental and analytical tools for the aeroelastic instability evaluation seem to be accuracy and reliable enough so far. It seems that the aeroelastic instability is usually studied and experimented under the smooth wind flows which are proved in almost cases to exhibit more critical conditions than naturally turbulent wind flows (Scanlan 1990, Matsumoto et al. 1996). In the some extent, the aeroelastic instability is seldom to occur with the modern bridges. Evidently, there is no aeroelastic catastrophe observed after the Tacoma Narrow bridge since 1940.

Recently, the unsteady buffeting forces and the stochastic gust response of bridges attract more attention due to its potential effects and uncertainties on bridges such as aerodynamic fatigue and unpredicted extreme deflection and sectional forces as well as analytical risk on overestimation, underestimation of the its response prediction. As far as concerned, the gust response prediction of bridges has been treated thanks to some assumptions and theories such as the quasi-steady theory and the strip theory which are no longer to be accuracy so far. The buffeting forces determined under scope of two theories can be considered as quasi-steady buffeting forces. So-called correction functions, however, such as aerodynamic admittance function, spatial coherence function have been supplemented to cope with limitations of these two theories. In this case when the correction functions are added, the unsteady buffeting forces are determined.

Aerodynamic admittance function is defined as transfer function between output turbulent-induced buffeting forces and input wind turbulence in the frequency domain. This experimental approach of the transfer function will compensate deference between turbulence and turbulent-induced forces due to their deference in spectral distribution in the frequency domain. Thus, the aerodynamic admittance is frequency dependant function. However, recent approach of the transfer function measurement and analytical method contains some

uncertainties as follows: (i). In the direct measurement of output aerodynamic forces, it is difficult to defer contribution proportion of turbulent-induced forces (due to turbulence) and self-excited forces (due to wind-structure interaction), thus the transfer function between input turbulence and output aerodynamic forces contain the self-excited forces which considerably influence from medium to high wind velocity ranges and flexible girder bridges; (ii). In the gust response analysis, it is assumed that longitudinal turbulent component u(t) and vertical turbulent one w(t) contribute equally on power spectra of output turbulent-induced forces in the frequency domain, this means that the transfer function between the longitudinal turbulence and the output turbulent-induced forces is correspondent to that between the vertical turbulence and input forces. Simplified model of the frequency-dependant aerodynamic admittance function (so-called single-variate quasi-steady the aerodynamic admittance) has been widely applied in the gust response prediction of bridges so far. Recently, some further approaches such as nonlinear, multivariate and complex aerodynamic admittance functions have been mentioned anywhere in some literatures.

Spatial coherence function is defined as normalized quantity between cross spectra and auto spectra in order to characterize for the spatial distribution of the full-scale buffeting forces. It is assumed so far that the coherence of buffeting forces is similar to that of the wind turbulence, therefore the empirical exponential formulae based on coherence of turbulence have been widely used in the gust response theory. However, some literatures pointed out that the coherence of force exhibits higher than that of turbulence thanks to series of physical measurements (eg., Larose et al. 1997, Jakobsen et al. 1997, Kimura et al. 1997, Matsumoto et al. 2003). Mechanism of the higher coherence of the buffeting forces as well as effects of not only the spanwise separation, the ongoing flow conditions but also of the bluff body flow due to wind-structure interaction on the coherences of turbulence and buffeting forces should be investigated for more understanding and clarification. Intermittent distribution and instantaneous correspondence in both the frequency domain and the time domain between the coherence of turbulence and that of forces also require to be studied.

The buffeting response analysis of bridges can be treated by either frequency-domain or time-domain approach. The frequency-domain buffeting analysis has first introduced for civil engineering applications by Davenport (1962), Irwin (1974) thanks to spectral analysis method and so far still applied dominantly and consistently, however, the most disadvantageous is that this only applies for linear behavior analysis. Recently, linear and non-linear buffeting response analysis can be solved under the time-domain approach. Time-domain buffeting forces can be transferred into frequency-domain ones thanks to the Fourier Transform, moreover, the spectral analysis method and modal analysis technique in generalized coordinates has been applied for step transforms from spectral functions of 2D buffeting forces to that of 3D buffeting ones, and

from spectral function of 3D buffeting forces to that of response, and from response of single mode to that of multi-modes. The correction functions have been added to carry out such step transforms. This method is effective and dominant practices in civil engineering applications, however, incapable to deal with non-linear structural behavior that being common sense for buffeting response analysis of recently long-span flexible cable-supported bridges. In the time-domain buffeting analysis, the external wind forces can be treated as multi-dimensional stationary random processes and subjected to discrete nodes in structure. Discretization of time-history wind forces at structural nodes is due to simulation techniques of random processes. Time-history analysis has been used to predict the buffeting response. The most applicable advantage is that so far non-linear structural behavior only solved under this method, therefore some non-linear finite element method computer programs with time-history analysis can be exploited for non-linear buffeting response prediction. This time-domain method, however, is time-consuming and complicated due to simulating of the random turbulent field as well as modeling and transforming the frequency-dependant correction functions such as the admittance function into time-dependant functions.

As a principle, the multi-degree-of-freedom motion equations of structures are decoupled into the generalized coordinates and the structural modes due to the structural modal transformation. Conventional methods of the gust response prediction of structures has used concept of the joint acceptance function to decompose the full-scale turbulent-induced forces, then to be associated with the generalized structural coordinates (Davenport 1962). New approach of the gust response prediction has been proposed recently by Carassale et al. 1999, Solari and Carassale 2000 with concept of the double modal transformations. In this approach, the structural modes are associated with turbulent-induced loading modes that are decomposed by proper transformations in order to determine the gust response of structures. The proper transformations can be carried out by new technique, known as proper orthogonal decomposition.

Proper orthogonal decomposition, or known as Karhunen-Loeve decomposition (Lumley 1970), has been applied popularly in many engineering fields including random processes/fields, stochastic methods, image processing, data compression, system identification and control and so on (Liang et al. 2002). In the wind engineering, the proper orthogonal decomposition has been used in the three following topics: i) stochastic decomposition and order-reduced modeling of random processes/fields and induced pressure/forces, ii) representation and simulation of random turbulent fields and iii) stochastic response of structures. The proper orthogonal decomposition has been applied to optimally approximate the multi-variate random processes through use of low-order basic orthogonal vectors from modal decomposition (eigenvector problem) of either zero-time-lag covariance matrix or cross spectral density one of

this multi-variate random field. According to type of basic matrix in the modal decomposition, the proper orthogonal decomposition has been branched by either covariance proper transformation or spectral proper transformation (Solari and Carassale 2000). Main advantage of the proper orthogonal decomposition is that the multi-variate correlated random processes/ fields can be decomposed and described in such simplified way as a combination of a few low-order dominant eigenvectors (modes) and omitting higher-order ones that is convenient for order-reduced representation of the random field, including random-induced force modeling and random response prediction. Furthermore, because the random field is described via few dominantly low-order orthogonal modes, therefore it is usually expected that these dominant modes can represent to any typically physical cause occurring on structure.

Objectives of studies in this dissertation are hinged as follows:

Firstly, mechanism of high correlation of the buffeting forces and effects of the turbulent flow conditions and bluff body flows on this high correlation are going to be studied via the spatial distribution and correlation coefficients of the unsteady pressure fields in the unsteady flows

Secondly, correction functions such as the aerodynamic admittance function and the spatial coherence function which are used so far in the unsteady buffeting forces and gust response prediction of bridges are going to be discussed thanks to some new approaches such as the nonlinear, multivariate aerodynamic admittance and the wavelet transform-based coherence. Effects of the ongoing flow conditions, the bluff body flow, the Karman vortex on the force coherence as well as the temporo-spectral distribution of coherence will be investigated for more knowledge on the spatial coherence function.

Finally, the proper orthogonal decomposition and its proper transformation branches are going to be applied and discussed for some recent topics in the wind engineering field: (i) analysis and identification of unsteady pressure field; (ii) representation and simulation of the random turbulent field; stochastic gust response prediction of bridges and (iii) the gust response prediction of bridges.

1.4 Structure and outlines of study

The dissertation aims to present and discuss about the unsteady buffeting forces and the gust response prediction of bridges with investigation on recent limitations and uncertainties in usage of the admittance function and coherence one as well as with emphasis on the proper orthogonal decomposition applications and its proper transformation branches. Moreover, higher correlation of the buffeting forces and influence of the bluff body flow will be

investigated on the spatial distribution and correlation of the unsteady pressure fields around physical cylinders. Three potential applications of the proper orthogonal decomposition to the wind engineering so far will be presented consisting of (i) simulation of the multi-variate spatially-correlated turbulent field around bridge deck; (ii) analysis and identification of the random pressure fields around some typical rectangular sections; and (iii) new approach in the gust response prediction of bridges. Both the physical measurements in the wind tunnel experiments and numerical examples will be used in this thesis.

The dissertation is organized by the 10 chapters including the general introduction and the conclusion. The outlines of main chapters are briefly presented as follows:

In the Chapter 2, the unsteady buffeting forces and gust response prediction of bridges formulated in the frequency domain and the time domain are going to be discussed as background research. Current assumptions and uncertainties in the unsteady buffeting forces and gust response evaluation which are mainly related to usage of the correction functions such as the frequency-dependant aerodynamic admittance function and the spatial coherence function are reviewed.

In the Chapter 3, the spatial distribution and correlation of the unsteady pressure fields around some rectangular cylinders under some typical unsteady flows are going to be studied with emphasis on higher correlation mechanism of the buffeting forces and influence of the bluff body flow around experimental models. Physical measurements of the unsteady pressure fields on some rectangular cylinders B/D=1 (without and with installation of splitter plate at the wake of model) and B/D=5 in some unsteady flows are carried out in the wind tunnel.

In the Chapter 4, the aerodynamic admittance functions between turbulence and induced buffeting forces will be studied with new concepts of nonlinear and multivariate admittance. Wind turbulence and turbulent-induced buffeting forces are measured directly on some physical models B/D=5 and B/D=20 under the turbulent flows in the wind tunnel.

In the Chapter 5, the temporal-spectral coherent structures of wind and pressure will be studied using both Fourier coherence and wavelet coherence. Effects of spanwise separations, bluff body flow and turbulent flow conditions on coherent structures of turbulence and pressure, comparison between wind and pressure coherence as well as intermittent distribution of wavelet spectrum and wavelet coherence will be discussed. Physical measurements of the surface pressure and turbulence have been carried out on some typical rectangular cylinders with side

ratios B/D=1 (without and with splitter plate at wake region) and B/D=5 under the artificial turbulent flows in the wind tunnel.

In the Chapter 6, the proper orthogonal decomposition and its proper transformations of the fluctuating pressure fields on some typical rectangular cylinders will be presented. Both recent branches: the covariance matrix and the cross spectral matrices of these pressure fields are applied. Analysis, identification and order-reduced reconstruction of the pressure fields will be carried out basing on characteristic functions resulted from both covariance matrix-branched and cross spectral matrix-branched proper orthogonal decompositions: covariance eigenvalues, covariance eigenvectors (covariance modes), covariance principal coordinates and spectral eigenvalues, spectral eigenvectors (spectral modes). Moreover, the linkage between the lowest modes and the physical phenomena can be revealed with combination of past understanding and knowledge of the bluff body flows and physical causes. The fluctuating pressure field has been determined through physical measurements on some rectangular models with side ratios of B/D=1 and B/D=5 in the turbulent flows in the wind tunnel.

In the Chapter 7, the representation, modeling and simulation of the multi-variate spatially-correlated turbulent field are going to be presented with emphasis on spectral representation methods using the proper orthogonal decomposition and its spectral proper transformation. Simulation of the multi-variate turbulent field along a bridge girder will be carried out as a numerical example.

In the Chapter 8, the spectral matrix-based proper orthogonal decomposition and its spectral proper transformation will be presented and application to decoupling the multi-variate turbulent loading processes. New comprehensive approach on the gust response prediction of structures then will be formulated using the spectral proper transformation with emphasis on numerical example of cable-stayed bridge. The turbulent-induced forces based on corrected quasi-steady theory with aerodynamic admittance also are used for more refinement. Numerical example of cable-stayed bridge will be taken into account for illustration and demonstration

In the Chapter 9, it is presented the application of the covariance matrix-branched proper orthogonal decomposition and its covariance proper transformation to decompose the random turbulent loading processes, then to formulate the time-domain gust response of structures. The Newton-beta integration method is also applied to obtain the time-domain solution of the gust responses in the generalized and global coordinates. Numerical example of cable-stayed bridge will be also taken into account for illustration and demonstration.

Chapter 2

Unsteady Buffeting Forces and Gust Response of Bridges

2.1 Introduction

The gust response prediction of bridges due to the turbulent-induced buffeting forces is usually required a must among aerodynamic responses, especially for long-span bridges. The gust response in the atmospheric turbulent flows can affect an extreme deflection and aerodynamic fatigue of bridge and its structural components. Conventionally, the buffeting forces for bridge sections are commonly determined under two main theories: (i) quasi-steady theory and (ii) strip theory which both are origin from the aeronautical field. In the former, it implies that the buffeting forces do not depend on the frequency and are proportional to instantaneous turbulent components as well as some linearized approximations are used to formulate the quasi-steady buffeting forces , whereas the buffeting forces on each deck element is not influenced by those on neighboring elements in the latter. However, two theories are not valid in the almost cases of practical engineering structures, and many certainties can be produced. In the modern buffeting analysis theory, some correction functions such as aerodynamic admittance function and spatial coherence function have been supplemented to treat with limitations of both the quasi-steady theory and strip one. Many literatures, however, indicated that recent models of the correction functions themselves contain limitations and uncertainties. The unsteady buffeting forces can be formulated in cases the correction functions are added. Moreover, it is observed that the unsteady aerodynamic forces are produced due to the wind-structure interaction and the bluff body flow at low reduced velocities, so-call ‘fluid memory effect’ should be considered in order to be taken the past histories into account for the present response. Therefore, the complete unsteady buffeting forces which account the fluid memory effect can be formulated in the time domain using either the indicial response function or impulse response function with convolution integration operation.

In this chapter, the unsteady buffeting forces and gust response prediction of full-scale bridges

in the frequency domain and the time domain will be presented as background research. Current assumptions and uncertainties due to the quasi-steady theory and the strip theory, as well as usage of correction functions in the unsteady buffeting forces and the gust response prediction of bridges will be discussed.

2.2 Methodological background

It is generally agreed that the gust response prediction of bridges can be treated by either analytical methods or experimental approaches. Analytical gust response of bridges can be formulated in either the frequency domain analysis or the time domain, in which the frequency-domain buffeting analysis has been applies for linear structural behaviors in the former, whereas the time-domain analysis has been applied to treat with geometrical and aerodynamic nonlinearities, unsteady aerodynamic forces as well that being increasingly common-sense for buffeting response prediction of 'flexible' long-span bridges in the later.

In the frequency-domain approach or indirect buffeting analysis, the Fourier transform is applied in associated with statistical computation and spectral analysis technique. The correction functions have been added in transformation steps. Furthermore, the modal analysis technique in generalized coordinates has been applied for decomposition from the multi-degree-of-freedom motion system into the single-degree-of-freedom. Thus, the core of the computational frequency-domain buffeting analysis relates to modal decomposition method and modal-based response superposition technique that are associated with the spectral analysis method. Stepwise procedure for the gust response prediction of bridge in the frequency domain is expressed in Figure 2.1. Spectral transformations in frequency-domain gust response are shown in Figure 2.2.

In the time-domain approach or direct buffeting analysis, the turbulent loading can be treated as multi-variate random Gaussian processes and acting on discrete structural nodes. Simulation techniques are usually used in many cases to generate the turbulent loading at structural nodes. Either unsteady buffeting forces (using correction functions as the aerodynamic admittance and coherence functions) or complete unsteady buffeting forces (using the indicial response functions or the impulse response function) are formulated in the time and frequency domain. Discrete frequency-dependant functions can be transformed into the continuous time functions using some techniques as the rational function approximation. Direct integration methods are applied to obtain time-history solutions of the generalized responses, and time-histories of global responses can be estimated accordingly. Geometrical nonlinearity and aerodynamic one can be taken into account in this time-domain buffeting analysis. Time domain procedure is shown in Figure 2.3.

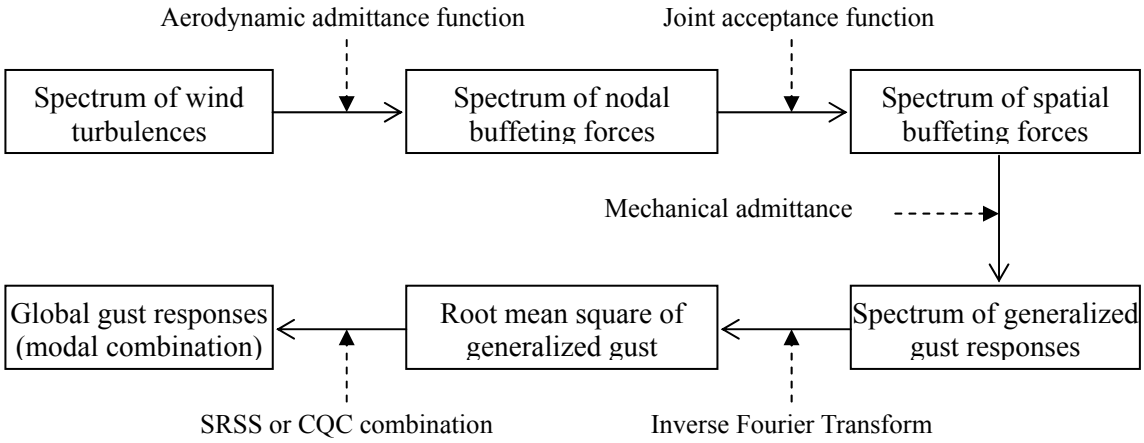

Fig 2.1 Stepwise flow for gust response prediction in the frequency domain

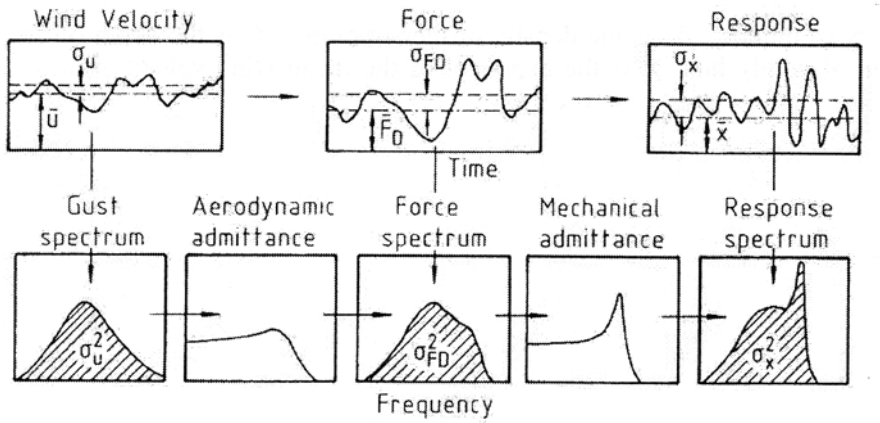

Fig. 2.2 Spectral transformations in frequency-domain gust response (Davenport 1967)

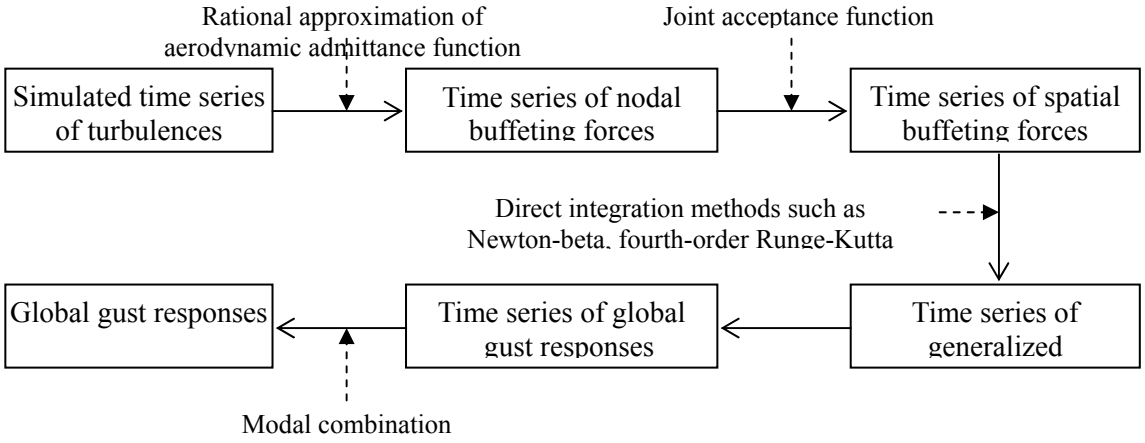

Fig 2.3 Stepwise flow for gust response prediction in the time domain

2.3 Literature reviews on buffeting forces and gust response prediction

It is supposed that the earliest works on computational buffeting response carried out for airplane's wings and airfoils carried out by some authors as Wagner 1925, Kusner 1936, Sears 1941 and Liepmann 1952. In their approach, the indicial function in the time domain was used to express relationship between the unsteady aerodynamic lift forces and instantaneous angle of attack, instantaneous force coefficient. In the Wagner 1925, the indicial functions were expressed under empirical form of polynomial one on the Laplace variable. Kusner 1936 developed the Wagner's problem to solve unsteady aerodynamic response of airfoil under uniform gust flow, whereas Sears 1941 obtained solution for the vertical gust flow. Liepmann 1952 went further with the theoretical buffeting analysis for the airplane's wings which the spectral and statistical analyses were introduced. Liepmann 1952, moreover, proposed the empirical formula for the frequency-dependant aerodynamic admittance as approximation of the Sears function. Two theories as the strip theory and the quasi-steady theory have been applied as the main milestone for the gust response problem. It is generally agreed that, however, framework on the buffeting forces and the gust response prediction of civil structures like towers and bridges in the frequency domain proposed by Davenport 1962 which the spectral analysis and statistical computation in associated with the modal-based structural analysis were cored in his theory on the gust response prediction of bridges. He also proposed to use so-called correction functions such as aerodynamic admittance function, coherence function to treat with some limitations of the quasi-steady theory and the strip theory. This spectral-based computational procedure (the Davenport's method) for the gust response prediction of towers, tall buildings and bridges has still been applied so far. Though some assumptions and uncertainties accepted for their existence, but the Davenport's method basically validates for the gust response prediction of practical structures and bridges. Iwin 1977 discussed about the Davenport's method with some developments and his practical application for the gust response analysis of the Lions' Gate suspension bridge. He suggested usage of the von Karman-typed power spectral densities for the atmospheric turbulence and coherence of the buffeting forces.

The buffeting forces generally depend on the geometrical configuration of bridge deck, ongoing turbulent flow and reduced frequency. The quasi-steady buffeting forces firstly proposed using the quasi-steady theory in the time domain. These buffeting forces are corrected by supplementing the frequency-dependant aerodynamic admittance function to account difference between the turbulence and the buffeting forces in the frequency domain as well as to cope with limitation of the quasi-steady theory (Davenport 1962, Iwin 1977). With account of the spatial

distribution characteristic of the buffeting forces, the spatial coherence function is added to treat with limitation of the strip theory, the unsteady buffeting forces are formulated. At low reduced velocities, however, the wind-structure interaction and the bluff body flow affect considerably on the unsteady buffeting forces, the so-called unsteady fluid memory effect must be taken into account (Scanlan 1974, Lin an Yang 1983, Chen and Kareem 2002). In these cases, the unsteady response of structures is affected by not only present state but also past history of response. The complete unsteady buffeting forces are also modeled comprehensively in the time domain using either the indicial response functions (Wagner 1925, Kussner 1936, Scanlan 1976&1993, Costa et al. 2007) or the impulse response functions (Lin and Yang 1983, Scanlan 1993, Chen and Kareem 2002), the convolution operation is also used in this time-domain formulation. Discrete frequency-dependant functions in the frequency domain can be transformed into the time-domain continuous function by using some techniques such as the rational function approximation (Chen and Kareem 2002).

Coupling between the buffeting forces and self-excited aeroelastic forces must be taken into account for the gust response prediction of structures because the unsteady aerodynamic forces are combined potentially by the turbulent-induced buffeting forces and the self-excited flutter ones in high reduced velocity range. It should be born in mind that the self-excited flutter forces can influence on the gust response of structures due to the aeroelastic forces related directly to response of structures themselves, but inversely the turbulent-induced forces can not affect on the critical condition of the aeroelastic instability of structures due to the aerodynamic damping-related mechanism. Frequency-domain formulation of the gust response prediction of bridges with the aeroelastic forces coupling developed and discussed by some authors (eg., Matsumoto et al. 1994, Jain et al. 1996, Katsuchi et al. 1997 and so on). Some studies and experiments (Matsumoto et al. 1997, Scanlan et al. 1999) indicated that the flutter derivatives determined in the turbulent wind are more favorable condition for critical instability than that in smooth wind, however, some recent studies also pointed out in some cases that flutter derivatives in the turbulent wind impress the flutter instability. The gust response of bridges is formulated in the time domain using the rational function approximation and the state-space transformation in some literatures (eg., Matsumoto et al. 1996, Chen, Matsumoto et al. 2000, Aas-Jakobsen and Strommen 2001, Borri et al. 2005 and so on).

Prospectively, the state-of-the-art buffeting response prediction have cored on some computational techniques and research orientations, new fronts such as follows: (i) New approaches on the correction functions as the aerodynamic admittance and coherence for refinement of the gust response prediction; (ii) Time-domain gust response prediction and the gust response controls in coupling with the aeroelastic forces and with account of geometrical and

aerodynamic nonlinearities; and (iii) New approaches on the gust response prediction using some other tools such as the proper orthogonal decomposition (POD).

2.4 Current assumptions and uncertainties

Until now, the unsteady buffeting forces and the gust response prediction of bridges still exist some main assumption and uncertainties as follows:

(1) *Wind simulation*: Unsteady buffeting loading formulated from atmospheric turbulence is considered as the stationary random processes. So far, the ongoing wind turbulence itself is assumed as stationary Gaussian random processes, however, the turbulence is generated by not only ongoing turbulent flow itself, but the wind-structure interaction and the bluff body flow. Some studies indicated that unsteady turbulence and forces can be generated due to wind-structure interaction at high reduced velocities and the fluid memory effect should be taken into account for the unsteady buffeting forces. Moreover, turbulent simulation that is used for the unsteady forces in the time domain always contain source of input uncertainty. Therefore, accurate modeling, representation and simulation of the wind turbulence still remain further interesting questions.

(2) *Quasi-steady theory*: The static aerodynamic coefficients with the relative attacked angles for modeling the unsteady forces have been approximately linearized around balanced attacked angle (usual as zero angle) in the quasi-steady theory. The relative unsteady velocity, moreover, also has been simplified and linearized under the quasi-steady theory. Another interpretation of this quasi-steady theory is the instantaneous buffeting forces are proportional to the instantaneous fluctuating velocities, or spectral contribution of the buffeting forces is similar to that of the turbulence in the frequency domain. Although, the quasi-steady theory is corrected via using the frequency-dependant aerodynamic admittance, but uncertainty still remains from linearized approximations and expansion used in this theory.

(3) *Strip theory*: It is assumed that the unsteady buffeting forces on certain finite element (or strip) are generated by only the turbulence on this element. However, the turbulent field behaviors as typical coherent, in which the turbulence at any point is affected from surrounding points in the field. Spatial distribution characteristic of the unsteady buffeting forces play very important role in the gust response of bridges. It is generally agreed that the strip theory can be applied for the buffeting response prediction when some following conditions are validated: (i) The scale of turbulence (L_{ux}) are much higher than the chord-wise width of bridge deck. This condition might be invalid in case the reattachment and the local separation bubble occur in the chordwise model surface. Influence of ratios of L_{ux}/B and B/D on the occurrence of separation bubble, reattachment and spatial

distribution of fluctuating surface pressure must be clarified on further studies; (ii) Only 2D wind-structure interaction is taken in consideration, the influence of 3D interaction or one of structural components (stays, towers, curb, handrail…) on the ongoing flow might not occur, this also means that structure do not obstacle in the ongoing flow; (iii) The wind direction might be relatively normal to structure axis.

It seems that the strip theory is valid with streamlined girders and thin plates, however, it is inapplicable in cases of the bluffer bodies, when the wind-structure interaction and the bluff body flow exhibit strongly.

(4) *Correction functions*: The aerodynamic admittance function and the spatial coherence function have been used to treat with limitations of the quasi-steady theory and the strip one as well as to formulate the unsteady buffeting forces. Firstly, the frequency-dependant aerodynamic admittance is used to compensate difference between the spectrum of turbulence and the spectrum of unsteady buffeting forces in the frequency domain. So far, the quasi-steady single-variate aerodynamic admittance function is extracted from physical measurements as the transfer function between the turbulences and the buffeting forces. Recently, some literatures discussed new approaches on determination of the admittance function using nonlinear and multi-variate admittance functions, complex admittance function and so on. Secondly, the spanwise coherence is used in account of spanwise distribution of the full-scale buffeting forces. It is also assumed coherence of forces is similar to that of turbulence, thus the turbulent coherence has been used for replacing the force coherence in the experiments and for formulating empirical formula of the force coherence. Some recent researches pointed out that the force coherence always exhibits more-correlated than turbulent coherence. This higher coherence can be convinced with the wind-structure interaction and the bluff body flow (Matsumoto et al. 2003).

(5) *Coupling between structural modes*: Under the assumption that natural frequencies are not be close enough that multimode coupling might not occur, thus the structural responses are superposed among modal responses (mode-by-mode superposition) thanks to the Squared Root of Sums of Squares (SRSS) principle. Also the superposition principle of the response of each mode can be applied under the linear behavior of structure. For long-span flexible bridges (cable-supported bridges), free frequencies of fundamental modes trend low values and close together, thus under mechanical oscillations and aerodynamic vibrations, they must have coupled. When fundamental modes couple or nonlinear approach accounts, the modal superposition and generalization might not be active. Further superposition techniques of generalized response should be proposed.

2.5 Unsteady buffeting forces

In the time domain, the uniform buffeting forces per unit deck length (consisting of Lift, Drag, Moment: $L_b(t)$, $D_b(t)$, $M_b(t)$) are determined in the time domain from the turbulent field u(t), w(t) due to the corrected quasi-steady theory (Davenport 1962):

$$L_b(t)=\frac{1}{2}\rho U^2 B[C_L(\alpha_0)\chi_{Lu}(n)\frac{2u(t)}{U}+(C_L^{'}(\alpha_0)+C_D(\alpha_0))\chi_{Lw}(n)\frac{w(t)}{U}] \qquad (2.1\text{-a})$$

$$D_b(t)=\frac{1}{2}\rho U^2 B[C_D(\alpha_0)\chi_{Du}(n)\frac{2u(t)}{U}+(C_D^{'}(\alpha_0)-C_L(\alpha_0))\chi_{Dw}(n)\frac{w(t)}{U}] \qquad (2.1\text{-b})$$

$$M_b(t)=\frac{1}{2}\rho U^2 B^2[C_M(\alpha_0)\chi_{Mu}(n)\frac{2u(t)}{U}+C_M^{'}(\alpha_0)\chi_{Mw}(n)\frac{w(t)}{U}] \qquad (2.1\text{-c})$$

where C_L, C_D, C_M: aerodynamic static coefficients at balanced angle of attack α_0 (usual $\alpha_0 = 0^o$); $C_L^{'}, C_D^{'}, C_M^{'}$: first derivatives with respect to angle of attack at balanced angle $C_F^{'} = {dC_F(\alpha)}/{d\alpha}\big|_{\alpha_0=0}$, $F = L, D, M$; $\chi_{F\upsilon}(n)$ $(F = L, D, M; \upsilon = u, w)$: aerodynamic transfer functions between turbulent components and turbulent-induced forces (their absolute magnitudes refer as aerodynamic admittance functions); ρ, B, U: air density, width and mean velocity, respectively.

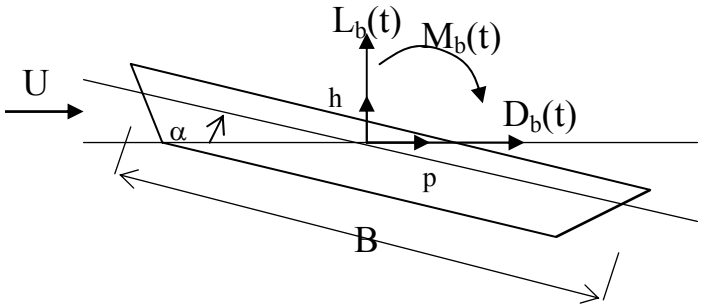

Fig. 2.4 Uniform buffeting forces on bridge deck

In the frequency domain, transforming the time-domain uniform buffeting forces into a form of power spectral density using second-order Fourier transform, omitting cross correlation components between u(t) and w(t), the power spectral densities of the uniform buffeting forces can be obtained:

$$S_L(n)=(\frac{1}{2}\rho U^2 B)^2[C_L^2\chi_{Lu}^2(n)\frac{4S_{uu}(n)}{U^2}+(C_L^{'}+C_D)^2\chi_{Lw}^2(n)\frac{S_{ww}(n)}{U^2}] \qquad (2.2\text{-a})$$

$$S_D(n)=(\frac{1}{2}\rho U^2 B)^2[C_D^2\chi_{Du}^2(n)\frac{4S_{uu}(n)}{U^2}+(C_D^{'}-C_L)^2\chi_{Dw}^2(n)\frac{S_{ww}(n)}{U^2}] \quad (2.2\text{-b})$$

$$S_M(n)=(\frac{1}{2}\rho U^2 B^2)^2[C_M^2\chi_{Mu}^2(n)\frac{4S_{uu}(n)}{U^2}+C_M^{'\,2}\chi_{Mw}^2(n)\frac{S_{ww}(n)}{U^2}] \quad (2.2\text{-c})$$

where $S_L(n), S_D(n), S_M(n)$: power spectra of lift, drag and moment, respectively; $S_{uu}(n), S_{ww}(n)$: auto power spectra of uni-variate turbulent processes u(t), w(t).

It is indicated that at low and medium reduced velocity ranges, however, the unsteady fluid dynamics must account for both past and present motion histories, therefore the fluid memory effect of the unsteady fluid flow should be considered in the unsteady buffeting forces. Therefore, complete unsteady buffeting forces can be formulated comprehensively in the time domain using convolution integration operation and response functions. The response functions can exploit either the indicial response functions or the impulse response functions.

The unsteady buffeting forces using the indicial response functions are determined in the time domain as follows (Scanlan 1974, Chen and Kareem 2002, Borri et al. 2005):

$$L_b(t)=\frac{1}{2}\rho U^2 B\{\int_{-\infty}^{t} 2C_L\Phi_{Lu}(t-\tau)\frac{\dot{u}(\tau)}{U}d\tau+\int_{-\infty}^{t}(C_L^{'}+C_D)\Phi_{Lw}(t-\tau)\frac{\dot{w}(\tau)}{U}d\tau\} \quad (2.3\text{-a})$$

$$D_b(t)=\frac{1}{2}\rho U^2 B\{\int_{-\infty}^{t} 2C_D\Phi_{Du}(t-\tau)\frac{\dot{u}(\tau)}{U}d\tau+\int_{-\infty}^{t}(C_D^{'}-C_L)\Phi_{Dw}(t-\tau)\frac{\dot{w}(\tau)}{U}d\tau\} \quad (2.3\text{-b})$$

$$M_b(t)=\frac{1}{2}\rho U^2 B^2\{\int_{-\infty}^{t} C_M\Phi_{Mu}(t-\tau)\frac{\dot{u}(\tau)}{U}d\tau+\int_{-\infty}^{t}C_M^{'}\Phi_{Mw}(t-\tau)\frac{\dot{w}(\tau)}{U}d\tau\} \quad (2.3\text{-c})$$

where $\Phi_{Lu}, \Phi_{Lw}, \Phi_{Du}, \Phi_{Dw}, \Phi_{Mu}, \Phi_{Mw}$: indicial response functions defined as relation functions between lift, drag, moment and indicial first-order derivatives of turbulent components u(t), w(t).

The unsteady buffeting forces using the impulse response functions are modeled in the time domain as follows (Lin and Yang 1983, Chen and Kareem 2002):

$$L_b(t)=\frac{1}{2}\rho U^2\{\int_{-\infty}^{t} I_{Lu}(t-\tau)\frac{u(\tau)}{U}d\tau+\int_{-\infty}^{t}I_{Lw}(t-\tau)\frac{w(\tau)}{U}d\tau\} \quad (2.4\text{-a})$$

$$D_b(t)=\frac{1}{2}\rho U^2\{\int_{-\infty}^{t} I_{Du}(t-\tau)\frac{u(\tau)}{U}d\tau+\int_{-\infty}^{t}I_{Dw}(t-\tau)\frac{w(\tau)}{U}d\tau\} \quad (2.4\text{-b})$$

$$M_b(t)=\frac{1}{2}\rho U^2\{\int_{-\infty}^{t} I_{Mu}(t-\tau)\frac{u(s)}{U}d\tau+\int_{-\infty}^{t}I_{Mw}(t-\tau)\frac{w(\tau)}{U}d\tau\} \quad (2.4\text{-c})$$

where $I_{Lu}, I_{Lw}, I_{Du}, I_{Dw}, I_{Mu}, I_{Mw}$: impulse response functions defined as relation functions between lift, drag, moment and impulse turbulent components u(t), w(t).

The inter-relations between the indicial response functions and the impulse response functions can be deduced as follows (Chen and Kareem 2002):

$$I_{Lu}(s) = 2BC_L\left[\Phi_{Lu}(0)\delta(s) + \Phi'_{Lu}(s)\right],\ \ I_{Lw}(s) = B(C'_L + C_D)\left[\Phi_{Lw}(0)\delta(s) + \Phi'_{Lw}(s)\right] \quad (2.5\text{-a})$$

$$I_{Du}(s) = 2BC_D\left[\Phi_{Du}(0)\delta(s) + \Phi'_{Du}(s)\right],\ \ I_{Dw}(s) = B(C'_D - C_L)\left[\Phi_{Dw}(0)\delta(s) + \Phi'_{Dw}(s)\right] \quad (2.5\text{-b})$$

$$I_{Mu}(s) = 2BC_M\left[\Phi_{Mu}(0)\delta(s) + \Phi'_{Mu}(s)\right],\ \ I_{Mw}(s) = BC'_M\left[\Phi_{Mw}(0)\delta(s) + \Phi'_{Mw}(s)\right] \quad (2.5\text{-c})$$

where s: time-nondimensional variable $s = Ut/B$; δ: Dirac delta function.

The inter-relations among parameters of the unsteady buffeting forces such as aerodynamic admittance functions, indicial functions and impulse functions can be obtained as follows (Chen and Kareem 2002):

$$\bar{I}_{Lu} = 2BC_L\chi_{Lu}(n);\ \ \bar{I}_{Lw} = B(C'_L + C_D)\chi_{Lw}(n) \quad (2.6\text{-a})$$

$$\bar{I}_{Du} = 2BC_D\chi_{Du}(n);\ \bar{I}_{Dw} = B(C'_D - C_L)\chi_{Dw}(n) \quad (2.6\text{-b})$$

$$\bar{I}_{Mu} = 2B^2C_M\chi_{Mu}(n);\ \bar{I}_{Mw} = B^2C'_M\chi_{Mw}(n) \quad (2.6\text{-c})$$

$$\bar{\Phi}_{F\upsilon} = \chi_{F\upsilon}(n) \quad (2.6\text{-d})$$

where $\bar{I}_{F\upsilon}$: Fourier transform of the impulse response functions ($F = L, D, M\ \ \upsilon = u, w$) as $\bar{I}_{F\upsilon} = \int_0^\infty I_{F\upsilon}(t)e^{-i\omega t}dt = \int_0^\infty I_{F\upsilon}(s)e^{-iKs}ds$; $\bar{\Phi}_{F\upsilon}$: Laplace transform of the indicial response functions ($F = L, D, M\ \ \upsilon = u, w$) as $\bar{\Phi}_{F\upsilon} = (ik)\int_0^\infty \Phi_{F\upsilon}(s)e^{-iks}ds$.

2.6 Frequency-domain gust response prediction

The spectral-based gust response prediction of full-scale bridges in the frequency domain is briefly presented hereafter. Multi-degree-of-freedom motion equation of structures immersed in the atmospheric turbulent flow subjected to the turbulent-induced forces is expressed:

$$M\ddot{X}(t) + C\dot{X}(t) + KX(t) = F_b(t) \quad (2.7)$$

where *M, C, K*: globally mass, damping and stiffness matrices, respectively; $X, \dot{X}, \ddot{X}$: deflection vector and its derivative vectors; F_b(t): full-scale buffeting forces.

Transforming into generalized coordinates normalized by the mass matrix using $\overline{M}$ truncated low-order structural modes ($\overline{M} << M$, M: number of dynamic degree-of-freedom of structure), it satisfies:

$$X(t) = \Phi\xi(t) \approx \sum_{i=1}^{\overline{M}} \phi_i \xi_i(t) \; ; \Phi^T M \Phi = I \; ; \;\; \Phi^T C \Phi = \Xi \; ; \Phi^T K \Phi = \Omega \tag{2.8}$$

where ξ : generalized coordinate vector $\xi(t) = \{\xi_1(t), \xi_2(t), ..., \xi_M(t)\}^T$; Φ : modal matrix $\Phi = [\phi_1, \phi_2, ..., \phi_M]$; I: unit matrix; Ξ : diagonal damping matrix; Ω : diagonal stiffness matrix containing squared natural frequencies $\Omega = diag(\omega_1^{\,2}, \omega_2^{\,2}, ..., \omega_M^{\,2})$. Single-degree-of-freedom motion equation in the i-th generalized coordinate excited by generalized buffeting forces can be obtained accordingly:

$$\ddot{\xi}_i(t) + 2\zeta_i \omega_i \dot{\xi}_i(t) + \omega_i^2 \xi_i(t) = \phi_i^T F_b \; (t) \tag{2.9}$$

where $\xi_i(t)$: i-th generalized coordinate; ω_i, ζ_i : circular frequency and damping ratio, respectively.

Uniform buffeting forces in unit length has been defined in Eqs.(2.1-a,b,c). However, the buffeting forces are correlated due to their spatial distribution, thus the full-scale buffeting forces must be taken into account this spatial force distribution. Difficulty here is how to decompose the full-scale buffeting forces onto the generalized coordinate in order to determine the generalized response. Davenport 1962 proposed a decomposition technique basing on the joint acceptance function which characterize for combination between the coherence function and the structural modal functions.

The single-degree-of-freedom equation Eq.(2.9) in the i-th generalized coordinates is transformed in to frequency domain using second-order Fourier transform:

$$S_{\xi,i}(n) = | H(n_i) |^2 \;\; \phi_i^T S_{F,i}(n) \phi_i \tag{2.10}$$

where $S_{\xi,i}(n)$, $S_{F,i}(n)$: power spectral densities of the i-th generalized response and of generalized full-scale buffeting forces, respectively; $| H(n_i) |^2$: mechanical admittance function or frequency response function corresponding to natural frequency n_i of the i-th structural mode as $| H(n_i) |^2 = \left[(1 - n^2/n_i^2)^2 + 4\zeta_i^2 \, n^2/n_i^2 \right]^{-1}$.

Three displacement components of bridges can be expressed such following forms as:

$$h(x,t) = \sum_i h_i(x) B \xi_i(t) \; ; \; p(x,t) = \sum_i p_i(x) B \xi_i(t) \; ; \;\; \alpha(x,t) = \sum_i \alpha_i(x) \xi_i(t) \tag{2.11}$$

where x: spanwise local coordinate; $h_i(x), p_i(x), \alpha_i(x)$: modal values corresponding to vertical, lateral and rotational displacement components.

Thus, power spectral densities of the full-scale buffeting forces associated with the i-th generalized coordinate can be obtained:

$$S_{L,i}(n)=[\frac{4L_1^2}{U^2}|J_{Lu}(n)|^2|\chi_{Lu}(n)|^2\ S_{uu}(n)+\frac{L_2^2}{U^2}|J_{Lw}(n)|^2|\chi_{Lw}(n)|^2\ S_{ww}(n)] \quad (2.12\text{-a})$$

$$S_{D,i}(n)=[\frac{4D_1^2}{U^2}|J_{Du}(n)|^2|\chi_{Du}(n)|^2\ S_{uu}(n)+\frac{D_2^2}{U^2}|J_{Dw}(n)|^2|\chi_{Dw}(n)|^2\ S_{ww}(n)] \quad (2.12\text{-b})$$

$$S_{M,i}(n)=[\frac{4M_1^2}{U^2}|J_{Mu}(n)|^2|\chi_{Mu}(n)|^2\ S_{uu}(n)+\frac{M_2^2}{U^2}|J_{Mw}(n)|^2|\chi_{Mw}(n)|^2\ S_{ww}(n)] \quad (2.12\text{-c})$$

where $L_1, L_2, D_1, D_2, M_1, M_2$: force coefficients defined as $L_1=\frac{1}{2}\rho U^2 C_{L0}B^2$, $L_2=\frac{1}{2}\rho U^2 C_L^{'}B^2$, $D_1=\frac{1}{2}\rho U^2 C_{D0}B^2$, $D_2=\frac{1}{2}\rho U^2 C_D^{'}B^2$, $M_1=\frac{1}{2}\rho U^2 C_{M0}B^2; M_2=\frac{1}{2}\rho U^2 C_D^{'}B^2;$

$|J_{F\upsilon}|^2$: joint acceptance functions defined as $|J_{L\upsilon}(n)|^2=\int_0^L\int_0^L COH_\upsilon(x_A,x_B,n)h_i(x_A)h_j(x_B)dxdx$,

$|J_{D\upsilon}(n)|^2=\int_0^L\int_0^L COH_\upsilon(x_A,x_B,n)p_i(x_A)p_j(x_B)dxdx$, $|J_{M\upsilon}(n)|^2=\int_0^L\int_0^L COH_\upsilon(x_A,x_B,n)\alpha_i(x_A)\alpha_j(x_B)dxdx$;

$COH_\upsilon(x_A,x_B,n)$: spanwise coherence function of turbulent component υ(t) between two points x_A and x_B, $\upsilon(t)=u(t)\ or\ w(t)$.

It is noted that in the practical applications, some availably empirical formulae have been used to determine: (i) Auto spectral density function of the longitudinal and vertical turbulent components $S_{uu}(n), S_{ww}(n)$; (ii) Aerodynamic admittance functions $\chi_{F\upsilon}(n), F=L,D,M\ and\ \upsilon=u,w$; (iii) Spanwise coherence functions $COH_\upsilon(x_A,x_B,n)$.

Covariance of the generalized response can be obtained accordingly:

$$\sigma_{\xi,i}^2=\int_0^\infty S_{\xi,i}(n)dn \quad (2.12)$$

Covariance of the global response can be estimated due to the squared root of the sums of the squares (SRSS) principle as follows:

$$\sigma_X^2=\sqrt{\sum_{i=1}^{N_r}\delta_r^2 r_{r,i}^2(x)\sigma_{r,i}^2} \quad (2.14)$$

where r: displacement components $r=h,p,\alpha$; $\phi_{r,i}$: modal vector of i-th mode in displacement component r; N_r: number of combined modes for displacement component r; δ_r: parameter $\delta_r=\begin{cases}B\ when\ r=h\ or\ p\\1\ when\ r=\alpha\end{cases}$.

Due to influence of the frequency response function, the resonant responses occur locally at

the structural natural frequencies and background one at other frequencies outside these natural ones. Contribution of the resonant and background responses on the global responses can be estimated as follows:

$$\sigma_X^2 = \sigma_B^2 + \sigma_R^2 \tag{2.15}$$

where σ_B^2, σ_R^2: background response and resonant one, which are determined as:

$$\sigma_B^2 = \sqrt{\sum_{i=1}^{N_r} \delta_i^2 r_i^2(x) \int_0^\infty S_{\xi,i}(n) dn} \tag{2.16-a}$$

$$\sigma_R^2 = \sqrt{\sum_{i=1}^{N_r} \delta_i^2 r_i^2(x) \frac{\pi n_i}{4\zeta_i} S_{\xi,i}(n_i)} \tag{2.16-b}$$

In practical applications, the resonant response dominates the global response for flexible long-span structures, especially for vertical and rotational displacements, whereas the background response generally dominates for column-like structures such as tall buildings, towers.

2.7 Time-domain gust response prediction

In the time-domain gust response prediction, the time histories of turbulence acting on structural nodes are input data. The turbulent field is considered as multi-variate spatially-correlated random Gaussian processes. Since it is difficult to obtain the time histories of turbulence field in the structural site, therefore the digital simulation techniques must be required to generate the time histories of turbulence field. So far, digital simulation of the turbulent field is based on two approaches: spectral representation methods and time series representation ones. In the former, decomposition techniques such as the Cholesky' decomposition and modal one have been applied, whereas some methods such as the auto-regressive technique (AR), moving-average technique (MA) and auto-regressive and moving average technique (ARMA) include in the later.

Either the unsteady buffeting forces using the aerodynamic admittance or the complete unsteady buffeting forces using the indicial response functions or the impulse response function can be used for the time-domain buffeting analysis. Relationship between the aerodynamic admittance and the indicial response function, the impulse response function has been established. The aerodynamic admittance functions determined as discrete frequency-dependant ones which are required to transform into the continuous functions in the time-domain analysis. Rational function approximation, known as the Roger's approximation is the mostly utilized for this purpose. Aerodynamic transfer functions can be expanded using rational function approximation:

$$\chi_{F\upsilon}(n) = A_{F\upsilon,1} + (iK)\sum_{j=1}^{m_{F\upsilon}} \frac{A_{F\upsilon,j+1}}{iK + d_{F\upsilon,j}} \tag{2.17}$$

where $A_{F\upsilon,1}, A_{F\upsilon,j+1}, d_{F\upsilon,j}$ frequency-dependant coefficients ($j = 1,2,...,m_{F\upsilon}$) determined by nonlinear curve-fitting technique.

Then the indicial response function, the impulse response functions and the unsteady buffeting forces can be determined as follows (Chen and Kareem 2000):

$$\Phi_{Lw}(s) = A_{Lw,1} + \sum_{j=1}^{m_{Lw}} A_{Lw,j+1} \exp(-d_{Lw,j}s) \tag{2.18-a}$$

$$I_{Lw}(s) = B(C_D + C_L^{'})\left[\left(A_{Lw,1} + \sum_{j=1}^{m_{Lw}} A_{Lw,j+1}\right)\delta(s) - \sum_{j=1}^{m_{Lw}} A_{Lw,j+1} d_{Lw,j} e^{-d_{Lw,j}s}\right] \tag{2.18-b}$$

$$L_{b,w}(s) = \frac{1}{2}\rho U^2 B(C_D + C_L^{'})\left[\left(A_{Lw,1} + \sum_{j=1}^{m_{Lw}} A_{Lw,j+1}\right)\frac{w(t)}{B} - \sum_{j=1}^{m_{Lw}} \frac{d_{Lw,j}U}{B}\phi_{Lw,j}(t)\right] \tag{2.18-c}$$

$$\dot{\phi}_{Lw,j}(t) = -\frac{d_{Lw,j}U}{B}\phi_{Lw,j}(t) + A_{Lw,j+1}\frac{w(t)}{U} \tag{2.18-d}$$

where $\phi_{Fw,j}(t)$: augmented aerodynamic state coefficient. Noting that components of lift force due to w-turbulence are expressed here for sake of brevity. Similar formulation for other buffeting force components due to u-,w-turbulences can be deduced.

Full-scale buffeting forces over entire length L can be determined (Chen and Kareem 2000):

$$L_b(t) = L\int_0^L \left[J_{Lu}(t-\tau)L_{bu}^c(\tau) + J_{Lw}(t-\tau)L_{bw}^c(\tau)\right]d\tau \tag{2.19}$$

where subscript c denotes to the center of the element; $J_{Lu}(t), J_{Lw}(t)$: impulse functions whose Fourier transform counterparts $\overline{J}_{Lu}(t), \overline{J}_{Lw}(t)$ referred as the joint acceptance functions.

Solution of the single-degree-of-freedom equation Eq.(2.9) can be found thanks to any direct integration methods as Newton-beta or fourth-order Runge-Kutta methods. Accordingly, the time histories of generalized response and global response can be obtained.

2.8 Conclusion

Modeling of the unsteady buffeting forces and background of the gust response prediction of full-scale bridges has been presented in this chapter. Moreover, limitation and uncertainties in the theory of the gust response prediction of bridge have been also discussed.

References

Boonyapinyo, V., Miyata, T., Yamada, H. (1999), "Advanced aerodynamic analysis of suspension bridges by state-space approach", *J. Struct. Engrg.*, ASCE **125(12)**, 1357-1366.

Chen, X., Matsumoto, M., Kareem, A. (2000a), "Aerodynamic coupling effects on flutter and buffeting of bridges", *J. Engrg. Mech.*, ACSE, **126(1)**, 17-26.

Chen, X., Matsumoto, M., Kareem, A. (2000b), "Time domain flutter and buffeting response analysis of bridges", *J. Engrg. Mech.*, ACSE, **126(1)**, 7-16.

Chen, X., Kareem, A. (2002), "Advances in modeling of aerodynamic forces on bridge decks", *J. Engrg. Mech.*, ACSE, **128(11)**, 1193-1203.

Davenport, A.G.(1962), "The response of slender, line-like structures to a gusty wind", *Proc. Inst. Civ. Eng.*, 23, 389-408.

Gu, M., Chen, S.R., Chang, C.C. (2002), "Background component of buffeting response of cable-stayed bridges", *J. Wind Eng. Ind. Aerodyn.*, **90(12-15)**, 2045-2055.

Katsuchi, H., Jones, N.P., Scanlan, R.H. (1999), "Multimode coupled flutter and buffeting analysis of the Akashi-Kaikyo bridge", *J. Struct. Engrg.*, ASCE, **125(1)**, 60-70.

Jakobsen, J.B., Tanaka, H. (2003), "Modeling uncertainties in prediction of aerodynamic bridge behavior", *J. Wind Eng. Ind. Aerodyn.*, **91**, 1485-1498.

Jakobsen, K.A., Strommen, E. (2002), "Time domain buffeting response calculation of slender structures", *J. Wind Eng. Ind. Aerodyn.*, **89(15)**, 341-364.

Jain, A., Jones, N.P., Scanlan, R.H. (1996), "Coupled flutter and buffeting analysis of long-span bridges", *J. Struct. Engrg.*, ASCE, **122(7)**, 716-725.

Matsumoto, M., Chen, X., Shiraishi, H. (1994), "Buffeting analysis of long-span bridges with aerodynamic coupling", *The 13th Nat. Sympo. on Wind Eng.*, JAWE, 227-232.

Matsumoto, M., Chen, X. (1996), "Time domain analytical buffeting responses for long-span bridges", *Proc. 14th National Symposium on Wind Engineering*, JAWE 515-520.

Matsumoto, M. (2000), *Aeroelasticity and bridge aerodynamics*, Text book for Int'l Advanced Course in Wind Engineering, Genoa, Italy.

Nguyen, N.M., Miyata, T., Yamada, H., Sanada, Y. (1999), "Numerical simulation of wind turbulence and buffeting response of long-span bridges", *J. Wind Eng. Ind. Aerodyn.*, **83**, 301-315.

Pagnini, L.C., Solari, G. (2002), "Gust buffeting and turbulence uncertainties", *J. Wind Eng. Ind. Aerodyn.*, **90(4-5)**, 441-459

Chapter 3

Spatial Distribution and Correlation of Unsteady Pressure Fields around Rectangular Cylinders

3.1 Introduction

One of the key elements the gust response prediction of structures is to determine characteristic of the spatial distribution of the turbulent-induced forces (known as the buffeting forces), because atmospheric turbulence is considered as typical coherent field in which spatially mutual influence of point-like turbulences and point-like turbulent-induced forces plays very important role. This is known as limitation and uncertainty of the strip theory which has been applied for the gust response problem of airplane wings in the aeronautical field, and so far become the key point for modern analytical method to predict the random gust response of bridges and structures due to turbulent wind. Davenport 1962 mentioned about the strip theory as follow: "… *that the structures (or structural members) are sufficiently slender for the secondary spanwise flow and redistribution of pressures to be neglected, such the pressure on any section of the span are only due to the wind incident on that section,…*". This declaration suggests that the influence of structure on the ongoing turbulent flow must be not negligible. For spaced structures, spatial distribution of the buffeting forces can be considered in all three direction of turbulence corresponding to three axes of structure to which are deepwise, chordwise and spanwise directions of structural section in the cases of line-like structures such as bridges. Dimensions of turbulence can be defined via nine scales of turbulence in the three direction of turbulent wind with respect to the three structural axes. Accordingly, the strip theory might be valid only in cases that the dimensions of structures are smaller than those of ongoing turbulences in which the wind-structure interaction does not occur. Concretely, some experience indicated that this strip theory validated for the case of buffeting drag forces due to the turbulent wind where the scale of longitudinal turbulence (≈100÷200m) is much higher (about 100 times) than the depth of structures, whereas in the case of buffeting vertical forces the scale of vertical turbulence in the chordwise direction (≈30÷50m) is about 10 times higher than the width of structure (Larose

2003). This means that validation can be met only with small-size structural components immersed in large turbulence, but not to satisfy with the modern large-scale structures. Davenport 1962 also discussed that this assumption was reasonable for such structures as open lattice truss girders and cables, but not likely to be reasonable for large-scale structures such as bridges, buildings and spaced structures and so on.

In the modern large-scale structures, when the spatial scales of turbulence exhibit not much higher than structural dimensions as validation of the strip theory required, the wind-structure interaction occurs with appearance of the bluff body flow and secondary flow on the sectional surface. Therefore, effects of the bluff body flow and the secondary flow induce the redistribution of the unsteady pressure field and buffeting forces on structures as well (Davenport 1962, Matsumoto 2000). The redistribution of the unsteady pressure field on the sectional surface is convincing for the failure and uncertainty of the strip theory assumption in determination of the full-scale buffeting forces and the gust response prediction of structures. Relation between the wind turbulence and turbulent-induced pressure/ forces contains uncertainties from limitation of the quasi-steady theory and the strip theory (Kawai 1983). Theoretically, spatial distribution of the unsteady pressure and buffeting forces exhibits in all the three directions of structures, however, only the spanwise distribution play important role and is usually taken into account for the line-like structures and bridges. In the gust response analysis of bridges, the spanwise distribution of the buffeting forces is considered via the spanwise coherence function in the nodal (point-like) buffeting forces or the so-called joint acceptance function in the full-scale (line-like) buffeting forces and structurally generalized coordinates.

It is agreed that spatial distribution and coherence of the buffeting forces can be determined by experimental approach. In many practical cases, however, it is difficult to obtain characteristics of the spatial distribution of the buffeting forces. Therefore, it is generally assumed as the simplified approach that the spatial distribution and coherence of the buffeting forces are similar to those of the ongoing turbulences which are more appropriately obtained by both the experimental tools and empirical formulae. Some recent literatures, however, indicated that the spatial distribution and spanwise coherence function of the buffeting loading are better correlated than those of wind turbulence (Matsumoto et al. 2003, Larose 2003). Full-scale measurements of the buffeting lift forces accompanying with model test observations in the boxed girder deck of Ikara bridge also confirmed again the result above. Accordingly, the uncertainty of the strip theory and the coherence model so far can cause underestimation or overestimation of the buffeting response prediction.

Further studies on the spatial distribution of buffeting forces must be required for more understanding and clarification of mechanism of the better correlation of the buffeting forces than

the turbulence. The better correlation mechanism of the buffeting forces is related to the bluff body flow and secondary one which are associated with the wind-structure interaction phenomena such as formations of separation bubble and reattachment flow, of vortex shedding on the sectional surface. Obviously, as above-mentioned the mechanism of higher correlation of the buffeting forces can not be clarified by the forces themselves, but the unsteady pressure field around sectional surface. Moreover, the buffeting forces are obtained easily by the integration of unsteady pressures in chordwise strips and distributed area of pressure taps on the model section.

In this chapter, the spatial distribution and spanwise correlation of the fluctuating pressures will be discussed to be more understanding of the high correlation of the pressure and buffeting forces than the ongoing turbulence. Physical measurements of the unsteady pressure fields are carried out on some typical rectangular cylinders B/D=1 and B/D=5 in some unsteady flow conditions of smooth, turbulent and fluctuating flows with emphasis on the effect of the bluff body flow on the better correlation of the buffeting forces.

3.2 Some literature reviews on spatial distribution and correlation of unsteady pressure field

In the wind engineering and the wind effects on structures, the experimental studies of unsteady pressure fields around physical models in the wind tunnels play very important role. Especially, it is very essential in studying on the bluff body aerodynamics and mechanism of wind-structure interaction phenomena (Matsumoto 2000). It is discussed that the local pressure distribution at the leading edge zone of models can reveal generation mechanisms of aerodynamic phenomena and wind-induced vibrations (Matsumoto et al. 1996, Matsumoto 2000). Moreover, the buffeting forces (drag, lift and moment) can be estimated thanks to the spatial integration of the fluctuating pressure field around the sectional model. Chordwise distribution of the unsteady pressure field on the harmonic oscillatory models can be used for identification of the aerodynamic derivatives of the self-excited flutter forces (Matsumoto et al. 1996), that on motionless models can reveal the bluff body flow pattern around model's surface (Hiller and Cherry 1981) and so on. Studying on the spanwise distribution of the unsteady pressure field on the physical models can clarify mechanism of correlation and coherence of the buffeting forces and its dependence on the bluff body flow (Matsumoto et al. 20003, Larose 2003).

In order to investigate the relationship between chordwise distribution of the unsteady pressure field and the wind-structure interaction phenomena, Hiller et al. 1981 and Cherry et al. 1984 carried out the physical measurements of the surface pressure on the rectangular section as semi-infinity flat plate with slenderness ratio B/D=16 in smooth and turbulent flows associated

with the smoke visualization. They obtained that occurrence of the high pressure region (both normalized mean pressures and fluctuating pressures) in an effect of the separation bubble, moreover, the reattaching point appeared at transition of low mean pressure or near afterward peak of pressure fluctuation. Furthermore, the effect of free-stream turbulence affected the dimension of separation bubble in which the lengths of separation bubble were 5D (D: model depth) in the smooth flow and 3D in the turbulent flow, especially, the spanwise scale of longitudinal velocity fluctuation was found to enlarge near reattachment region. Kiya et al. 1983 also investigated the pressure distribution on the semi-infinite rectangular model. They found that the enhancement of rolled-up vortices associated with the separation bubble produced larger and larger vortices out of the separation bubble.

Matsumoto et al. 2003 focused on clarification the mechanism of higher spanwise coherence of buffeting forces due to both distribution of surface pressure and the wind-body interaction. Series of experiments on two rectangular and hexagonal sections with B/D=5 in the different unsteady flows: smooth, turbulent and 2D fluctuating flows were carried out. It is discussed the the formation of separation bubble from the leading edge to roughly 7B/8 long in smooth flow and 3B/8 long in turbulent flow with rectangular section, whereas expanding almost B in both flow conditions with hexagonal section. They suggested that the secondary spanwise flow or 3D separating bluff body flow affected by the formation of separation bubble and reattachment on model and the approaching flow itself. Investigation on surface pressure of B/D=5 sectional model in two unsteady flows: 2D (uniform) and 3D (non-uniform) gust flows were also presented by Matsumoto et al. 2004, Matsumoto et al. 2005a, Shirato, Matsumoto et al. 2005 with description of around-body flow pattern. They argued that the elongation of separation bubble due to reduced frequencies of gust flow, the formation of vortex shedding near the leading edge and the movement toward the trailing edge affected to the spanwise distribution of surface pressure. Effect of harmonic motion on pressure distribution, power spectral densities and spanwise coherence have been investigated by Matsumoto et al. 2004, they observed that pressure distribution, spanwise coherence did not be affected by the harmonic body motion.

Larose et al. 1998, Larose 2003 measured the pressure fields on streamlined boxed models with the different side ratios and with respect to different turbulent flow characteristics, attacked angles and geometrical configuration (with and without barriers). Haan et al. 1998 carried out physical measurements of the unsteady pressure field on rectangular boxed section in different turbulent flow conditions to investigate the effects of turbulence on the spanwise coherence of the surface pressures. He showed how the aerodynamic lift and moment are correlated over spanwise separations larger than any characteristic length of the turbulent flows, and discussed on how this correlation reduces with increase of intensities of turbulence and increase of scales of turbulence.

3.3 Wind tunnel experiments

Direct measurements of the unsteady surface pressures on some typical rectangular cylinders with slender ratio B/D=1, B/D=5are carried out on the open-circuit wind tunnel of the Bridge and Wind Engineering Laboratory at the Kyoto University, with a working section of 1.0m wide x 1.8m high x 6.55m long under some unsteady flows of the smooth flows, turbulent flows and three-dimensional fluctuating flows as well. In some cases of usage of the model B/D=1, the Splitter Plate (S.P) is also installed at the wake of model B/D=1 in order to study the effect of the wake flow and the Karman vortex shedding on the spatial distribution of unsteady pressure fields.

It can be predicted from previous studies that model B/D=1 is favorable for dominant formation of Karman vortex shedding in the wake of model, whereas model B/D=5 is typical for formation of separated and reattached flows on model surface. In case the splitter plate was installed in the wake of model B/D=1 in order to suppress the wake flow and effect of Karman vortex shedding. Identification of the bluff body flow is usually required for understanding flow behavior and mechanism of oscillation on physical model. The bluff body flow can be identified directly due to flow visualization techniques. Pressure distribution is also used for this purpose with experience and knowledge of flow behavior on some typical models.

3.3.1 *Experimental apparatus in turbulent flows*

Motionless models of the rectangular cylinders B/D=1 and B/D=5 are used, in which the model B/D=1 is installed without/with the Splitter Plate. Turbulent flows are generated artificially by grid devices which was located in 750mm upstream from the model's leading edge. Wind turbulence and unsteady pressures are measured in the three turbulent flows corresponding to three mean wind velocities U=3, 6 and 9m/s (flow case 1, flow case 2 and flow case 3, respectively). Basic turbulent flow parameters are determined as the turbulent intensities as follows: I_u=11.56%, I_w=11.23% (case 1), I_u=10.54%, I_w=9.28% (case 2), I_u=9.52%, I_w=6.65% (case 3). Pressure taps are arranged on one surface of models, consisting of 10 pressure taps of model B/D=1 and 19 pressure taps of the model B/D=5 in the chordwise direction (see Figure 3.1). Mean and turbulent components of the basic turbulent flow (without installation of the model) are measured thanks to the hot-wire anemometer using x-type probes (Model 0252, Kanomax Japan, Inc.) and calibrated and linearized by a constant-temperature anemometer (CTA) (Models 1013, 1011, Kanomax Japan, Inc.). Unsteady surface pressures are measured by multi-channel pressure measurement system (ZOC23, Ohte Giken, Inc.). It is noted that turbulent

components and surface pressures are imultaneously obtained in order to investigate in the time domain. Electric signals were filtered by 100Hz low-pass filters (E3201, NF Design Block Co., Ltd.) before passed through A/D converter (Thinknet DF3422, Pavec Co., Ltd.) with sampling frequency at 1000Hz in 100 seconds.

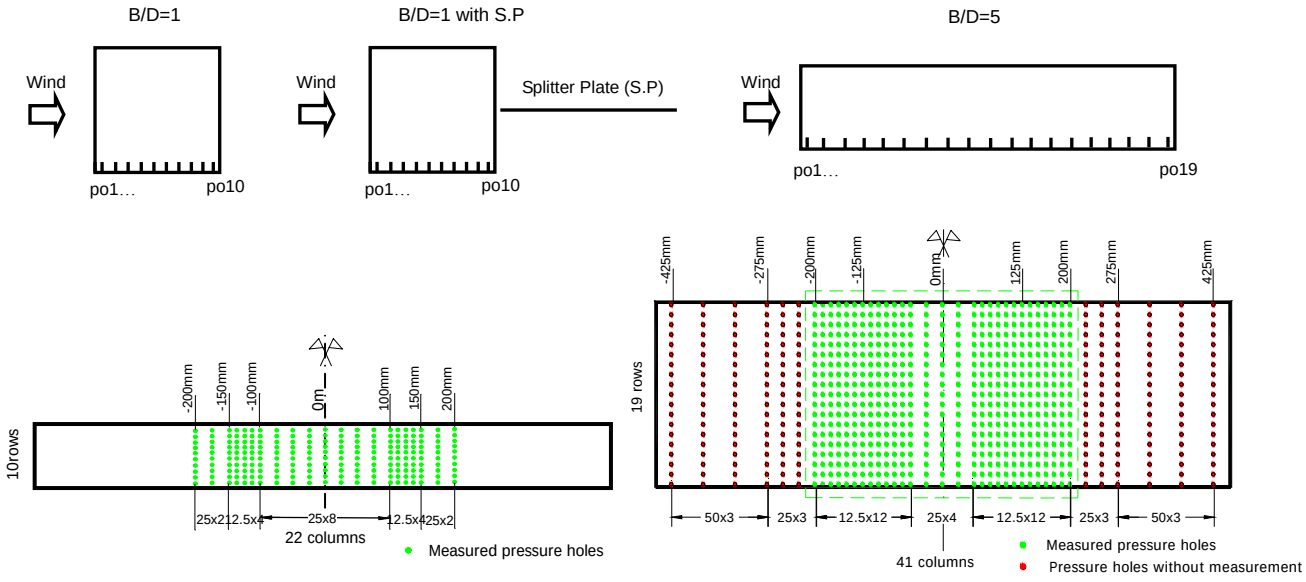

Fig. 3.1 Experimental models and pressure tap arrangement

a. Model B/D=1

b . Model B/D=5

Fig. 3.2 Images of experimental models in wind tunnel test: a. model B/D=1, b. model B/D=5

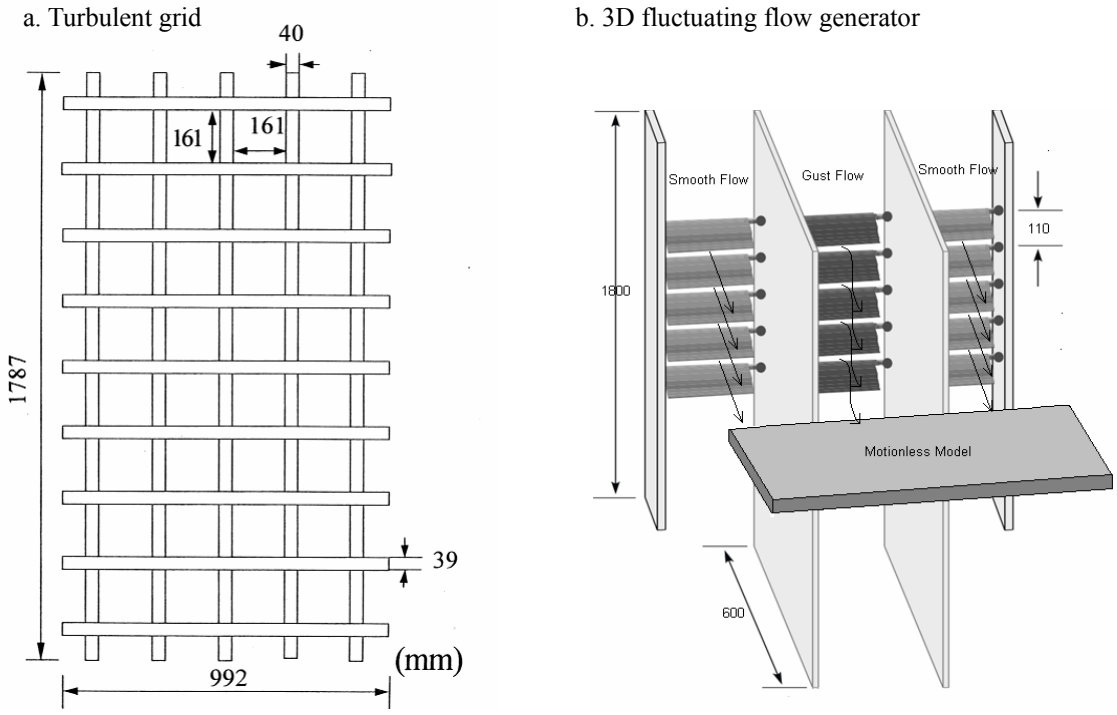

Fig. 3.3 Flow generation devices: a. grid turbulent generator, b. 3D fluctuating flow generator

3.3.2 *Experimental apparatus in fluctuating flows*

Motionless model of the rectangular cylinder B/D=5 with dimension of 300mm wide x 60mm deep x 890mm is used. Mean wind velocity and fluctuating velocity are measured by the hot-wire anemometer with x-type probes (model 0252, Kanomax Co., Ltd.). Though 779 pressure holes including 19 chordwise and 41 spanwise columns are arranged on one side of the model surface, but only limited number of pressure taps in region between 0mm and 250mm in the spanwise direction is used in this study. Three-dimensional fluctuating flow is generated by specific devide (see Figure 3.3b) which is located in 600mm (=10D, D: model depth) upstream from the model's leading edge. This device consists of the three parts: two side parts with motionless blades which produce the smooth flows and the center one with harmonic moving blades which generate the fluctuating sinusoidal flow. Spanwise convection between the smooth flows in the side parts and the sinusoidal one in the center part produces the so-called three-dimensional fluctuating flow.

It is noted that the moving blades in the center part is driven harmonically by electric motor at fixed frequency of 3Hz (also known as characteristic frequency of the fluctuating flow). The reduced frequencies ($k = b\omega / U$ where ω: circular frequency of fluctuating flow, b: half of

model width $b = B/2$) are controlled in the range between 0.72 and 1.92, corresponding to the reduced velocities ($U_{re} = U / fD$, D: model depth) between 22.22 and 8.33 (see Table 3.1) which must be higher than a potential reduced frequency of vortex-based motion-induced vibration according to Kiya et al. 1983 ($fL_{sb}/U = 0.7$, L_{sb} : separation bubble length from leading edge to reattachment point, thus reduced frequency of motion-induced vibration $k \approx 2.4 \div 2.7$).

Unsteady surface pressures are also measured simultaneously by multi-channel pressure measurement system (ZOC23, Ohte Giken, Inc.). Electric signals are filtered by 50Hz low-pass filters (E3201, NF Design Block Co., Ltd.) before passed through A/D converter (Thinknet DF3422, Pavec Co., Ltd.) with the sample rate at 1000Hz over 100s.

The longitudinal and vertical intensities of turbulence of the fluctuating flow are measured as I_u=5.12% and I_w=4.12%, respectively. The scales of turbulence are determined as L_{ux}=73.94mm, L_{wx}=73.66mm in the chordwise direction and L_{uy}=23.59mm and L_{wy}=22.99mm in the spanwise direction.

Tab. 3.1 Parameters of fluctuating flows

B(m)	f(Hz)	U(m/s)	U_{re}	k
0.3	3.00	1.47	8.33	1.92
0.3	3.00	1.64	9.25	1.73
0.3	3.00	1.97	11.11	1.44
0.3	3.00	2.20	12.46	1.28
0.3	3.00	2.32	13.13	1.22
0.3	3.00	2.95	16.66	0.96
0.3	3.00	3.93	22.22	0.72

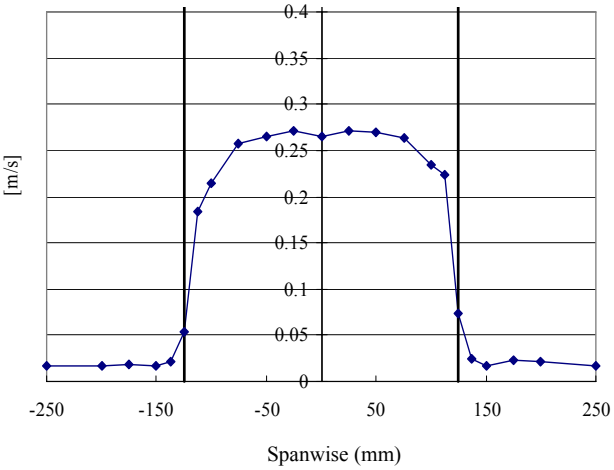

Fig. 3.4 Amplitude of vertical velocity fluctuation at base reference points [Matsumoto,Shirato et al. 2005]

The vertical fluctuating velocity (w-turbulence) is measured at different spanwise positions at center of model location (but measurement without model) to study the effectiveness of the fluctuating flow at the mean velocity U=7m/s (see Figure 3.4). It can be seen in Figure 3.4 that the wind fluctuation varies in the spanwise direction corresponding to characteristic of the ongoing fluctuating flow: sinusoidal flow and smooth flow and the transit region between two these flows.

3.4 Chordwise pressure distribution

The chordwise pressure distribution in the turbulent flows is discussed at first, then that in the fluctuating flows at next. In some extent, knowledge about the wind-structure interaction phenomena and the bluff body flow which are usually characterized by formation of separated and reattached flows with separation bubble and that of vortex shedding as well can be obtained based on distributions of mean and fluctuating pressures in the chordwise direction (Hillier and Cherry 1981 and Cherry et al. 1984). Normalized mean pressures and normalized root-mean-square fluctuating pressures in the chordwise positions can be determined from measured time series of unsteady pressures as following formulae:

$$C_{p,mean} = \frac{\overline{p}}{0.5\rho U^2} \tag{3.1-a}$$

$$C_{p,rms} = \frac{\sqrt{1/N \sum_{N} (p - \overline{p})^2}}{0.5\rho U^2} \tag{3.1-b}$$

where $\overline{p}$: mean value; p: unsteady pressure; $0.5\rho U^2$: dynamic pressure.

Normalized mean and fluctuating pressure distributions in the chordwise positions in three models are expressed in Figure 3.5. As can be seen that the normalized mean and fluctuating pressures distribute homogeneously on the models B/D=1 without/with the Splitter Plate, whereas distribute locally near leading edge on the model B/D=5. Normalized mean and fluctuating pressures on model B/D=1 without splitter plate exhibit higher than those on the same model but with splitter plate. Moreover, the distributions of the fluctuating pressures depend on the turbulent flow conditions, whereas the mean pressure distributions on three models seem not to with respect to turbulent flow conditions.

Figure 3.6 shows the power spectral densities of the fluctuating pressures at some referred positions on the three models in the three turbulent flows. Peak frequencies are observed at 4.15Hz, 8.79Hz and 12.94Hz corresponding to three turbulent flows in the case of model B/D=1 without Splitter Plate. It is clear that the Karman vortex formed and shed in the wake in which the Karman vortex frequency depends on the Strouhal number (S_t) which can be determined at S_t=0.1285 in these cases. Therefore, the bluff body flow is separated at sharp corners, dominated by formation of Karman vortex and frequently shed in the wake on the model B/D=1 without Splitter Plate. In case of the model B/D=1 with Splitter Plate, no frequency peaks are observed, the Karman vortex is suppressed by the splitter plate. It is supposed the bluff body flow separated at the sharp corners, expanded all model surface and reattached at the splitter plate.

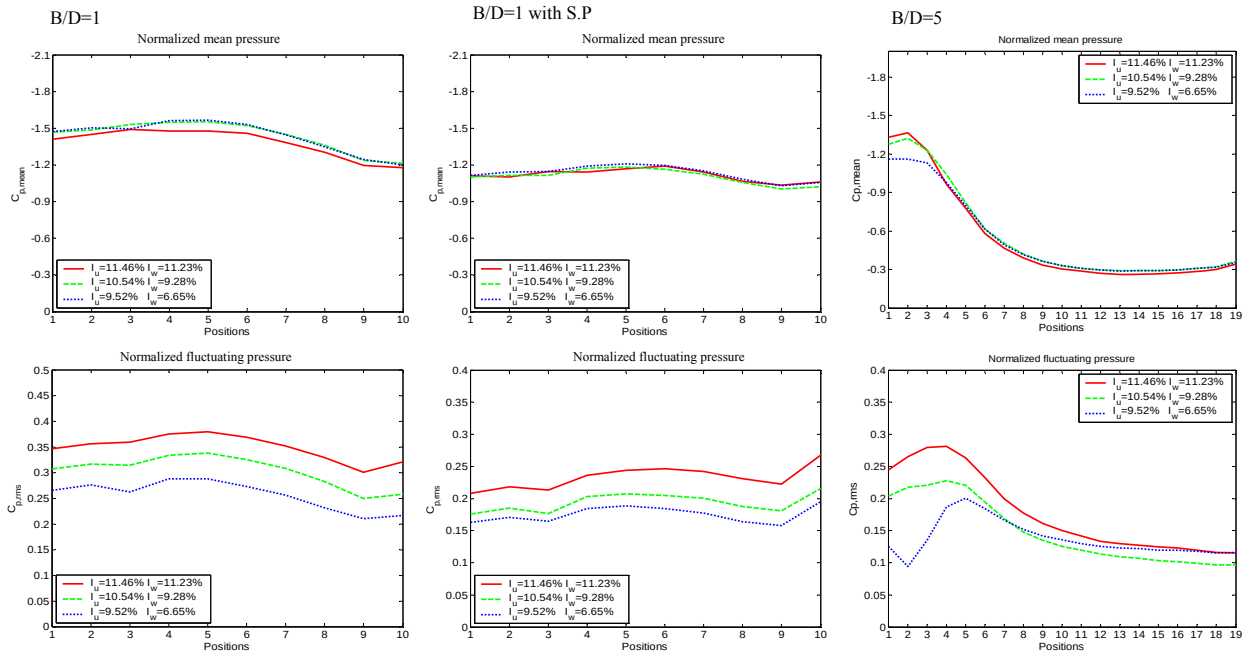

Fig. 3.5 Normalized mean and fluctuating pressures at chordwise positions in turbulent flows

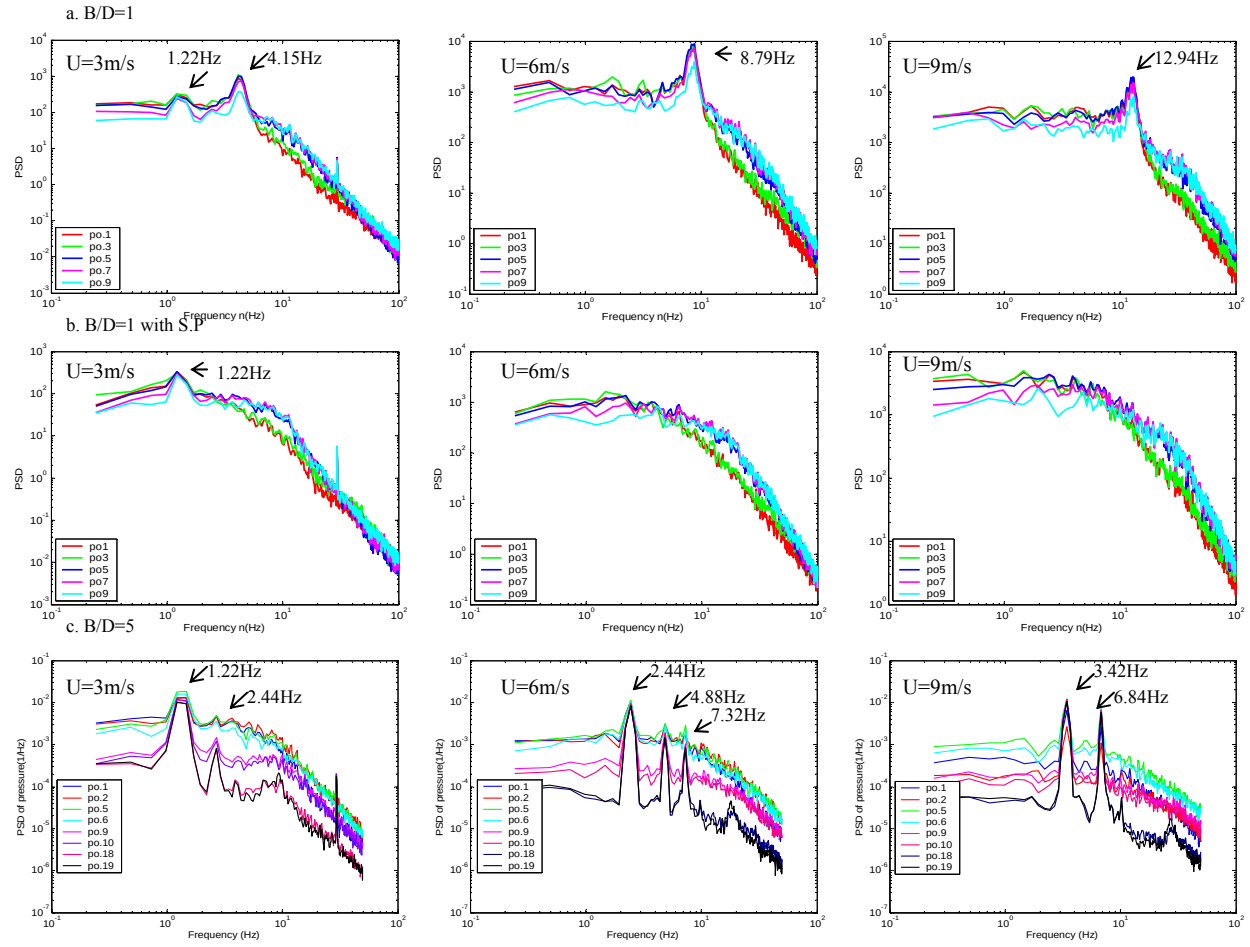

Fig. 3.6 Power spectral densities of fluctuating pressures in turbulent flows [Matsumoto, Shirato et al. 2006]

In case of the model B/D=5, frequency peaks are observed at 1.22Hz and 2.44Hz (case 1); at 2.44Hz, 4.88Hz, 7.32Hz (flow case 2); at 3.42Hz and 6.84Hz (flow case 3). According to Hiller and Cherry 1981; Cherry et al. 1984, reattachment point of separated flow may locate at near after the peak position of fluctuating pressure, and the observed frequency peaks are induced by rolled-up turbulent vortices shed away at reattachment points toward trailing edge. Thus, bluff body flow is separated and reattached on the model surface to form separation bubble. Reattachment points can be determined at roughly positions 6, 7, 8 with respect to an increase of mean velocities. High mean and fluctuating pressures are observed locally at the leading edge region in the influence of separation bubble due to local circulation of turbulent vortex inside it.

Figure 3.7 shows distributions of the normalized mean pressures and the normalized fluctuating pressures in the chordwise direction corresponding to different reduced frequencies in the fluctuating flows. As can be seen that both the mean pressures and fluctuating pressures reduce with decrease of the reduced frequencies or increase of the reduced velocities. Peak locations of the fluctuating pressures seem to move forward to trailing edge with respect to decrease of the reduced frequencies, this also means that the locations of reattachment point of separated flows on the model surface move forward with increase of reduced velocities. In comparison with results of the turbulent flows, moreover, it is noted that the mean pressures change with the increase of the reduced velocities (or mean velocities) in the fluctuating flows, whereas the mean pressures stay constant with the increase of the mean velocities in the turbulent flows.

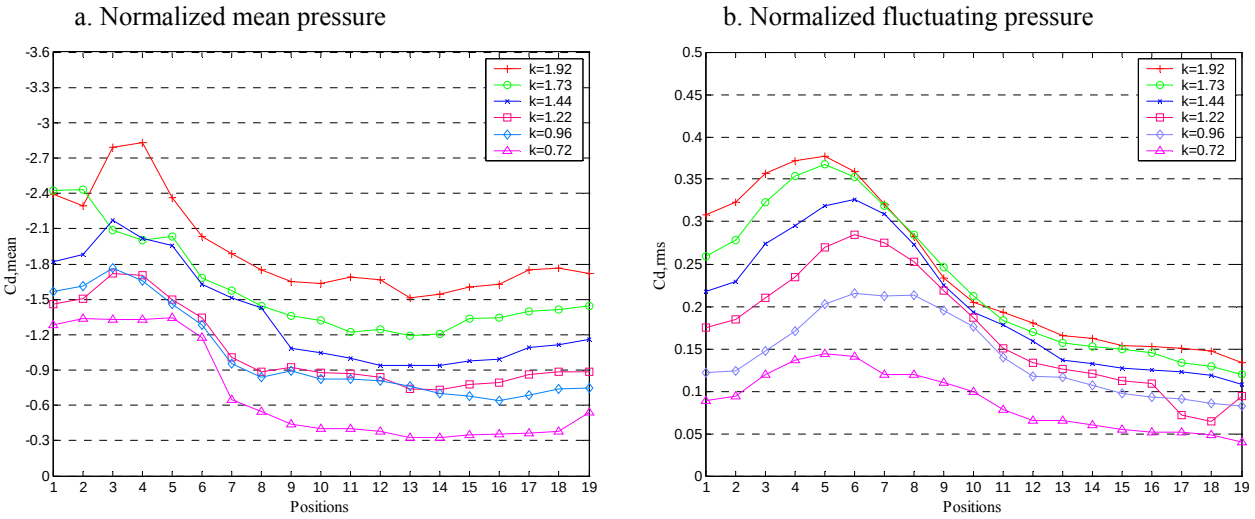

Fig. 3.7 Normalized mean and fluctuating pressure distributions on chordwise direction in different fluctuating flows [Matsumoto, Shirato et al. 2005]

a. k=1.92 (U_{re}=8.33)

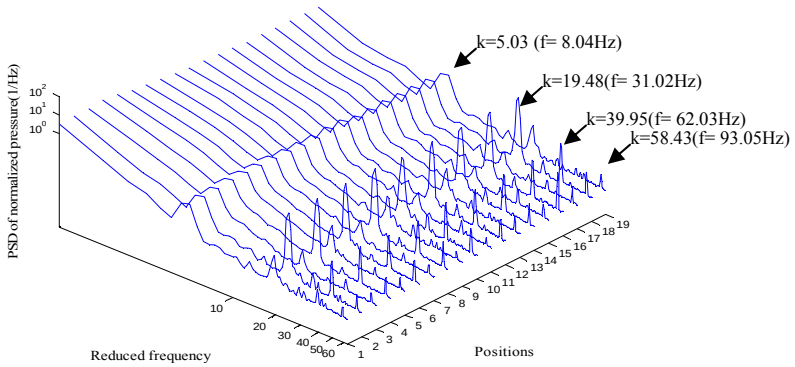

b. k=1.45 (U_{re}=11.11)

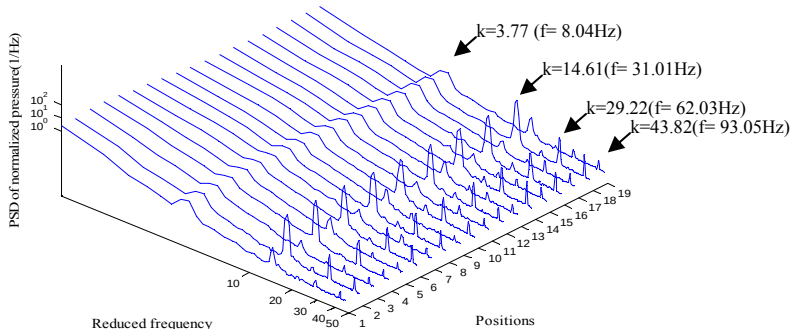

b. k=0.72 (U_{re}=22.22)

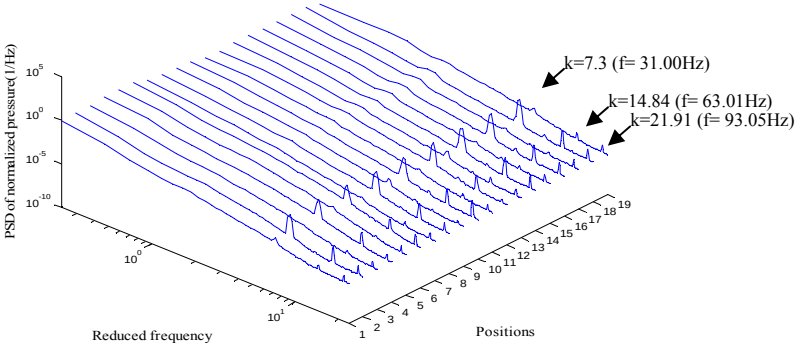

Fig. 3.8 Power spectral densities of normalized chordwise pressures in fluctuating flows [Matsumoto, Shirato et al. 2005]

Figure 3.8 shows power spectral densities of all chordwise pressures corresponding to different fluctuating flows. It is observed that spectral peaks of physical events appear which might relate to occurrence and movement of roll-up vortices on surface of the experimental models.

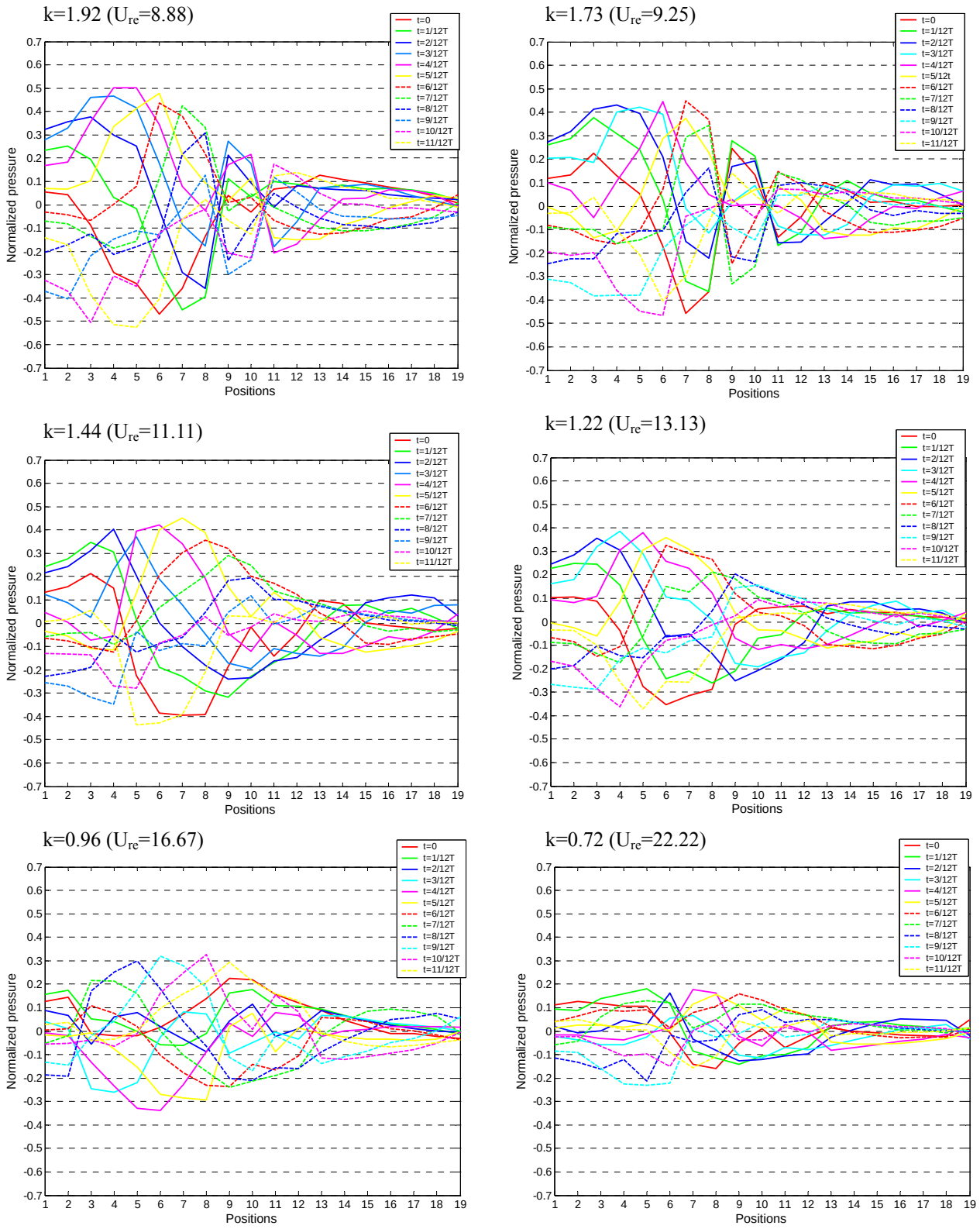

Fig. 3.9 Instantaneous normalized pressure distribution of chordwise positions on a cycle T of 3D fluctuating flow at different reduced frequencies [Shirato, Matsumoto et al. 2005]

a. Normalized mean pressure

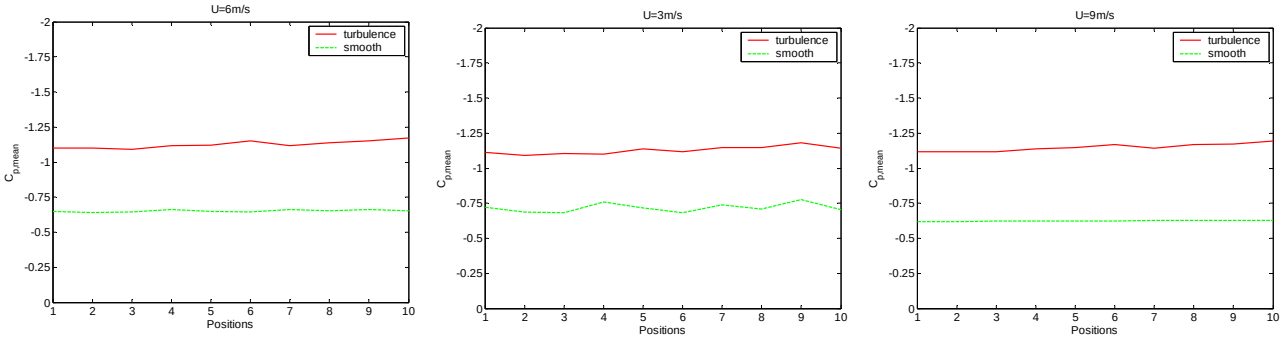

b. Normalized fluctuating pressure

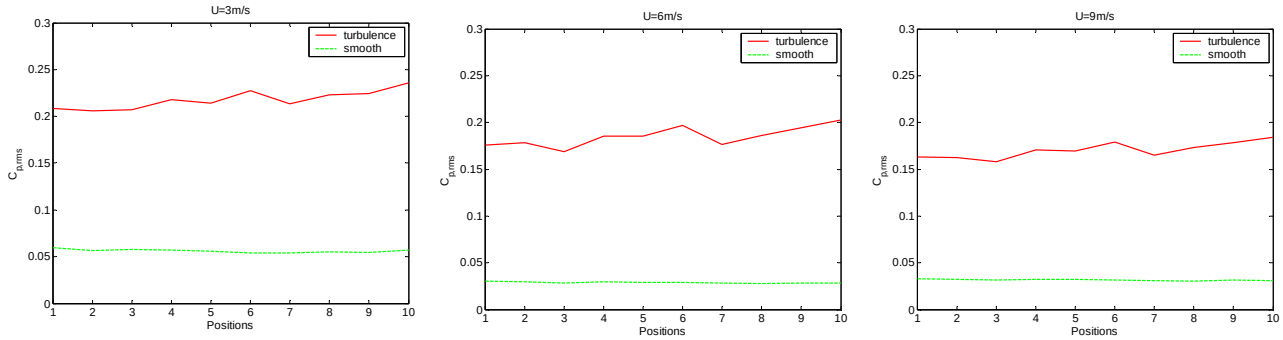

Fig. 3.10 Comparison of pressures on model B/D=1 due to turbulent and smooth flows

a. Normalized mean pressure

[Matsumoto, Shirato et al. 2006]

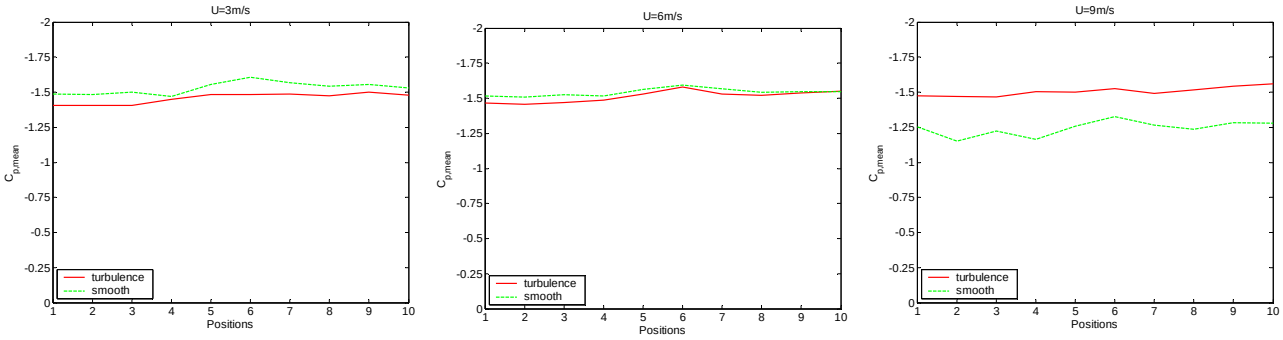

b. Normalized fluctuating pressure

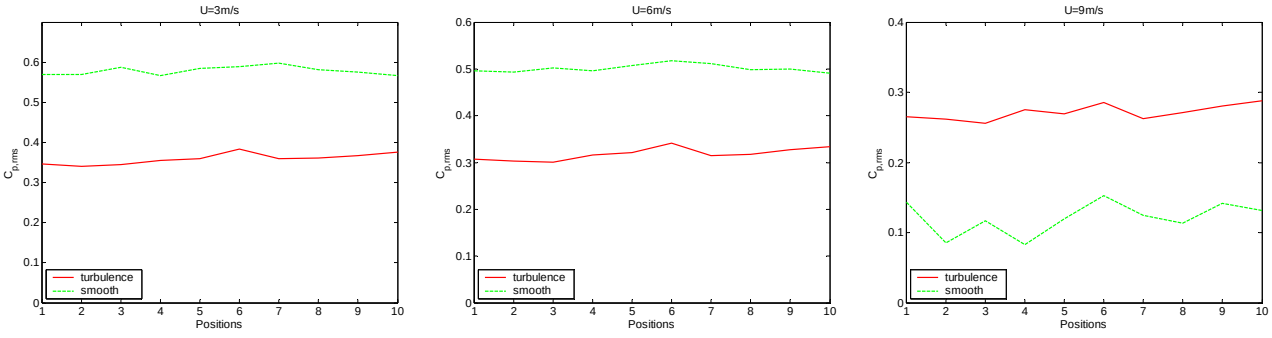

Fig. 3.11 Comparison of pressures on model B/D=1 with S.P due to turbulent and smooth flows [Matsumoto, Shirato et al. 2006]

a. Normalized mean pressure

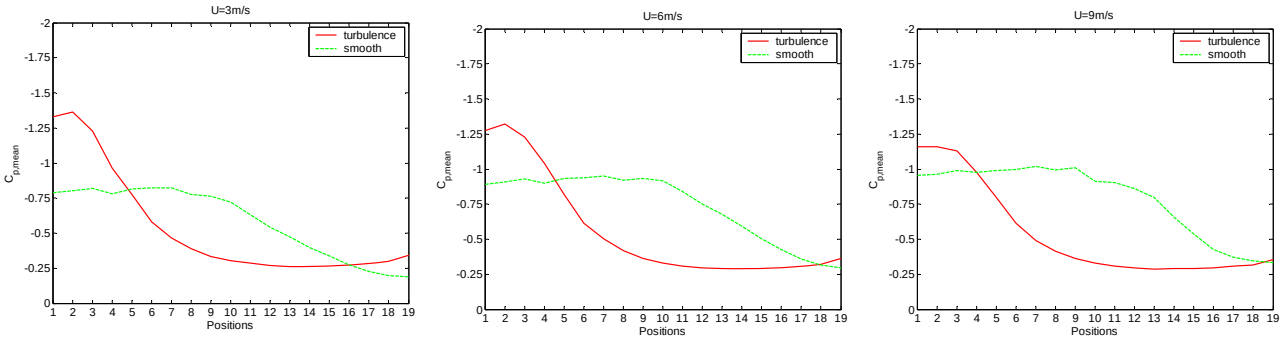

b. Normalized fluctuating pressure

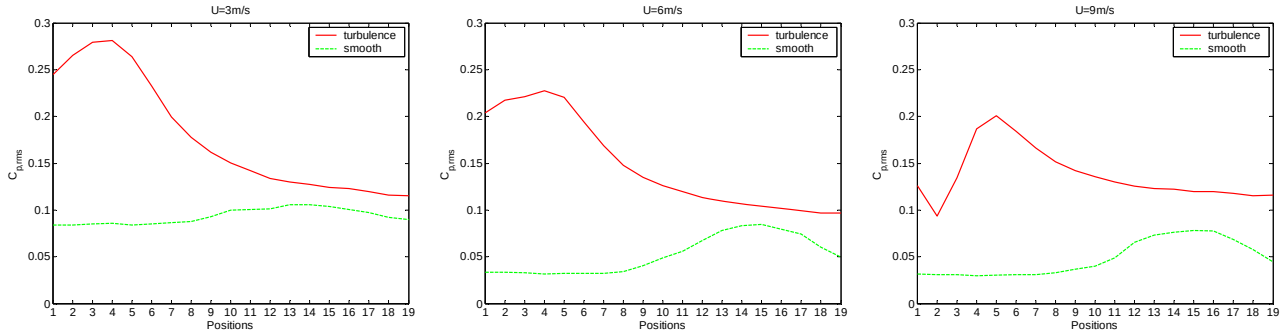

Fig. 3.12 Comparison of pressures on model B/D=5 due to turbulent and smooth flows [Matsumoto, Shirato et al. 2006]

As can be seen from 3.8, it is supposed that large-scale vortex appear and move on the model surface at frequency 8.04Hz in the fluctuating flow conditions k=1.92, k=1.45, this large-scale vortex does not appear at low reduced frequency k=0.72 (or high reduced velocity U_r=22.22). The frequency peaks at multiple frequencies 31.02Hz, 62.03Hz, 93.05Hz occur at all investigated fluctuating flows k=1.92, 1.45 and 0.72. These multiple frequencies are due to small-scale rolled-up vortices which break up into smaller vortices during moving from the leading edge to the trailing edge. However, energy contribution of rolled-up vortices reduces with increase of the reduced velocities, for example in the case U_r=22.22, occurrence of these frequency peaks of the rolled-up vortices is not clear (see Figure 3.8).

Instantaneous pressures distributions in the chordwise direction at different time points on one cycle T of the fluctuating flows in different reduced frequencies k=0.72÷1.92 are shown in Figure 3.9. High instantaneous pressure regions distribute at leading edge of the model, moreover, the instantaneous pressures reduce with respect to increase of reduced velocities. It seems that the instantaneous pressure distribution recover after half of cycle T, this corresponds to the characteristic of ongoing flows as the sinusoidal fluctuating flow. This finding can be used to estimate chordwise pressure distribution on other side of model.

Comparisons of the chordwise mean and fluctuating pressures on three experimental models depending on the ongoing flow conditions (smooth and turbulent ones) are expressed in Figures 3.10÷3.12. In the model B/D=1, both mean and fluctuating pressures on the turbulent flow exhibit higher than those on the smooth flow, especially large difference in the fluctuating pressures can observed (see Figure 3.10). Due to effect of the Splitter Plate installed at model wake, there is no difference in the mean pressures between smooth and turbulent flows, but the fluctuating pressures in the smooth flow express higher than those in turbulent ones at U=3m/s, 6m/s (see Figure 3.11). In the model B/D=5, it is seen that mean and fluctuating pressures in the turbulent flow distribute strongly at local leading edge region, whereas those in the smooth flow distribute wider forward trailing edge. Moreover, the fluctuating pressures in the turbulent flows exhibit larger than those in the smooth flows.

3.5 Identification of bluff body flow pattern

As mentioned above, the bluff body flow around B/D=1 is dominated by separated flow on the model surface and formation of the Karman vortex and shedding at the model wake. With model B/D=1 with the Splitter Plate, the separated flow is formed at sharp corners of the leading edges, however reattachment does not occur on the model surface, but stagnate at the wake and no Karman vortex occurs, this flow is known as time-integrated flow field. In the case of model B/D=5, it is supposed that both separated and reattached flows occur on the model surface. The bluff body flow patterns on models B/D=1, B/D=1 with S.P and B/D=5 are expressed in Figure 3.13.

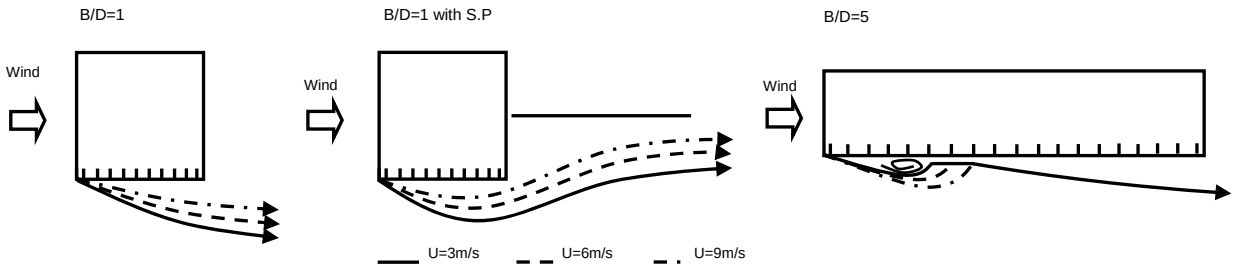

Fig. 3.13 Bluff body flow pattern of three experimental models in turbulent flows [Matsumoto, Shirato et al. 2006]

The bluff body flow patterns at the chorwise direction on the model B/D=5 in the different fluctuating flows can be identified based on the chordwise distribution of instantaneous surface

pressure and the relative angle of attack (defined by quasi-steady formula: $\alpha_{re} \approx \overline{w}/U$, $\overline{w}$: amplitude of gust flow) as can be shown in Figure 3.14. As a result, the formation of separation bubble due to the instability of shear layer and formation of vortex-shedding on surface model are the potential cause to change from the ongoing fluctuating flow on model.

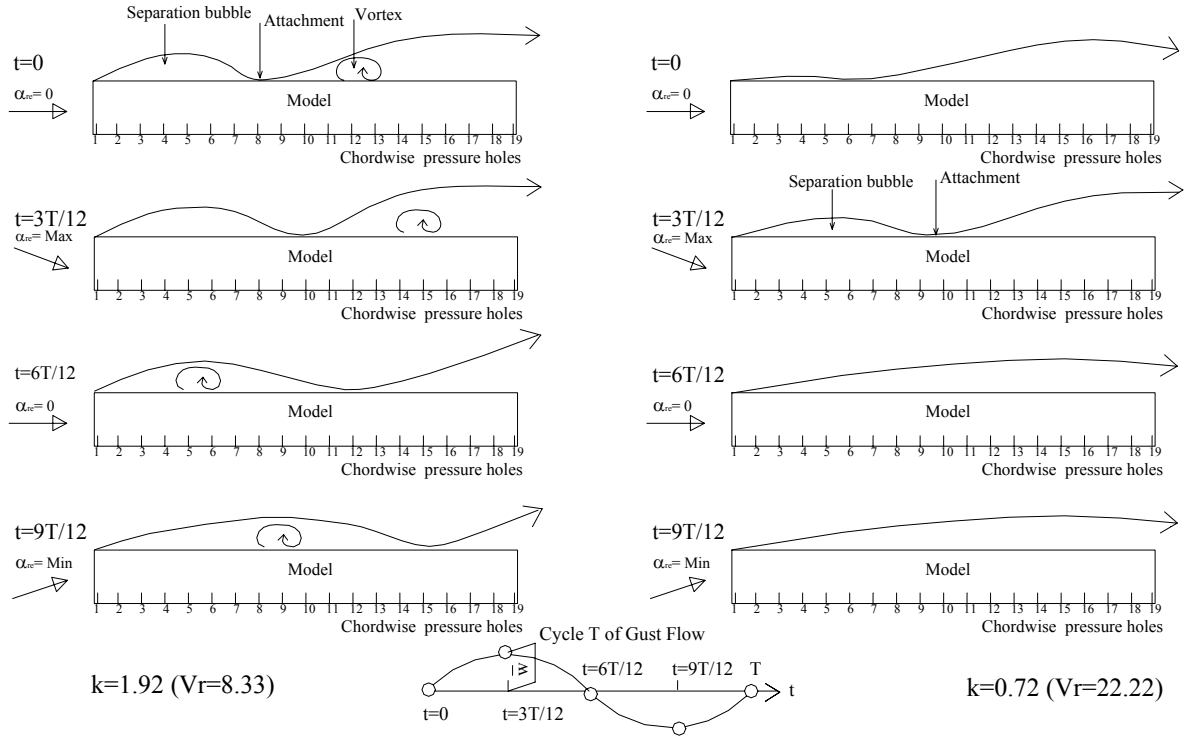

Fig. 3.14 Bluff body flow patterns in cycle T of fluctuating flows
[Shirato, Matsumoto et al. 2005]

In the case of high reduced frequency k=1.92 (low reduced velocity Ur=8.33) in the fluctuating flow, it is supposed the separated and reattached flow with formation of vortex shedding on model surface characterize for the bluff body flow. Moreover, the vortex moves forward to trailing edge due to change of attack angles. Frequency of this vortex is supposed at 8.04Hz. This well corresponds to the finding in Matsumoto et al. 1986 about the onset of the shear layer instability enhancement around the frequency k=1.88. 2D-like separation bubble, furthermore, forms and almost spreads on the entire model surface at the low reduced frequency k=0.72 (high reduced velocity U_r=22.22).

3.6 Spatial distribution of unsteady pressure fields

Spatial distribution of normalized mean and fluctuating pressures that is taken into account area of whole chordwise length and 200mm spanwise width on the model B/D=5 in the different turbulent flows is shown in Figure 3.15. It is commented that the spatial distribution of both the mean and fluctuating pressures in the three turbulent flows (corresponding to mean velocities U=3m/s,6m/s and 9m/s) concentrates locally at the leading edge region in the chordwise direction, and exhibit constantly in the spanwise direction.

Figure 3.16 expresses the spatial distribution of normalized mean and fluctuating pressures on model B/D=5 in different fluctuating flows k=1.92÷0.72 (Ur=8.33÷22.22). It is noted that the spanwise length between 0mm÷125mm is in scope of the fluctuating flow, whereas the spanwise length between 125mm÷200mm is in scope of the smooth flow. As can be seen from Figure 3.16 that the mean pressures distribute constantly in the spanwise direction and localize at leading edge region in the chordwise direction at the investigated reduced frequencies. At the high reduced frequencies (low reduced velocities), however, the fluctuating pressures distributes strongly near leading edge in the influence part of the fluctuating flow, moreover, these fluctuating pressures also distribute considerably in the part of the smooth flow. The fluctuating pressures distribute more homogeneously in influence of both fluctuating and smooth flows at the low reduced frequencies (high reduced velocities), furthermore, the fluctuating pressure distribution at two flows seems to be similar together.

This can be explained that at the high reduced frequencies (low reduced velocities) the convection between two fluctuating and smooth flows in the spanwise direction occurs weaker than that at the low reduced frequencies (high reduced velocities).

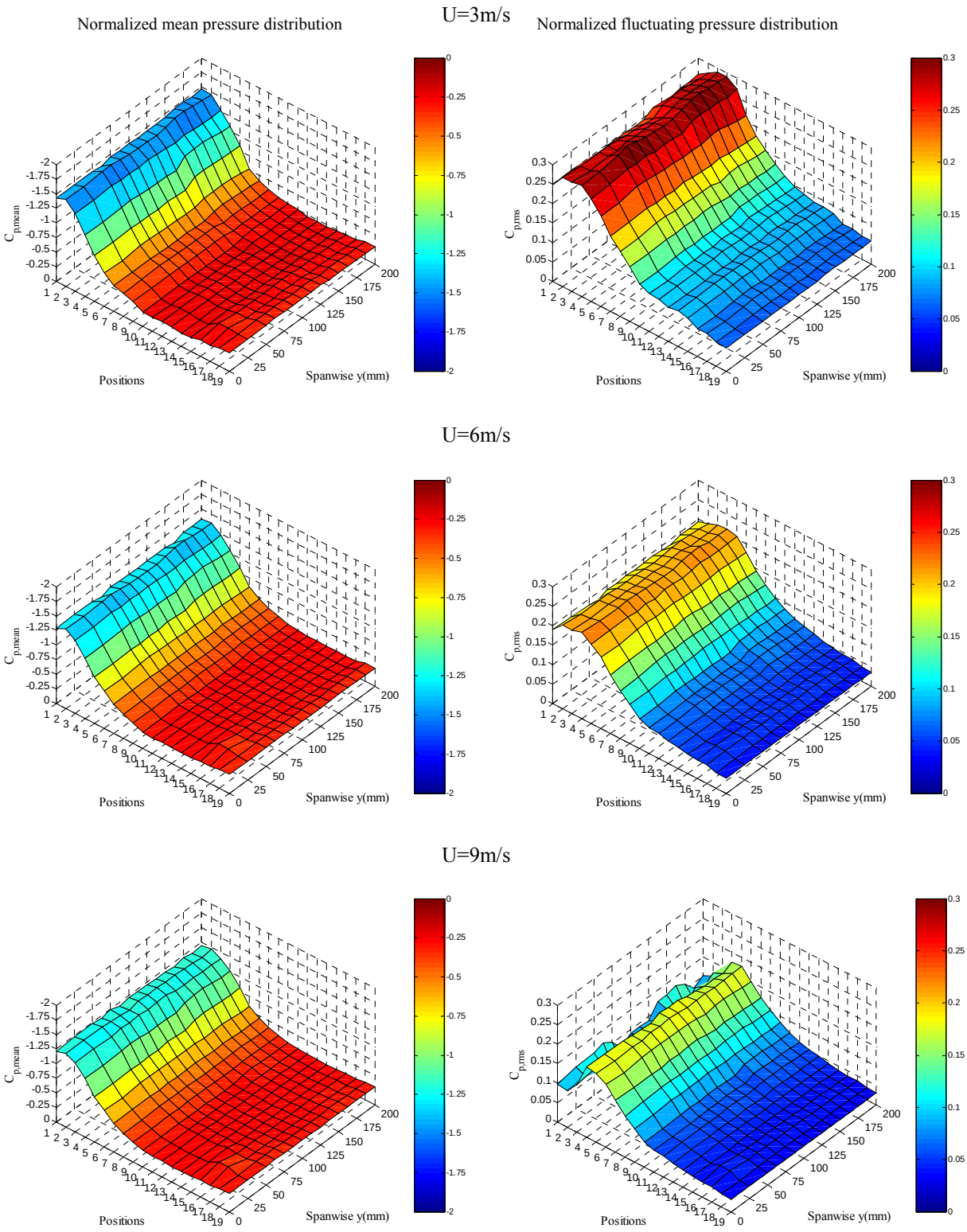

Fig 3.15 Spatial distribution of normalized mean and fluctuating pressures on model B/D=5 in different turbulent flows [Matsumoto, Shirato et al. 2006]

Normalized mean pressure distribution

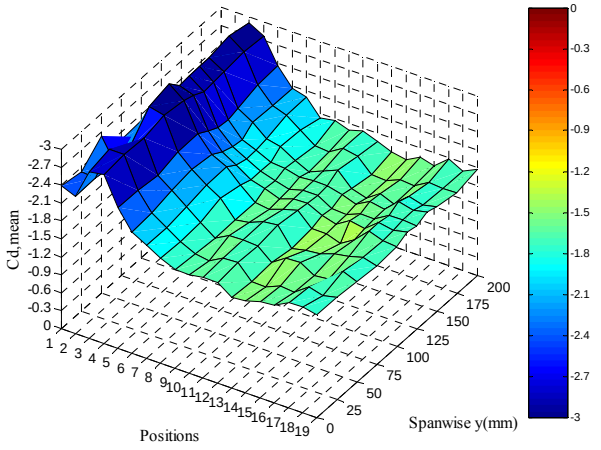

k=1.92 Normalized mean pressure distribution

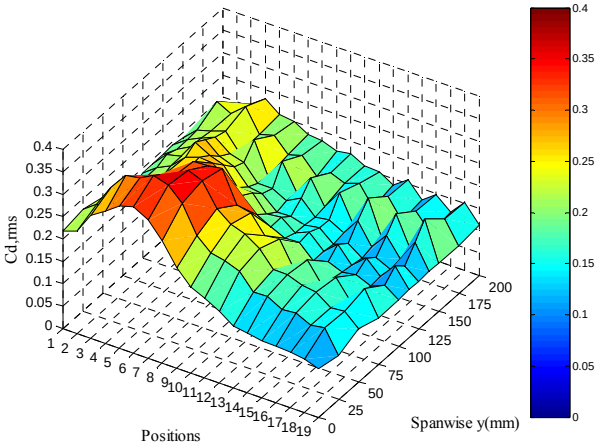

k=1.73

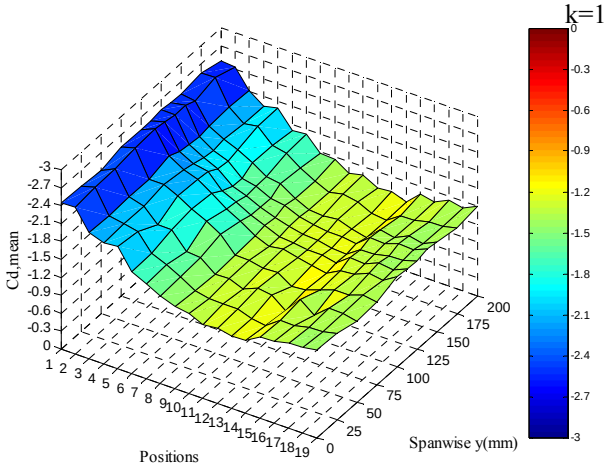

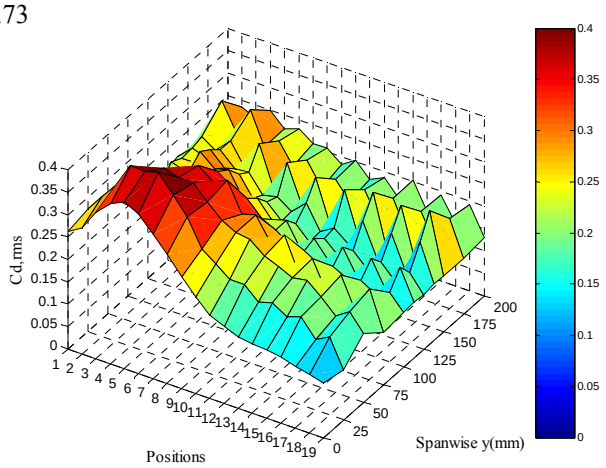

k=1.44

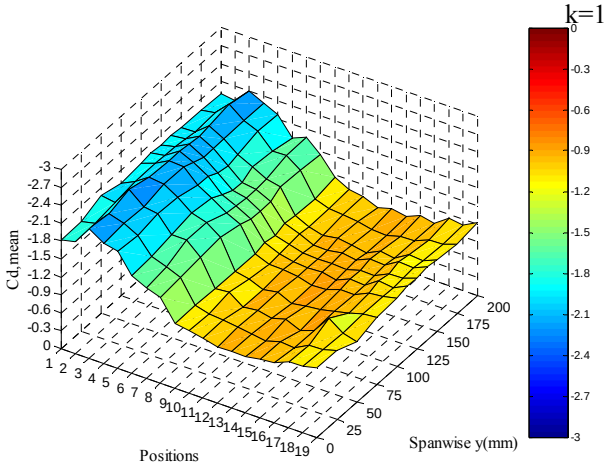

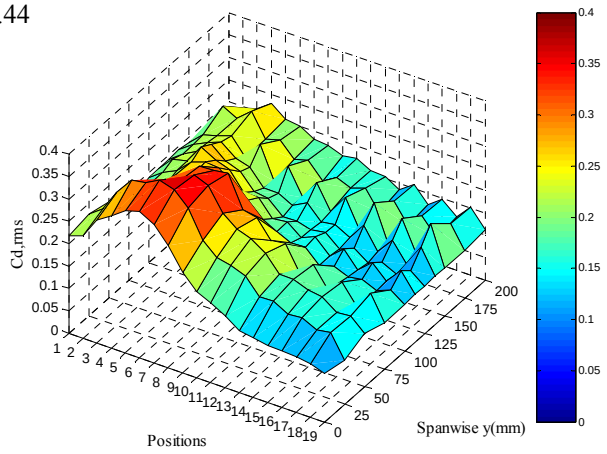

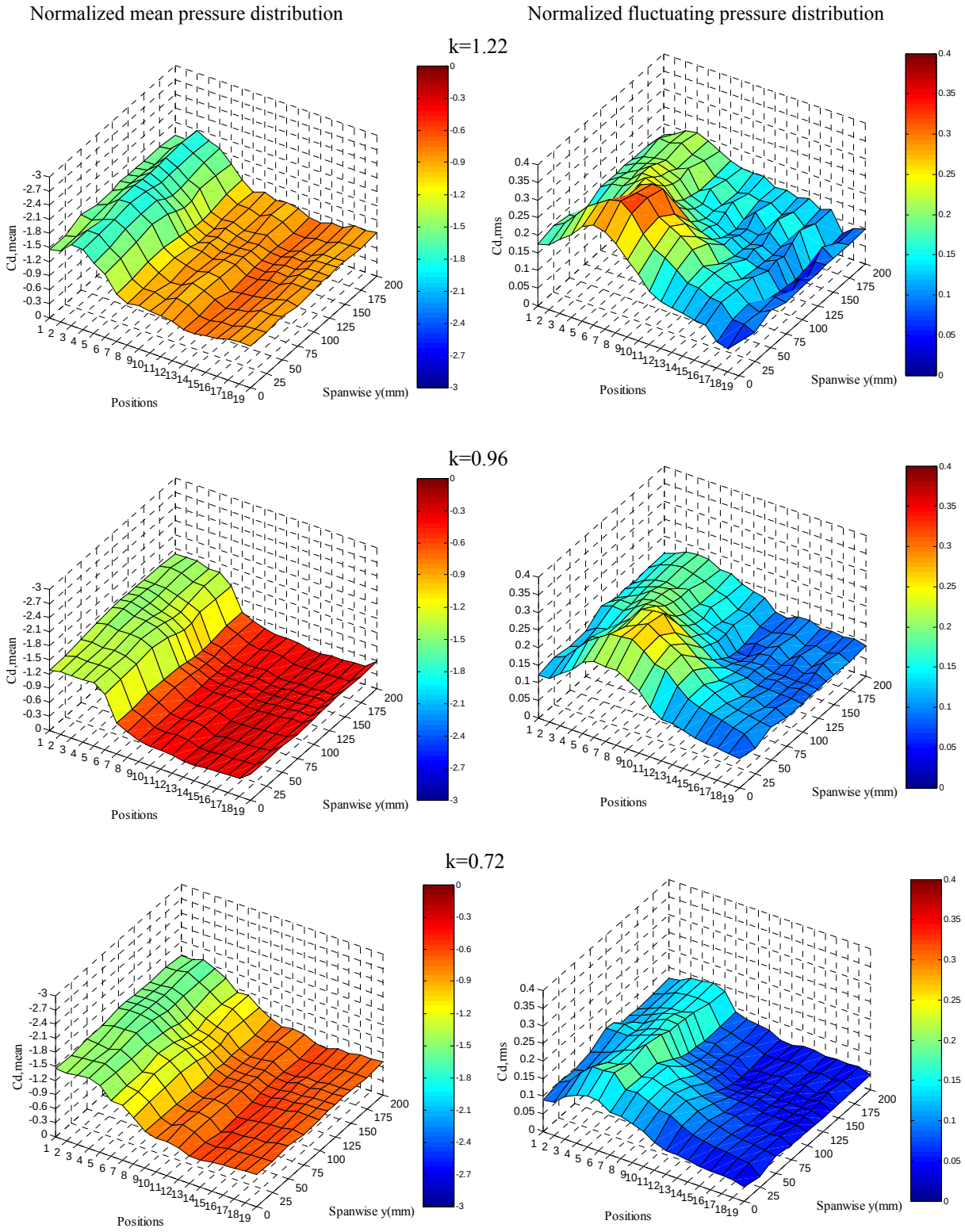

Fig. 3.16 Spatial distribution of normalized mean and fluctuating pressures on model B/D=5 in different fluctuating flows [Matsumoto, Shirato et al. 2005]

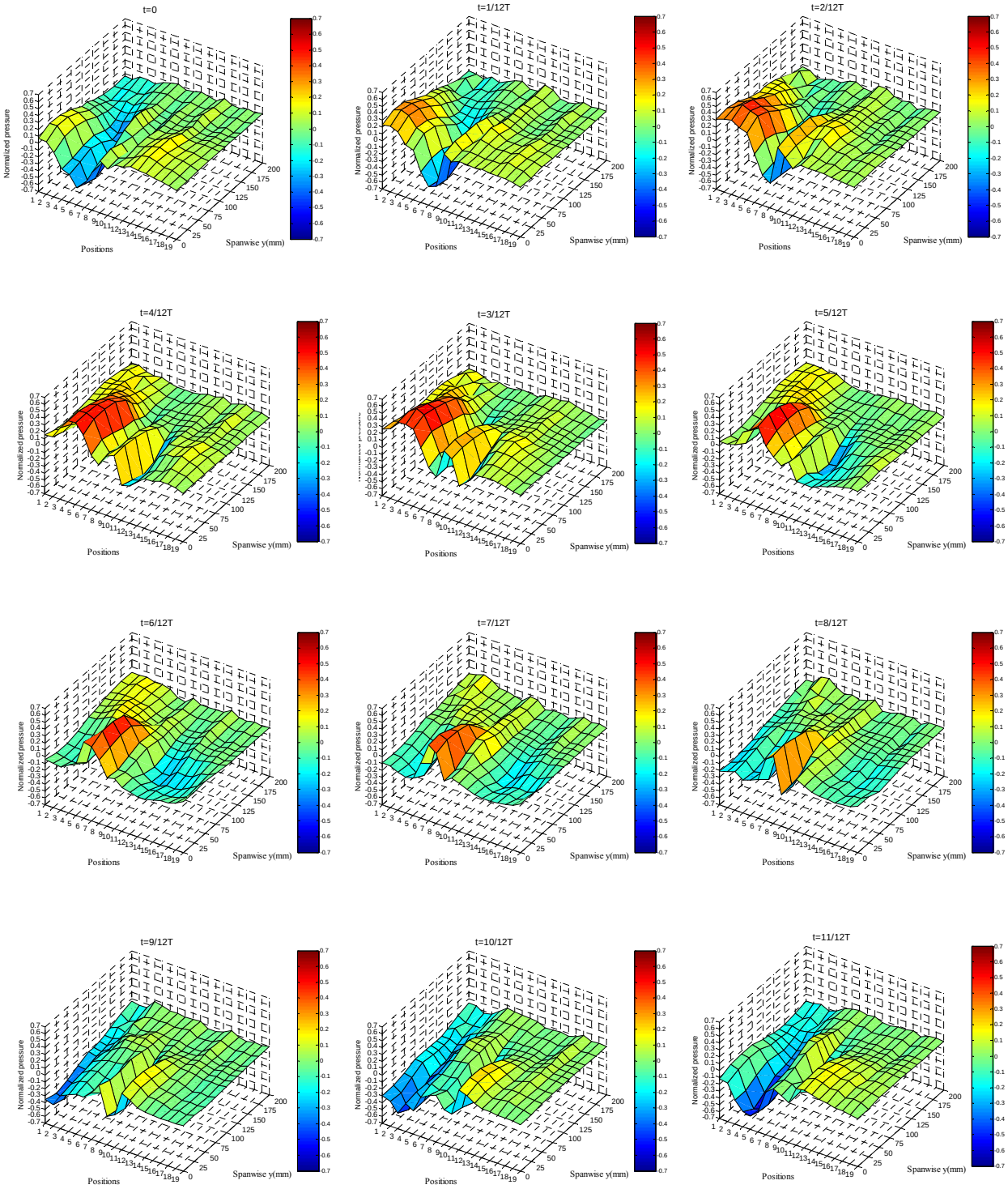

Fig. 3.17 Instantaneous normalized pressure distribution in a cycle T of fluctuating flow at reduced frequency k=1.92 (U_{re}=8.33) [Matsumoto, Shirato et al. 2005]

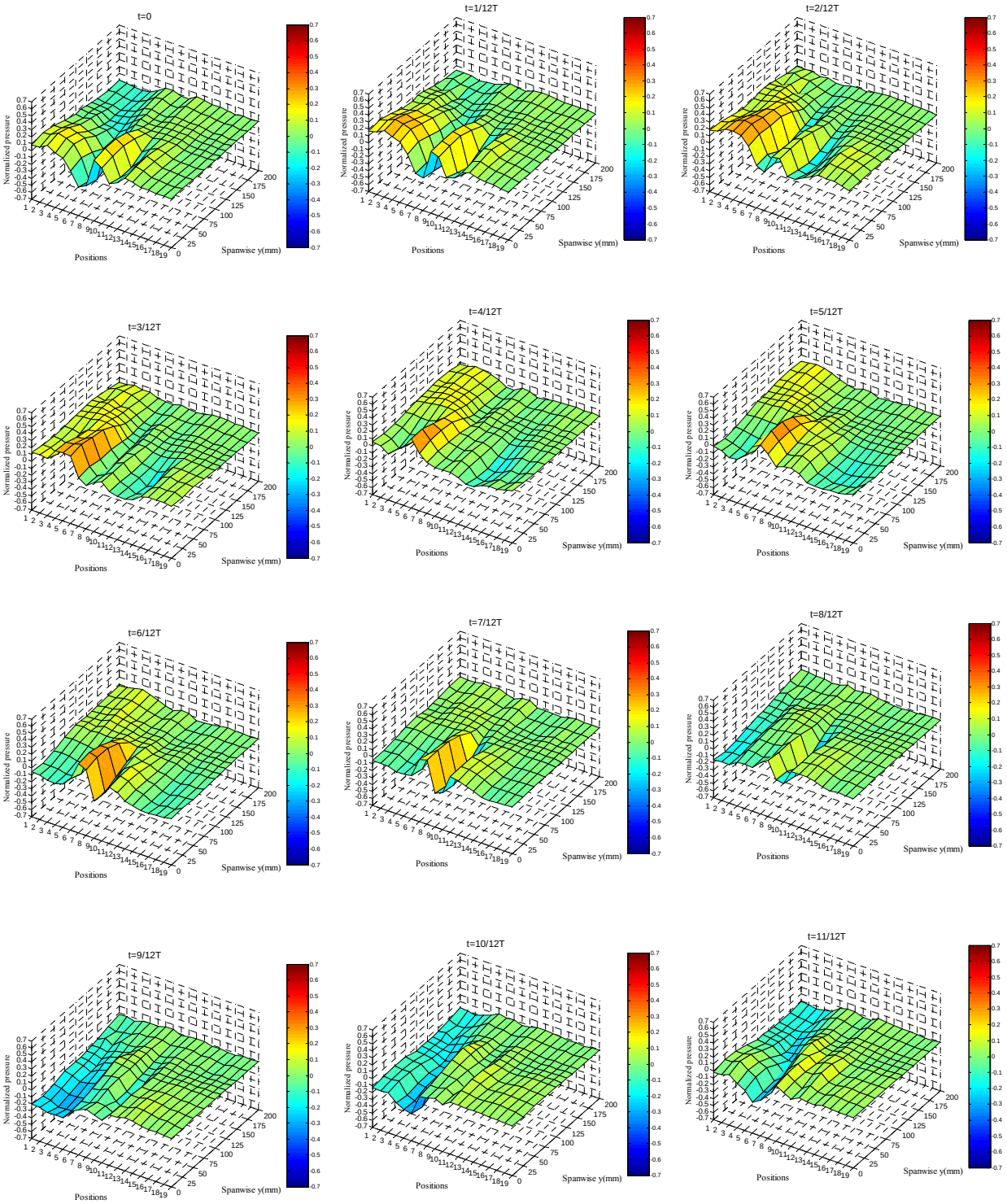

Fig. 3.18 Instantaneous normalized pressure distribution in a cycle T of fluctuating flow at reduced frequency k=1.44 (U_{re}=11.11) [Matsumoto, Shirato et al. 2005]

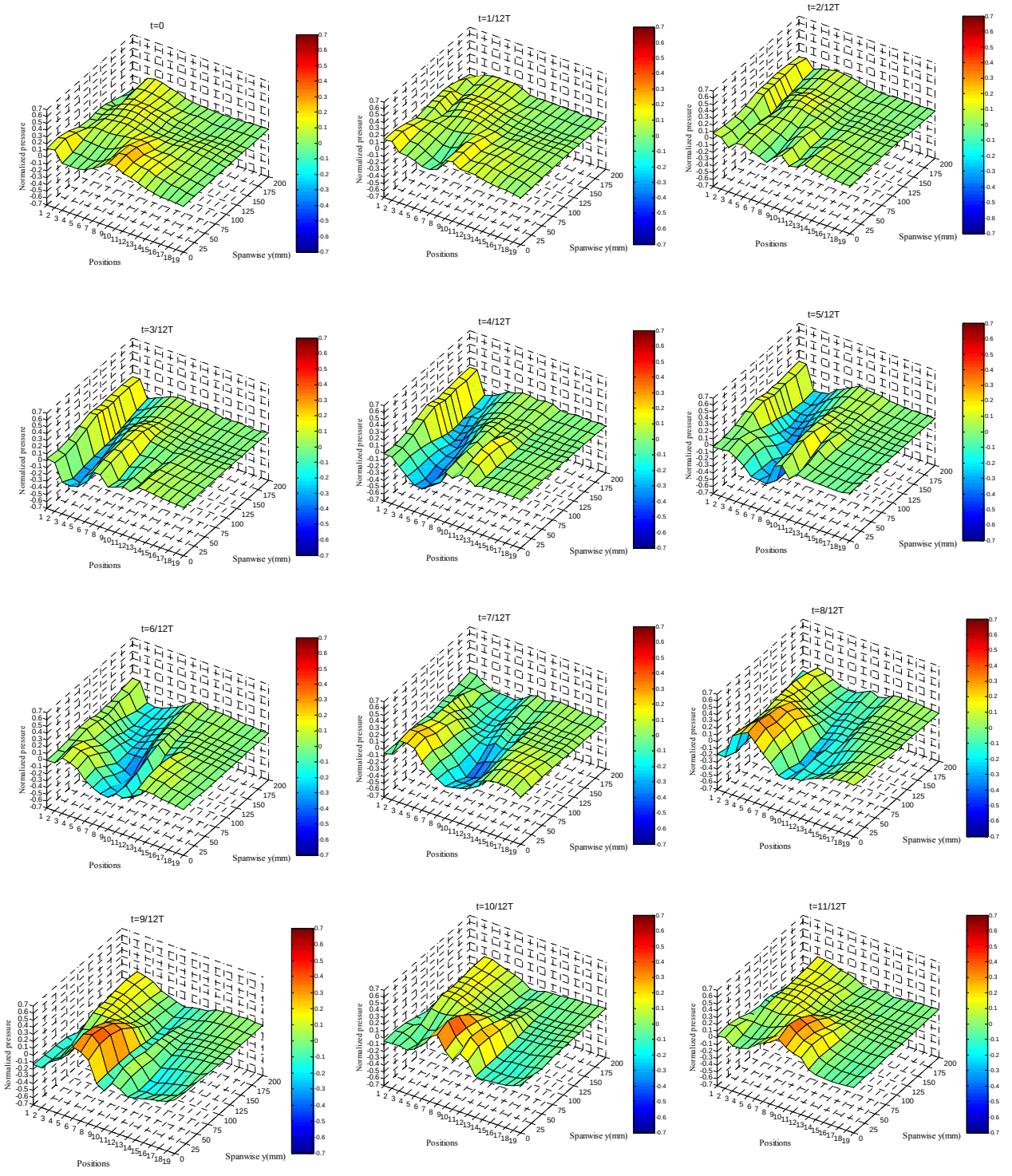

Fig. 3.19 Instantaneous normalized pressure distribution in a cycle T of fluctuating flow at reduced frequency k=0.96 (U_{re}=16.67) [Matsumoto, Shirato et al. 2005]

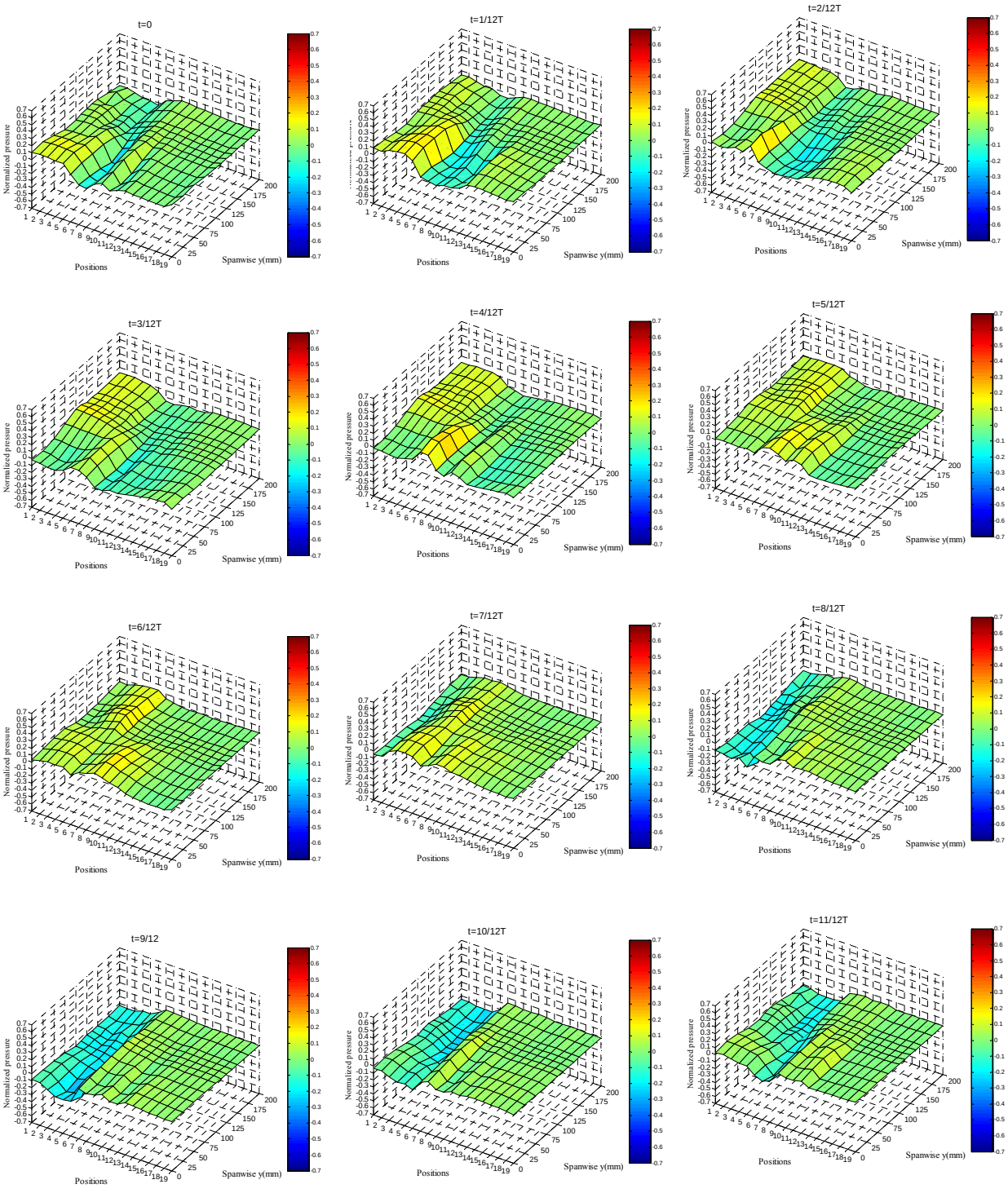

Fig. 3.20 Instantaneous normalized pressure distribution in a cycle T of fluctuating flow at reduced frequency k=0.72 (U_{re}=22.22) [Matsumoto, Shirato et al. 2005]

Instantaneous normalized pressure distribution at time intervals of a cycle T of the 3D fluctuating flows at different reduced frequency k=1.92, 1.44, 0.96 and 0.72, corresponding to the reduced velocities U_{re}=8.33, 11.11, 16.67 and 22.22 are expressed in Figures 3.17÷3.20. As can be seen in Figure 3.17, the high pressure regions (both negative and positive pressures) appear in the fluctuating part on the model surface at the high reduced frequency k=1.92 (or low reduced velocity U_r=8.33), moreover, the movement of these high pressure regions from leading edge to trailing edge corresponding to each time interval in the cycle T of the fluctuating flow. On the contrary, the high pressure regions and its movement also are observed on model surface at the low reduced frequencies (high reduced velocities), but the high pressure region distributes spanwise more homogenously on both parts of fluctuating and smooth flows (see Figures 3.18, 3.19 and 3.20). In comparison, the pressure values appear higher at the high reduced frequencies than the low reduced ones.

It also can be discussed that at the high reduced frequency of the fluctuating flow the convection or secondary spanwise flow between the fluctuating and smooth flows happens to be very weak, this can explain why the high pressure region locally appear on only fluctuating flow part where the fluctuating flow dominates on contribution of the surface pressure fluctuation and not to spread into smooth flow one, whereas this secondary spanwise flow seems to be strong at the low reduced frequencies that deduce the spanwise distribution of surface pressure. In the other word, the spanwise secondary flow and spanwise distribution of the surface pressure have strengthened corresponding to decrease of the reduced frequency (or increase of reduced velocities), and low reduced frequencies (high reduced velocities) influence stronger on the spanwise distribution of the surface pressure.

3.7 Spatial correlation of unsteady pressure field

Spatial correlation coefficient of the fluctuating pressures on three experimental models and at some flow conditions is studied here. The spanwise correlation coefficient which characterize for the cross correlation of two time series in the time domain is defined as normalized ratio between auto correlation and covariance as follows:

$$C_{\upsilon_i\upsilon_j}(\Delta y)=\frac{R_{\upsilon_i\upsilon_j}(\Delta y)}{\sigma_{\upsilon_i}\sigma_{\upsilon_j}}=\frac{\overline{\upsilon_i(t,y)\upsilon_j(t,y+\Delta y)}}{\sqrt{\overline{\upsilon_i(t,y)^2}}\sqrt{\overline{\upsilon_j(t,y+\Delta y)^2}}} \tag{3.2-a}$$

$$C_{p_ip_j}(\Delta y)=\frac{R_{p_ip_j}(\Delta y)}{\sigma_{p_i}\sigma_{p_j}}=\frac{\overline{p_i(t,y)p_j(t,y+\Delta y)}}{\sqrt{\overline{p_i(t,y)^2}}\sqrt{\overline{p_j(t,y+\Delta y)^2}}} \tag{3.2-b}$$

where: υ denotes to turbulence (υ=u(t) or w(t)); p denotes to fluctuating pressures; Δy: spanwise separation.

Figures 3.21÷3.23 express the spatial correlation coefficients of chordwise fluctuating pressures in the spanwise direction at the turbulent flows corresponding to mean velocities U=3m/s, 6m/s and 9m/s on models B/D=1, B/D=1 with S.P and B/D=5, respectively. Figure 3.24 show the spanwise correlation coefficients of chordwise fluctuating pressures on model B/D=5 at the fluctuating flows. It is generally agreed that the correlation coefficients in the spanwise direction depend on concretely investigated positions on the chordwise direction, this is supposed due to effects of wind-structure interaction and bluff body flow on the model surface.

As can be seen from Figure 3.21 that in the model B/D=1 the correlation coefficients of the fluctuating pressures in the leading edge exhibits higher that those in the trailing edge. Therefore, high span correlation of the fluctuating pressures can be observed in the region of high pressure distribution at the leading edge. In the case of model B/D=1 with Splitter Plate, it seems that the spanwise correlation coefficients reduce gradually from leading edge positions to trailing edge ones, however, no much difference in the spanwise correlation of the chordwise fluctuating pressures can be seen (see Figure 3.22). Thus, installation of the Splitter Plate at the model wake has suppressed the local distribution of high pressure region at the leading edge and high spanwise correlation coefficients at this region are not accordingly appeared. As can be seen in Figure 3.23 as the case of model B/D=5, the spanwise correlation affects to close spanwise separations between 0mm and 125mm, the spanwise correlation decays after this distant separation 125mm for all cases of mean velocities U=3m/s, 6m/s and 9m/s. Moreover, the high spanwise correlation is observed at positions 3,4 near the leading edge and in the influence of separation bubble formed in the model surface. In the fluctuating flows as shown in Figure 3.24, the spanwise correlation strongly depends on investigated positions. It seems that the high spanwise correlation occurs at the leading edge region where the high pressure region is observed at the high reduced frequencies k=1.92 and k=11.11. However, at the low reduced frequency k=0.72, the high spanwise correlation is observed not in the leading edge region, but in the trailing edge one.

Spanwise correlation coefficients are compared between smooth and turbulent flows, between without S.P and with S.P by measurements at some chordwise positions Nos.2,4,6 and 8 in model B/D=1, effect of Karman vortex on correlation coefficients is also investigated. As can be seen in Figure 3.25, in the investigated case of model B/D=1, the spanwise correlation in the smooth flows exhibit larger that that in the turbulent ones. Moreover, it is observed that the spanwise correlation on model without S.P expresses higher that on model with S.P in both the smooth flows and turbulent ones.

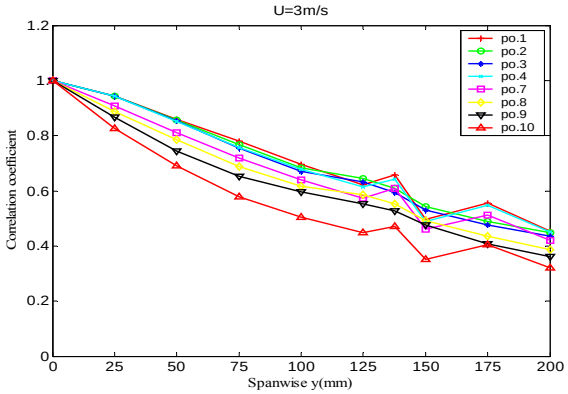

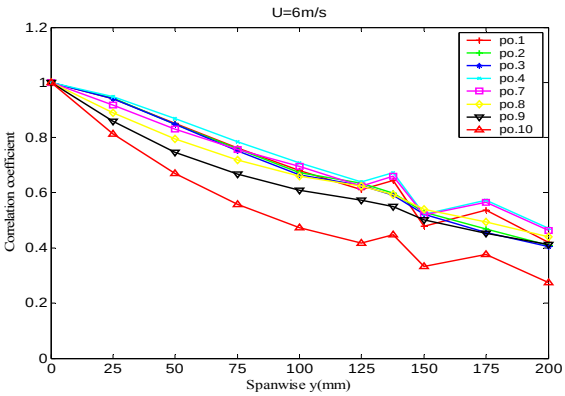

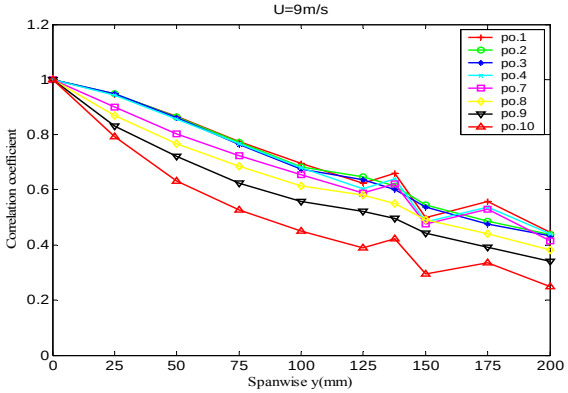

Fig.3.21 Spatial correlation coefficients of chordwise fluctuating pressures at turbulent flows (B/D=1)

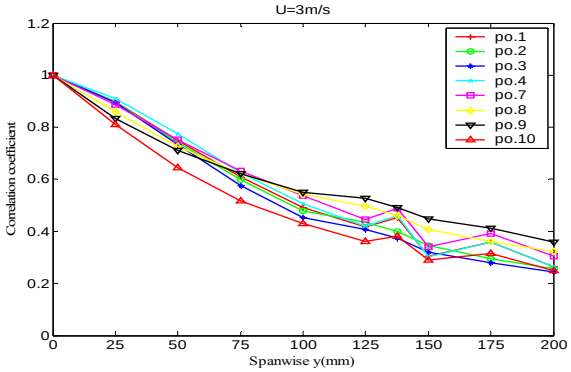

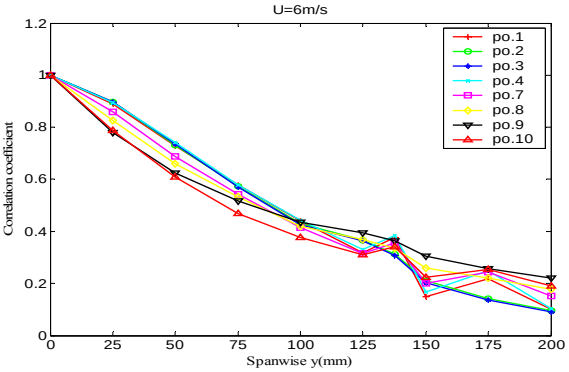

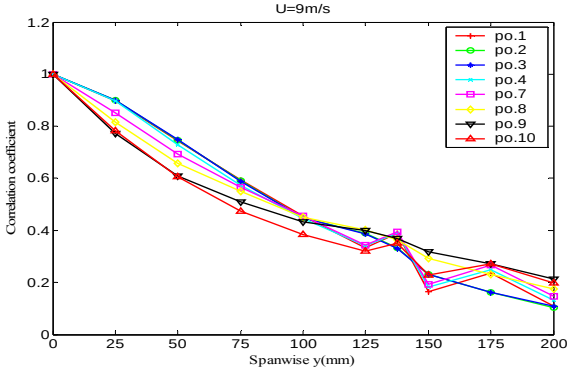

Fig.3.22 Spatial correlation coefficients of chordwise fluctuating pressures at turbulent flows (B/D=1 with S.P)

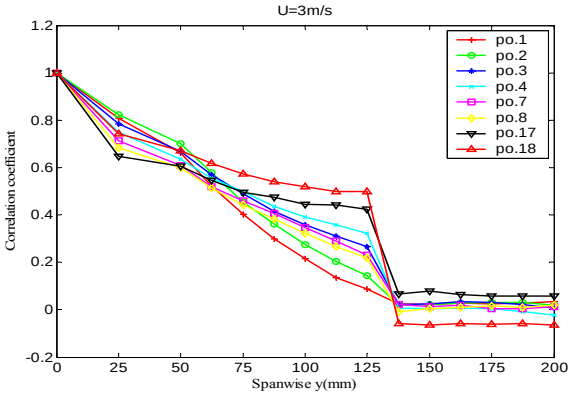

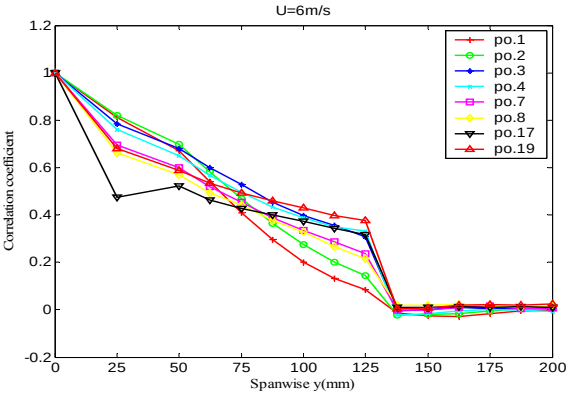

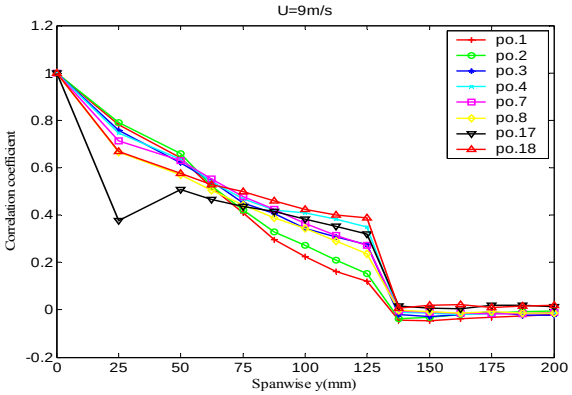

Fig.3.23 Spatial correlation coefficients of chordwise fluctuating pressures at turbulent flows (B/D=5)

a. k=1.92 (U_{re}=8.33)

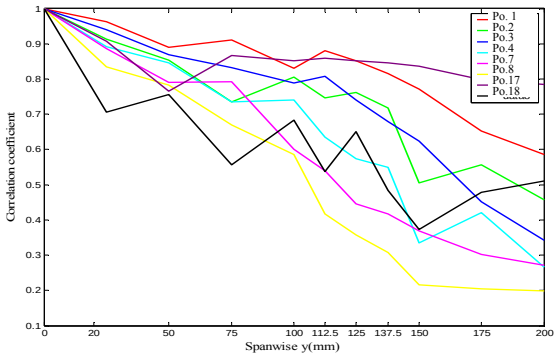

b. k=1.45 (U_{re}=11.11)

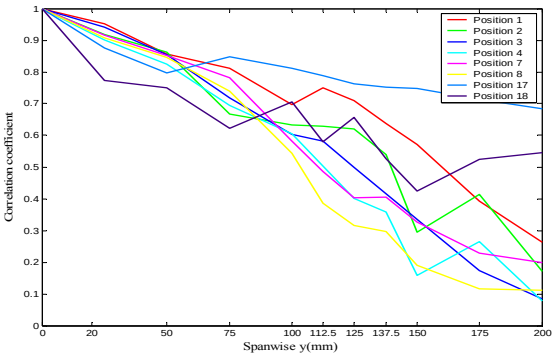

c. k=0.72 (U_{re}=22.22)

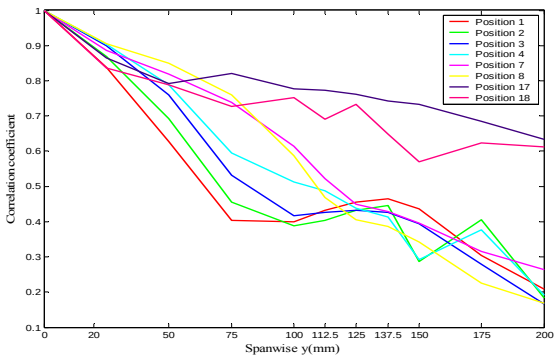

Fig.3.24 Spatial correlation coefficients of chordwise fluctuating pressures at fluctuating flows (B/D=5)

U=3m/s

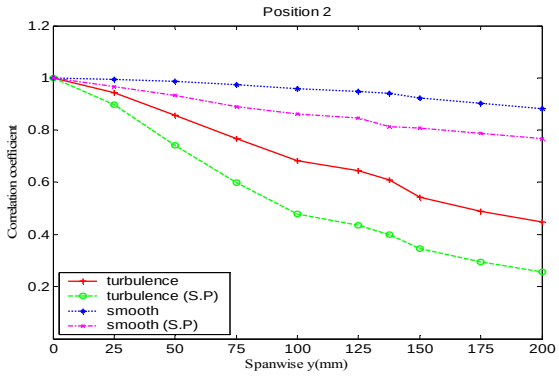
Position 2
Correlation coefficient
Spanwise y(mm)
turbulence
turbulence (S.P)
smooth
smooth (S.P)

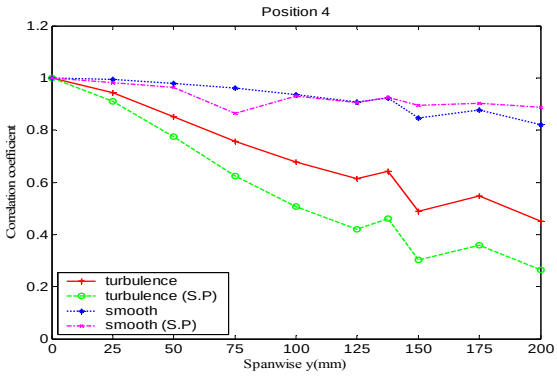
Position 4
Correlation coefficient
Spanwise y(mm)
turbulence
turbulence (S.P)
smooth
smooth (S.P)

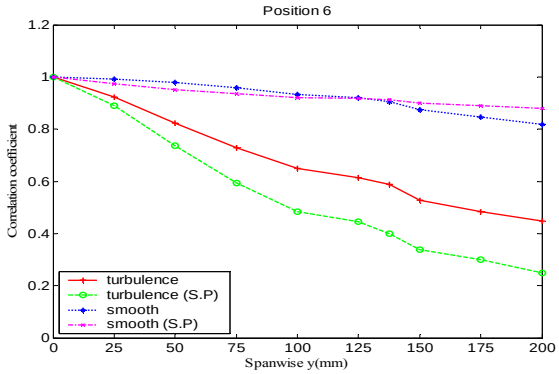
Position 6
Correlation coefficient
Spanwise y(mm)
turbulence
turbulence (S.P)
smooth
smooth (S.P)

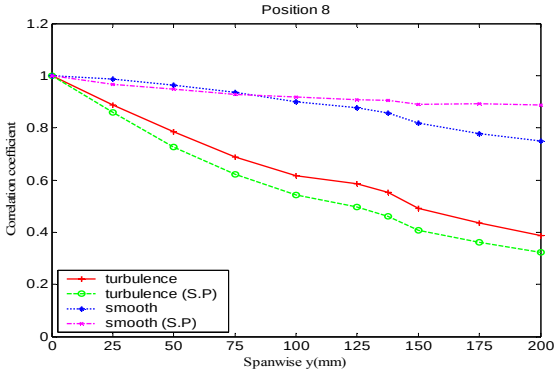
Position 8
Correlation coefficient
Spanwise y(mm)
turbulence
turbulence (S.P)
smooth
smooth (S.P)

U=6m/s

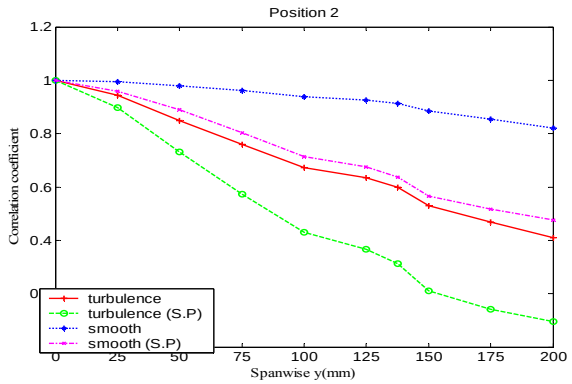
Position 2
Correlation coefficient
Spanwise y(mm)
turbulence
turbulence (S.P)
smooth
smooth (S.P)

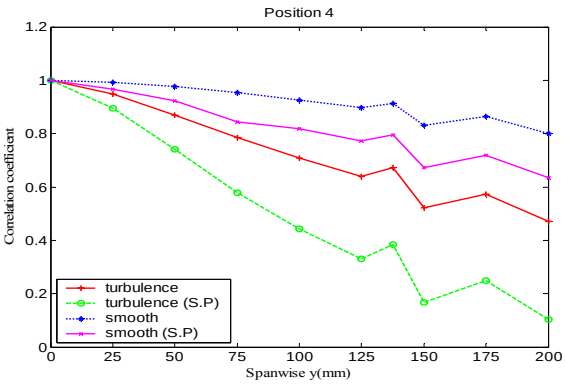
Position 4
Correlation coefficient
Spanwise y(mm)
turbulence
turbulence (S.P)
smooth
smooth (S.P)

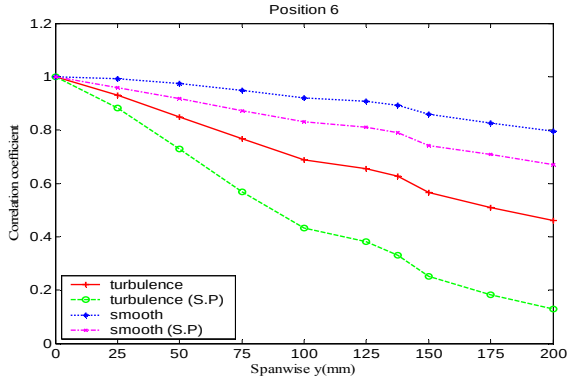
Position 6
Correlation coefficient
Spanwise y(mm)
turbulence
turbulence (S.P)
smooth
smooth (S.P)

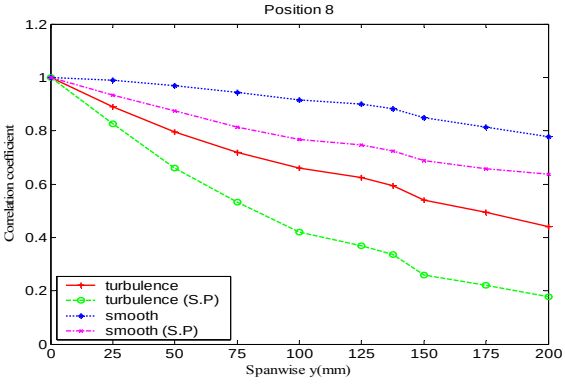
Position 8
Correlation coefficient
Spanwise y(mm)
turbulence
turbulence (S.P)
smooth
smooth (S.P)

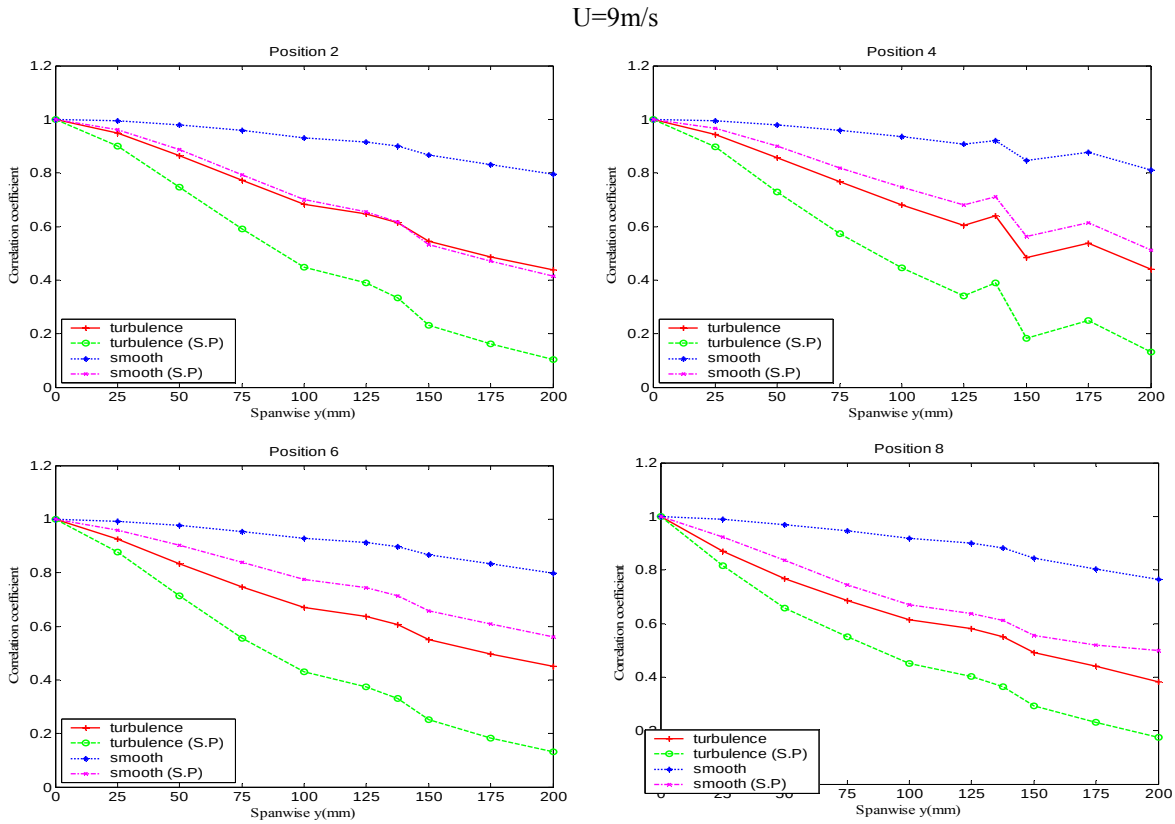

Fig. 3.25 Comparison of correlation coefficients between smooth and turbulent flows and between without S.P and with S.P, effect of Karman vortex on correlation coefficients

This finding implies that the Karman vortex (in the case without S.P) increases the spanwise correlation in such a way as enhancement of the spanwise convection. In almost investigated cases, furthermore, difference between without S.P and with S.P in the turbulent flows exhibit larger than that in the smooth flow. Therefore, it is commented that the effect of the Karman vortex on higher spanwise correlation in the turbulent flows is higher than that in the smooth flow (see Figure 3.25).

B/D=1

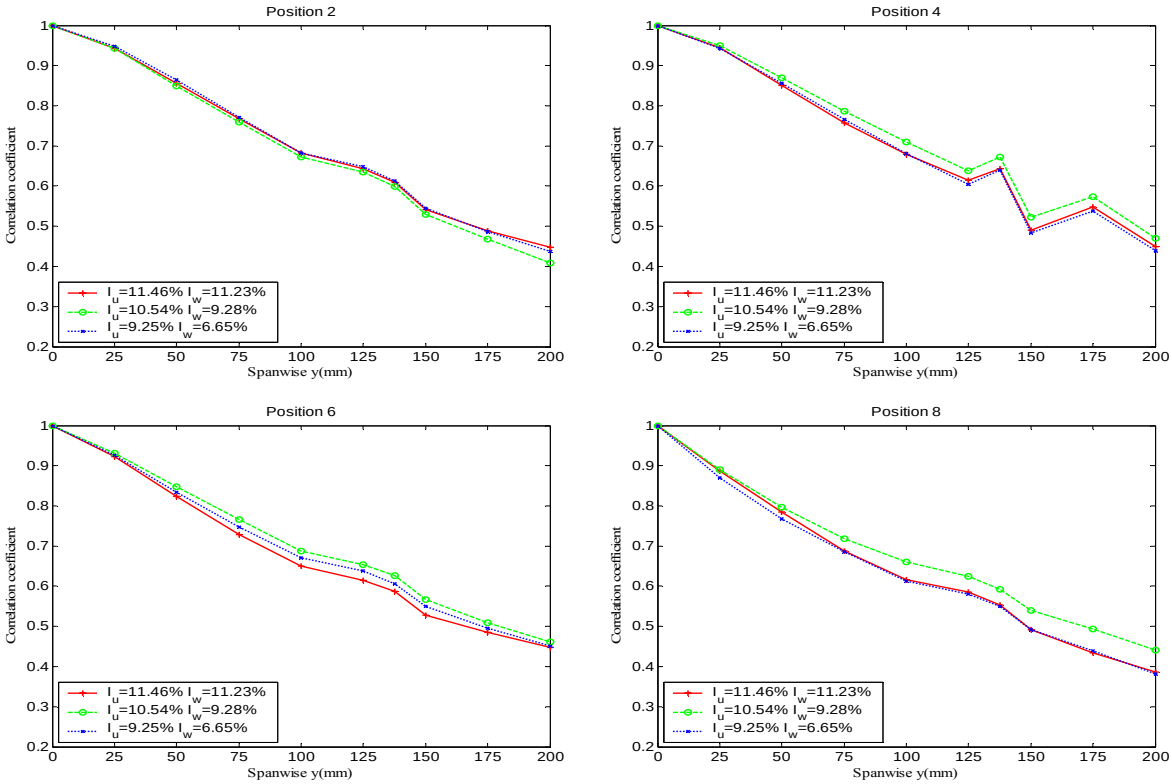

B/D=1 with S.P

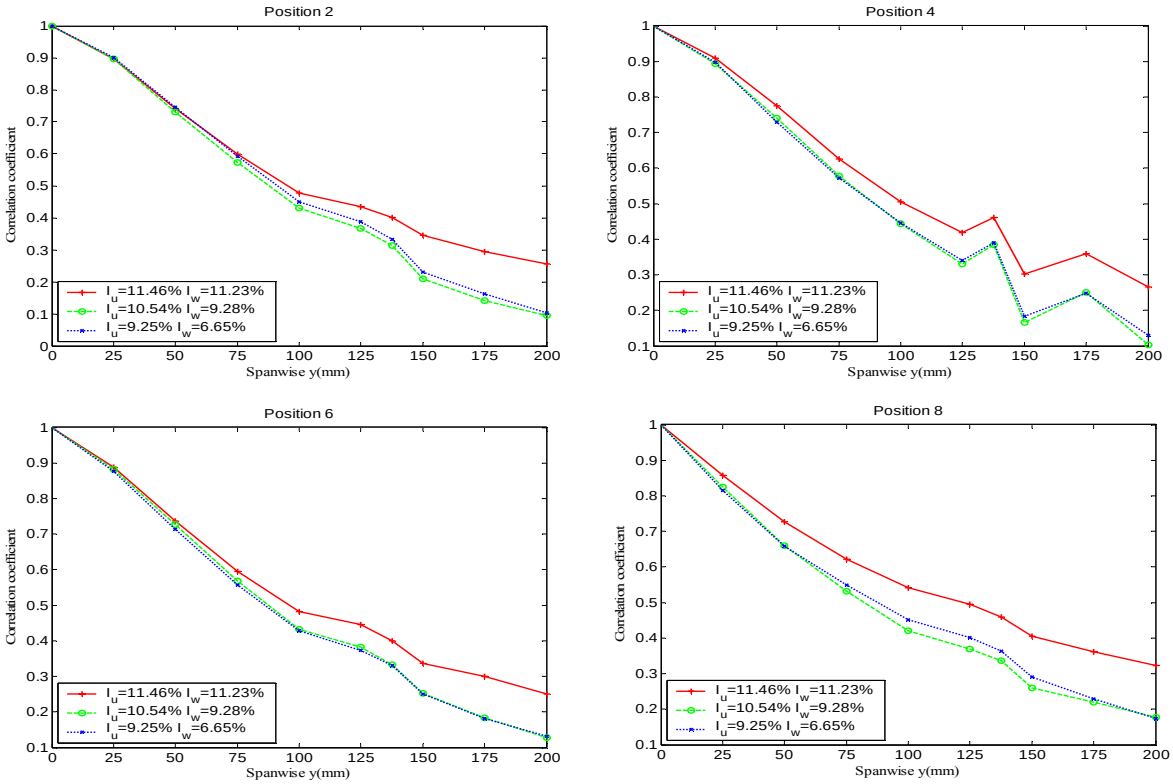

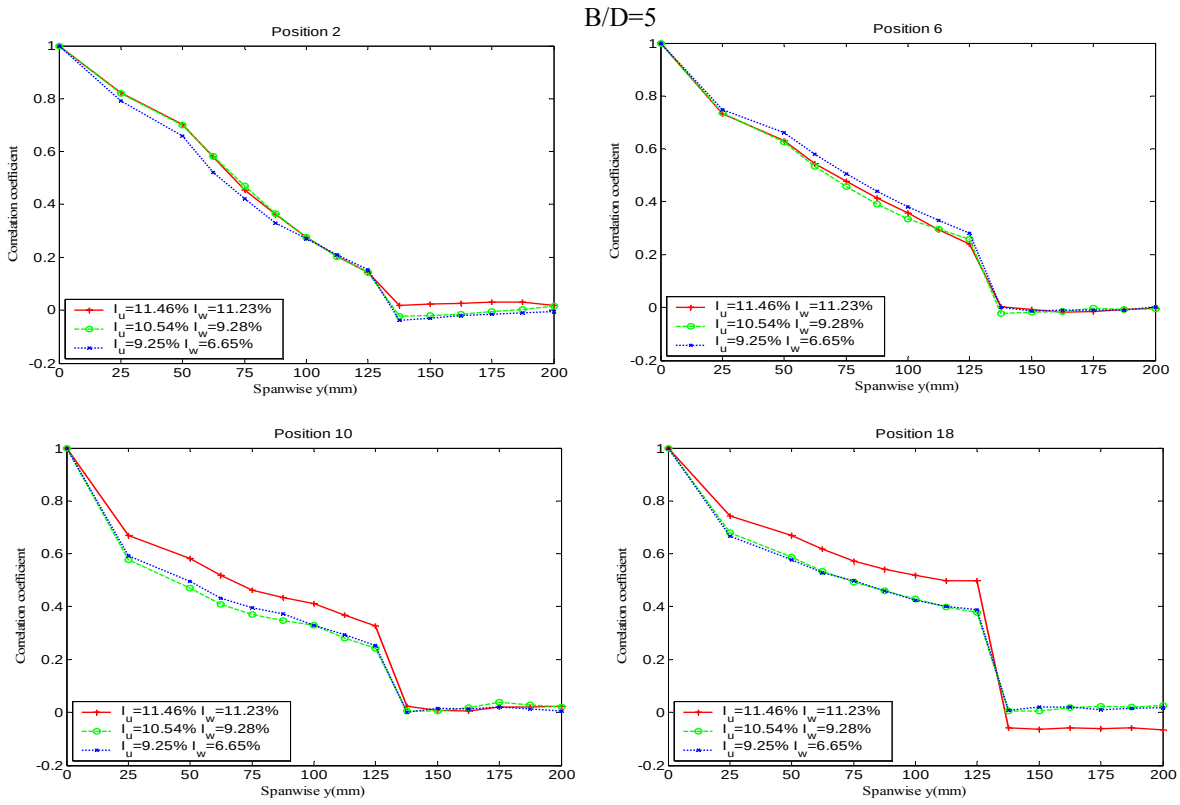

Fig. 3.26 Comparison of correlation coefficients in different turbulent conditions and effect of intensities of turbulence on correlation coefficients

Figure 3.26 shows comparison of the correlation coefficients in different turbulent conditions and effect of turbulent intensities on correlation coefficients as well. Here the turbulent conditions and the turbulent intensities correspond to mean velocities U=3m/s, 6m/s and 9m/s in the turbulent flow. As can be seen that no much difference in the spanwise correlation can be observed with respect to intensities of turbulence, especially on models B/D=1 without S.P and B/D=5. In comparison, however, higher spanwise correlation can be seen at high intensity of turbulence (low mean velocity) on the models B/D=1 with S.P and B/D=5.

U=3m/s

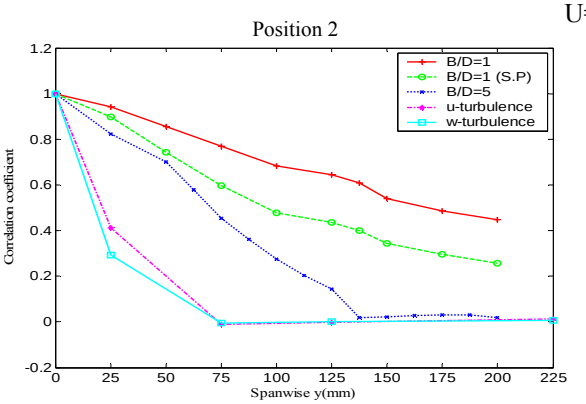
Position 2
B/D=1
B/D=1 (S.P)
B/D=5
u-turbulence
w-turbulence
Correlation coefficient
Spanwise y(mm)

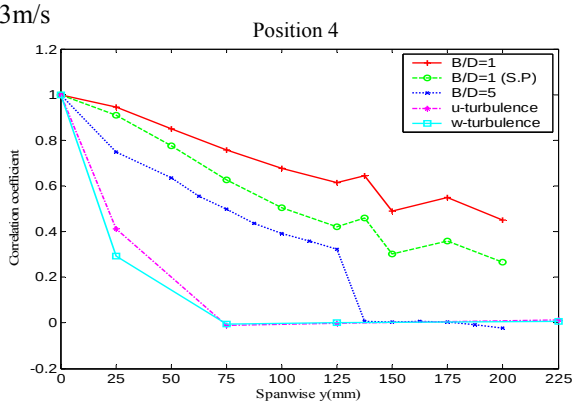
Position 4
B/D=1
B/D=1 (S.P)
B/D=5
u-turbulence
w-turbulence
Correlation coefficient
Spanwise y(mm)

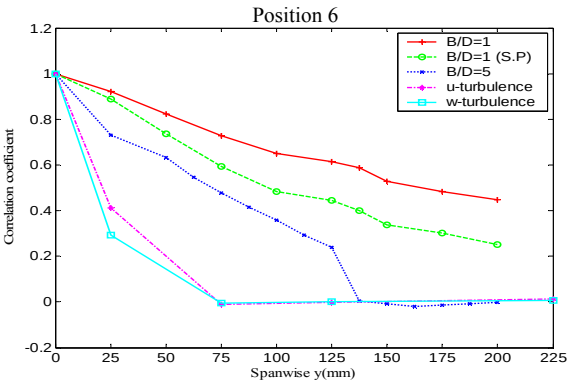
Position 6
B/D=1
B/D=1 (S.P)
B/D=5
u-turbulence
w-turbulence
Correlation coefficient
Spanwise y(mm)

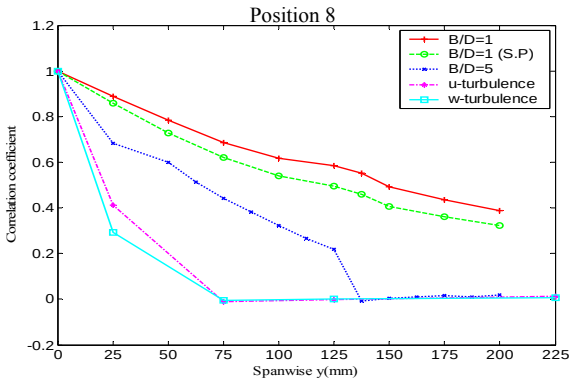
Position 8
B/D=1
B/D=1 (S.P)
B/D=5
u-turbulence
w-turbulence
Correlation coefficient
Spanwise y(mm)

U=6m/s

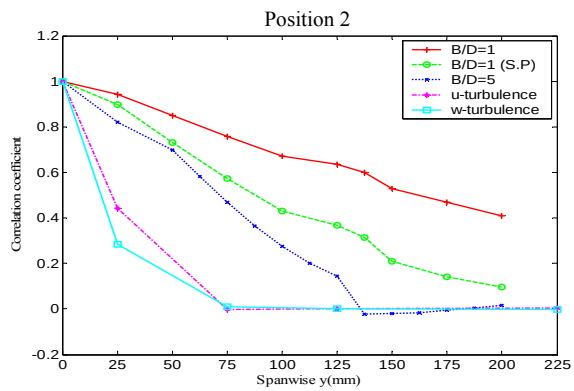
Position 2
B/D=1
B/D=1 (S.P)
B/D=5
u-turbulence
w-turbulence
Correlation coefficient
Spanwise y(mm)

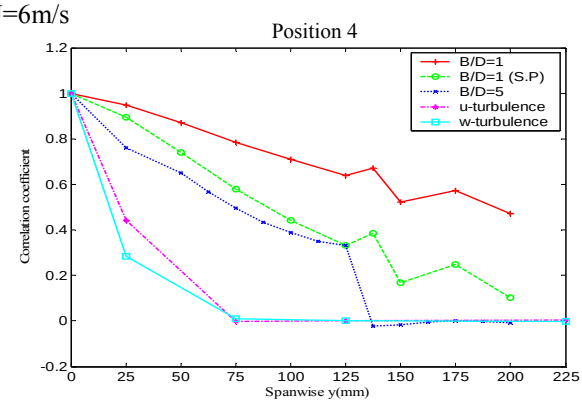
Position 4
B/D=1
B/D=1 (S.P)
B/D=5
u-turbulence
w-turbulence
Correlation coefficient
Spanwise y(mm)

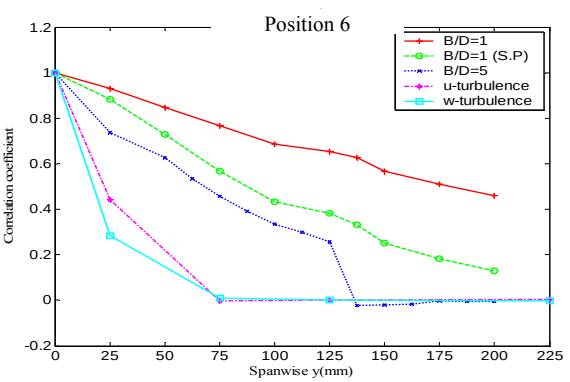
Position 6
B/D=1
B/D=1 (S.P)
B/D=5
u-turbulence
w-turbulence
Correlation coefficient
Spanwise y(mm)

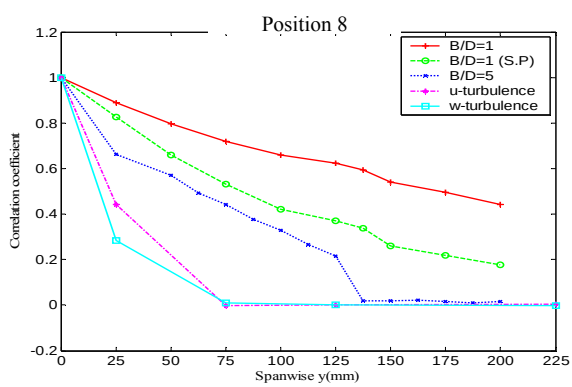
Position 8
B/D=1
B/D=1 (S.P)
B/D=5
u-turbulence
w-turbulence
Correlation coefficient
Spanwise y(mm)

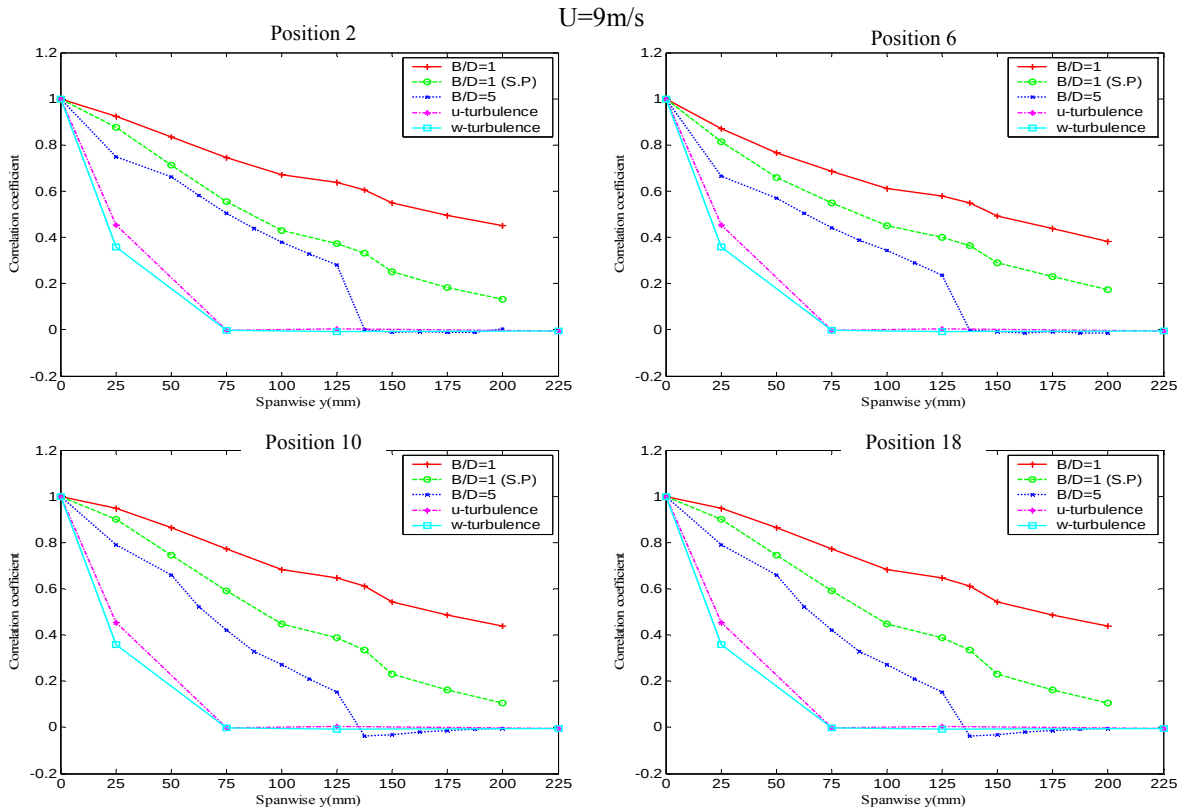

Fig. 3.27 Comparison of spanwise correlation coefficients between wind turbulence and induced pressure, and between experimental models at different turbulent flows

Figure 3.27 shows comparison of spanwise correlation coefficients between wind turbulence and induced pressure, that between experimental models B/D=1, B/D=1 with S.P and B/D=5 at different turbulent flows (corresponding to mean velocities U=3m/s, 6m/s and 9m/s). Physical pressure data have measured at some chordwise positions Nos. 2,4,6 and 8 on the model B/D=1 and Nos. 2,6,10 and 18 on model B/D=5, whereas the fluctuating velocities measured along spanwise centerline of the models but without installation of the models.

In comparison of the spanwise correlation between the three models, it is observed that the spanwise correlation coefficients of the induced pressures gradually reduce from the model B/D=1 without S.P, to the model B/D=1 with S.P and the model B/D=5. It is discussed that the spanwise correlation reduces with increase of slender ration B/D in the investigated cases. Its is also supposed that dependence of the spanwise correlation on the spanwise separations decreases with respect to increase of the slender ratios, as can be seen that the spanwise correlation on model B/D=5 affect on only separations 0mm÷125mm, whereas on separations 0mm÷200mm on model B/D=1. In comparison in the spanwise correlation between u-turbulence and w-turbulence

in the turbulent flows, it is seen that the spanwise correlation of the u-turbulence expresses little higher that that of the w-turbulence. However, the spanwise correlation of the wind turbulence decays fast with respect to increase of the spanwise separations. Concretely, the spanwise correlation of the turbulence only affects at very close separation 0mm÷75mm, the turbulence is uncorrelated after 75mm in the spanwise direction in these measurements. Obviously, the spanwise correlation of the pressures exhibits larger than that of the turbulence.

3.8 Conclusion

Spatial distribution and correlation of the pressures has been studied here. Physical measurements of the pressure and turbulence have been carried out on some experimental models B/D=1, B/D=5 in some ongoing flows including the smooth flows, the turbulent flows and the three-dimensional fluctuating flows. With the model B/D=1, the installation of Splitter Plate at the model wake has been used in some cases in account of investigation of the Karman vortex effect on the spanwise correlation.

It can be concluded as some following points:

(1) Fluctuating pressure distribute strongly and locally on the leading edge region. In the fluctuating flows, the spanwise convection and the spanwise distribution of the surface pressure have been strengthened with respect to decrease of the reduced frequencies (increase of reduced velocities). It is supposed that the low frequency components can play more important role on spanwise distribution of induced pressure than high frequency ones.

(2) Generally, the spanwise correlation depends strongly on such parameters as flow conditions, investigated positions, experimental models and their slender ratios B/D in the investigated cases. High spanwise correlation has observed at some positions near the leading edge regions where the high pressure region localized. The spanwise correlation in the smooth flows is larger than that in the turbulent ones. Moreover, the effect of Karman vortex (in the case without S.P) on increases of the spanwise correlation is also seen. It is discussed that the spanwise correlation reduces with increase of slender ration B/D.

(3) From the physical measurements, it is verified obviously that the spanwise correlation of the turbulent-induced forces always exhibits larger than that of the turbulence. The wind-structure interaction and the bluff body flow reason for the higher mechanism of spanwise correlation of induced forces than that of the turbulence.

References

Cherry, N.J., Hillier, R., Latour, M.E.M. (1984), "Unsteady measurements in a separated and reattaching flow", *J. Fluid Mech.*, 144, 13-46.

Davenport, A.G.(1962), "The response of slender, line-like structures to a gusty wind", *Proc. Inst. Civ. Eng.*, 23, 389-408.

Hann Jr, F.L., Kareem, A., Szewczyk, A.A. (1998), "The effect of turbulence on the pressure distribution around a rectangular prism", *J. Wind Eng. Ind. Aerodyn.*, **77-78**, 381-392.

Hillier, R., Cherry, N.J. (1981), "The effects of stream turbulence on separation bubbles", *J. Wind Eng. Ind. Aerodyn.*, **8**, 49-58.

Jakobsen, J. B.(1997), "Span-wise structure of lift and overturning moment on a motionless bridge girder", *J. Wind Eng. Ind. Aerodyn.*, **69-71**, 795-805.

Kareem, A., Cermak, J.E. (1984), "Pressure fluctuations on a square building model in boundary layer flows", *J. Wind Eng. Ind. Aerodyn.*, **16**, 17-41.

Kareem, A. (1997), "Correlation structure of random pressure field", *J. Wind Eng. Ind. Aerodyn.*, **69-71**, 507-516.

Kawai, H. (1983), "Pressure fluctuations on square prisms – applicability of strip and quasi-steady theories", *J. Wind Eng. Ind. Aerodyn.*, **13**, 197-208.

Kimura, K., Fujino, Y., Nakato, S., Tamura, H. (1997), "Characteristics of buffeting forces on plat cylinders", *J. Wind Eng. Ind. Aerodyn.*, **69-71**, 365-374.

Kiya, M., Sasaki, K.(1983), "Structure of a turbulent separation bubbles", *J. Fluid Mech.*, **137**, 83-113.

Larose, G.L.(1996), "The span-wise coherence of wind forces on streamlined bridge decks", *Proc. 3rd Int'l Colloquium on Bluff Body Aerodynamics and Applications*, Blacksburg, USA.

Larose, G.L.(2003), "The spatial distribution of unsteady loading due to gusts on bridge decks", *J. Wind Eng. Ind. Aerodyn.*, **91**, 1431-1443.

Le, T.H., Matsumoto, M., Shirato, H., Mizuno, T., Yamane, K., Furukawa, T. (2005), "Spatial distribution characteristics of surface pressure on 2D rectangular section in 3D fluctuating flow", *Proc. 60th JSCE Annual Meeting on Civil Engineering*, September 9-11, Wasada Japan.

Lee, B.E. (1975), "Effect of turbulence on the surface pressure on a square prisms", *J. Fluid Mech.*, **69**, 263-282.

Matsumoto, M., Shiraishi, N., Shirato, H. (1988), "Bluff body aerodynamics in pulsating flow", *J. Wind Eng. Ind. Aerodyn.*, **28**, 261-270.

Matsumoto, M. (2000), *Aeroelasticity and bridge aerodynamics*, Text book for Int'l Advanced

Course in Wind Engineering, Genoa, Italy.

Matsumoto, M., Shirato, H., Araki, K., Haramura, T., Hashimoto, T.(2003), "Spanwise coherence characteristics of surface pressure field on 2-D bluff bodies", *J. Wind Eng. Ind. Aerodyn.*, **91**, 155-163.

Matsumoto, M., Shirato, H., (2004), Matsuura (2004), "Spatial pressure distribution on rectangular section B/D=5 in separated and reattached flow", *Proc. the 17th KKCNN Symposium on Civil Engineering*, December 15-17, Thailand.

Matsumoto, M., Shirato, H., Le, T.H., Mizuno, T., Furukawa, T. (2005a), "Spanwise coherence and distribution characteristics of surface pressure on 2D rectangular cross section in 3D fluctuating flow", *Proc. 18th KKCNN Symposium on Civil Engineering*, December 19-21, Caoshung Taiwan.

Matsumoto, M., Shirato, H., Mizuno, T., Furukawa, T., Le, T.H. (2005b), "Effect of harmonic body motion on gust forces", *Proc. 18th KKCNN Symposium on Civil Engineering*, December 19-21, Caoshung Taiwan.

Matsumoto, M., Shirato, H., Yagi, T., Mizuno, T. (2005), *Study on spatial characteristics of gust force on rectangular cylinder (B/D=5) in fluctuating flow*, Internal Report (in Japanese)

Matsumoto, M., Shirato, H., Yagi, T., Yamane, K. (2006), *Study on spatial characteristics of gust force on rectangular cylinder in turbulent flow,* Internal Report (in Japanese)

Matsumoto, M., Shirato, H., Yagi, T., Furukawa, T. (2007), *Study on spatial characteristics of gust forces on rectangular cylinder in gusty flow*, Internal Report (in Japanese)

Nagao, F., Utsunomiya, H., Noda, M., Oshima, Y. (2003), "Basic study on spatial correlation of fluctuating lifts acting on plates", *J. Wind Eng. Ind. Aerodyn.*, **91**, 1349-1361.

Ricciardelli, F., de Grenet, E.T., Hangan, H. (2002), "Pressure distribution, aerodynamic forces and dynamic response of box bridge sections", *J. Wind Eng. Ind. Aerodyn.*, **90**, 1135-1150.

Robertson, A.P., Hoxey, R.P., Short, J.L., Ferguson, W.A., Blackmore, P.A. (1998), "Prediction of structural loads from fluctuating wind pressures: Validation from full-scale force and pressure measurements", *J. Wind Eng. Ind. Aerodyn.*, **74-76**, 631-640.

Saathhoff, P.J., Melbourne, W.H.(1997), "Effects of free-stream turbulence on surface pressure fluctuations in a separation bubble", *J. Fluid Mech.*, **337**, 1-24.

Shirato, H., Matsumoto, M., Mizuno, T. (2005), "Spanwise and chordwise pressure distribution on B/D=5 rectangular section in sinusoidal gust", *Proc. 6th Asia-Pacific Conference on Wind Engineering (APCWE VI)*, Seoul, Korea.

Chapter 4

Aerodynamic admittance of unsteady buffeting forces on rectangular cylinders

4.1 Introduction

It is generally agreed that until now the buffeting forces and the gust response of bridges are being treated under two main assumptions of (1) the quasi-steady theory and (2) the strip theory. The quasi-steady theory assumes that the turbulent-induced buffeting forces apply the linear approximation and expansion of instantaneous force coefficients and instantaneous relative velocity. Moreover, correspondence in the spectral distribution and contribution between the turbulence and the turbulent-induced buffeting forces in the frequency domain has been accepted in this quasi-steady theory, this implies that the buffeting forces do not depend on the frequency. However, behavior of the buffeting forces exhibits much more complicated than that of turbulence due to representation of the wind-structure interaction and the bluff body flow phenomena. Dependence of the quasi-steady buffeting forces on the frequency has been observed due to series of physical measurements. A lot of attempts have been proposed to cope with the limitation of the buffeting forces. The corrected quasi-steady approach in the frequency domain proposed by Davenport (1962) with usage of the frequency-dependant aerodynamic admittance function.

The aerodynamic admittance function is determined as transfer function in the frequency domain between the input turbulence and the output turbulent-induced forces. This transfer function compensates deference between the turbulence and turbulent-induced forces of their spectral distribution in the frequency domain. Therefore, the aerodynamic admittance function can be experimentally obtained by simultaneous measurements of the turbulence and the buffeting forces in wind tunnels. However, the physical measurements and recent researches on the aerodynamic admittance exist some limitations. Firstly, the aerodynamic admittance function is usually determined from the quasi-steady theory in which some quantities such as the static aerodynamic coefficients and the relative velocity are linearized, thus nonlinear effects on the

quasi-steady aerodynamic admittance need to be further discussed. Secondly, in the direct measurements of the output aerodynamic forces in many cases, it can not differ between turbulent-induced buffeting forces (due to the turbulence) and self-excited flutter forces (due to the wind-structure interaction) in the measured aerodynamic forces, thus the transfer function contains influence of the self-excited forces. However, it is believed that the measured aerodynamic forces on the motionless fixed models are considered as unique contribution of the turbulent-induced buffeting forces. Thirdly, it is usually assumed that contributions of the longitudinal turbulence u(t) and the vertical turbulence are equal to the aerodynamic admittance. Therefore, the aerodynamic admittance between the longitudinal turbulence and the buffeting forces is similar to that between the vertical turbulence and the forces. Simplified model of the frequency-dependant aerodynamic admittance function, so-called single-variate quasi-steady admittance has been widely used in the gust response prediction of bridges so far. Recently, some further approaches such as nonlinear, multivariate and complex aerodynamic admittance functions have been mentioned anywhere in some literatures. By using the time-domain indicial function approach, furthermore, the mechanical relationship between the aerodynamic admittance and the flutter derivatives has been discussed. It is discussed, moreover, that the pressure redistribution occurs on surface models due to effects of the wind-structure interaction and the bluff body flow, in the other words, the aerodynamic admittance might be affected by the bluff body flow. However, this effect of the bluff body is still not clarified by any literature.

This chapter will discuss on the aerodynamic admittance function in comparison with some new approaches of the nonlinear and multivariate admittance functions, as well as the mechanical relationship between the aerodynamic admittance and the flutter derivatives is going to be mentioned. Wind turbulence and turbulent-induced buffeting forces are measured directly on some physical models B/D=5 and B/D=20 under the different turbulent flows in the wind tunnel.

4.2 Literature reviews

Sears 1941 developed analytical solution for the unsteady aerodynamic response of the airfoil in the vertical gust flows, that used the indicial function and initial works of Wagner 1925 and Kusner 1936. Sears 1941 used so-called Sears function to establish spectral relation between unsteady aerodynamic forces and wind turbulence, thus this Sears functions was treated as the aerodynamic admittance function. Theoretically, the Sears function is only valid for the unsteady aerodynamic response prediction of airfoil or thin plate. Liepmann 1952 proposed the theoretical buffeting analysis for subject of airplane wing that based on both spectrum analysis and statistical computation, he also proposed the empirical formula for the aerodynamic admittance as

approximation solution from the Sears function which is the most commonly used for the lift force aerodynamic admittance of the airfoil and the thin plate in the fully-correlated gust flow (Liepmann 1952). Davenport 1962 firstly introduced a framework method for buffeting analysis of bridges and tower structures, that combined by spectrum analysis and statistical computation in the structural modal space. Some correction functions such as the aerodynamic admittance, the coherence and the joint acceptance function have been used in the Davenport's theory. He also approached the empirical formula for the drag force aerodynamic admittance. However, by series of physical measurements on practical sections (i.e., bluff bodies), many literatures (eg., Konishi, Shiraishi and Matsumoto 1975, Walshe and Wyatt 1983, Jancauskas and Melbourne 1986, Sankaran and Jancauskas 1992) discussed the aerodynamic admittance exhibits differently from empirical formulae such as Sears function, Liepmann function, Davenport one. The empirical formulae can be applicable to few certain types of structures. Konishi, Shiraishi and Matsumoto 1975 modified the Sear function for evaluation of the lift force the aerodynamic admittance of bridge sections, so-called equivalent Sear function proposed to validate with physical measurements on thin plate and stiffness girder. Some authors (eg., Larose 1999, Scanlan 2001) discussed on the aerodynamic admittance function in account of spatial distribution of the aerodynamic forces by evaluation of the coherence function and the joint acceptance functions.

In the time-domain approach of both the buffeting forces and self-excited flutter ones using the classical indicial function, the relationship between the aerodynamic admittance and the flutter derivatives is established. Equivalent aerodynamic admittance can be determined via the indicial functions by some authors (Scanlan 2001, Hatanaka and Tanaka 2002, Tubino 2005). Chen and Kareem 2002, however, approximated the aerodynamic admittance via the rational function rather than via the indicial function in the impulse response function, but the approximation of the impulse response function and the aerodynamic admittance is significantly employed for the self-excited flutter forces, but not for the buffeting forces and the aerodynamic admittance.

4.3 Quasi-steady aerodynamic admittance and empirical models

4.3.1 *Quasi-steady aerodynamic admittance*

The unsteady aerodynamic forces (Lift, Drag and Moment) acting on bridge section are determined to be proportional to the relative velocity and the relative aerodynamic force coefficient as follows:

$$L(t)=\frac{1}{2}\rho V^2(t)BC_L(\alpha(t));\quad D(t)=\frac{1}{2}\rho V^2(t)BC_D(\alpha(t));\quad M(t)=\frac{1}{2}\rho V^2(t)B^2C_M(\alpha(t)) \quad (4.1)$$

where V(t): relative velocity; $C_F(\alpha(t)), F=L, D or M$: relative mean force coefficients with

respect to wind angle of attack $\alpha(t)$.

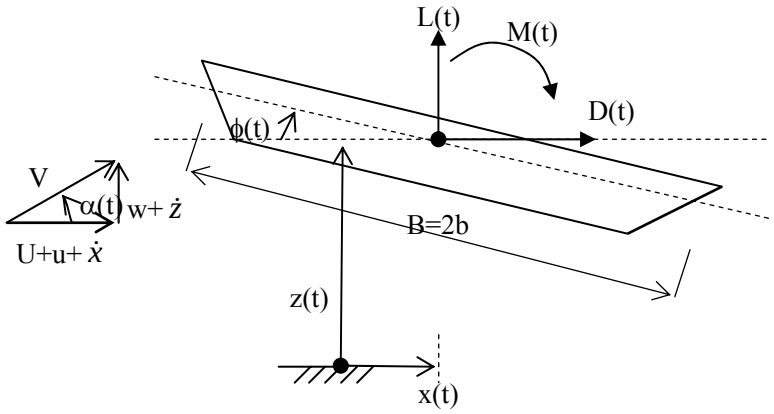

Fig. 4.1 Quasi-steady forces on bridge section

The relative velocity can be expanded and approximated linearly as follows:

$$V^2(t) = (U+u+\dot{x})^2 + (w+\dot{z})^2 = U^2 + u^2 + \dot{x}^2 + 2Uu + 2U\dot{x} + 2u\dot{x} + w^2 + \dot{z}^2 + 2w\dot{z}^2 \quad (4.2\text{-a})$$

$$V^2(t) \approx U^2 + 2Uu(t) \quad (4.2\text{-b})$$

Moreover, the relative mean force coefficients can be expanded by the Taylor's series at the balanced angle of attack ($\alpha = 0$), only linear components are taken into account, we have:

$$C_F(\alpha(t)) = \alpha^0 C_{F0|\alpha=0} + \alpha^1 \frac{dC_F(\alpha)}{d\alpha} + \alpha^2 \frac{d^2C_F(\alpha)}{d\alpha^2} \approx C_{F0} + \alpha C_F^{'}\text{; F=L,D,M} \quad (4.3)$$

Because of very small attacked angles, sinusoidal approximation is accepted as follows:

$$\alpha \approx \sin\alpha = \phi + \frac{w+\dot{z}}{U+u+\dot{x}} \approx \phi + \frac{w}{U} \quad (4.4)$$

After expansion, the unsteady aerodynamic forces are determined due to the quasi-steady theory as follows (only the unsteady lift force in account for a sake of brevity):

$$\begin{aligned} L_{ae} \approx & [\frac{1}{2}\rho BU^2 C_{L0}] + [\frac{1}{2}\rho BU^2 (2C_{L0}\frac{u}{U} + C_L^{'}\frac{w}{U}) + [-\frac{1}{2}\rho BUC_L^{'}\dot{z} + \frac{1}{2}\rho BU^2 C_L^{'}\phi + ... \\ & \rho BUu' C_L^{'}\phi - \frac{1}{2}\rho B^2 UnC_L^{'}\dot{\phi} - \rho BUC_{L0}\dot{x} + 2\rho BUC_L^{'}\dot{x}\phi] \end{aligned} \quad (4.5)$$

where the first term is the mean force, the second one is the buffeting forces, the last one is the aeroelastic flutter forces.

As a result, the buffeting forces on deck section due to the quasi-steady theory are expressed:

$$L(t) = \frac{1}{2}\rho U^2 B\left[C_L \frac{2u(t)}{U} + (C_L^{'} - C_D)\frac{w(t)}{U}\right] \quad (4.6\text{-a})$$

$$D(t)=\frac{1}{2}\rho U^2 B\left[C_D\frac{2u(t)}{U}+(C_D^{'}+C_L)\frac{w(t)}{U}\right] \tag{4.6-b}$$

$$M(t)=\frac{1}{2}\rho U^2 B^2\left[C_M\frac{2u(t)}{U}+C_M^{'}\frac{w(t)}{U}\right] \tag{4.6-c}$$

Power spectral densities of the uniform buffeting forces are obtained thanks to second-order Fourier transformation (cross spectra between two turbulent components $S_{uw}(n)$ are omitted):

$$S_L(n)=(\frac{1}{2}\rho UB)^2[4C_L^2\chi_{Lu}^2(n)S_u(n)+C_L^{'2}\chi_{Lw}^2(n)S_w(n)] \tag{4.7-a}$$

$$S_D(n)=(\frac{1}{2}\rho UB)^2[4C_D^2\chi_{Du}^2(n)S_u(n)+C_D^{'2}\chi_{Dw}^2(n)S_w(n)] \tag{4.7-b}$$

$$S_M(n)=(\frac{1}{2}\rho UB^2)^2[4C_M^2\chi_{Mu}^2(n)S_u(n)+C_M^{'2}\chi_{Mw}^2(n)S_w(n)] \tag{4.7-c}$$

In the formulae above, the frequency-dependant aerodynamic admittance functions are added in order to compensate difference between the unsteady forces and the quasi-steady ones in the frequency domain.

Furthermore, it is usually assumed that contribution of the longitudinal turbulence is similar to that of the vertical turbulence on the buffeting forces as $\chi_{Fu}^2(n)=\chi_{Fw}^2(n)=\chi_F^2(n);F=L,D,M$. Accordingly, the quasi-steady aerodynamic admittance functions can be determined as follows:

$$\chi_L^2(n)=\frac{U^2S_L(n)}{4L_0^2S_u(n)+L^{'2}S_w(n)} \tag{4.8-a}$$

$$\chi_D^2(n)=\frac{U^2S_D(n)}{4D_0^2S_u(n)+D^{'2}S_w(n)} \tag{4.8-b}$$

$$\chi_M^2(n)=\frac{U^2S_M(n)}{4M_0^2S_u(n)+M^{'2}S_w(n)} \tag{4.8-c}$$

where $L_0=\frac{1}{2}\rho U^2BC_L$; $L^{'}=\frac{1}{2}\rho U^2BC_L^{'}$; $D_0=\frac{1}{2}\rho U^2BC_D$; $D^{'}=\frac{1}{2}\rho U^2BC_D^{'}$; $M_0=\frac{1}{2}\rho U^2B^2C_M$; $M^{'}=\frac{1}{2}\rho U^2B^2C_M^{'}$

In many cases of the symmetrical sections and the rectangular sections, some force coefficients at the balanced attacked angle are equal zeros as $C_L\approx 0;\ C_M\approx 0;\ C_D^{'}\approx 0$. Therefore, more simplified quasi-steady aerodynamic admittance can be obtained as follows:

$$\chi_L^2(n)=\frac{U^2S_L(n)}{L^{'2}S_w(n)};\chi_D^2(n)=\frac{U^2S_D(n)}{4D_0^2S_u(n)};\chi_M^2(n)=\frac{U^2S_M(n)}{M^{'2}S_w(n)} \tag{4.9}$$

4.3.2 *Empirical models*

The Sears function is usually used for the aerodynamic admittance of lift force on the airplane wings and thin plate section expressed by the Bessel functions of first kind (Fung 1955):

$$\phi(k) = C(k)[J_0(k) - iJ_1(k)] + iJ_1(k) \tag{4.10}$$

where $J_0(k)$: Bessel function of first kind and 0 order; $J_1(k)$: Bessel function of first kind and 1 order; k: reduced frequency; C(k): Theodorsen's complex circulation function:

$$C(k) = \frac{H_1^{(2)}(k)}{H_1^{(2)}(k) + iH_0^{(2)}(k)} \tag{4.11}$$

where $H_1^{(2)}(k)$: Hankel function of second rank and 1 order; $H_0^{(2)}(k)$: Hankel function of second rank and 0 order.

Konishi, Shiraishi and Matsumoto (1975) modified the Sears function which is valid only for the thin plate, airfoil to be the so-called equivalent Sear function which can be applied as the aerodynamic admittance function of lift force on various girder types.

$$\phi_{eq}(k) = \phi(k)\frac{C_L'}{2\pi} \tag{4.12}$$

where C_L' : first-order derivative of lift force coefficients ($C_L' = dC_L(\alpha)/d\alpha$)

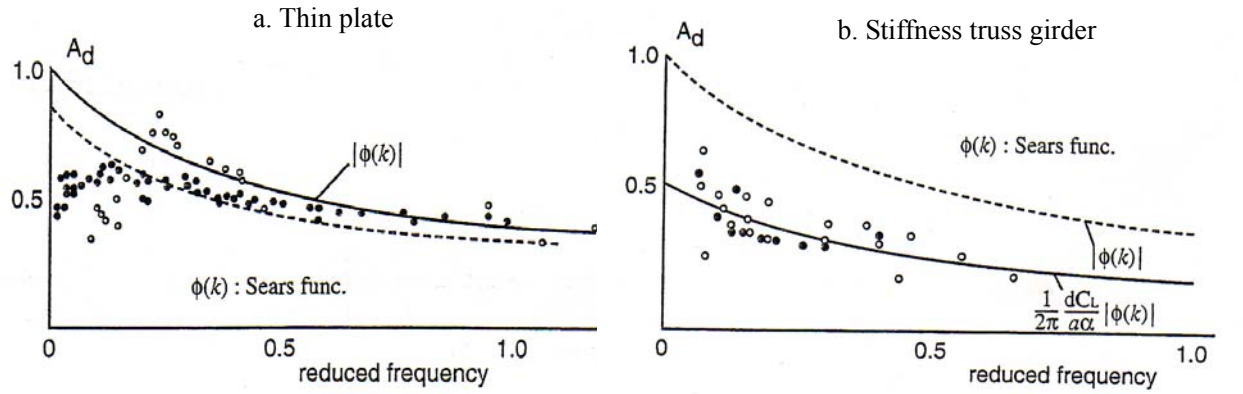

Fig 4.2 Comparison between aerodynamic admittance and Sears function [Matsumoto 2000]

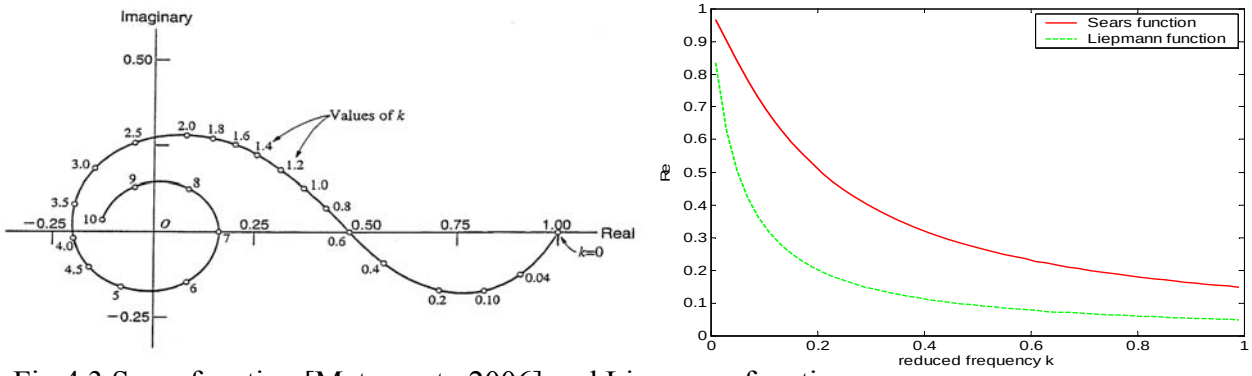

Fig 4.3 Sears function [Matsumoto 2006] and Liepmann function

Liepmann (1953) proposed new formula of the aerodynamic admittance as approximation of the Sears function, as well as Davenport (1962) introduced the aerodynamic admittance of the drag force:

$$\left|\chi_F(K)\right|^2 = \frac{1}{1+2\pi^2 K} \tag{4.13-a}$$

$$|\chi(n)|^2 = \frac{2}{\left(ck^*\right)^2}\left[ck^* - 1 + \exp(-ck^*)\right] \tag{4.13-b}$$

where c: decay factor (c=8); k^* : reduced frequency ($k^* = nD/U$)

Comparison between the Sears function and the Liepmann one is given in Figure 4.3.

4.4 Nonlinear and multivariate aerodynamic admittance

4.4.2 *Nonlinear aerodynamic admittance*

Because the instantaneous velocity can be written in the nonlinear expansion Eq.(4.3-a) on account with squared velocity components $u(t)^2$, $w(t)^2$ as $V^2(t) = U^2 + u^2 + w^2 + 2Uu$. Then transforming in the frequency domain, omitting cross spectra between u and v, u and w, w and v, we have power spectral density of lift force as:

$$S_L(n) = (\frac{1}{2}\rho U^2 B)^2 \chi_L^2(n)[4C_L^2 \frac{S_u(n)}{U^2} + C_L'^2 \frac{S_w(n)}{U^2} + C_L^2 \frac{S_{u^2}(n)}{U^4} + (2C_L'^2 + C_L^2)\frac{S_u(n)}{U^4}] \tag{4.14}$$

Therefore, the nonlinear aerodynamic admittance functions of the buffeting forces can be estimated as follows:

$$\chi_L^2(n) = \frac{U^4 S_L(n)}{4L_0^2 U^2 S_u(n) + L'^2 U^2 S_w(n) + L_0^2 S_{u^2}(n) + (L_0^2 + 2L'^2)S_u(n)} \tag{4.15-a}$$

$$\chi_D^2(n) = \frac{U^4 S_D(n)}{4D_0^2 U^2 S_u(n) + D'^2 U^2 S_w(n) + D_0^2 S_{u^2}(n) + (D_0^2 + 2D'^2)S_u(n)} \tag{4.15-b}$$

$$\chi_M^2(n) = \frac{U^4 S_M(n)}{4M_0^2 U^2 S_u(n) + M'^2 U^2 S_w(n) + M_0^2 S_{u^2}(n) + (M_0^2 + 2M'^2)S_u(n)} \tag{4.15-c}$$

Thus, squared turbulent components are taken into account in the nonlinear admittance.

4.4.3 *Multivariate aerodynamic admittance*

As above-mentioned, linear or nonlinear models of aerodynamic admittance contain spectral components of u, w and u^2, w^2 , however, one assumes that such turbulence components play the

equal role on contribution to the buffeting forces. Thus, single-variate aerodynamic admittance has been applied for both linear and nonlinear models. Relationship between spectral components of turbulence, their squares and spectral components of forces can be treated as the multi-input and single-output system (MISO) as following scheme:

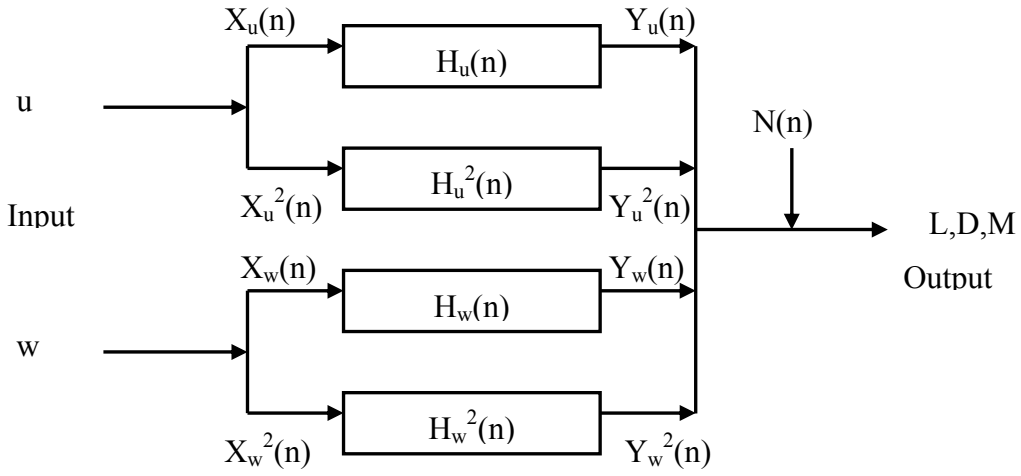

Fig. 4.4 Scheme of multivariate aerodynamic admittance

In Figure 4.2, X(n) and Y(n): power spectra of input and output; H(n): transfer functions (also frequency response function); N(n): system noise. Relationship between the input turbulence and the output buffeting forces can be expressed as following sums (here lift is taken for instance):

$$S_L(n) = S_{Yu}(n) + S_{Yu^2}(n) + S_{Yw}(n) + S_{Yw^2}(n) + S_N(n) \qquad (4.16\text{-a})$$

$$S_L(n) = |H_{Lu}(n)|^2 S_u(n) + |H_{Lu^2}(n)|^2 S_{u^2}(n) + |H_{Lw}(n)|^2 S_w(n) + |H_{Lw^2}(n)| S_{w^2}(n) + S_N(n) \quad (5.16\text{-b})$$

where $|H_{Lu}(n)|^2, |H_{Lu^2}(n)|^2, |H_{Lw}(n)|^2, |H_{Lw^2}(n)|$: transfer functions between input turbulent-related components u(t), $u^2(t)$, w(t), $w^2(t)$ and output lift L(t); $S_N(n)$: noise signal spectrum.

System identification of the transfer functions can be obtained as follows:

$$|H_{Lu}(n)|^2 = \left|\frac{S_L(n)}{S_u(n)}\right|^2 ; |H_{Lu^2}(n)|^2 = \left|\frac{S_L(n)}{S_{u^2}(n)}\right|^2 ; |H_{Lw}(n)|^2 = \left|\frac{S_L(n)}{S_w(n)}\right|^2 ; |H_{Lw^2}(n)|^2 = \left|\frac{S_L(n)}{S_{w^2}(n)}\right|^2 \quad (4.17)$$

Thus, comprehensive form of the nonlinear approach with multivariate admittance functions is

$$S_L(n) = 4L^2{}_0 \chi^2_{Lu}(n) \frac{S_u(n)}{U^2} + L'^2 \chi^2_{Lw}(n) \frac{S_w(n)}{U^2} + L^2{}_0 \chi^2_{Lu^2}(n) \frac{S_{u^2}(n)}{U^4} + (2L'^2 + L_0^2) \chi^2_{Lw^2}(n) \frac{S_{w^2}(n)}{U^4} \quad (4.18)$$

As a result, the multivariate admittance functions of lift force can be obtained as follows:

$$\chi_{Lu}^2(n)=\frac{U^2\,|H_{Lu}(n)|^2}{4L_0^2};\ \chi_{Lw}^2(n)=\frac{U^2\,|H_{Lw}(n)|^2}{L'^2} \tag{4.19-a}$$

$$\chi_{Lu^2}^2(n)=\frac{U^4\,|H_{Lu^2}(n)|^2}{L_0^2};\quad \chi_{Lw^2}^2(n)=\frac{U^4\,|H_{Lw^2}(n)|^2}{(2L'^2+L_0^2)} \tag{4.19-b}$$

Similarly, the multivariate admittance functions of drag force and moment can be determined in the same manner.

$$\chi_{Du}^2(n)=\frac{U^2\,|H_{Du}(n)|^2}{4D_0^2};\ \chi_{Dw}^2(n)=\frac{U^2\,|H_{Dw}(n)|^2}{D'^2} \tag{4.20-a}$$

$$\chi_{Du^2}^2(n)=\frac{U^4\,|H_{Du^2}(n)|^2}{D_0^2};\quad \chi_{Dw^2}^2(n)=\frac{U^4\,|H_{Dw^2}(n)|^2}{(2D'^2+D_0^2)} \tag{4.20-b}$$

$$\chi_{Mu}^2(n)=\frac{U^2\,|H_{Mu}(n)|^2}{4M_0^2};\ \chi_{Mw}^2(n)=\frac{U^2\,|H_{Mw}(n)|^2}{M'^2} \tag{4.20-c}$$

$$\chi_{Mu^2}^2(n)=\frac{U^4\,|H_{Mu^2}(n)|^2}{M_0^2};\ \chi_{Mw^2}^2(n)=\frac{U^4\,|H_{Mw^2}(n)|^2}{(2M'^2+M_0^2)} \tag{4.20-d}$$

Therefore, all multivariate aerodynamic admittance functions are obtained.

4.5 Relationship between aerodynamic admittance and derivatives

Due to time-domain formulation of the buffeting forces and aeroelastic flutter ones using the classical indicial response functions or impulse response ones, the relationships between the aerodynamic admittance and the aerodynamic derivatives, indicial response functions, impulse response functions have been already established (Scanlan 2001, Hatanaka and Tanaka 2002, Tubino 2005).

Accordingly, six different aerodynamic admittances can be formally derived from the some aerodynamic derivatives as follows (Scanlan 2001):

$$2C_L\chi_{Lu}(n)=K[H_5^*-iH_6^*];(C_L'+C_D)\chi_{Lw}(n)=-K[H_1^*-iH_4^*] \tag{4.21-a}$$

$$2C_D\chi_{Du}(n)=K[P_1^*-iP_4^*];(C_D'-C_L)\chi_{Dw}(n)=K[P_5^*-iP_6^*] \tag{4.21-b}$$

$$4C_M\chi_{Mu}(n)=K[A_5^*-iA_6^*];2C_M'\chi_{Mw}(n)=K[A_1^*-iA_4^*] \tag{4.21-c}$$

In the above-mentioned equations, in many cases of practical analyses and experiments the aerodynamic derivatives corresponding to lateral direction with subscripts 5 and 6 are negligible, thus remaining important aerodynamic admittances $\chi_{Lw}(n),\chi_{Mw}(n)$ can be obtained by this approach from the aerodynamic derivatives.

4.6 Experimental apparatus

Physical measurements of the turbulence and the turbulent-induced forces are carried out in the Kyoto University's open-circuit wind tunnel. Two models of rectangular sections with slender ratios B/D=5 and B/D=20 are used in experiments. Models are rigidly fixed by support. Turbulent flows are artificially generated by the grid configuration in the wind tunnel at different mean wind velocities U=3m/s, 6m/s and 9m/s, corresponding to the flow case 1, case 2 and case 3. Intensities of turbulence are I_u=11.46%, I_w=11.23% (case 1); I_u=10.54%, I_w=9.28% (case 2) and I_u=9.52%, I_w=6.65% (case 3). Two turbulent components: longitudinal u(y) and vertical w(t) are measured by the X-probe hot-wire thermal constant anemometer (CTA): X-probe (Model 1011, Kanomax Inc., Japan), CTA and linearization (Model DC Voltmeter 1008, Nihon Kagaku Kogyo, Japan). Three force components: drag, lift and moment are measured thanks to the dynamic multi-component loadcells (Model LMC 3505-30N, Nissho Electric Works, Co., Japan). Electric signals of measured forces are amplified by the 8-channel conditioner (Model DCM 8A, Kyowa Corp., Japan), then are filtered by 100Hz low-pass filters (E3201, NF Design Block Co., Ltd.). Signals of the turbulence and the forces are digitally sampled by A/D converter at the sampling rate 1000Hz over 100 seconds (Thinknet DF3422, Pavec Co., Ltd., USA). Experimental set-ups are shown in Figure 4.5.

Model B/D=5 Model B/D=20

Fig. 4.5 Experimental set-ups and models

Static aerodynamic coefficients and their first-order derivatives also are determined thanks to the force measurements using the loadcells with respect to change of various attacked angles of -10^o, -6^o, -2^o, 0^o, 2^o, 4^o, 6^o, 8^o, 10^o at two referred mean velocities U=8m/s, 12m/s. The static aerodynamic coefficients with respect to different attacked angles of two experimental models

B/D=5 and B/D=20 are shown in Figure 4.6 and Figure 4.7. Aerodynamic coefficients and the first-order derivatives at the balanced angle ($\alpha = 0^o$) are determined and given in Table 4.1.

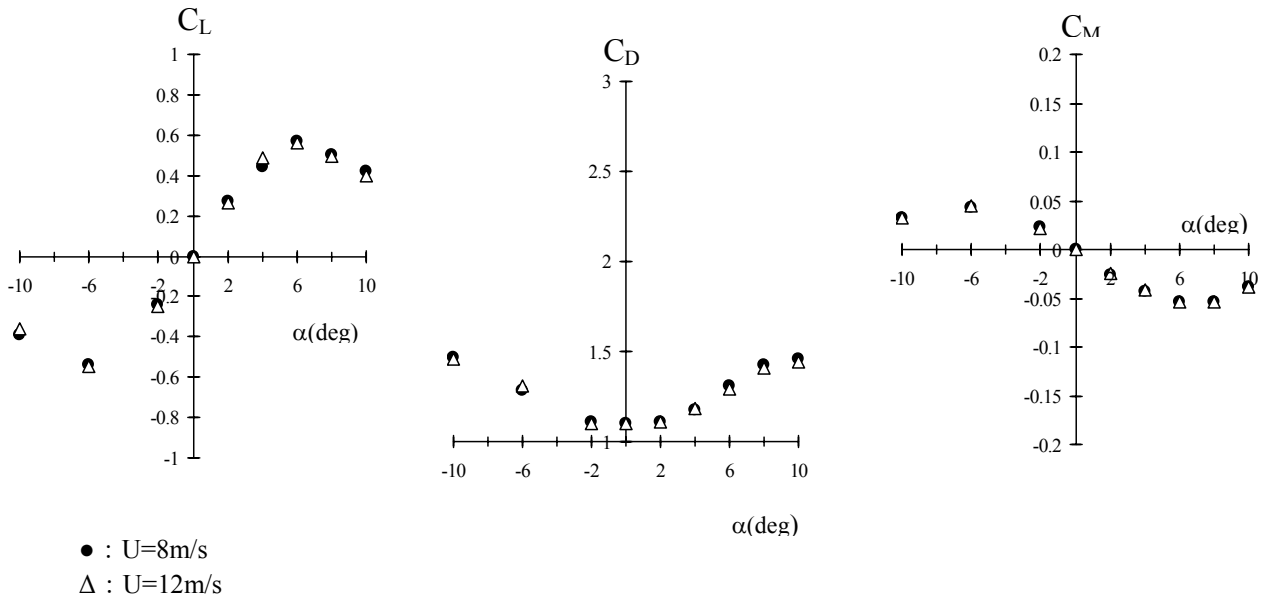

Fig. 4.6 Aerodynamic force coefficients on models B/D=5 [Matsumoto et al. 2006]

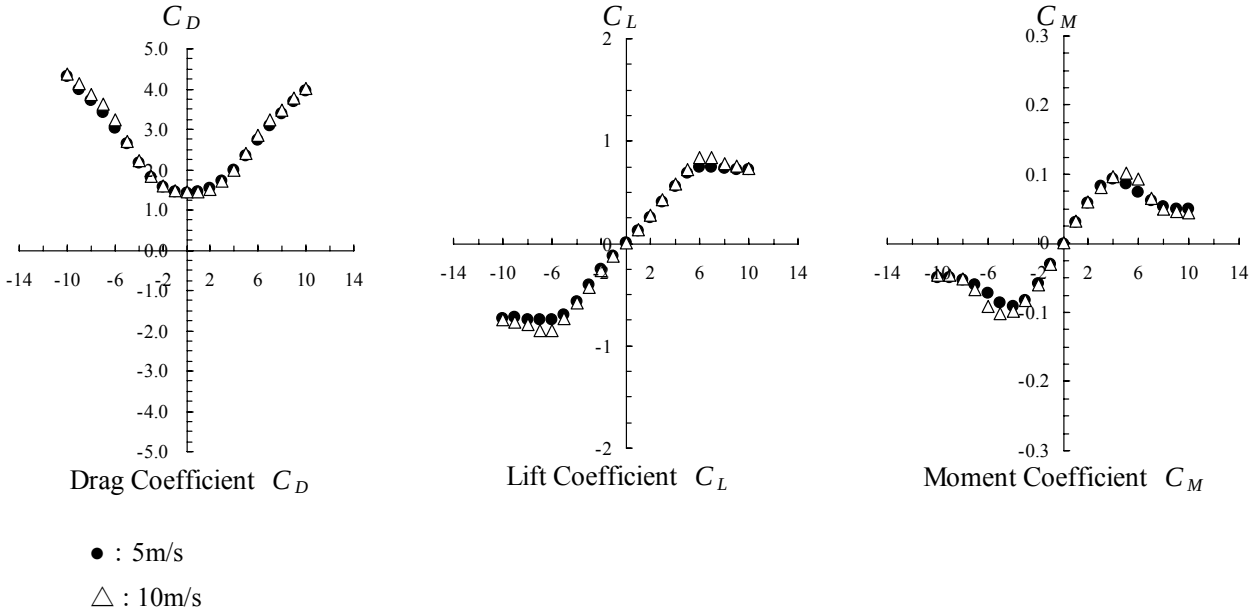

Fig. 4.7 Aerodynamic force coefficients on models B/D=20 [Matsumoto et al. 2006]

Table 4.1 Static aerodynamic coefficients and their first-order derivatives

B/D=5					
C_L	C_D	C_M	C_L'	C_D'	C_M'
0	1.098	0	6.412	0	0.609
B/D=20					
C_L	C_D	C_M	C_L'	C_D'	C_M'
0	1.423	0	7.067	0	0.701

The static aerodynamic coefficients and its derivatives are used in further computation here, with notice that some force coefficients $C_L, C_M, C_L^{'}$ are zero.

4.7 Results and discussion

Figure 4.8 shows the power spectral densities of turbulence and buffeting forces (lift and moment) on two physical models B/D=5 and B/D=20 at three turbulent flows corresponding to mean velocities U=3m/s, 6m/s and 9m/s. As can be seen that the spectra of lift force on model B/D=20 are generated higher than those on model B/D=5 at all flow conditions, however, the spectra of moment on the B/D=5 are larger than those on B/D=20.

Figure 4.9 expresses the quasi-steady aerodynamic admittances of lift and moment under three turbulent flows in comparison between models B/D=5 and B/D=20. It is also seen that the admittance function of lift force on the model B/D=20 exhibit higher than that on the model B/D=20, but the admittance of moment on B/D=20 is smaller than that on B/D=5, these correspond to the spectra of forces as observed in Figure 4.8. Moreover, some spectral peaks are observed on the aerodynamic admittance to correspond to those on the spectra of forces.

Effect of intensities of turbulence corresponding to three mean velocities on the aerodynamic admittance of the lift and moment on two models is expressed on Figure 4.10. It seems that the admittances reduce with decrease of the intensity of turbulence (increase of mean velocity) at low frequency range (0÷0.3Hz), however, the admittances increase with respect to increase of intensity of turbulence (decrease of mean velocity) at high frequency range (higher than 0.3Hz). This finding is also observed at the admittances of both the lift and the moment and on both the models.

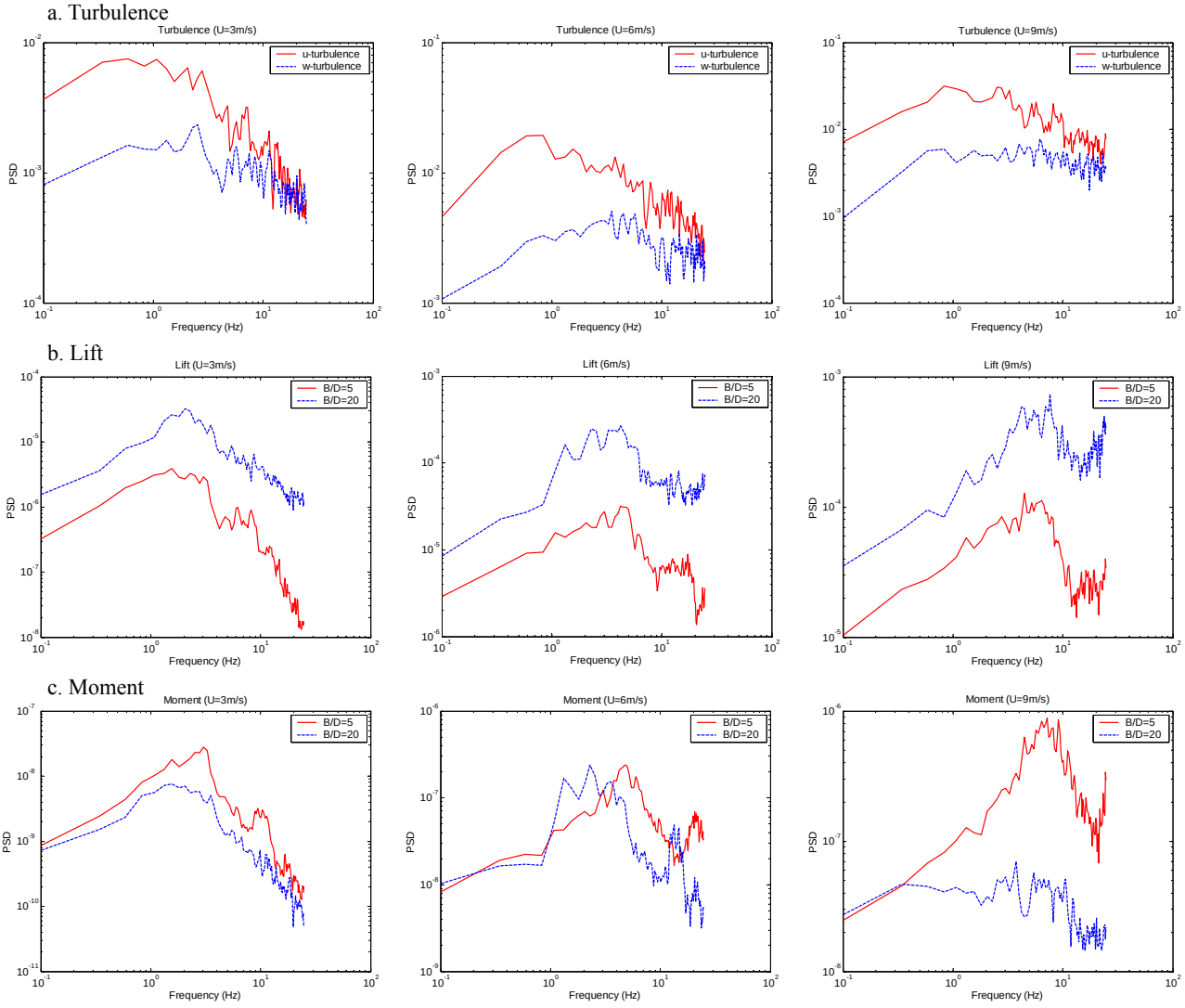

Fig. 4.8 Power spectral densities of turbulence and forces: a. turbulence, b. lift, c. moment

Comparison between quasi-steady aerodynamic admittances and nonlinear aerodynamic admittances of lift and moment on two models is shown in Figure 4.11. Squared turbulent components $u^2(t)$ and $w^2(t)$ are taken into account for the aerodynamic admittance to extend the nonlinear approximation in the quasi-steady theory. As can be seen from Figure 4.11, the nonlinear admittances express smaller than the quasi-steady ones in all investigated cases. Therefore, the nonlinear velocity components influence on the aerodynamic admittance in such the way to reduce the aerodynamic admittances, accordingly to reduce the buffeting forces as well.

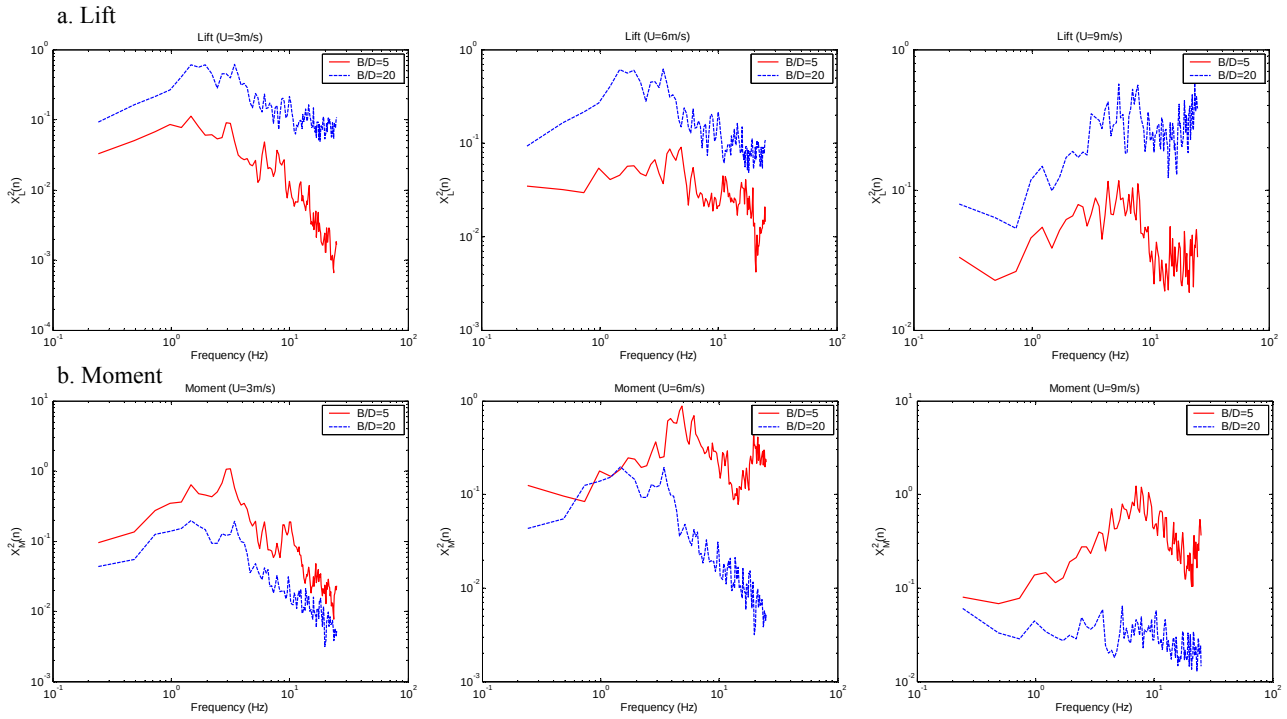

Fig. 4.9 Quasi-steady aerodynamic admittance: a. lift, b. moment

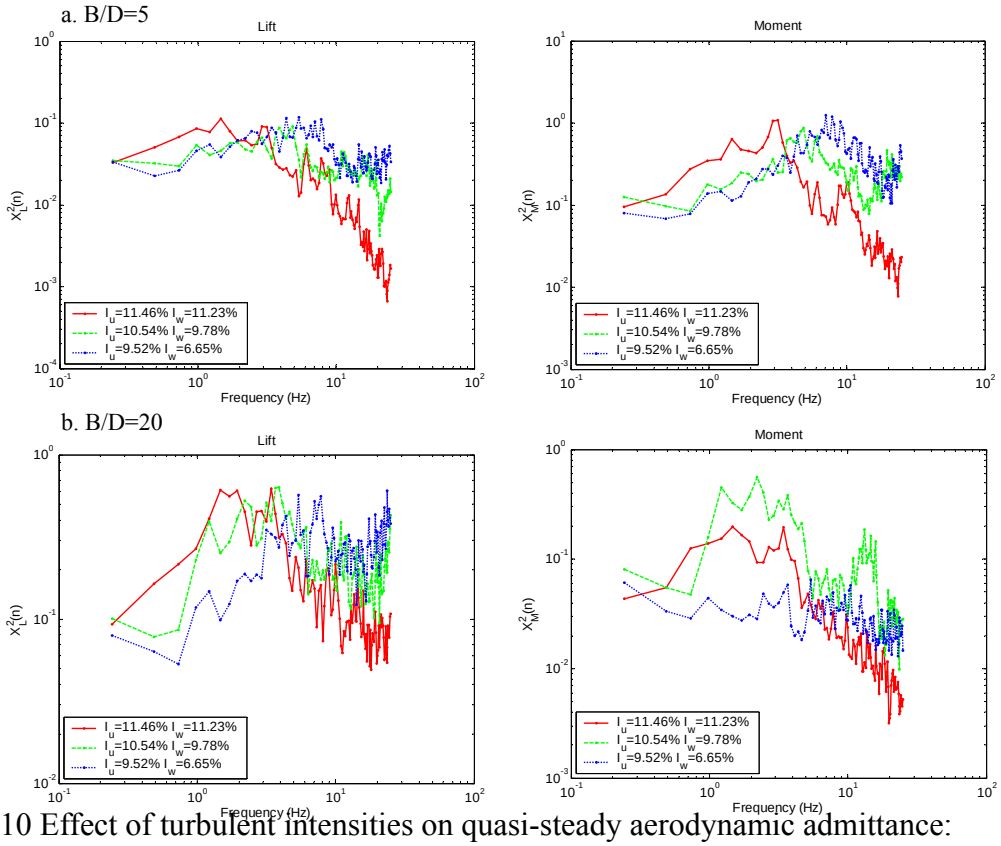

Fig. 4.10 Effect of turbulent intensities on quasi-steady aerodynamic admittance:
a. model B/D=5, b. model B/D=20

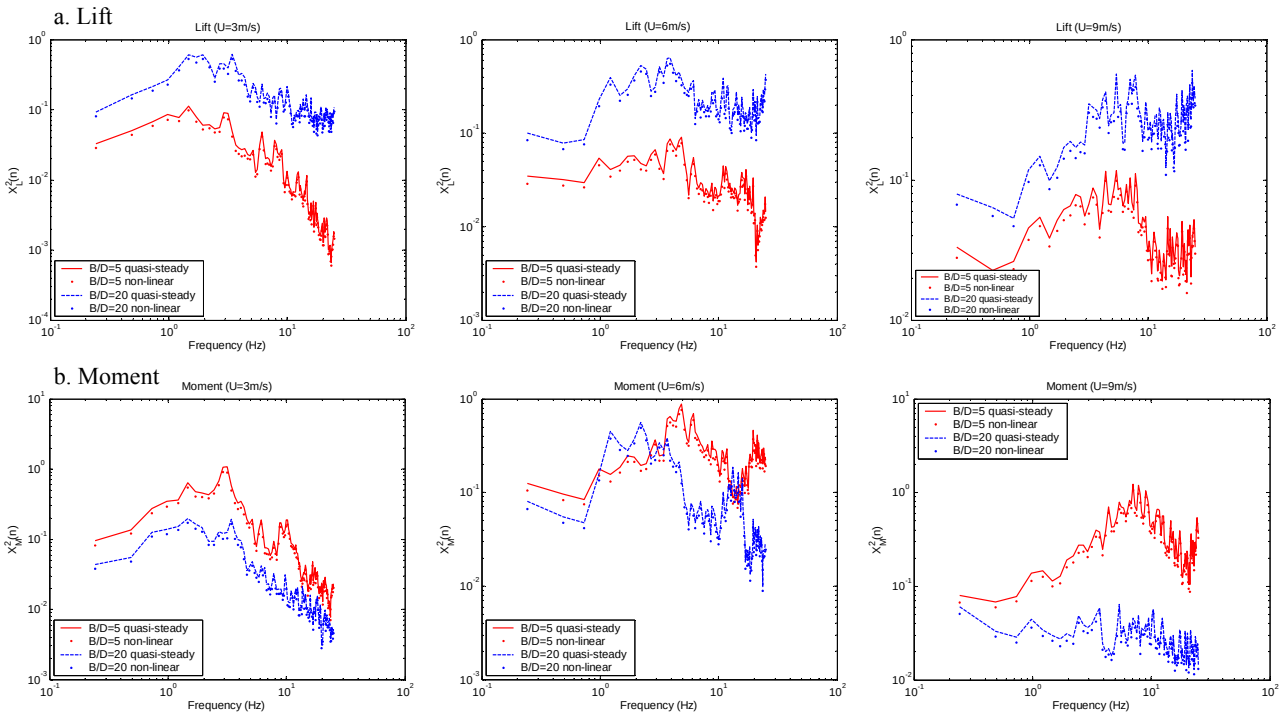

Fig. 4.11 Comparison between quasi-steady aerodynamic admittance and nonlinear aerodynamic admittance: a. lift, b. moment

Contributions from multi inputs (turbulent components u(t), w(t) and their squared components $u^2(t)$, $w^2(t)$, including cross correlation between them u(t)w(t) can be simultaneously taken into account as inputs) on the output forces can be determined using the multivariate variable model and the system identification technique. Figure 4.12 expresses the multivariate admittances corresponding to spectral contributions of spectra of w-turbulence and its squared component on spectra of forces, as well as comparison between the quasi-steady aerodynamic admittance and multivariate ones, in which $\chi_L^2(n)$, $\chi_{Lw}^2(n)$, $\chi_{Lw^2}^2(n)$ denote to the quasi-steady aerodynamic admittance, multivariate admittance due to the w-turbulence and squared w-turbulence, respectively. It is seen that the multivariate admittances due to w-turbulence is similar to that of quasi-steady admittances.

Figure 4.13 shows the multivariate transfer functions between lift and u-turbulence, lift and w-turbulence, moment and u-turbulence, moment and w-turbulence. The transfer function can characterize for contribution of each input turbulent components (u(t), w(t), $u^2(t)$, $w^2(t)$) on the output forces. As can be seen, there is different on contributions of each input components on the buffeting forces, this contradicts to the assumption of the quasi-steady aerodynamic admittances.

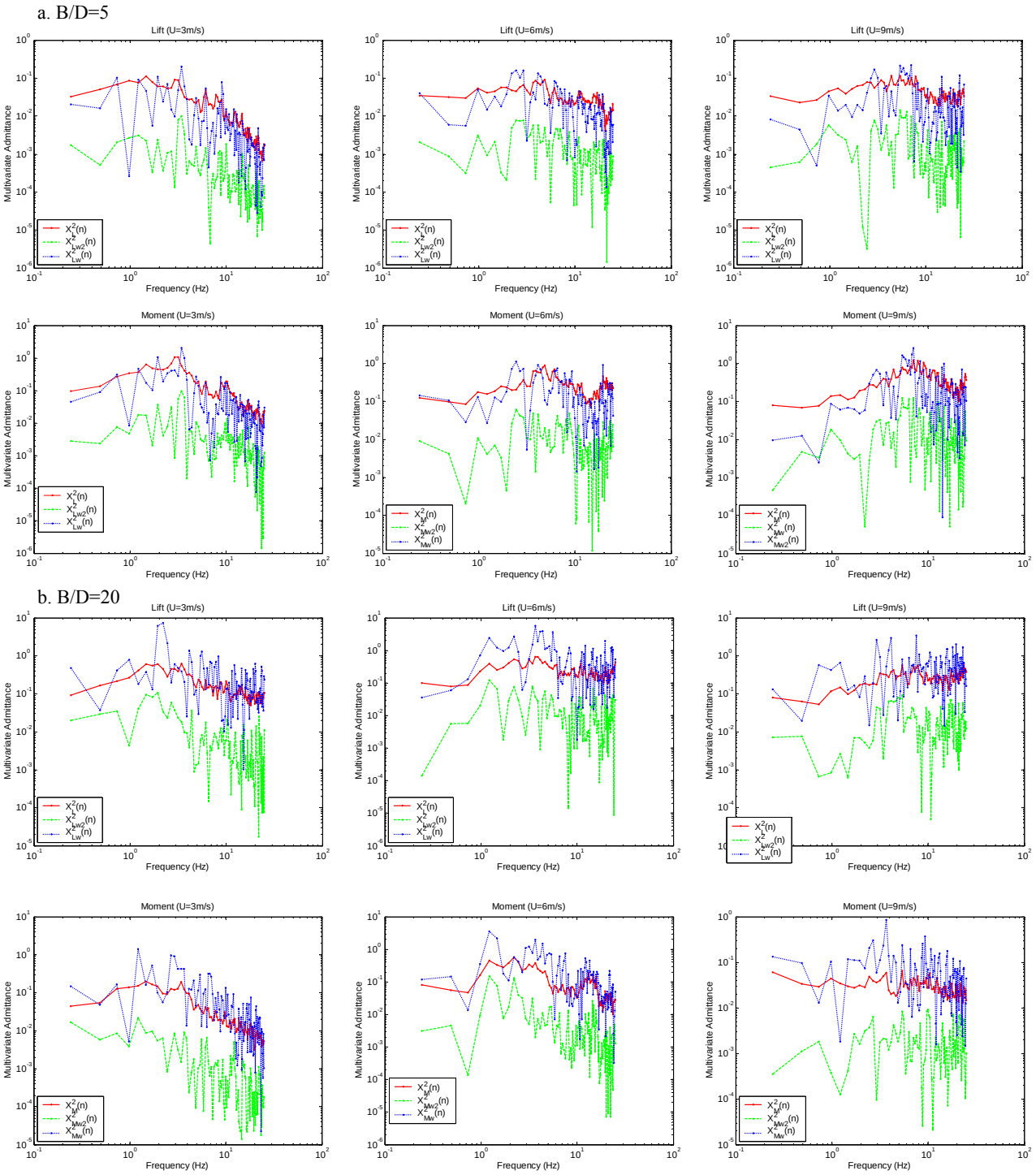

Fig. 4.12 Comparison between quasi-steady aerodynamic admittance and multi-variate aerodynamic admittance: a. model B/D=5, b. model B/D=20

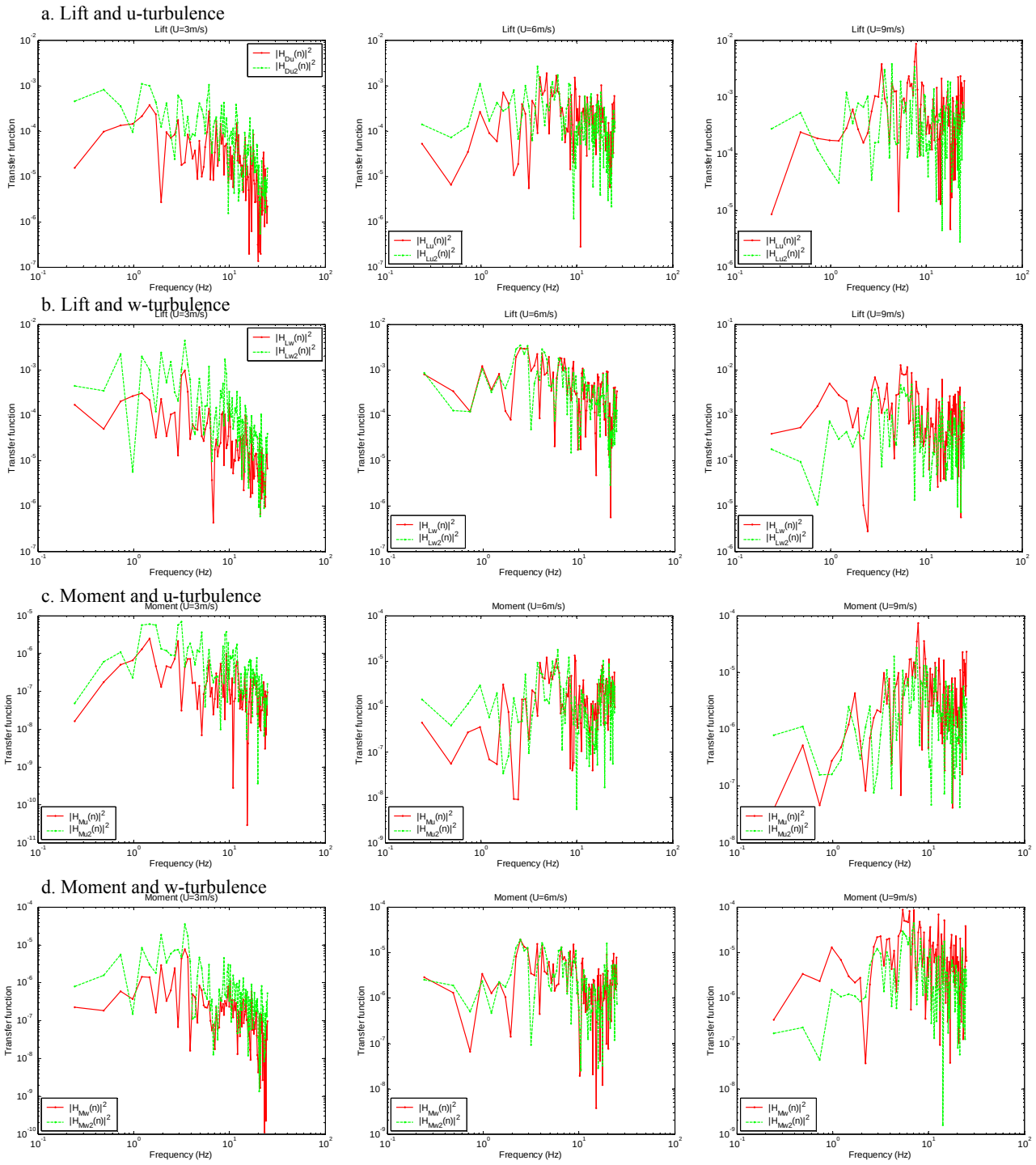

Fig 4.13 Transfer functions between input turbulent components and output buffeting forces on model B/D=5: a. lift and u-turbulence, b. lift and w-turbulence, c. moment and u-turbulence, d. moment and w-turbulence

4.8 Conclusion

Quasi-steady aerodynamic admittance and new concept of nonlinear and multivariate aerodynamic admittances have been discussed and investigated in this chapter. It can be concluded with some following points:

(1) It is found that the squared turbulent components influence on the aerodynamic admittance. How much and how importance of their contributions on the output buffeting forces need to be further studied with series of physical measurements on different physical models in different unsteady flows. It is supposed that effect of the squared velocity components on the admittance is not considerable in such cases that behaviors of ongoing flow and bluff body flow are not complicated. However, effect of these squared components is supposed to increase with complexity of bluff body flow and ongoing flow. In these investigations, influence of u-turbulence and its squared component on multivariate admittance can not evaluated due to their relating force coefficients $C_L = 0, C_M = 0, C_D^{'} = 0$ are zero.

(2) New comprehensive approach to determine the aerodynamic admittance has been studied, in which contributions from multi inputs (turbulent components u(t), w(t) and their squared components $u^2(t)$, $w^2(t)$, including cross correlation between them u(t)w(t) can be simultaneously taken into account as inputs) on the output forces can be determined using the multivariate variable model and the system identification technique

Further studies on the aerodynamic admittances should be needed to clarify influence of bluff body flows on the aerodynamic admittances as well as to verify application of multivariate aerodynamic admittance.

References

Caracoglia, L., Jones, N.P. (2003), "Time domain vs. frequency domain characterization of aeroelastic forces for bridge deck sections", *J. Wind Eng. Ind. Aerodyn.*, **91**, 371-402.

Cigada, A., Diana, G., Zappa, E. (2002), "On the response of a bridge deck to turbulent wind: a new approach", *J. Wind Eng. Ind. Aerodyn.*, **90**, 1173-1182.

Chen, X.Z., Kareem, A. (2002), "Advances in modeling of aerodynamic forces on bridge decks", *J. Engrg. Mech.*, **128(11)**, 1193-1203.

Davenport, A.G. (1962), Buffeting of a suspension bridge by storm winds, Proc. ASCE, **88**, ST3.

Diana, G., Bruni, S., Cigada, A., Zappa, E. (2002), "Complex aerodynamic admittance function role in buffeting response of a bridge deck", *J. Wind Eng. Ind. Aerodyn.*, **90**, 2057-2072.

Fung, Y.C. (1955), *Introduction to the theory of aeroelasticity*, John Wiley & Sons.

Hatanaka, A., Tanaka, H. (2002), "New estimation method of aerodynamic admittance function", *J. Wind Eng. Ind. Aerodyn.*, **90**, 2073-2086.

Kawai, H. (1983), "Pressure fluctuations on square prisms – applicability of strip and quasi-steady theories", *J. Wind Eng. Ind. Aerodyn.*, **13**, 197-208.

Larose, G.L. (1999), "Experimental determination of the aerodynamic admittance of a bridge deck segment", *J. Fluids Struct.*, 13, 1029-1040.

Matsuda, K., Hikami, Y., Fujiwara, T., Moriyama, A. (1999), "Aerodynamic admittance and the 'strip theory' for horizontal buffeting forces on a bridge deck", *J. Wind Eng. Ind. Aerodyn.*, **83**, 337-346.

Matsumoto, M. (2000), *Aeroelasticity and bridge aerodynamics*, Textbook for Int'l Course on Wind Engineering, Genoa Italy.

Matsumoto, M., Shirato, H., Yagi, T., Yamane, K. (2006), *Study on spatial characteristics of gust force on rectangular cylinder in turbulent flow,* Internal Report (in Japanese)

Matsumoto, M., Shirato, H., Yagi, T., Furukawa, T. (2007), *Study on spatial characteristics of gust forces on rectangular cylinder in gusty flow*, Internal Report (in Japanese)

Peil, U., Behrens, M. (2005), "Spectral aerodynamic admittance analysis", *Proc. 4th European & African Conference on Wind Engineering (EACWE4)*, Prague Czech, July 11-15.

Sakaran, R., Jancauskas, E.D. (1992), "Direct measurement of the aerodynamic admittance of two-dimensional rectangular cylinders in smooth and turbulent flows", *J. Wind Eng. Ind. Aerodyn.*, **41-44**, 601-611.

Scanlan, R.H. (2001), “Reexamination of sectional aerodynamic force function for bridges”, *J. Wind Eng. Ind. Aerodyn.*, **89**, 1257-1266.

Tubino, F. (2005), “Relationship among aerodynamic admittance, flutter derivatives and static coefficients for long-span bridges”, *J. Wind Eng. Ind. Aerodyn.*, **93**, 929-950.

Chapter 5

Spanwise Coherence of Wind Turbulence and Induced Pressure on Rectangular Cylinders

5.1 Introduction

The gust response prediction of structures or long-span bridges immersed in atmospheric turbulent flows subjected by turbulent-induced forces (or buffeting forces) has been based on a strip theory, by which the spatial distribution characteristic of forces on structure must be taken into account. For a sake of simplification, however, the spatial distribution of turbulent field can represent for that of the induced force one. Thus, it is assumed that the spanwise coherence of the induced forces is similar to that of the ongoing turbulence (or velocity fluctuating components) that was simplified as an exponential coherent formula in the gust response prediction (Davenport 1963). Recent literatures, however, found out that the coherence of the buffeting forces was larger than that of the ongoing turbulence (Larose 1996; Jakobsen 1997; Kimura et al. 1997; Matsumoto et al. 2003). This suggests that influence of structure on the ongoing turbulent flow must not be negligible, and interaction phenomena between ongoing flow and structure might have involved in modification of the ongoing turbulent flow around the structure (one is mentioned as a bluff body flow). Moreover, relationship between turbulence and induced pressure/ forces contains uncertainties due to limitation of the quasi-steady theory and the strip theory as discussed in somewhere (Kawai 1983). Uncertainty from the force coherence higher than the turbulent coherence can cause either underestimation or overestimation on the gust response prediction of structures. Mechanism of higher force coherence, coherent structures of turbulence and induced forces as well as effect of bluff body flow on the force coherence should be further clarified in order to reduce the analytical uncertainty. Coherent structure of the turbulent-induced forces has been studied ideally by the mean of surface pressure measurement by which the induced forces can be deducted by integration of the surface pressure field around structural section. Identification of bluff body flow around structural section (such as separation bubble, flow reattachment, vortex shedding), furthermore, can be roughly obtained thanks to previous

experience and chordwise distribution of mean and fluctuating pressures which has been verified by means of smoke visualization (Hiller and Cherry 1981; Cherry et al. 1984).

The Fourier transform has been most popularly and conventionally used to study in spectral-based computations, physical data analysis, coherent structures in the frequency domain so far. No time information, however, can be obtained from the Fourier transform-based tools such as Fourier coefficient, auto power spectrum, cross power spectrum, coherence and phase difference which have been applied to identify the dominant frequency components and the cross correlation between two given time series in the frequency domain. These tools, moreover, is accurately applicable only for purely stationary time series. Wavelet transform has been recently proposed to represent any time series in a time-scale (frequency) plane, known as a time-frequency analysis (Daubechies 1992). First-order wavelet coefficient has been used almost so far, however, some wavelet transform-based advanced tools corresponding to conventional Fourier transform-based ones such as wavelet power spectrum, wavelet coherence and wavelet phase difference can be developed to express and detect auto, cross correlations of any time series and between two time series in the time-frequency plane (Torrence and Compo 1998; Kareem and Kijewski 2002). The wavelet transform-based tools, furthermore, are advantageous over the Fourier transform as powerfully analyzing tool for non-stationary, non-linear and intermittent time series.

In this chapter, the temporal-spectral coherent structures of wind and pressure will be studied using both Fourier coherence and wavelet coherence. Effects of spanwise separations, bluff body flow and turbulent flow conditions on coherent structures of turbulence and pressure, comparison between wind and pressure coherence as well as intermittent distribution of wavelet spectrum and wavelet coherence will be discussed. Physical measurements of the surface pressure and turbulence have been carried out on some typical rectangular cylinders with side ratios B/D=1 (without and with splitter plate at wake region) and B/D=5 under the artificial turbulent flows in the wind tunnel.

5.2 Fourier transform-based coherence

The Fourier transform-based coherence is approximately expressed as the normalized correlation coefficient of two spectral quantities of *X(t)* and *Y(t)* in the frequency domain (Bendat and Piersol 2000):

$$COH_{XY}^{2}(f) = \frac{|S_{XY}(f)|}{\sqrt{S_X(f)S_Y(f)}} \tag{5.1}$$

where $|\ |$: absolute operator; f: Fourier frequency variable; $S_X(f), S_Y(f), S_{XY}(f)$: Fourier auto power spectra and Fourier cross power spectrum at/between two separated points, respectively defined as:

$$S_X(f) = E[\hat{X}(f)\hat{X}(f)^{*T}];\ S_Y(f) = E[\hat{Y}(f)\hat{Y}(f)^{*T}];\ S_{XY}(f) = E[\hat{X}(f)\hat{Y}(f)^{*T}] \qquad (5.2)$$

where E[]: expectation operator; *,T: complex conjugate and transpose operators; $\hat{X}(f), \hat{Y}(f)$: Fourier transform coefficients of time series $X(t), Y(t)$ respectively. The Fourier coherence is normalized between 0 and 1, thus two time series *X(t), Y(t)* are fully-correlated, coherence is unit, whereas coherence is zero, two time series are uncorrelated in the frequency domain.

5.3 Wavelet transform-based coherence

5.3.1 *Definition*

The wavelet transform (also called as continuous wavelet transform) of the given time series *X(t)* is defined as the convolution operator between *X(t)* and the wavelet function $\psi_{\tau,s}(t)$:

$$W_X^{\psi}(\tau, s) = \left\langle X, \psi_{\tau,s} \right\rangle = \int_{-\infty}^{\infty} X(t)\psi_{\tau,s}^*(t)dt \qquad (5.3)$$

where $W_X^{\psi}(s,\tau)$: the wavelet coefficients at translation τ and scale s in the time-scale plane; the brackets $\langle,\rangle$ denote the convolution operator; $\psi_{\tau,s}(t)$: wavelet function at translation τ and scale s of the basic wavelet function $\psi(t)$ (the mother wavelet):

$$\psi_{\tau,s}(t) = \frac{1}{\sqrt{s}}\psi\left(\frac{t-\tau}{s}\right) \qquad (5.4)$$

The wavelet coefficients $W_X^{\psi}(s,\tau)$ can be considered as a correlation coefficient and a measure of similitude between wavelet and given time series in the time-scale plane. The wavelet scale has its meaning as an inverse of the Fourier frequency, thus inter-relationship between the wavelet scale and the Fourier frequency can be obtained. One would like to develop wavelet transform-based tools such as the wavelet auto spectra and the wavelet cross spectrum at time shift index i and scale s of two signals *X(t)* and *Y(t)*, based on their wavelet coefficients $W_{Xi}(s)$, $W_{Yi}(s)$ can be defined as following formulae:

$$WPS_{XXi}(s) = \left\langle W_{Xi}(s)W_{Xi}^{*T}(s) \right\rangle;\ WPS_{YYi}(s) = \left\langle W_{Yi}(s)W_{YYi}^{*T}(s) \right\rangle;\ WPS_{XYi}(s) = \left\langle W_{Xi}(s)W_{Yi}^{*T}(s) \right\rangle \qquad (5.5)$$

where $WPS_{XXi}(s), WPS_{YYi}(s)$: wavelet auto spectra of *X(t),Y(t);* $WPS_{YYi}(s)$: wavelet cross spectrum between *X(t)* and *Y(t)*; $\langle\ \rangle$ denotes smoothing operator in both time and scale directions.

With respect to the Fourier coherence, the squared wavelet coherence of *X(t), Y(t)* is defined as the absolute value squared of the smoothed wavelet cross spectrum, normalized by the smoothed wavelet auto spectra (Torrence and Compo, 1998):

$$WCO_{XY\,i}{}^{2}(s) = \frac{|\left\langle s^{-1} WCS_{XY\,i}(s) \right\rangle|^{2}}{\left\langle s^{-1} |WPS_{XX\,i}(s)| \right\rangle \left\langle s^{-1} |WPS_{YY\,i}(s)| \right\rangle} \tag{5.6}$$

where $|\,|$ denotes the absolute operator; s^{-1} is used to convert to an energy density.

Note that the wavelet coherence $WCO_{XY\,i}{}^{2}(s) \in [0,1]$ has the same meaning as the Fourier coherence, which wavelet coherence comes to unit, two signals *X(t), Y(t)* are fully-correlated, whereas wavelet coherence reduces to zero, two signals *X(t), Y(t)* are uncorrelated, however, its advantage over the conventional Fourier coherence is to represent the spectral correlation in both the frequency- and the time-domains.

Interrelation between the central frequency, wavelet scale and the Fourier frequency can be determined approximately as follows:

$$f = \frac{f_0 f_s}{s} \tag{5.7}$$

where f_s: sampling frequency of given time series.

5.3.2 *Complex Morlet wavelet*

The complex Morlet wavelet is the most applicable for physical measurement analysis in the wavelet transform, thanks to its containing of harmonic components and its analogs to the Fourier transform (see Figure 6.1):

$$\psi(t) = (2\pi)^{-1/2} \exp(i2\pi f_0 t) \exp(-t^2/2) \tag{5.8-a}$$

$$\hat{\psi}(sf) = (2\pi)^{-1/2} \exp\left(2\pi^2 (sf - f_0)^2\right) \tag{5.8-b}$$

where f_0, s: central frequency and wavelet scale of the complex Morlet wavelet.

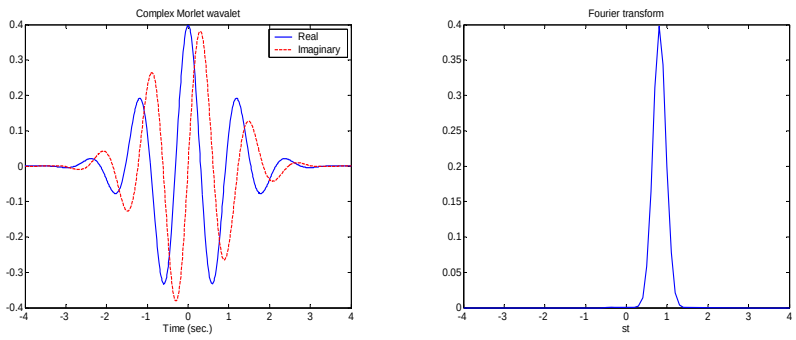

Fig. 5.1 Complex Morlet wavelet and its Fourier transform

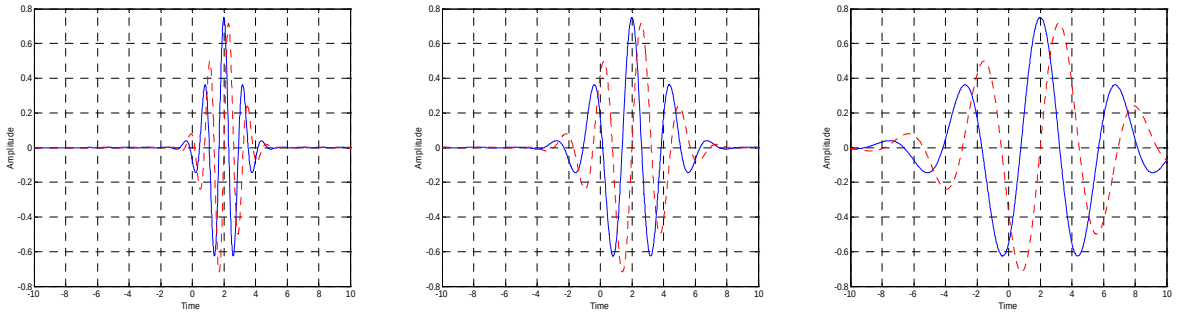

Fig. 5.2 Morlet wavelet at time shift τ=2 seconds and at scales s=1,2 and 4seconds (solid line : real part & dashed line: imaginary parts)

5.3.3 *Time and scale smoothing and end-effect elimination*

Averaging in both time and scale directions must be required in the wavelet transform, especially in computing the wavelet spectrum and wavelet coherence. The averaging techniques of the wavelet spectrum in time and scale at the time-shifted index p can be expressed as (Torrence and Compo 1998):

Time domain smoothing $$\left\langle WPS_i^2(s)\right\rangle = {1}/{N_a}\sum_{i=i_1}^{i_2}|\,WPS_i\,(s)\,|^2 \qquad (5.9\text{-a})$$

Scale domain smoothing $$\left\langle WPS_i^2(s)\right\rangle = {\delta j\,\delta t}/{C_\delta}\sum_{j=j_1}^{j_2}{|\,WPS_i\,(s_j)\,|^2}/{s_j} \qquad (5.9\text{-b})$$

where j assigned between j_1 and j_2; N_a: number of averaged points ($N_a = j_2 - j_1 + 1$); $\delta j, \delta t$: factor of window width and sampling period ; C_δ: constant.

Because the wavelet transform deals with finite-length of time series, errors and bias values usually occur at two ends of time series, known as the end effect. One simple solution to eliminate the end effect is to truncate number of discrete results at two ends of time series after the wavelet transform is completed. Removed number, however, depend on the wavelet scale, thus so-called cone of influence should be estimated for more accuracy.

5.4 Experimental apparatus

Analyzing data were obtained by physical measurements in the Kyoto University's open-circuit

wind tunnel. Physical models of rectangular cylinders with slender ratios B/D=1 and B/D=5 were used, in which model B/D=1 was installed without/with a splitter plate (S.P) in the wake of model on account of effect of wake flow. Motionless models were fixed on a working section. Turbulent flow was generated artificially by grid devices which was located in 750mm upstream from model's leading edge. Wind turbulence and surface pressures were measured in the three turbulent flows at mean wind velocities U=3, 6 and 9m/s corresponding to flow case 1, flow case 2 and flow case 3, respectively. Basic turbulent flow parameters were given as turbulent intensities I_u=11.56%, I_w=11.23% (case 1), I_u=10.54%, I_w=9.28% (case 2), I_u=9.52%, I_w=6.65% (case 3). Pressure taps were arranged on one surface of models, consisting of 10 pressure taps of model B/D=1 and 19 pressure taps of the model B/D=5 in the chordwise direction (see Figure 5.3). Mean and turbulent components (fluctuating velocity components) of the basic turbulent flow (without model) were measured thanks to a hot-wire anemometer using x-type probes (Model 0252, Kanomax Japan, Inc.) and calibrated and linearized by a constant-temperature anemometer (CTA) (Models 1013, 1011, Kanomax Japan, Inc.). Unsteady surface pressures were measured by multi-channel pressure measurement system (ZOC23, Ohte Giken, Inc.). It is noted that turbulent components and surface pressures were simultaneously obtained in order to investigate in the time domain. Electric signals were filtered by 100Hz low-pass filters (E3201, NF Design Block Co., Ltd.) before passed through A/D converter (Thinknet DF3422, Pavec Co., Ltd.) with sampling frequency at 1000Hz in 100 seconds.

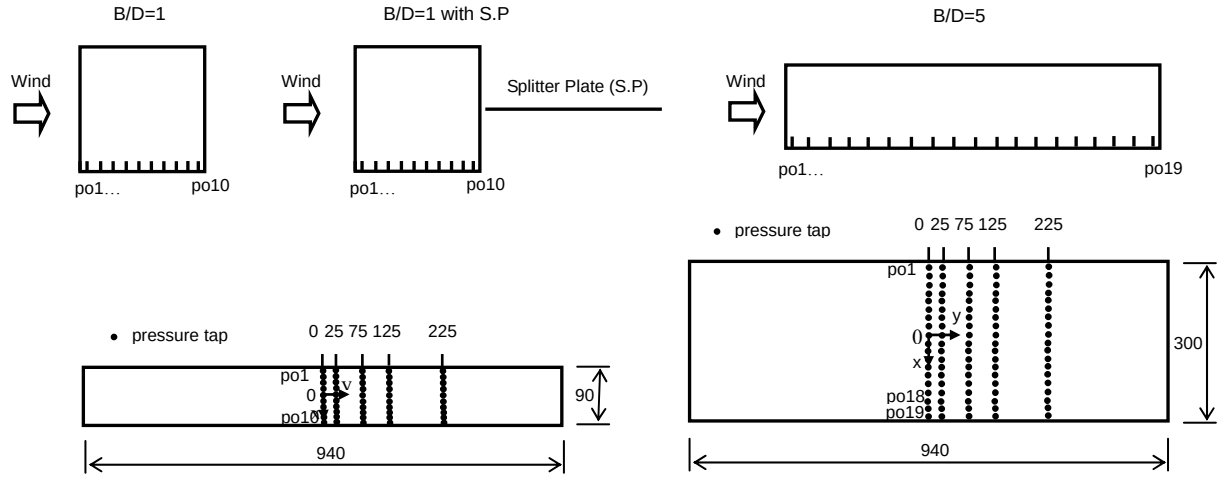

Fig. 5.3 Experimental models and pressure tape layout

Though large number of pressure taps have been arranged on model surfaces, concretely 10 rows and 21 columns on the model B/D=1, 19 rows and 41 columns on the model B/D=5, but only pressure taps arranged columns at spanwise distances y=0, 25, 75, 125 and 225mm were used in this study (Figure 5.3).

5.5 Chordwise pressure distribution and bluff body flow pattern

Flow around models due to interaction between ongoing flow and model section is usually known as the bluff body flow, which characterized by formation of separated and reattached flows with separation bubble and that of vortex shedding as well. It can be predicted from previous studies that model B/D=1 is favorable for dominant formation of Karman vortex shedding in the wake of model, whereas model B/D=5 is typical for formation of separated and reattached flows on model surface. In case the splitter plate was installed in the wake of model B/D=1 in order to suppress the wake flow and effect of Karman vortex shedding. Identification of the bluff body flow is usually required for understanding flow behavior and mechanism of oscillation on physical model. The bluff body flow can be identified directly due to flow visualization techniques. Pressure distribution is also used for this purpose with experience and knowledge of flow behavior on some typical models.

Normalized mean pressures and normalized root-mean-square fluctuating pressures in the chordwise positions can be determined from measured time series of unsteady pressures as follows:

$$C_{p,mean}^{(i)} = \overline{p}^{(i)} \Big/ \left(0.5\rho U^2\right) \tag{5.10-a}$$

$$C_{p,rms}^{(i)} = \sigma_p^{(i)} \Big/ \left(0.5\rho U^2\right) \tag{5.10-b}$$

where i: index of pressure time series at chordwise positions; $0.5\rho U^2$: dynamic pressure; $\overline{p}$: mean value of pressure time series; σ_p: standard deviation of pressure time series.

Figure 5.4 shows normalized mean and fluctuating pressure distributions on the chordwise positions. As can be seen that the normalized mean and fluctuating pressures distribute homogeneously on the models B/D=1 without/with the splitter plate, whereas distribute locally near leading edge on the model B/D=5. Normalized mean and fluctuating pressures on model B/D=1 without splitter plate exhibit higher than those on the same model but with splitter plate. Moreover, normalized mean pressure distributions on three models seem not to with respect to turbulent flow conditions.

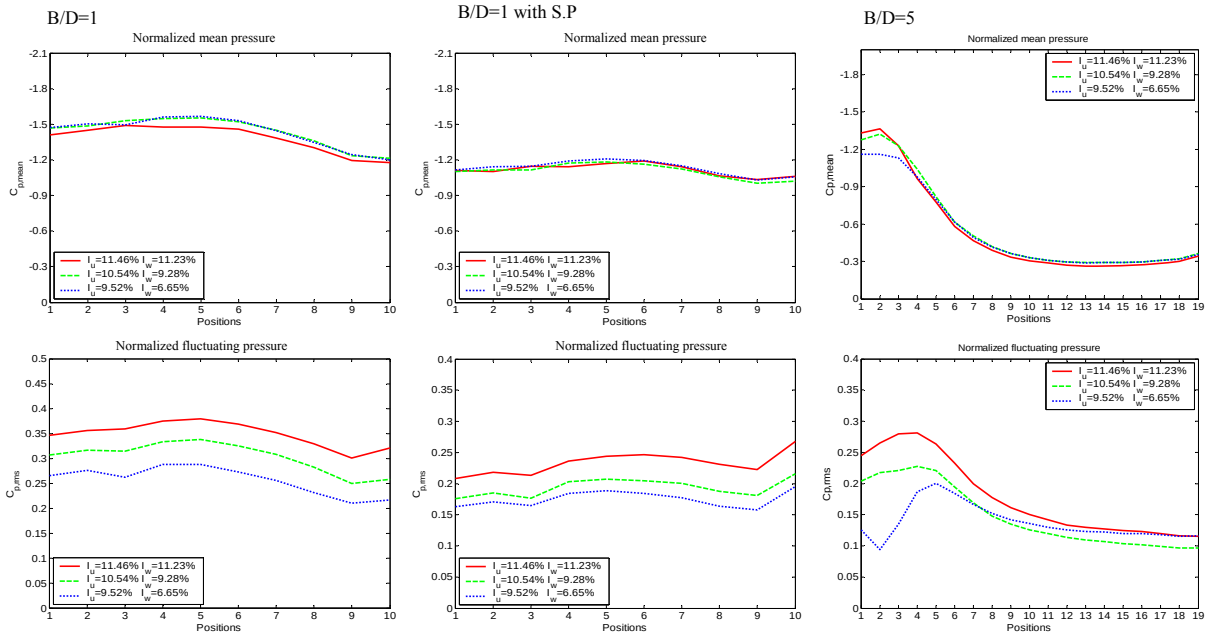

Fig. 5.4 Normalized mean and fluctuating pressure distributions on chordwise positions

Power spectral densities (PSD) of the fluctuating pressures at some represented positions on the three experimental models in the turbulent flow case 1 are expressed in Figure 5.5. As can be seen with the model B/D=1 (without splitter plate) that peaked frequencies are observed at 4.15Hz, 8.79Hz and 12.94Hz respective to the three turbulent flow conditions. It is agreed that the Karman vortex formed and shed in the wake in which the Karman vortex frequency depends on the Strouhal number (St) of model section and mean wind velocity. Moreover, the Strouhal number can be determined as St=0.1285. Thus, on the model B/D=1 without splitter plate the bluff body flow is separated at sharp corners, dominated by formation of Karman vortex and frequently shed in the wake. In case of the model B/D=1 with splitter plate, no frequency peaks are observed, this means that the Karman vortex is suppressed by the splitter plate. It is supposed the bluff body flow separated at the sharp corners, expanded all model surface and reattached at the splitter plate. In case of the model B/D=5, frequency peaks are observed at 1.22Hz and 2.44Hz (flow case 1); at 2.44Hz, 4.88Hz, 7.32Hz (flow case 2); at 3.42Hz and 6.84Hz (flow case 3). According to Hiller and Cherry 1981; Cherry et al. 1984, reattachment point of separated flow may locate at near after the peak position of fluctuating pressure, and the observed frequency peaks are induced by rolled-up turbulent vortices shed away at reattachment points toward trailing edge. Thus, bluff body flow is separated and reattached on the model surface to form

separation bubble. Reattachment points can be determined at roughly positions 6, 7, 8 with respect to an increase of mean velocities. High mean and fluctuating pressures are observed locally at the leading edge region in the influence of separation bubble due to local circulation of turbulent vortex inside it.

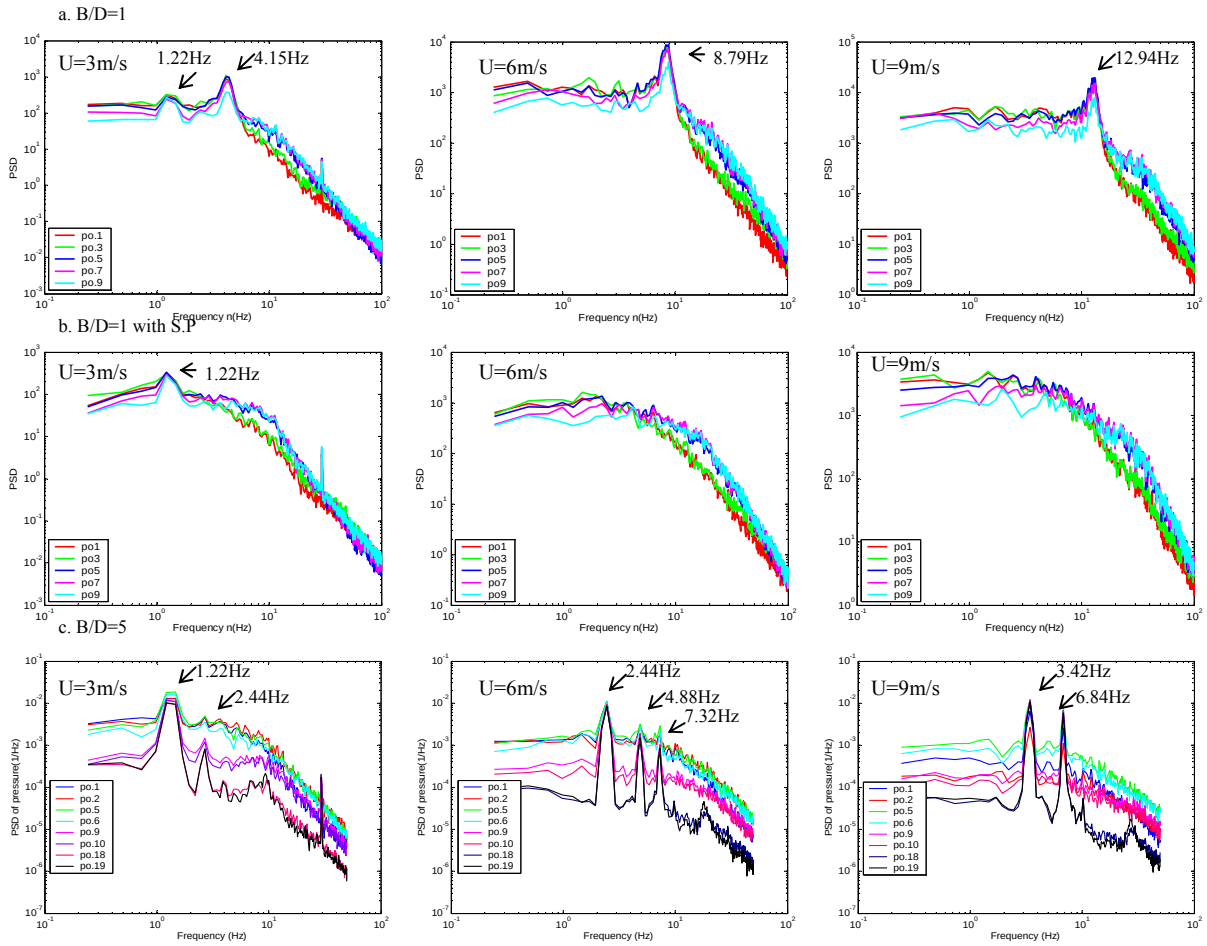

Fig. 5.5 Auto power spectra of normalized fluctuating pressures at three turbulent flows: a. B/D=1, b. B/D=1 with splitter plate, c. B/D=5 [Matsumoto, Shirato et al. 2006]

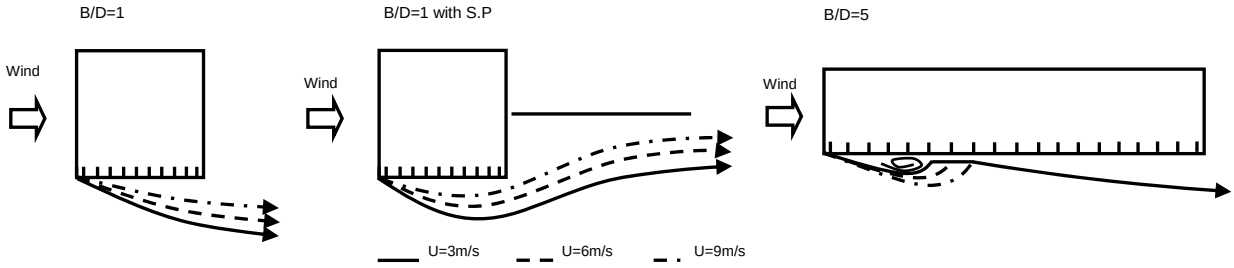

Fig. 5.6 Bluff body flow patterns around experimental models [Matsumoto,Shirato et al.2006]

The bluff body flow patterns around three models can be predicted as shown in Figure 6.6

5.6 Spectral coherence of turbulence and pressure

Effects of spanwise separations, pressure positions, turbulent flow conditions and Karman vortex on the spectral coherent structures of turbulence and pressure have been investigated using the Fourier coherence. Figure 5.7 shows the effect of spanwise separations ($\Delta y = 25,75,125,225mm$) on the pressure coherence (with all models B/D=1, B/D=1 with S.P and B/D=5) and turbulent coherence on frequency band 0÷100Hz and in the flow case 1. It is agreed that the coherences of turbulences and pressures reduce considerably with respect to an increases of the spanwise separations and of observed frequencies.

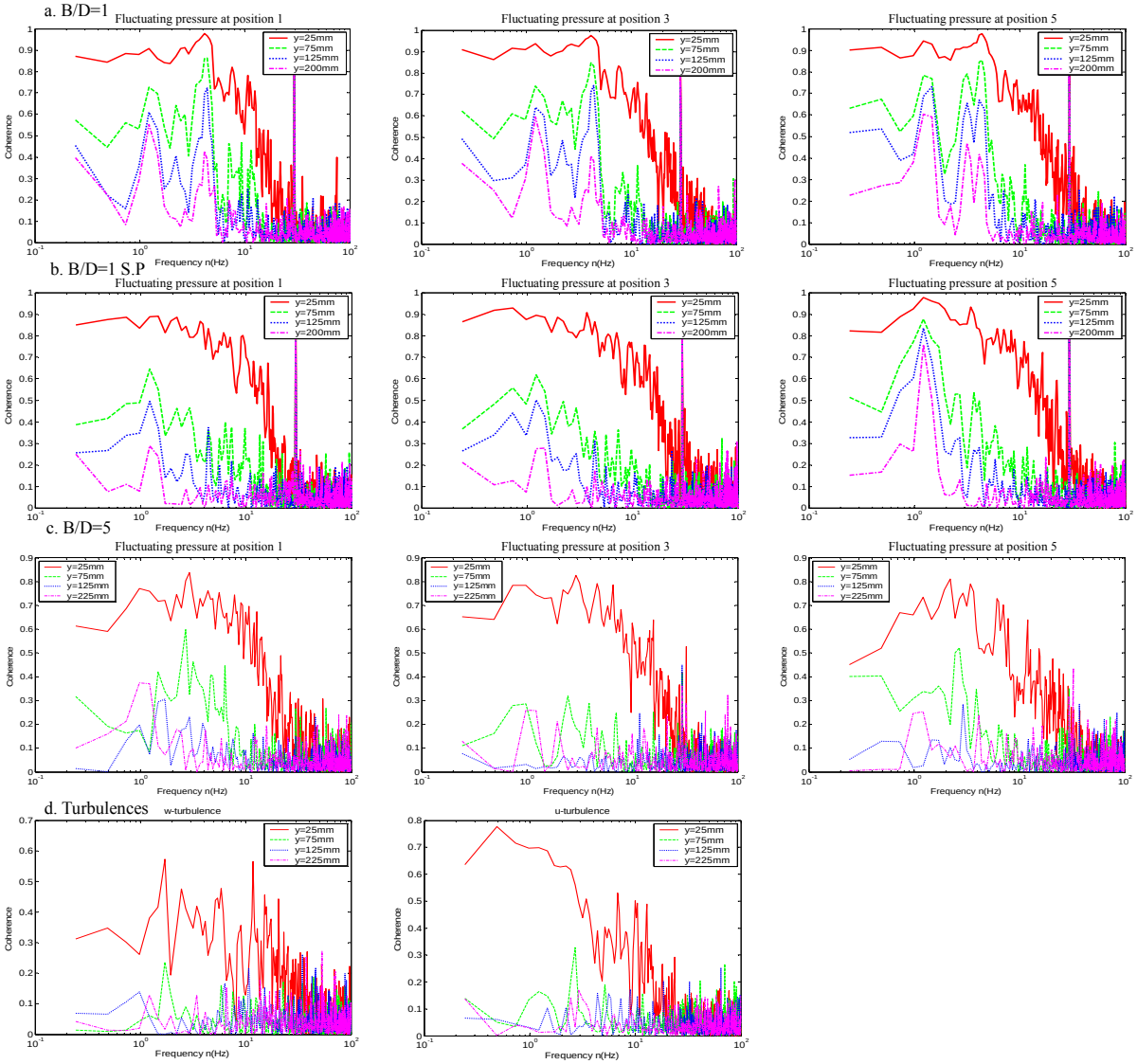

Fig. 5.7 Effect of spanwise separations on pressure and turbulent coherences in the flow case 1: a. B/D=1, b. B/D=1 with S.P, c. B/D=5, d. turbulences

Coherences of both turbulence and pressure dominate only at low frequency band roughly lower than 50Hz, and they decay fast beyond this frequency. Furthermore, separation influences on the pressure coherence stronger than on the turbulent one. The turbulent coherence is significant in close separation (y=25mm), but inconsiderable in another ones (y=75, 125 and 225mm). The pressure coherence, however, suddenly rises even in distant separations at some certain frequencies where any physical phenomenon occurs on model surface, here are the Karman vortex shedding at wake and the rolled-up vortex shedding at reattachment point. Thus, it is discussed that wind-structure interaction influences higher pressure coherence than the turbulent one due to enhancing spanwise flow convection.

Figure 5.8 shows pressure coherences at positions Nos. 1, 3, 5, 7, 9 (models B/D=1 without and with S.P) and Nos. 1, 4, 8, 19 (model B/D=5) and at separations $y = 25,75\,and\,125mm$. As can be seen from Figure 5.8, the pressure coherences on models B/D=1 seem to be not different, except at frequencies of vortex shedding phenomena, whereas difference in the pressure coherences on model B/D=5 has been observed. In model B/D=5, the coherence at position 1 (at the leading edge) seem to be strong in the close separation y=25mm and to be small at the distant separations y=75,125mm; strong in all separations at position 4 (in the separation bubble); small in all separations at position 8 (at the attachment point); and seem to be small in close separation y=25mm and strong in distant separations y=75, 125mm at position 19 (at the trailing edge) (see Figure 5.8c). Thus, it might be supposed that the pressure coherences seem to be relatively high at positions in the separation bubble region, to be relatively small at positions near the reattachment region. Effect of pressure positions and bluff body flow must be involved for higher mechanism of the pressure coherence.

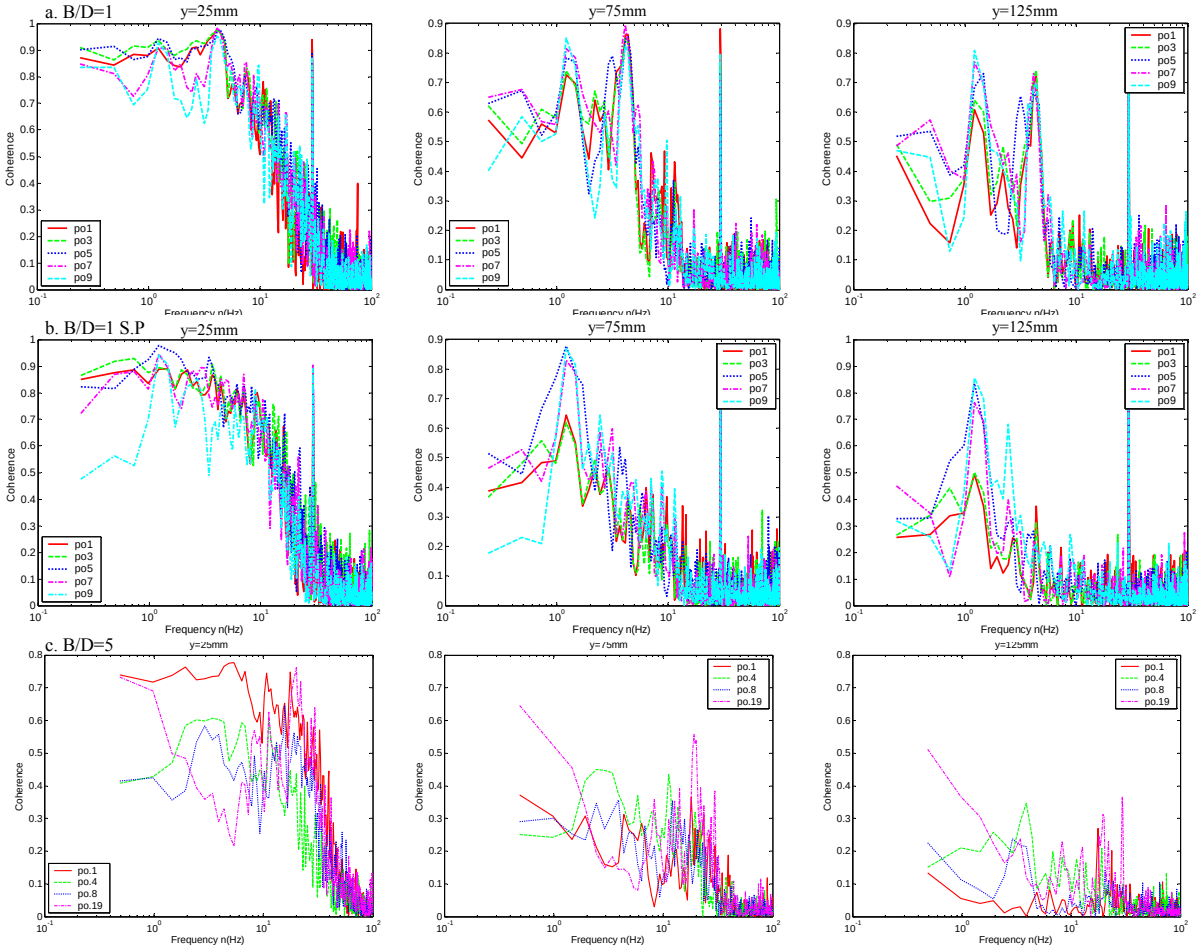

Fig. 5.8 Effect of pressure positions on pressure coherence: a. B/D=1, b. B/D=1 with S.P, c. B/D=5

Effect of the turbulent flow conditions on pressure and turbulent coherences of pressure at represented separation y=25mm is presented in Figure 5.9. It seems that the pressure coherence and turbulent one reduce with increase of intensity of turbulence (corresponding to decrease of mean velocity in grid turbulent flow). It might be explained that high intensity of turbulence is to ruin formation of separation bubble and vortex shedding to resist the spanwise convection of the bluff body flow. Thus, both the turbulent and pressure coherences depend on parameters of the ongoing turbulent flow, not only the mean velocity.

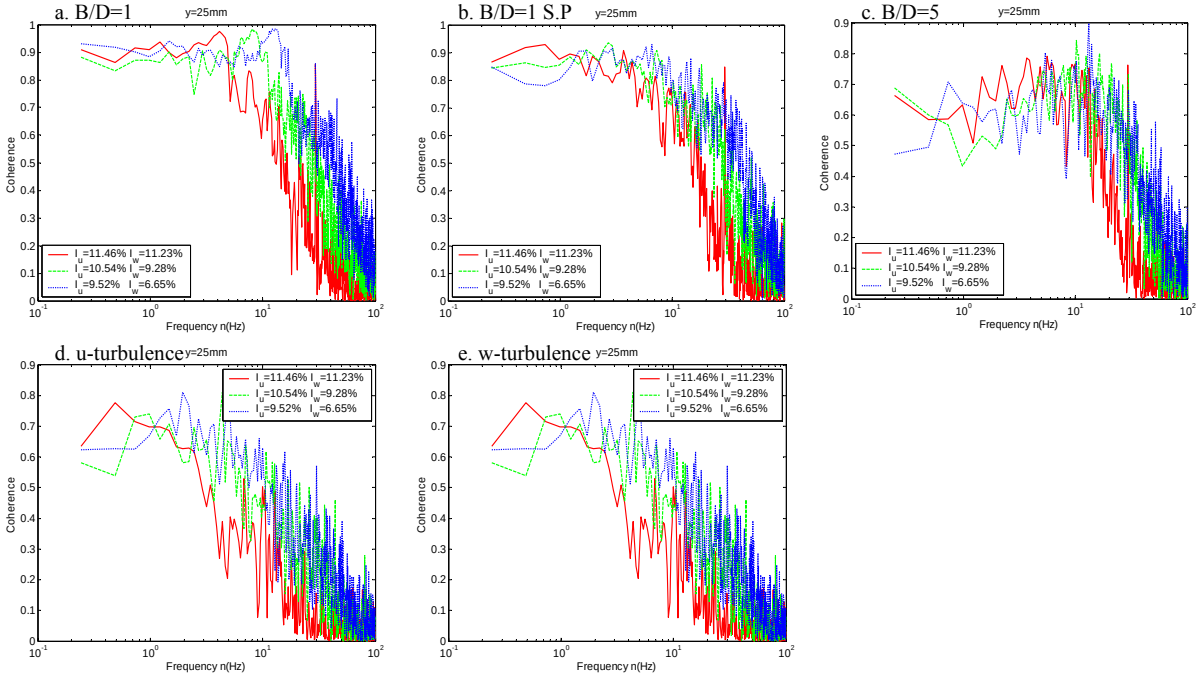

Fig. 5.9 Efect of turbulent flow conditions of pressure coherence: a. B/D=1, b. B/D=1 with S.P, c. B/D=5, d. u-turbulence, e. w-turbulence

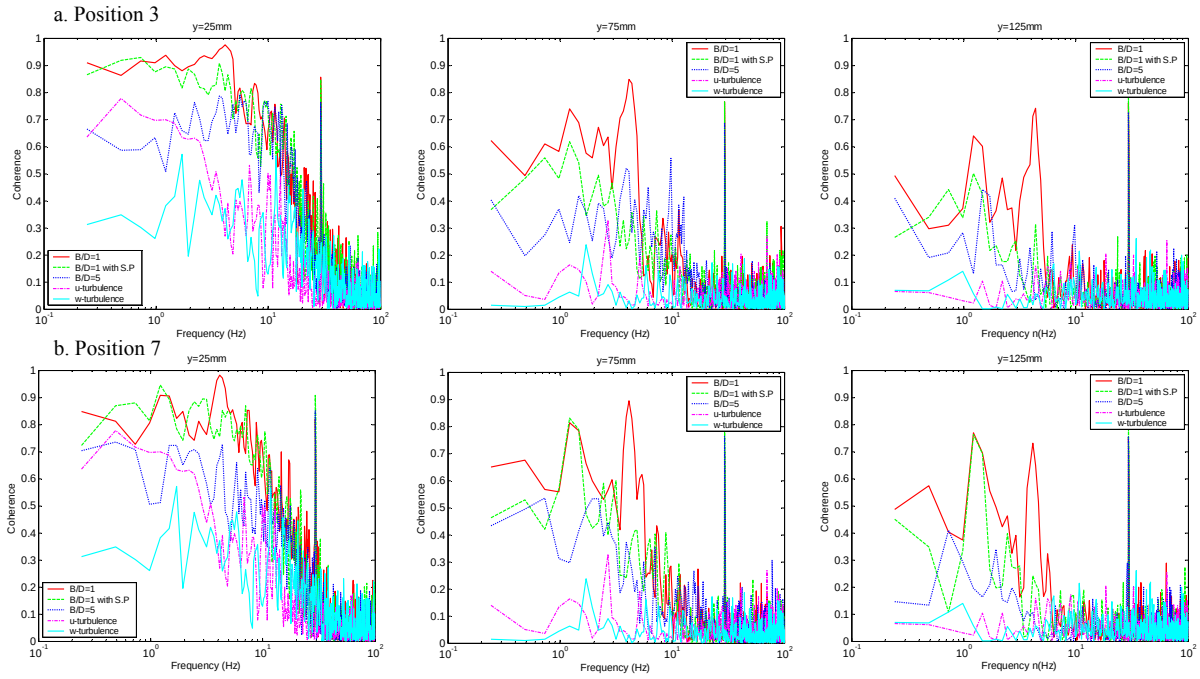

Fig. 5.10 Comparison between turbulent coherence and pressure coherence: a. at position 3, b. at position 7

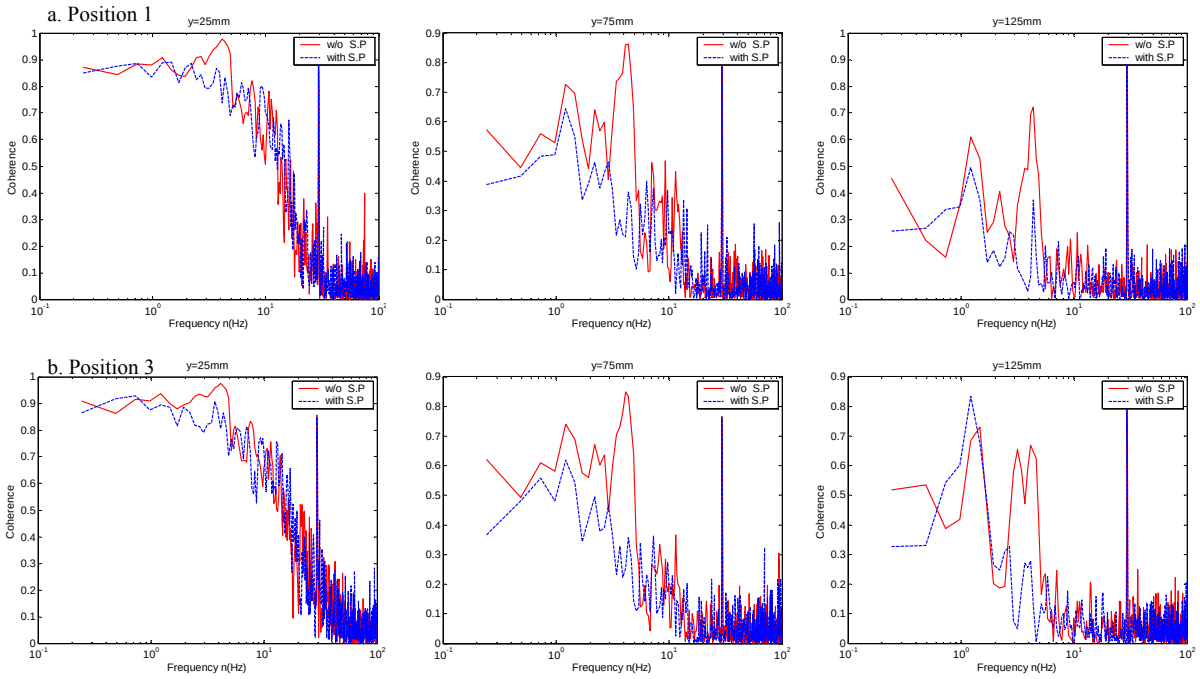

Fig. 5.11 Effect of Karman vortex shedding on pressure coherence: a. position 1, b. position 3

Figure 5.10 expresses the comparison between the turbulent and pressure coherences at the spanwise separations y=25, 75 and 125mm, in which the pressure coherences are determined in tap positions 3, 7 at all three experimental models. Obviously, the pressure coherences exhibit higher than the turbulent coherence at the same separations. In the comparison, the coherence of u-turbulence seems to be higher than that of w-turbulence at the close separations y=25, 75mm, but not to be different at the distant one y=125mm. Moreover, the pressure coherences on the three models decrease respectively from model B/D=1 without S.P, B/D=1 with S.P to model B/D=5. Effect of the Karman vortex shedding on the pressure coherences is more clarified by using the models B/D=1 without S.P (formation of the Karman vortex) and with S.P (suppression of the Karman vortex) as seen in Figure 5.11. Clearly, the pressure coherence in presence of the Karman vortex exhibits larger than that in without Karman vortex. It implies that the Karman vortex enhances spanwise convection of the bluff body flow, and consequently increases the spanwise coherence. In some extent, side ratio B/D of rectangular sections is basic parameter to characterize for the bluff body flow patterns, it can be generalized that the pressure coherence or force one within influenced spanwise separations reduce with respect to increase of side ratio B/D and parameters relating bluff body flow modification such as the splitter plate at the flow wake, cutting-sharp corners at trailing edge and so on.

5.7 Temporo-spectral coherence of turbulence and pressure

Temporo-spectral coherent structures of pressure and turbulence have been studied in the time-frequency plane using the wavelet transform-based tools. The wavelet coefficients, wavelet auto spectra and wavelet cross spectra of pressure and turbulence have been calculated before the wavelet coherence has been estimated. Figure 6.12 shows the wavelet coherences of pressure and turbulences corresponding to three experimental models, separations y=25, 75 and 125mm, on 1÷50Hz band and 5÷95 second interval.

As can be seen from Figure 5.12, some discussions can be given as follows. Firstly, similar to the previous results from the Fourier coherence, the wavelet coherence maps also indicate that coherence reduce with increase of the spanwise separations, furthermore, the pressure coherences are higher than the turbulent ones at the same separations. However, the coherences of pressure and turbulence are represented in the time-frequency plane in which the coherences are localized and temporo-spectral information determined. Secondly, the coherences of pressure and turbulence are also distributed intermittently and discretely in the time-frequency plane. This implies that intermittent distributions of turbulent and pressure coherences are observed as the nature of coherence in the time-frequency plane. Thirdly, high coherence events (even to be nearly fully-correlated at some local zones) still exist in both the turbulent and pressure coherences at distant spanwise separations but in localized time-frequency areas, this can not clarified from the conventional Fourier coherence where averaging technique in the time domain has been carried out. Finally, high coherence events of pressure and turbulence do not correspond in the time-frequency plane, although time series of pressure and turbulence have been measured simultaneously.

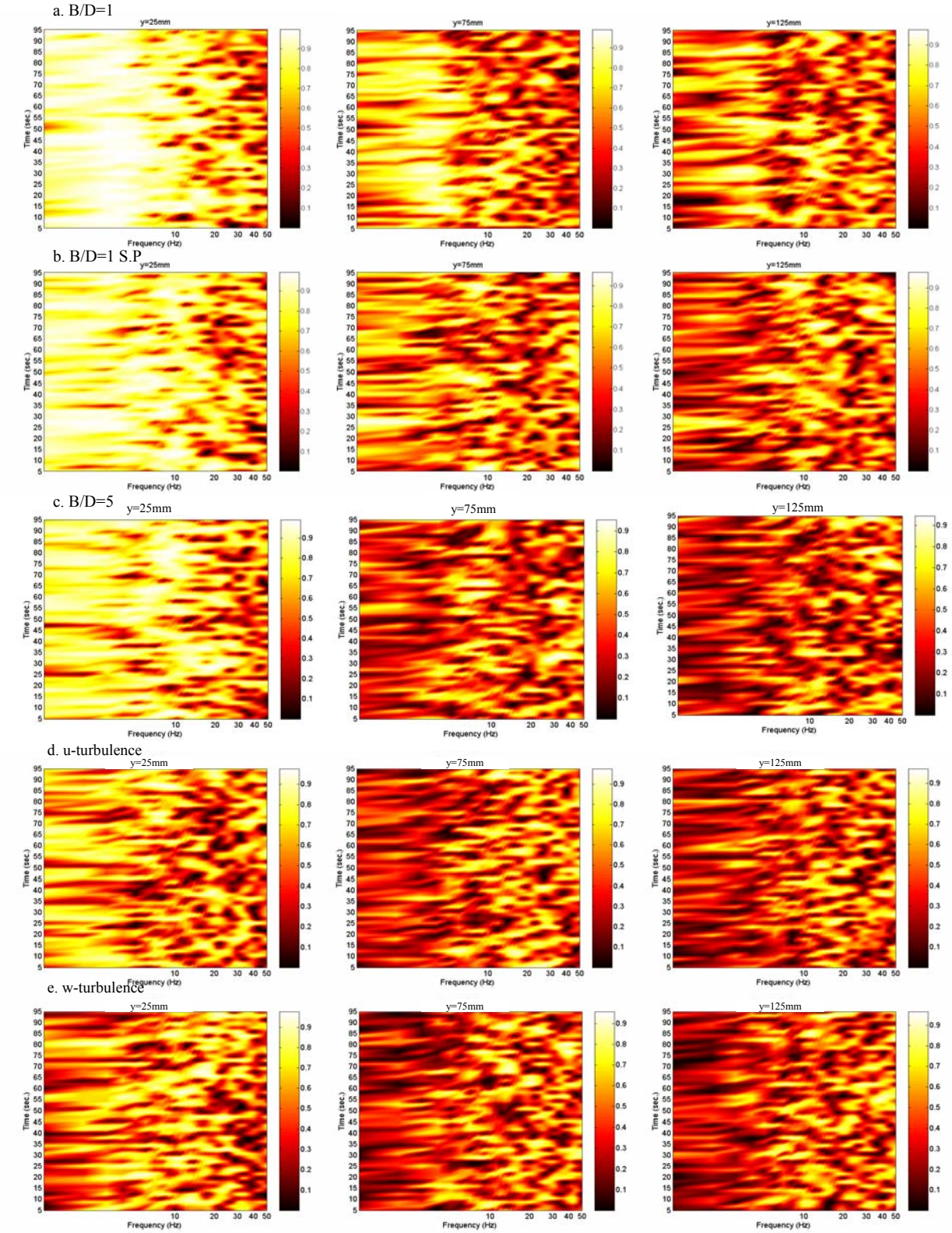

Fig. 5.12 Wavelet coherence maps of pressure in turbulent flow case 1: a. B/D=1, B/D=1 with S.P, c. B/D=5, d. u-turbulence, e. w-turbulence

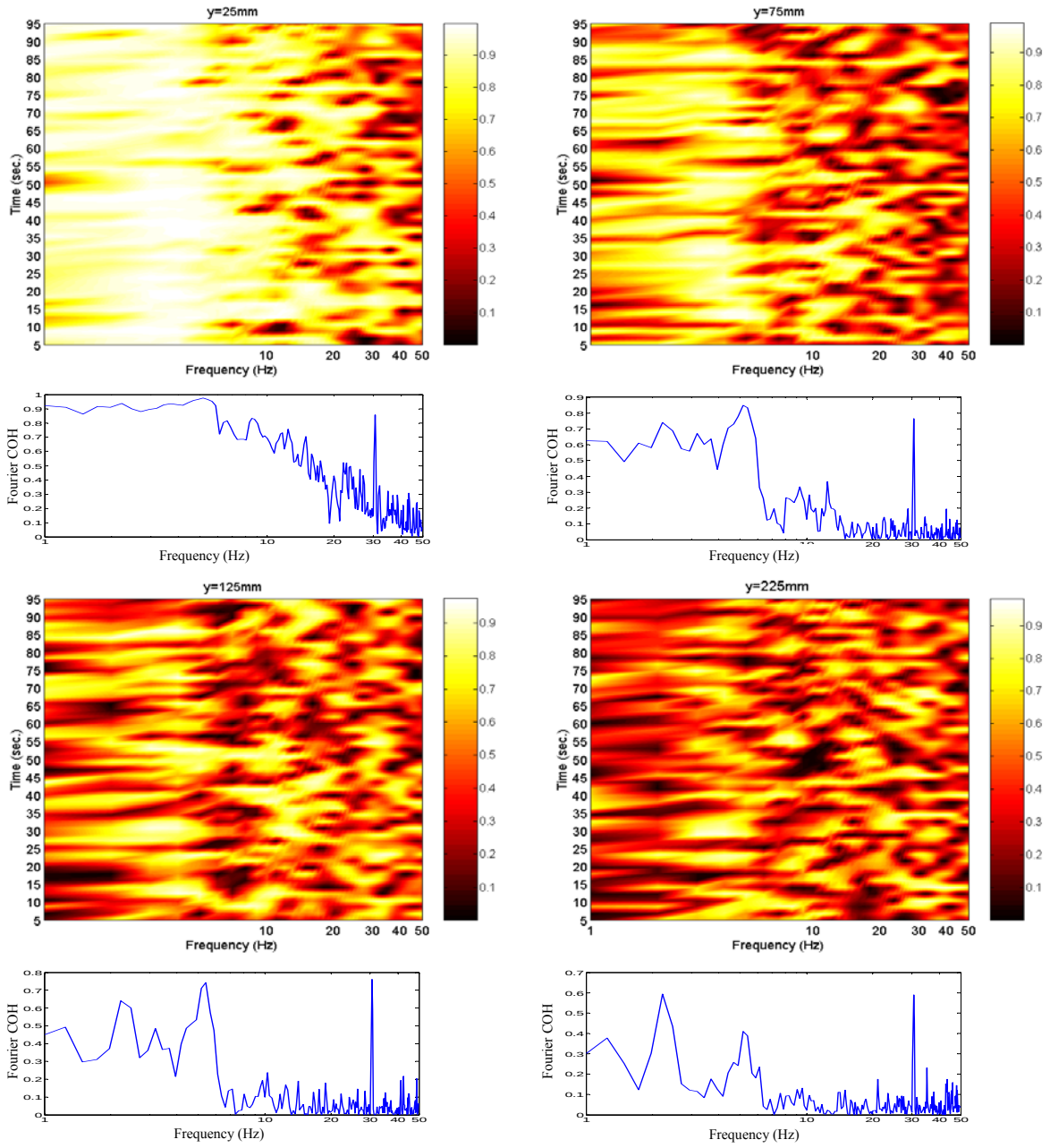

Fig. 5.13 Comparison between wavelet coherence and Fourier coherence

A comparison between the Fourier coherences and wavelet ones is presented in Figure 6.13, in which pressure coherences on model B/D=1 without S.P and at some spanwise separations is studied. As can be seen from Figure 6.13, there is correspondence in dominant spectral components between the wavelet coherence and the Fourier one. The Fourier coherence is appropriate to detect dominant frequencies of high coherence events, while the wavelet coherence

is to track frequency bands of these ones. However, there is no time information of high coherence events obtained at any observed frequencies in the Fourier coherence, but eventual time of those can be given in the wavelet coherence.

5.8 Conclusion

The coherent structures of turbulence and surface pressure have been discussed in the frequency domain and the time-frequency plane using the Fourier coherence and wavelet one. As above-discussed, some conclusions can be given as follows:

(1) Obviously, the pressure coherence exhibits higher than the turbulent one at influenced spanwise separations due to effect of the wind-structure interaction and the bluff body flow on model surface. Thus, existing formula of the force coherence based on turbulent field contain a lot of uncertainties.

(2) Coherent structures of turbulence and induced pressure depend on some parameters such as the ongoing flow, the spatial separations, the bluff body flow. It is reasonable that empirical formula for the coherence function of turbulent-induced forces must account for these parameters, not only as the ongoing flow characteristics (including parameters relating turbulent flow dimension as turbulent intensities and turbulent scales) and the spanwise separation in existing formulae, but effect of the bluff body flow should be included in the coherence formula. The side ratio B/D is suggested as one parameter relating to effect of the bluff body flow in the force coherence for cases of rectangular cylinders.

(3) The coherent structures of the turbulence and pressure depend on not only the frequency, but the time. Coherence is significant at the low spectral band and distribute intermittently and locally in the time domain. Thus, intermittency in time domain and low frequency bands can be considered as nature of the coherent structures.

(4) High coherent events distribute on localized areas in the time-frequency plane can be observed on the temporo-spectral structures of turbulence and pressure coherences, even at large separations. However, this finding can not obtain via the Fourier transform-based coherence. Thus, existence of localized high coherent events is the nature of coherence structure.

(5) No correspondence and simultaneous occurrence between high coherence events of turbulence and induced pressure have been observed in the time-frequency plane. This can add to uncertainties in the turbulent-induced response prediction of structures relating to the quasi-steady theory of turbulent-induced forces built from the turbulent components.

References

Bendat, J.S.; Piersol, A.G. (2000), *Random data: analysis and measurement procedures*, 3rd Edition, John Wiley and Sons.

Cherry, N.J., Hillier, R., Latour, M.E.M. (1984), "Unsteady measurements in a separated and reattaching flow", *J. Fluid Mech.*, **144**, 13-46.

Daubechies, I. (1992), *Ten lectures on wavelets*, Society for Industrial and Applied Mathematics (SIAM).

Davenport, A.G. (1963), "The response of slender, line-like structures to a gusty wind", *Proc. of Institution of Civil Engineers*, **23**, pp. 389-408.

Hillier, R., Cherry, N.J. (1981), "The effects of stream turbulence on separation bubbles", *J. Wind Eng. Ind. Aerodyn.*, **8**, 49-58.

Jakobsen, J. B. (1997), "Span-wise structure of lift and overturning moment on a motionless bridge girder", *J. Wind Eng. Ind. Aerodyn.*, **69-71**, 795-805.

Kareem, A., Kijewski, T. (2002), "Time-frequency analysis of wind effects on structures", *J. Wind Eng. Ind. Aerodyn.*, **90**, 1435-1452.

Kawai, H. (1983), "Pressure fluctuations on square prisms – applicability of strip and quasi-steady theories", *J. Wind Eng. Ind. Aerodyn.*, **13**, 197-208.

Kimura, K., Fujino, Y., Nakato, S., Tamura, H. (1997), "Characteristics of buffeting forces on plat cylinders", *J. Wind Eng. Ind. Aerodyn.*, **69-71**, 365-374

Larose, G.L. (1996), "The span-wise coherence of wind forces on streamlined bridge decks", *Proc. of the Third International Colloquium on Bluff Body Aerodynamics and Applications*, Blacksburg, USA.

Matsumoto, M., Shirato, H., Araki, K., Haramura, T., Hashimoto, T. (2003), "Spanwise coherence characteristics of surface pressure field on 2-D bluff bodies", *J. Wind Eng. Ind. Aerodyn.*, **91**,155-163.

Torrence, C., Compo, G.P. (1998), "A practical guide to wavelet analysis", *Bulletin of the American Meteorological Society*, **79(1)**, 61-78.

Chapter 6

Analysis and Identification of Random Pressure Fields on Rectangular Cylinders using Proper Transformations

6.1 Introduction

Aerodynamic phenomena and response of structures due to the atmospheric wind flows are generated by spatial distribution and correlation of the fluctuating pressure field around structural section. This pressure field is usually represented as spatially-correlated multi-variate random processes. More understanding and knowledge of the random pressure field as well as its spatial distribution, correlation are always required and it is possible to interpret mechanisms of excitations, identification and response of aerodynamic phenomena occurring on structures. Due to the nature of random field, however, the fluctuating pressure field is considered as superposition from some causes and excitation of dominant physical phenomena. It is logical thinking to decompose the total pressure field by sums of independently partial pressure fields, which can be related to a particular mechanism of excitation and certain physical phenomena. The random pressure field, moreover, can be represented under the matrix forms, and then the decomposition of this pressure field is carried out via that of its matrices. There are two decomposition methods widely used so far: Cholesky decomposition and modal decomposition. Accordingly, the matrix representation of the pressure field is decomposed by product of lower triangle matrix and upper triangle one in the former, or by sum of independently orthogonal functions in the later. The later is also named as the proper orthogonal decomposition. The main purpose of pressure field decomposition is to describe the complicated random pressure field as more simplified ways which is convenient to model aerodynamic forces and to estimate response from this pressure field.

Proper orthogonal decomposition, or known as Karhunen-Loeve decomposition (Lumley 1970), has been applied popularly in many engineering fields including random processes/fields, stochastic methods, image processing, data compression, system identification and control and so on (Liang et al. 2002). In the wind engineering, the proper orthogonal decomposition has been

used in the three following topics: i) stochastic decomposition and order-reduced modeling of random processes/fields and induced pressure/forces, ii) representation and simulation of random turbulent fields and iii) stochastic response of structures. The proper orthogonal decomposition has been applied to optimally approximate the multi-variate random processes through use of low-order basic orthogonal vectors from modal decomposition (eigenvector problem) of either zero-time-lag covariance matrix or cross spectral density one of this multi-variate random field. According to type of basic matrix in the modal decomposition, the proper orthogonal decomposition has been branched by either covariance proper transformation or spectral proper transformation (Solari and Carassale 2000). Main advantage of the proper orthogonal decomposition is that the multi-variate correlated random processes/ fields can be decomposed and described in such simplified way as a combination of a few low-order dominant eigenvectors (modes) and omitting higher-order ones that is convenient for order-reduced representation of the random field, including random-induced force modeling and random response prediction. Furthermore, because the random field is described via few dominantly low-order orthogonal modes, therefore it is usually expected that these dominant modes can represent to any typically physical cause occurring on structure.

This chapter will present the proper orthogonal decomposition and its proper transformations of the fluctuating pressure fields on some typical rectangular cylinders, which are based both recent branches: the covariance matrix and the cross spectral matrices of these pressure fields. Analysis, identification and order-reduced reconstruction of the pressure fields will be carried out basing on characteristic functions resulted from both covariance matrix-branched and cross spectral matrix-branched proper orthogonal decompositions: covariance eigenvalues, covariance eigenvectors (covariance modes), covariance principal coordinates and spectral eigenvalues, spectral eigenvectors (spectral modes). Moreover, the linkage between the lowest modes and the physical phenomena can be revealed with combination of past understanding and knowledge of the bluff body flows and physical causes. The fluctuating pressure field has been determined through physical measurements on some rectangular models with side ratios of B/D=1 and B/D=5 in the turbulent flows in the wind tunnel.

6.2 Literature reviews

The proper orthogonal decomposition also has been widely used for many fields such as analysis, simulation of random fields (including the random pressure field), numerical analysis, dynamic system identification, dynamic response and so on. Several literatures presented the proper orthogonal decomposition's application to decompose the spatially-correlated and multi-variate

random pressure fields into uncorrelated random processes and basic orthogonal vectors (also called as modes or shape functions). The proper orthogonal decomposition has been branched by either covariance matrix-based or spectral matrix-based proper orthogonal decompositions and associated proper transformations, which depend on how to build up a basic matrix from either zero-time-lag covariance or cross spectral matrices of the multi-variate random processes.

Up to now, analyses of the random pressure fields almost have based on the covariance matrix-branched proper orthogonal decomposition due to its straightforward in computation and interpretation. Some authors used the proper orthogonal decomposition to analyze random pressure field and to find out relation between the covariance modes and physical phenomena. Bienkiewicz et al. 1995 used the proper orthogonal decomposition analysis of mean and fluctuating pressure fields around low-rise building directly measured due to turbulent flows. A linkage between pattern of the pressure distribution and covariance modes, especially first two modes was discussed and interpreted, in which the 1^{st} mode was compatible to the pattern of the fluctuating pressure distribution, whereas the 2^{nd} mode similar to the mean pressure pattern. Holmes et al. 1997, however, reviewed that that no consistent linkages between physical phenomena and covariance mode due to series of physical measurements and proper orthogonal decomposition analyses of pressure fields in low-rise buildings. Effect of pressure tap positions on the same measured pressure area (uniform and non-uniform arrangements) on the covariance modes studied by Jeong et al. 2000, by which the covariance modes observed differently in two cases. Kikuchi et al. 1997 applied the proper orthogonal decomposition to pressure field of tall buildings, then fluctuating pressure field was reconstructed due to only few dominant covariance modes, used to estimate aerodynamic forces and corresponding responses. Tamura et al. 1997&1999 indicated distortion and wrong interpretation of the covariance modes due to presence of mean pressure data in the analyzed pressure field. Matsumoto et al. 2006 carried out the proper orthogonal decomposition analysis of the fluctuating pressure fields around oscillatory rectangular section B/D=4, then linkage between the first covariance modes and some typical physical causes such as Karman vortex shedding and motion-induced vortex shedding on the model surface can be clarified in some cases. It is argued that the proper orthogonal decomposition is appropriate tool to reveal physical phenomena on from experimental data where correspondence between the covariance modes and physical causes from the fluctuating pressure field. However, some others discussed that interpretation from the covariance modes is aprioristic and arbitrary based from previous knowledge of system behavior and response.

Because the low-order eigenvectors contribute to most of energy of the fluctuating pressure field, it is expected that those eigenvectors are likely to be associated with dominant physical phenomena and physical causes occurred on physical model. Many literatures have tried to

follow this direction to find out obvious linkage between low-order eigenvectors and physical phenomena, however, there is somewhat pessimistic that these relations are valid for few certain cases, most of others are fictitious based on past knowledge and experience of authors. Considering about the fictitious relationship between the eigenvectors (or modes) and the underlying physical phenomena, some authors have indicated in their literatures that:

> "*… there is no reason to suppose that spatial variation of the pressure fluctuations due to one physical cause are necessarily orthogonal with respect to that due to another cause. The mathematical constraints caused by orthogonality condition could therefore mean that in some cases, a unique physical cause cannot be associated with each eigenvector.*"
>
> Armitt, J. 1968

> "*… the shapes of the modes are constrained by the requirement of orthogonality, and hence any physical interpretation of these modes could be at least misleading, and probably fictitious in many cases. The most useful aspect of the proper orthogonal decomposition techniques is that it is an economical form for describing the spatial and temporal wind pressure variations on a buildings, or other bluff body, and is especially useful for relating the pressures to structural load effects.*"
>
> Holmes, J.D. 1997

This is explained that due to the mathematical constraints of orthogonality conditions from the random processes/ fields, unique physical cause cannot be associated with dominant eigenvector, moreover, fictitious interpretation about these relations between the covariance modes and physical causes may be based on past knowledge and previous experience about the flow behaviors. Many effects such as number of pressure positions, pressure position arrangement, presence of mean pressure values and so on can influence sensitively to resulting covariance modes (Tamura et al. 1999, Jeong et al. 2000). The covariance proper transformation, however, has effectively used few dominant covariance modes to approximate random-induced forces and response prediction of buildings and spaced structures (Kikuchi et al. 1997, Uematsu et al. 1997). Spectral matrix-based application to decompose the random field is rare due to its complexities in computation and interpretation, but it is promising due to its complete decoupling solution at every frequency, consequently decoupling in the time domain including zero-time-lag condition. De Grenet and Ricciardelli 2004 discussed in using the spectral proper transformation to study the fluctuating pressure fields around squared cylinder and boxed-girder deck.

6.3 Representation of unsteady surface pressure field

Similar to the turbulent fields, the wind-induced pressure field on structures is considered as multi-variate spatially-correlated random fields, in which the pressure at any point in the field is influenced by surrounding pressures at adjacent points. Thus, one calls the pressure field as coherent one. The unsteady surface pressure at any point in the field is expressed as summation between mean value and fluctuating pressure as:

$$P(\upsilon,t) = \overline{p}(\upsilon) + p(\upsilon,t) \tag{6.1}$$

where $P(\upsilon,t)$: unsteady pressure; $\overline{p}(\upsilon)$: mean pressure; $p(\upsilon,t)$: fluctuating pressure; υ : dimensional variables (υ=x;y;z). Fluctuating pressure field $p(\upsilon,t)$ is usually represented as N-variate random process with zero mean containing sub-processes at N points in the field:

$$p(\upsilon,t) = \left\{p_1(\upsilon,t), p_2(\upsilon,t),..., p_N(\upsilon,t)\right\}^T \tag{6.2}$$

Zero-time-lag covariance matrix and cross power spectrum density matrix are commonly used to characterize for the N-variate spatially-correlated random pressure field p(t) in the time domain and in the frequency one, which are defined as follows:

$$R_p = [R_{p_k p_l}(0)] = \begin{bmatrix} R_{p_1p_1}(0) & R_{p_1p_2}(0) & \cdots & R_{p_1p_N}(0) \\ R_{p_2p_1}(0) & R_{p_2p_2}(0) & \cdots & R_{p_2p_N}(0) \\ \vdots & \vdots & \cdots & \vdots \\ R_{p_Np_1}(0) & R_{p_Np_2}(0) & \cdots & R_{p_Np_N}(0) \end{bmatrix} \tag{6.3-a}$$

$$S_p = [S_{p_k p_l}(n)] = \begin{bmatrix} S_{p_1p_1}(n) & S_{p_1p_2}(n) & \cdots & S_{p_1p_N}(n) \\ S_{p_2p_1}(n) & S_{p_2p_2}(n) & \cdots & S_{p_2p_N}(n) \\ \vdots & \vdots & \cdots & \vdots \\ S_{p_Np_1}(n) & S_{p_Np_2}(n) & \cdots & S_{p_Np_N}(n) \end{bmatrix} \tag{6.3-b}$$

where R_p, S_p: zero-time-lag covariance and cross spectral matrices, respectively; $R_{p_k p_l}(0), S_{p_k p_l}(n)$: elements of the covariance matrix and the cross power spectral one between $p_k(t)$ and $p_l(t)$ at nodes k and l, are determined as follows:

$$R_{p_k p_l}(0) = E[p_k(t)\, p_l^T(t)] \tag{6.4-a}$$

$$S_{p_k p_l}(n) = \sqrt{S_{p_k p_k}(n) S_{p_l p_l}(n)}\, COH_{p_k p_l}(n, \Delta_{kl}) \tag{6.4-b}$$

where E[],T denote to the expectation and transpose operators; n: frequency variable; $S_{p_k p_k}(n), S_{p_l p_l}(n)$: auto power spectral densities of $p_k(t)$ and $p_l(t)$; $COH_{p_k p_l}(n, \Delta_{kl})$: coherence function between two separated nodes k, l accounting for spatial correlation of the random sub-processes in the frequency domain which can be determined by either empirical model or

physical measurement.

It is noted that the zero-time-lag covariance matrix is symmetric, real and positive definite, whereas the cross spectral one is symmetric, real (because the quadrature spectrum has been neglected) and Hermitian semi-positive definite at each frequency.

6.4 Proper orthogonal decomposition of pressure field

Proper orthogonal decomposition usually implies for the Karhunen-Loeve decomposition to differ to some other sister decomposition methods such as the principal component analysis and the singular value decomposition. Equivalence among these methods, however, was discussed by Liang et al. 2002.

The proper orthogonal decomposition is considered as optimum approximation of multi-variate random processes in which a set of orthogonal basic vectors is found out in order to expand the random process into a sum of products of these time-independent basic orthogonal vectors and time-dependant uncorrelated single-variate random processes. Let consider the multi-variate random process $\upsilon(t)$ containing correlated N-subprocesses $\upsilon(t) = \{\upsilon_1(t), \upsilon_2(t), ..., \upsilon_N(t)\}^T$ is approximated as follows:

$$\upsilon(t) = x(t)^T \Theta = \sum_{i=1}^{N} x_i(t)\theta_i \tag{6.5}$$

where $\upsilon(t)$: multi-variate random process with zero-mean; $x(t)$: principal coordinate vector $x(t) = \{x_1(t), x_2(t), ..., x_N(t)\}$ in which $x_i(t)$: i-th principal coordinate as zero-mean single-variate random subprocess; Θ: modal matrix or shape function matrix $\Theta = [\theta_1, \theta_2, ..., \theta_N]$ in which θ_i: i-th basic orthogonal vector.

In mathematical expression of optimality is to find out shape function matrix Θ to maximize the projection of random process $\upsilon(t)$ onto this shape function, suitably normalized due to the mean square basis (Lumley 1970):

$$Max \ \frac{\left\langle | (\upsilon(t) \otimes \Theta) |^2 \right\rangle}{\left\| \Theta \right\|^2} \tag{6.6}$$

where $(\otimes), \langle . \rangle, |.|, \|.\|$ denote to inner product, expectation, absolute and Euclidean squared norm operators, respectively.

Optimum approximation of the random process in Eq.(6.1) using the shape function matrix defined as Eq.(6.2) is known as the Karhunen-Loeve decomposition. It is proved that the shape function matrix in this optimality can be found out as eigenvector solution of eigen problem from

basic matrix that are either covariance matrix or cross spectral matrix formed by the multi-variate random process.

Multi-variate spatially-correlated random pressure field can be expressed by following optimum approximation, in which this pressure field is expand into a sum of products of time-independent basic orthogonal vectors and time-dependant uncorrelated random processes as follows:

$$p(\upsilon,t) = x(t)^T \Phi(\upsilon) = \sum_{j=1}^{N} x_j(t)\phi_j(\upsilon) \tag{6.7}$$

where $a_j(t)$: j-th principal coordinate as uni-variate zero-time random processes $E\lfloor a_j(t)\rfloor = 0$; $\phi_j(\upsilon)$: j-th basic orthogonal vector $\phi_i(\upsilon)^T \phi_j(\upsilon) = \delta_{ij}$ (δ_{ij} : Kronecker delta); $x(t) = \{x_1(t), x_2(t),..., x_N(t)\}, \Phi(\upsilon) = [\phi_1(\upsilon), \phi_2(\upsilon),..., \phi_N(\upsilon)]$. It is also notable that eigenvalues gained from this eigen solution usually reduce fast, accordingly, only very few number of low-order eigenvectors associated with low-order high eigenvalues can obtain optimum approximation in Eq.(6.1) and describe the whole random process.

$$\upsilon(t) \approx \sum_{i=1}^{\overline{N}} x_i(t)\theta_i \tag{6.8}$$

where $\overline{N}$: number of truncated shape functions (eigenvectors or modes) $\overline{N} << N$.

6.5 Covariance and spectral proper transformations of pressure field

The covariance matrix-based orthogonal vectors are found as the eigenvector solutions of the zero-time-lag covariance matrix $R_p(n)$ of the N-variate random pressure field $p(t)$:

$$R_p \Theta_p = \Gamma_p \Theta_p \tag{6.9}$$

where $\Theta_p = [\theta_{p1}, \theta_{p2},...\theta_{pN}]$, $\Gamma_p = diag(\gamma_{p1}, \gamma_{p2},...\gamma_{pN})$: covariance eigenvalue and eigenvector (covariance turbulent mode) matrices, which satisfy the orthonormal conditions:

$$\Theta_p \Theta_p^T = I;\ \Theta_p C_p \Theta_p^T = \Gamma_p \tag{6.10}$$

Accordingly, the turbulence field and its covariance matrix can be expressed as optimum approximation as follows:

$$p(t) = \Theta_p \widetilde{x}_p(t) \approx \sum_{j=1}^{\widetilde{N}} \theta_{pj} \widetilde{x}_{pj}(t) \tag{6.11-a}$$

$$R_p = \Theta_p \Gamma_p \Theta_p^T(n) \approx \sum_{j=1}^{\widetilde{N}} \theta_{pj} \gamma_{pj} \theta_{pj}^T \tag{6.11-b}$$

where $\widetilde{x}_p(t) = \{\widetilde{x}_{p1}(t), \widetilde{x}_{p2}(t), \ldots, \widetilde{x}_{p\widetilde{M}}\}^T$: covariance-based turbulent principal coordinates as the N-variate uncorrelated random process; $\widetilde{N}$: number of truncated turbulent modes ($\widetilde{N} << N$). This approximation is called the Covariance Proper Transformation (CPT).

Covariance principal coordinates can be determined from observed data:

$$\widetilde{x}_p(t) = \Theta_p{}^{-1} p(t) = p(t)\Theta_p = \sum_{j=1}^{N} p_j(t)\theta_{pj} \tag{6.12}$$

Similarly, the spectral eigenvalues and eigenvectors are found based on to the eigen problem of the cross spectral matrix $S_p(n)$ of random pressure process $p(t)$:

$$S_p(n)\Psi_p(n) = \Lambda_p(n)\Psi_p(n) \tag{6.13}$$

where $\Lambda_p(n) = diag(\lambda_{p1}(n), \lambda_{p2}(n), \ldots \lambda_{pN}(n))$, $\Psi_p(n) = [\psi_{p1}(n), \psi_{p2}(n), \ldots \psi_{pN}(n)]$: spectral eigenvalue and eigenvector (spectral turbulent mode) matrices, which also satisfy the orthonormal conditions:

$$\Psi_p^{*T}(n)\Psi_p(n) = I;\ \Psi_p^{*T}(n)S_p(n)\Psi_p(n) = \Lambda_p(n) \tag{6.14}$$

Thus, the Fourier transform and the cross spectral density matrix $S_p(n)$ can be represented approximately under the Spectral Proper Transformation (SPT) as follows:

$$\hat{p}(n) = \Psi_p(n)\hat{y}_p(n) \approx \sum_{j=1}^{\hat{N}} \psi_{pj}(n)\hat{y}_{pj}(n) \tag{6.15-a}$$

$$S_p(n) = \Psi_p(n)\Lambda_p(n)\Psi_p^{*T}(n) \approx \sum_{j=1}^{\hat{N}} \psi_{pj}(n)\lambda_{pj}(n)\psi_{pj}^{*T}(n) \tag{6.15-b}$$

where $\hat{y}_p(n)$: spectral-based turbulent principal coordinates as Fourier transforms of uncorrelated single-variate random processes; $\hat{N}$: number of truncated turbulent modes ($\hat{N} << N$); *,T denote to complex conjugate and transpose operation, respectively.

6.6 Gust response based on order-reduced pressure field

In many cases, the gust response prediction of spaced structure is required via measurement of fluctuating pressure field surrounding the structure in wind tunnel tests. The covariance proper transformation can be applied to represent the random fluctuating pressure field into simplified order-reduced model using truncated number of low-order covariance eigenvectors and associated covariance principal coordinates:

$$p(t) = \Theta_p x_p(t) \approx \sum_{j=1}^{\widetilde{N}} \theta_{p_j} x_{p_j}(t) \tag{6.16}$$

where p(t): multi-variate correlated random pressure field around structure $p(t)=\{p_1(t),p_2(t),...,p_N(t)\}^T$; Θ_p: covariance modes of the pressure field $\Theta_p=\lfloor\theta_{p_1},\theta_{p_2},...,\theta_{p_N}\rfloor$; $x_p(t)$: covariance principal coordianate containing uncorrelated subprocesses $x_p(t)=\{a_{p_1}(t),a_{p_2}(t),...,a_{p_N}(t)\}^T$.

Full-scale turbulent-induced loading can be estimated via order-reduced model of surrounding pressure field:

$$F_b(t)=\sum_{j=1}^{\tilde{N}}C_{Aj}p_j(t)\approx\sum_{j=1}^{\tilde{N}}C_{Aj}\theta_{p_j}x_{p_j}(t) \tag{6.17}$$

where C_{Aj}: representative area at node j.

Accordingly, generalized turbulent-induced loading can be expended as follows:

$$f_{bi}(t)=\phi_i F_b(t)\approx\phi_i\sum_{j=1}^{\tilde{N}}C_{Aj}\theta_{p_j}x_{p_j}(t)=\sum_{j=1}^{\tilde{N}}A_{p_{ij}}x_{p_j}(t) \tag{618}$$

where $A_p=\sum_{j=1}^{\tilde{N}}A_{pij}=\sum_{j=1}^{\tilde{N}}\phi_i C_{A_j}\theta_{p_j}$: cross modal factors between the covariance modes and structural ones.

Thus, the single-degree-of-freedom motion equation can be obtained directly in the time domain:

$$\ddot{\xi}_i(t)+2\zeta_i\omega_i\dot{\xi}_i(t)+\omega_i^2\xi_i(t)=\sum_{j=1}^{\tilde{N}}A_{p_{ij}}x_{p_j}(t) \tag{6.19}$$

Generalized responses can also be solved directly in the time domain using the direct integration methods such as the Newmark-beta or the fourth-order Runge-Kutta methods. Then, the globally structural responses are also obtained accordingly.

6.7 Wind tunnel experiments

Physical pressure measurements were carried out in the Kyoto University's open-circuit wind tunnel. Three typical rectangular models with slender ratios B/D=1, B/D=1(with Splitter Plate), B/D=5 were used. Artificial turbulent flows were generated in the wind tunnel at mean wind velocities 3m/s (case1), 6m/s (case 2) and 9m/s (case 3), corresponding to intensities of turbulence were I_u=11.46%,I_w=11.23%; I_u=10.54%,I_w=9.28%;I_u=9.52%,I_w=6.65%, respectively. Pressure measurement holes were arranged inside, in chordwise direction and on one surface of models in which model B/D=1 labeled pressure positions from 1 to 10, whereas model B/D=5 from 1 to 19. Unsteady surface pressures were simultaneously measured by the multi-channel

pressure measurement system (ZOC23 system: Z (Zero), O (Operation), C (Calibration)). Electric signals were filtered by 100Hz low-pass filters (E3201, NF Design Block Co., Ltd.) before passed through A/D converter (Thinknet DF3422, Pavec Co., Ltd.) with sampling frequency at 1000Hz in 100 seconds.

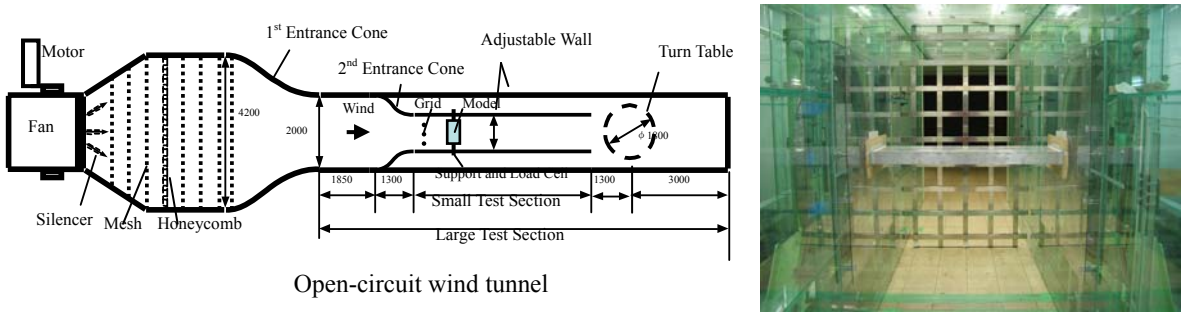

Fig. 6.1 Wind tunnel configuration, experimental set-ups and experimental models

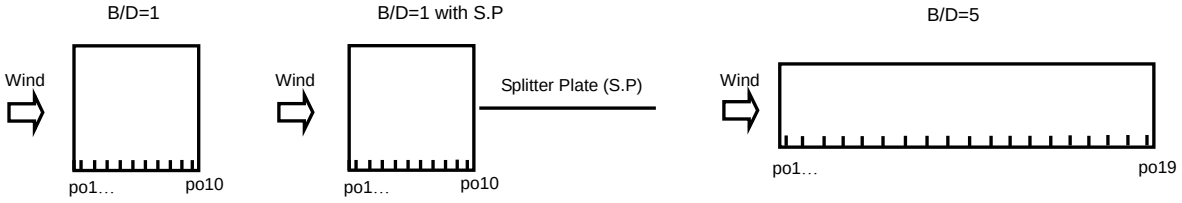

Fig. 6.2 Experimental models

Flow around models due to interaction between ongoing flow and model section is usually known as the bluff body flow, which characterized by formation of separated and reattached flows with separation bubble and formation of vortex shedding as well. It can be predicted from the past knowledge and previous understanding that model B/D=1 is favorable for formation of the Karman vortex shedding, where model B/D=5 is typical for formation of separated and reattached flows on model surface. The splitter plate was added to model B/D=1 in order to suppress effect of the Karman vortex shedding.

6.8 Surface pressure distribution and bluff body flow pattern

For convenient uses, mean and root-mean-square fluctuating pressure coefficients have been

normalized by dynamic pressure component from measured unsteady pressure data as follows:

$$C_{p,mean} = \overline{p} / \left(0.5\rho U^2\right) \quad (6.20\text{-a})$$

$$C_{p,rms} = \sigma_p / \left(0.5\rho U^2\right) \quad (6.20\text{-b})$$

where $0.5\rho U^2$: dynamic pressure; $\overline{p}$: mean value; σ_p : standard deviation of unsteady pressure.

Figure 6.3 shows the chordwise distributions of normalized fluctuating pressures on models at three turbulent flow conditions. As can be seen that the fluctuating pressure distributes steadily on whole surface of models B/D=1 but distributes dominantly on the leading region of the model B/D=5. The fluctuating pressures, furthermore, reduce with respect to decrease of intensities of turbulence.

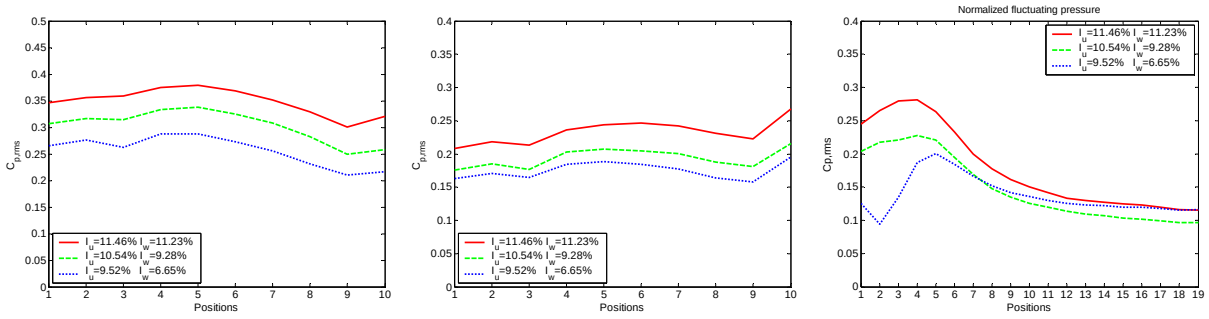

Fig. 6.3 Normalized fluctuating pressure distribution on chordwise positions
[Matsumoto, Shirato et al. 2006]

Figure 6.4 indicates power spectra of the fluctuating pressures at some chordwise positions with three models and turbulent conditions. As can be seen with the model B/D=1 (without splitter plate) that peaked frequencies are observed at 4.15Hz, 8.79Hz and 12.94Hz respective to the three turbulent flows. It is explained that the Karman vortex formed and shed at the wake of model. Shedding frequency depends on the Strouhal number (St) of cross section, moreover, the Strouhal number can be determined St=0.1285. In case B/D=1 with splitter plate, no peaked frequency is observed, it also means that no Karman vortex occurred and the splitter plate has suppressed effect of the Karman vortex. In case of the model B/D=5, spectral peaks are also observed at frequencies 1.22Hz and 2.44Hz (U=3m/s); at 2.44Hz, 4.88Hz, 7.32Hz (case 2); at 3.42Hz and 6.84Hz (case 3). It is predicted that the bluff body flow is separated and reattached one. Reattachment points are at roughly positions 6, 7, 8 with respect to an increase of mean velocities. It is supposed that the observed spectral peaks are induced by rolled-up vortices shed away at reattachment points toward trailing edge. This agrees well with findings presented in the

literatures of Hiller and Cherry 1981 and Cherry et al. 1984 which were proposed empirical formula to estimate frequency of rolled-up vortices shedding at reattachment point depending on mean velocity and length of separation bubble.

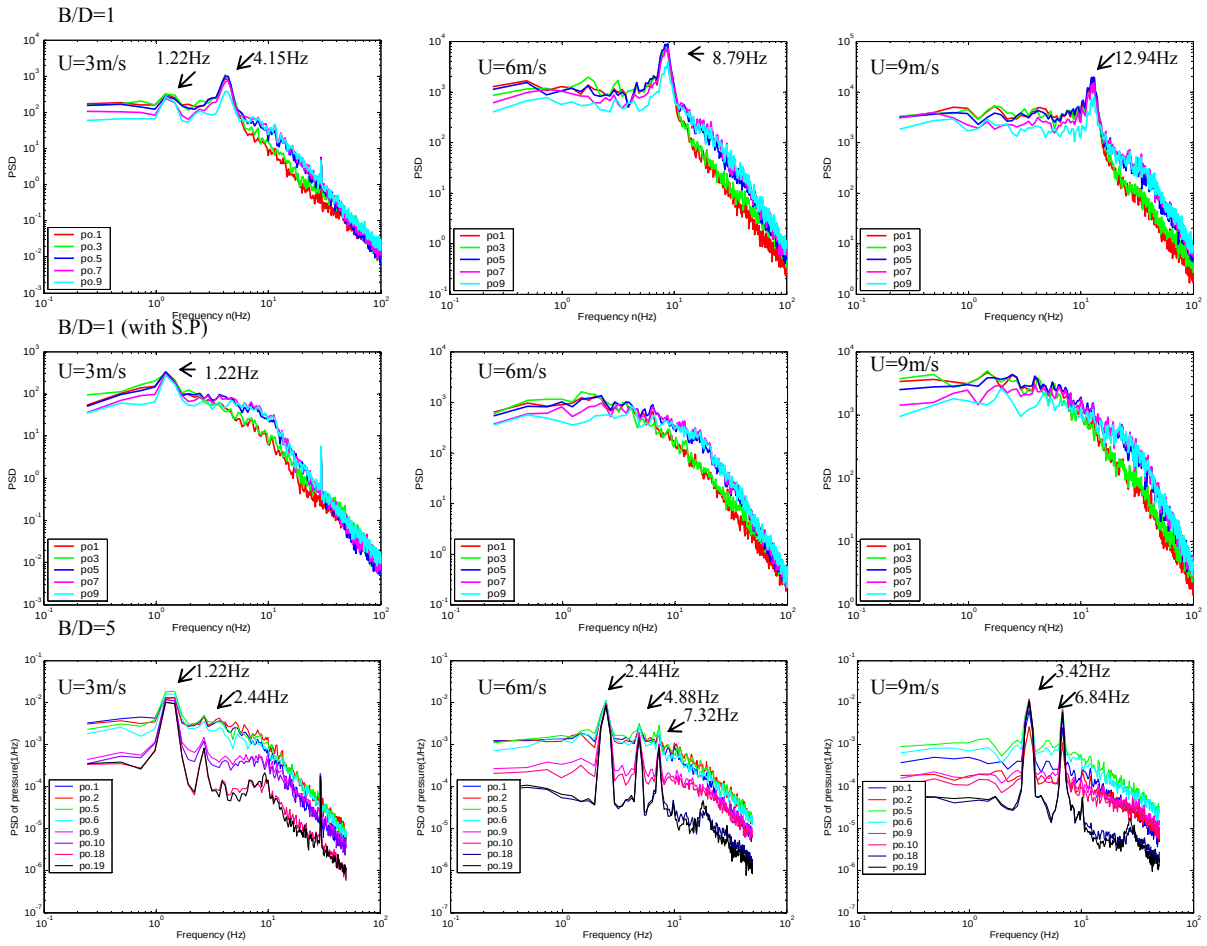

Fig. 6.4 Power spectra of fluctuating pressures at some chordwise positions [Matsumoto 2006]

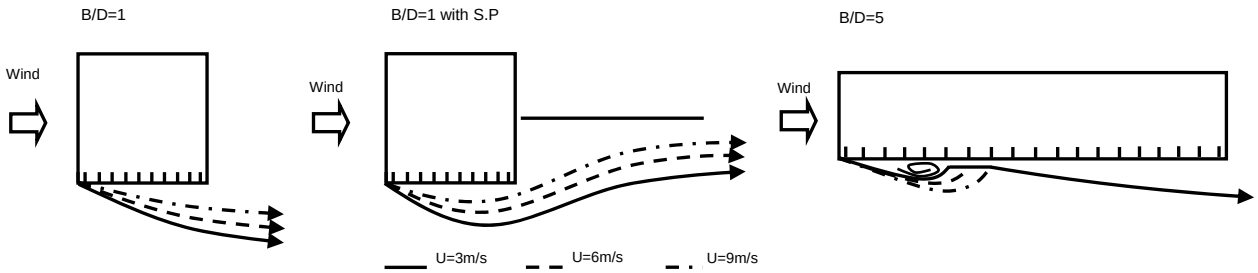

Fig. 6.5 Bluff body flow patterns around experimental models [Matsumoto, Shirato et al. 2006]

The bluff body flow patterns around three experimental models can be predicted as shown in Figure 6.5 (here flows on one surface are drawn).

6.9 Covariance matrix-branched proper orthogonal decomposition

Eigenvalues and eigenvectors (covariance modes) have been determined from covariance matrix of chordwise fluctuating pressures. Figure 6.6 shows first four covariance modes along chordwise positions at three turbulent flows case.

It is noted that all first modes look alike to the fluctuating pressure distributions (see with Figure 6.4).

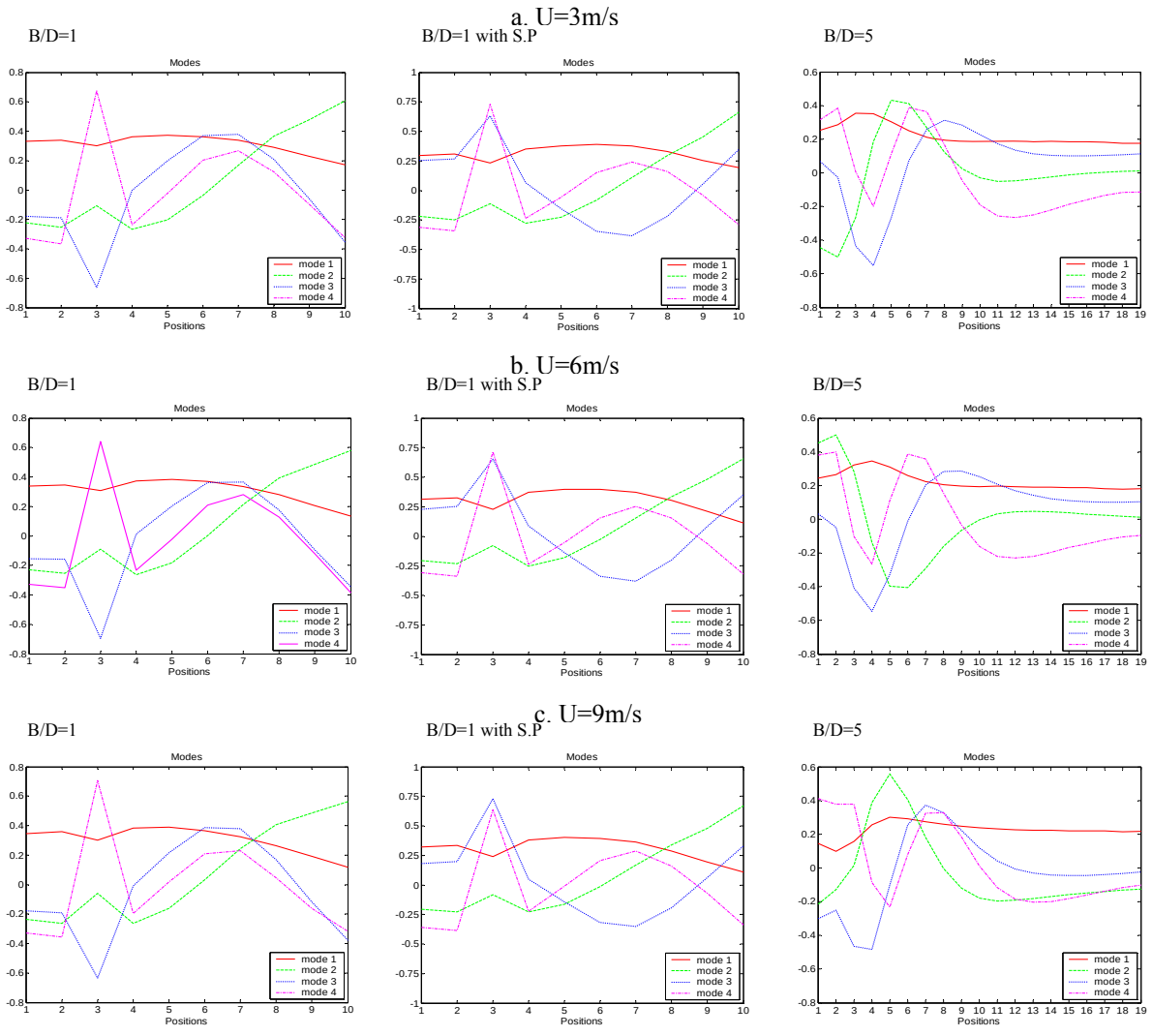

Fig. 6.6 First four covariance modes of experimental models at different turbulent flows

It is interesting in Figure 6.6 that all covariance eigenvectors (covariance modes) express almost the same shape and values, not to depend on the turbulent flow conditions, except the

second covariance mode in the model B/D=5 have changes its sign. Thus, it is appropriate to think that the low-order covariance modes can characterize and represent for any known physical cause, phenomenon as well as these dominant modes with the high energy contribution can be associated with any pattern of the bluff body flow on the model surface. However, it is impossible to identify the physical causes and the bluff body flow pattern from these dominant covariance modes without previous understanding and knowledge about physical causes or behavior of bluff body flows which have been studied from direct flow visualization techniques.

Tab. 6.1 Energy contribution of covariance modes (unit: %)

Mode	B/D=1			B/D=1 with S.P			B/D=5		
	3m/s	6m/s	9m/s	3m/s	6m/s	9m/s	3m/s	6m/s	9m/s
1	76.92	77.46	75.36	65.29	62.79	63.30	43.77	44.86	65.9
2	13.27	13.25	14.41	20.97	22.61	22.08	22.02	23.14	13.29
3	4.69	4.23	4.62	6.14	6.29	6.10	15.18	15.14	9.48
4	2.87	2.86	3.17	4.04	4.32	4.41	5.98	5.68	3.4
5	1.27	1.32	1.45	1.99	2.28	2.45	4.76	4.11	2.79

Energy contributions of the lowest five covariance modes of the fluctuating pressure fields corresponding to the three models and three turbulent flows are given in Table 6.1. Obviously, the first covariance mode contributes dominantly to the random pressure fields. The first covariance modes contribute 76.92%, 65.29%, 43.77% to total energy at the turbulent flow case 1; 77.46%, 62.79%, 44.86% at the flow case 2; 75.36%, 63.30%, 65.9% at the flow case 3 corresponding to three physical models: B/D=1, B/D=1 with the splitter plate and B/D=5, respectively. If the first two covariance modes are taken into account, the energy contribution of two covariance modes holds up to 90.19%, 86.26%, 65.79% of total energy at the flow case 1; 90.71%, 85.40%, 68.00% at the flow case 2; 89.77%, 85.38%, 79.19% at the flow case 3, corresponding to three above-mentioned models. In the other words, the first covariance modes contribute dominantly, and the first two modes contribute almost on the energy of the pressure fields. It is also seen that the energy contribution of the first covariance modes in the B/D=5 model is lower than those in the models B/D=1, thus it might be supposed that the contribution of the first modes reduce with more complicated expression of the pressure fields on surface.

a. U=3m/s

B/D=1 | B/D=1 with S.P | B/D=5

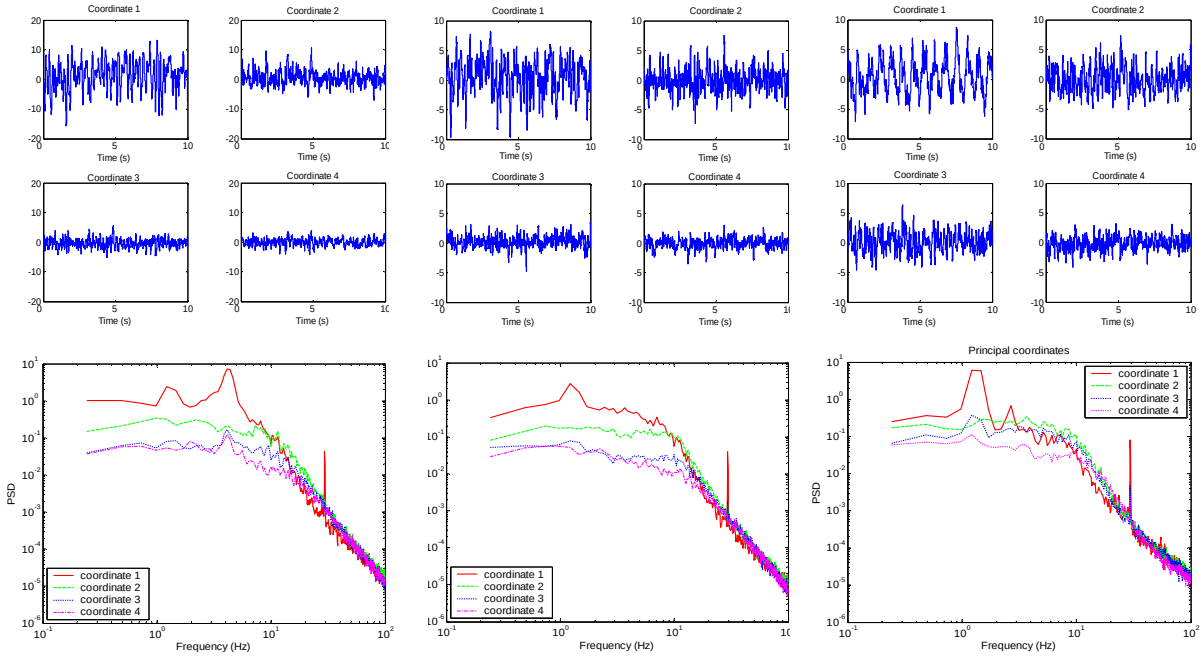

b. U=6m/s

B/D=1 | B/D=1 with S.P | B/D=5

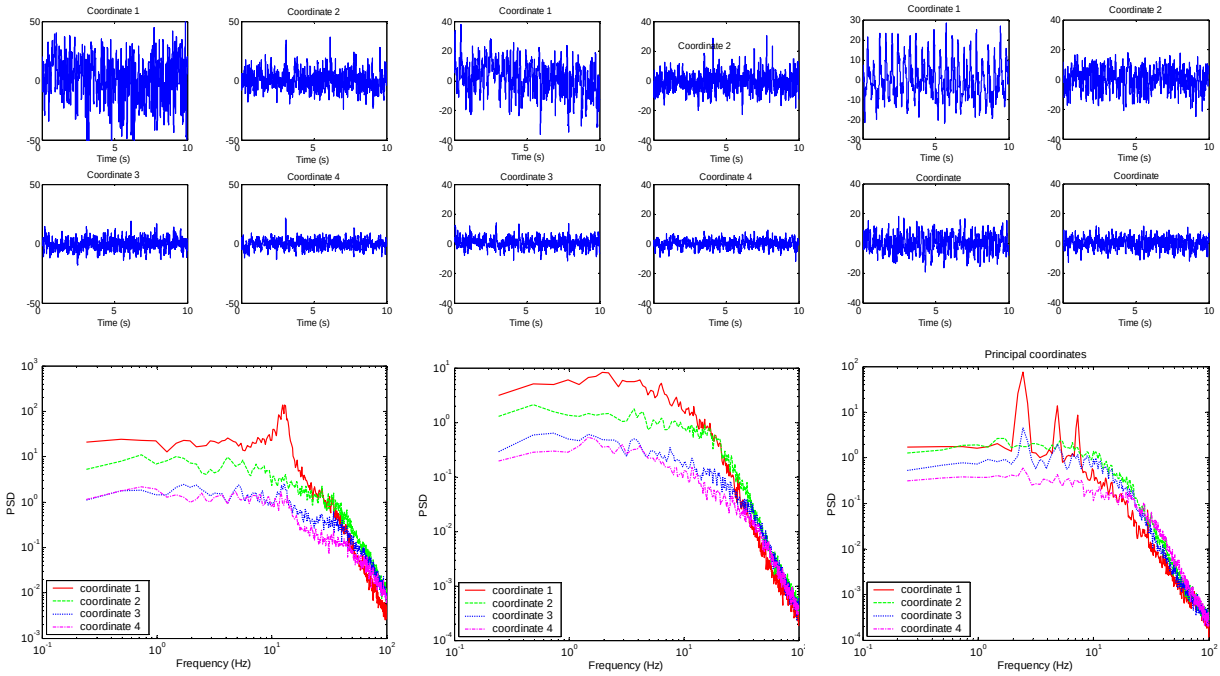

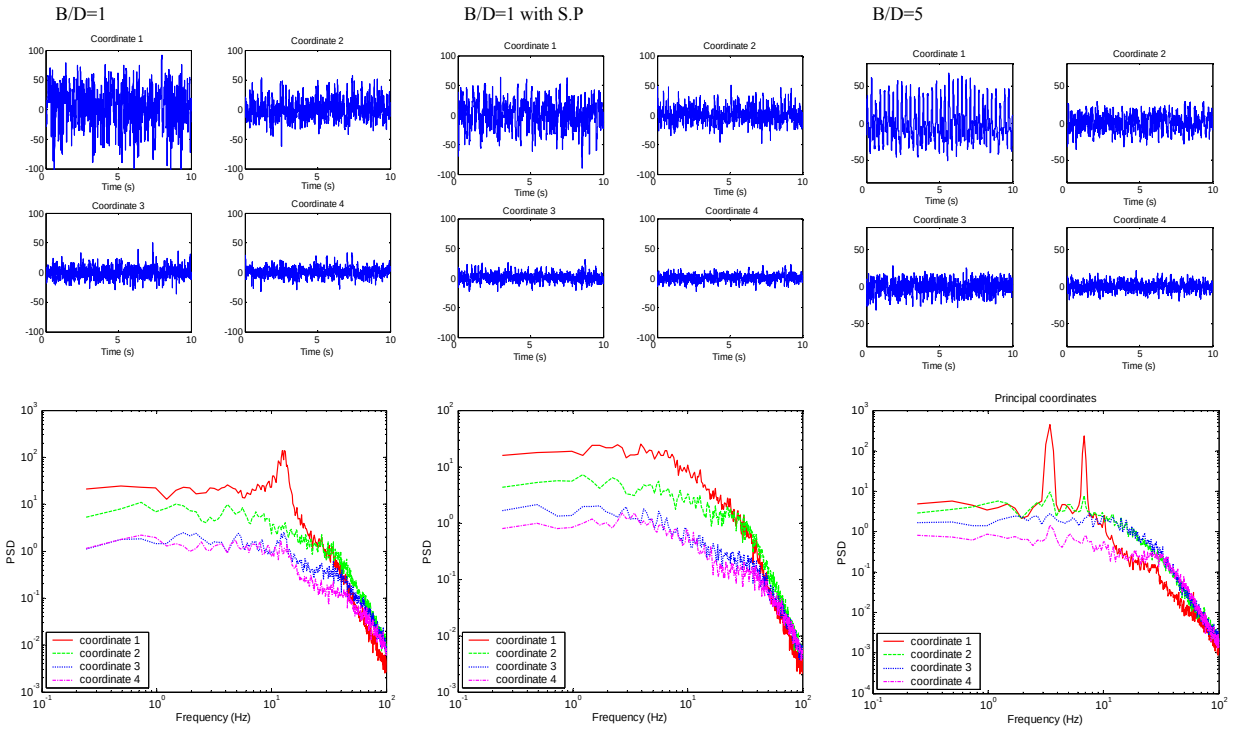

Fig. 6.7 First four principal coordinates and their corresponding power spectral densities at different flow conditions: a. U=3m/s, b. U=6m/s, c. U=9m/s

Covariance principal coordinates associated with the covariance modes to build up the original pressure field has been determined from the measured pressure data following Eq.(6.11). It is noted that the covariance principal coordinates are time-dependant uncorrelated processes. The first four covariance principal coordinates corresponding to the three physical models and three turbulent flows, and their power spectral densities are shown in Figure 6.7.

It is noteworthy that only the first and the second covariance principal coordinates express considerable amplitudes, whereas the amplitudes of the other coordinates are small and inconsiderable. In the aspect of power spectrum, furthermore, all the first covariance coordinates not only dominate in their power spectral densities but they also contain all frequency characteristics of the physical causes of the random pressure field, whereas the other coordinates do not contain these frequencies.

Thus, it can be commented that the first covariance modes and associated principal coordinates play important role in the description and identification of the random pressure field due to their dominant energy contribution and frequency containing of hidden physical events of the random pressure field.

6.10 Spectral matrix-branched proper orthogonal decomposition

Next, the proper orthogonal decomposition has been carried out in the spectral matrix branch. The three-dimensional frequency-dependant cross spectral matrix of the random pressure field has been formed, and the eigen problem of this cross spectral matrix has been solved to find out frequency-dependant spectral eigenvalues and spectral eigenvectors (or spectral modes). Figure 6.8 shows the first five spectral eigenvalues on frequency band 0÷50Hz at three flow cases and corresponding to three experimental models.

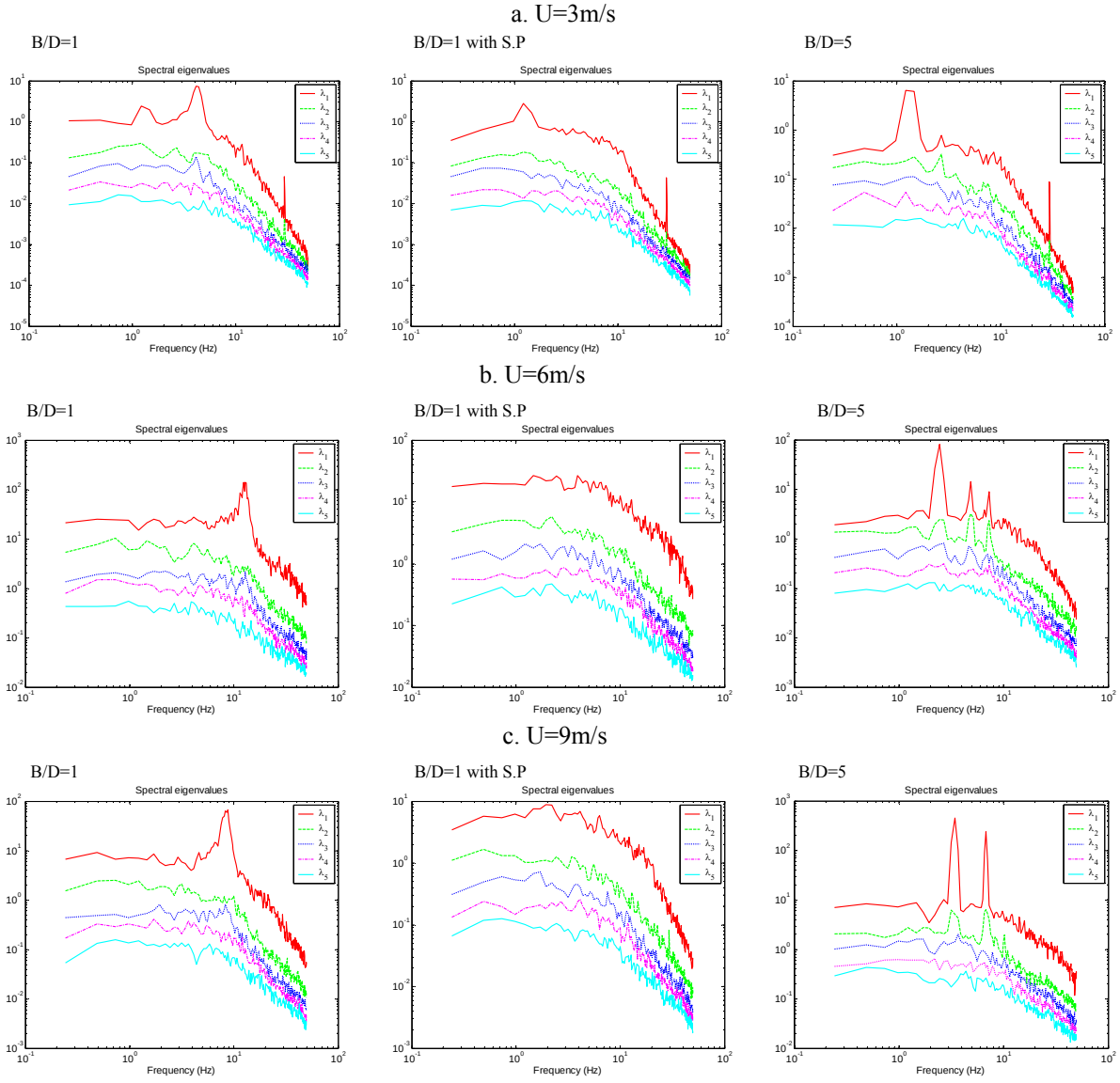

Fig. 6.8 First five spectral eigenvalues of experimental models at different turbulent flows: a. U=3m/s, b. U=6m/s, c. U=9m/s

As can be seen from Figure 6.8, all the first spectral eigenvalues corresponding to three experimental models and three flow conditions exhibit much dominantly than the others. Especially theses first spectral eigenvalues also contain all frequency peaks of the physical causes of the random pressure fields, whereas the others do not hold these frequency peaks.

Figures 6.9, 6.10 and 6.11 show the first three spectral modes of the pressure fields of the three models, which are associated with the spectral eigenvalues, corresponding to three turbulent flows, respectively. As can be seen, the spectral modes look alike corresponding to the order of modes at different turbulent flows. However, a linkage between the spectral modes and the physical cause on models is not clear.

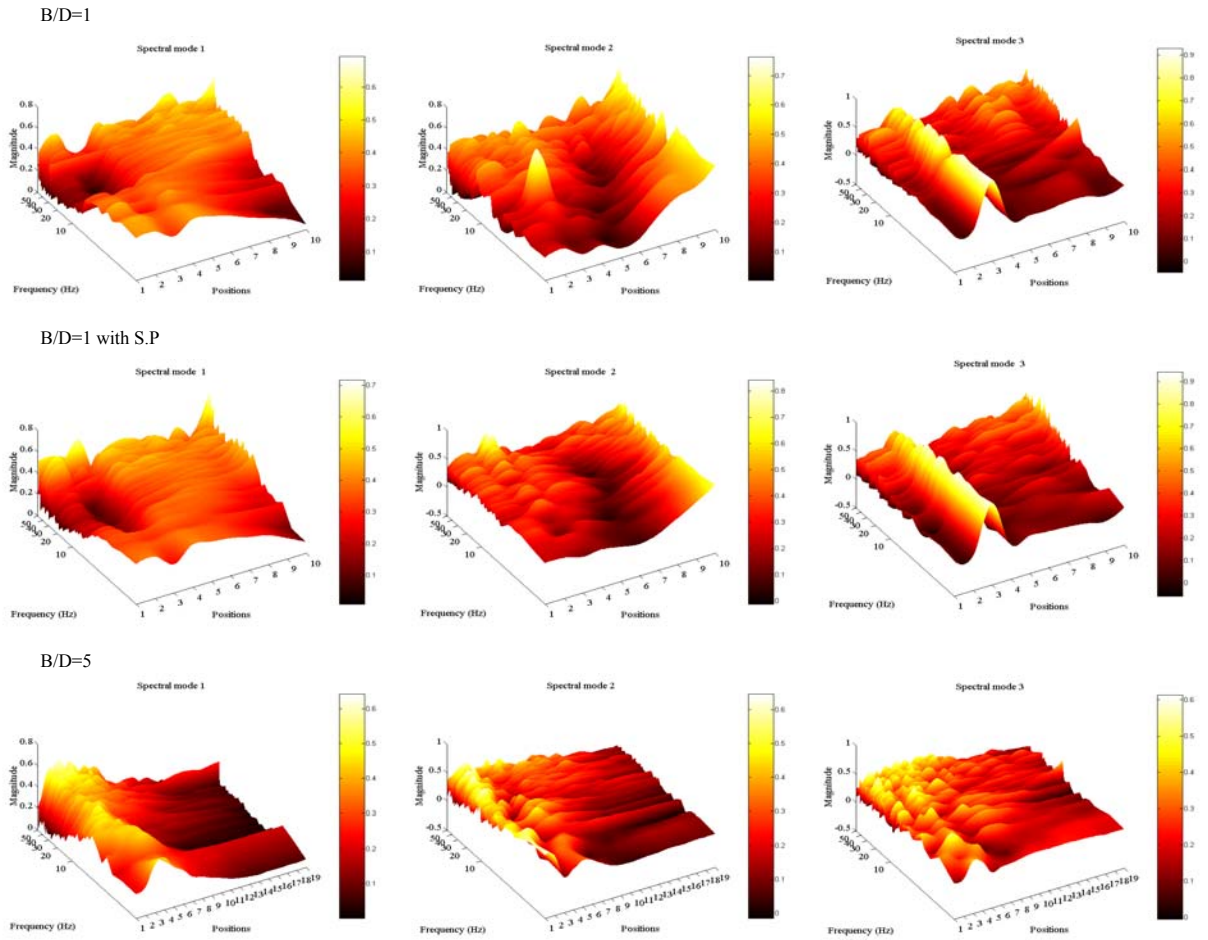

Fig. 6.9 First three spectral modes of experimental models at turbulent flow U=3m/s

B/D=1

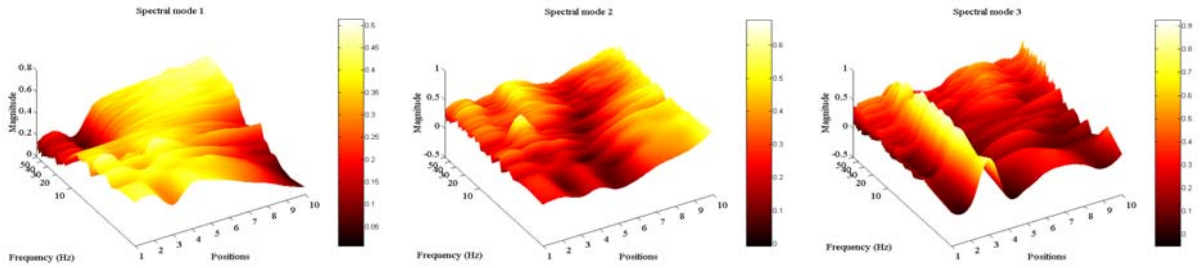

B/D=1 with S.P

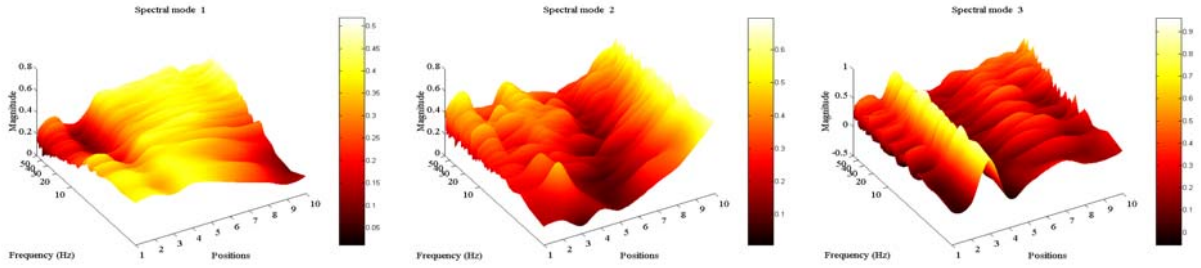

B/D=5

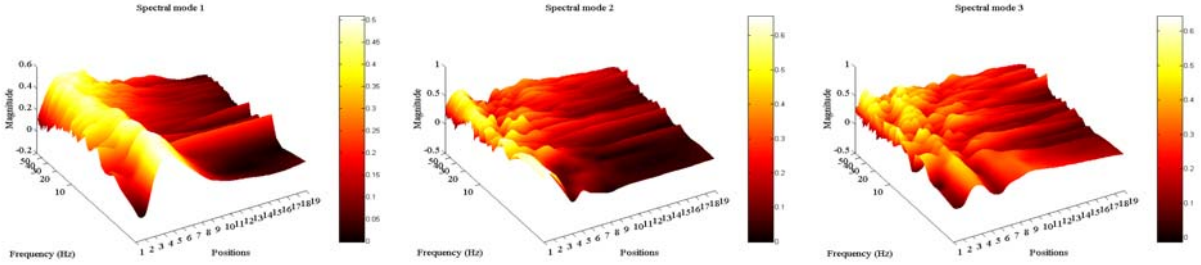

Fig. 6.10 First three spectral modes of experimental models at turbulent flow U=6m/s

B/D=1

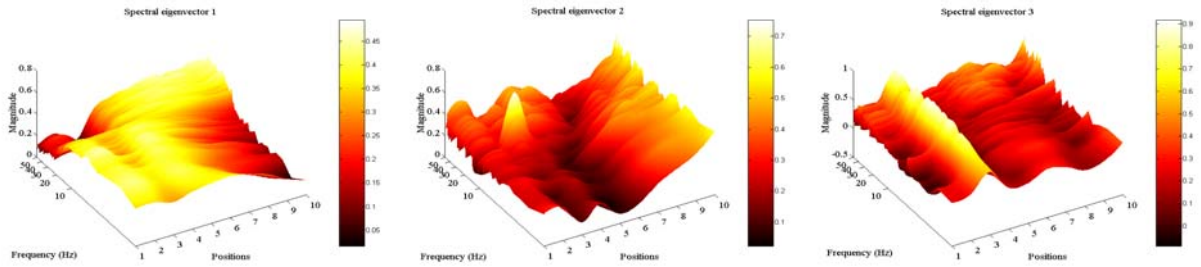

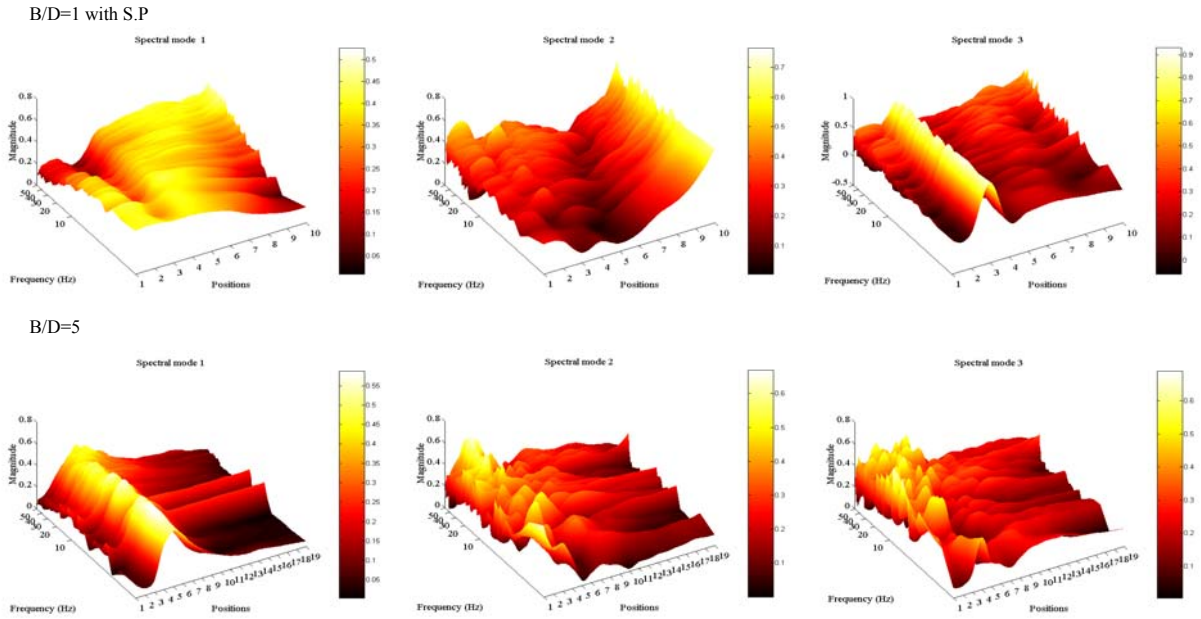

Fig. 6.11 First three spectral modes of experimental models at turbulent flow U=9m/s

Energy contributions in the percentage of the first five spectral eigenvalues and associated spectral modes corresponding to three models and three turbulent flows are given in Table 6.2 as below:

Tab. 6.2 Energy contribution of spectral modes (unit: %)

Mode	B/D=1			B/D=1 with S.P			B/D=5		
	3m/s	6m/s	9m/s	3m/s	6m/s	9m/s	3m/s	6m/s	9m/s
1	86.04	85.84	83.02	81.30	77.48	77.88	74.77	73.59	83.93
2	8.08	8.08	9.92	10.15	12.36	11.98	12.68	14.03	7.69
3	3.28	3.20	3.68	4.44	5.14	5.00	5.68	5.56	3.57
4	1.40	1.62	1.94	2.05	2.63	2.70	2.75	2.86	1.86
5	0.64	0.72	0.81	1.09	1.28	1.34	1.44	1.45	1.06

Similar to the covariance modes, the first spectral modes contribute dominantly on the energy of the pressure fields. Concretely, the first spectral modes contain 86.04%, 81.30%, 74.77%, respectively to the three experimental models at the turbulent flow U=3m/s; and 85.84%, 77.48%, 73.59% at the turbulent flow U=6m/s; and 83.02%, 77.88%, 83.93% at the turbulent flow U=9m/s. Thus, the first spectral modes dominate in the energy contribution at all three turbulent flows, this differs slightly from results of the covariance matrix analysis branch where the first

covariance mode reduce with more complicated distribution of the pressure fields as the case of model B/D=5. This suggests that the first spectral mode may express the better solution than the first covariance mode, because of higher energy contribution of the first spectral mode than the first covariance one. If the first two spectral modes are accounted, they contribute almost 94.12%,91.45%,87.45% on total energy of the pressure fields on three experimental models B/D=1, B/D=1 with splitter plate, B/D=5, respectively at the flow case 1; and 93.92%, 89.84%, 87.62% at the flow case 2; and 92.94%, 89.86%, 91.62% at flow case 3. In the other words, the first spectral modes contribute dominantly on energy of the pressure fields on all experimental models and at all three turbulent flows, moreover, the first two spectral modes contribute almost on the energy of these pressure fields.

6.11 Order-reduced modeling and reconstruction of pressure field

As above-mentioned, the original pressure fields can be reconstructed by using limited number of the low-order covariance modes or the low-order spectral modes. This simplified description is known as the order-reduced modeling of the random pressure field which has been applied for effectively modeling turbulent-induced buffeting forces and for effectively estimating gust responses of structures due to these buffeting forces. Effects of basic and cumulative modes on the pressure field reconstruction, as well as role of the first mode on the field identification are going to be verified and investigated here.

Figure 6.12 expresses the reconstruction of original fluctuating pressure at position 5 (near leading edge of models) corresponding to three models at the turbulent flow U=3m/s due to usage and contribution of the basic covariance modes (form the first covariance mode to the fourth covariance one). Figure 7.13 shows the pressure reconstruction at position 5 due to cumulative covariance modes using the first mode and the first two modes. Noting that only position 5 and at the flow case 1 are presented here on account of brevity, the another pressure positions on models and at the another flow conditions (U=6m/s, U=9m/s) have the same results. Verification in term of the spectral contribution between these covariance modes and the original pressure (as target) has been carried out.

As can be seen from Figure 6.12 that reconstructed pressure time series using the first mode is similar to the original pressure, especially its contribution portion contains the frequency peaks can be used to identify hidden characteristics and physical phenomena of the original pressure. In a comparison, reconstructed pressure portions using the second mode, the third mode, the fourth mode are minor contributions to the original pressure, moreover, these contribution portions do not contain the hidden frequency peaks in the original pressure.

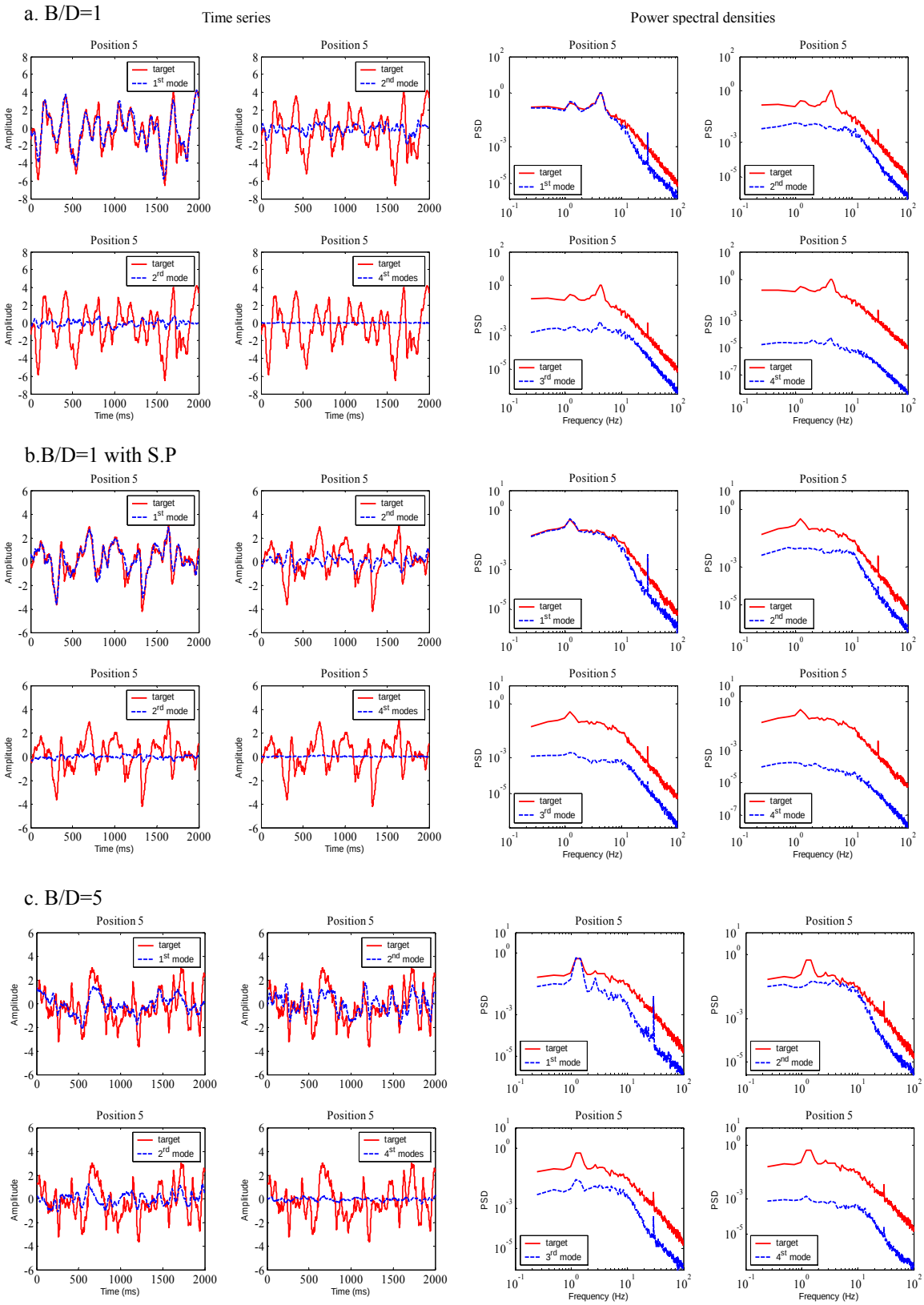

Fig. 6.12 Effect of covariance modes on pressure reconstruction at turbulent flow U=3m/s

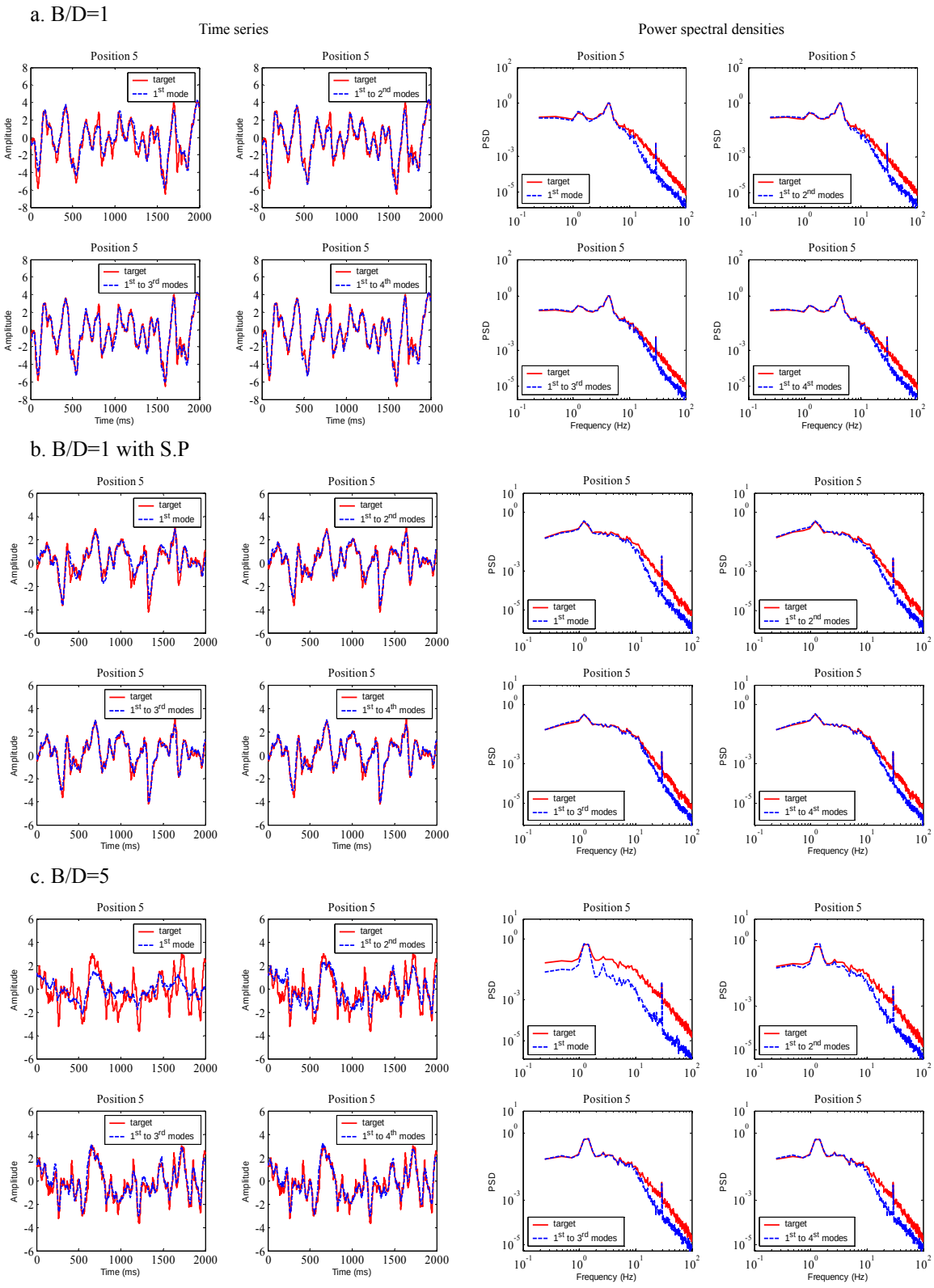

Fig. 6.13 Effect of cumulative covariance modes on pressure reconstruction at turbulent flow U=3m/s

It is also seen in Figure 6.12 in the power spectral densities, reconstructed pressure at the position 5 using the first covariance mode seems to be good agreement to the original pressure at low frequency range between 0÷10Hz in the models B/D=1 both without and with the splitter plate, but there is spectral difference between reconstructed pressure and original one at high frequency range 10÷100Hz. It implies that the first covariance mode is accuracy enough for reconstructing the original pressure at the low frequency range 0÷10Hz as well as for identifying the physical causes on all models, however, more cumulative covariance modes are required to reconstruct the original pressure at the high frequency range.

Although the reconstructed pressure due to the first covariance mode in all experimental models contain the typical frequencies of the physical causes, but it observes the first mode is not enough to reconstruct the original pressure in a case of the model B/D=5 because there is much difference in the power spectral contribution between its reconstructed pressure and the original one. This can be explained due to the energy contribution of the first covariance mode in the case of B/D=5 exhibits small proportion as 43.77% to total energy of the pressure field. In the model B/D=5, in the other words, the first mode can be used to identify the pressure field, but it is not accuracy enough to reconstruct the original pressure, and more low-order modes should be needed for the pressure reconstruction due to more complicated distribution of this pressure field.

In the Figure 6.13, the reconstructed pressures using number of the low-order covariance modes (the first mode, the first two modes, the first three modes and the first fourth modes) as well as their corresponding power spectral contributions are observed. It can be seen that the first covariance mode is enough to reconstruct the original pressure in the models B/D=1 without and with the splitter plate, but the first two modes should be needed in the model B/D=5. In the favorable condition, although all the first four covariance modes are used to reconstruct the original pressure, but it is only good agreement at the low frequency range, and it is not accuracy at the higher frequency range.

Figure 6.14 shows effects of basic spectral modes (basic four modes) and cumulative spectral modes (first mode and first two modes) on reconstructing auto spectra densities of the original pressures on all three experimental models at the reference position 5 and at the turbulent flow U=3m/s.

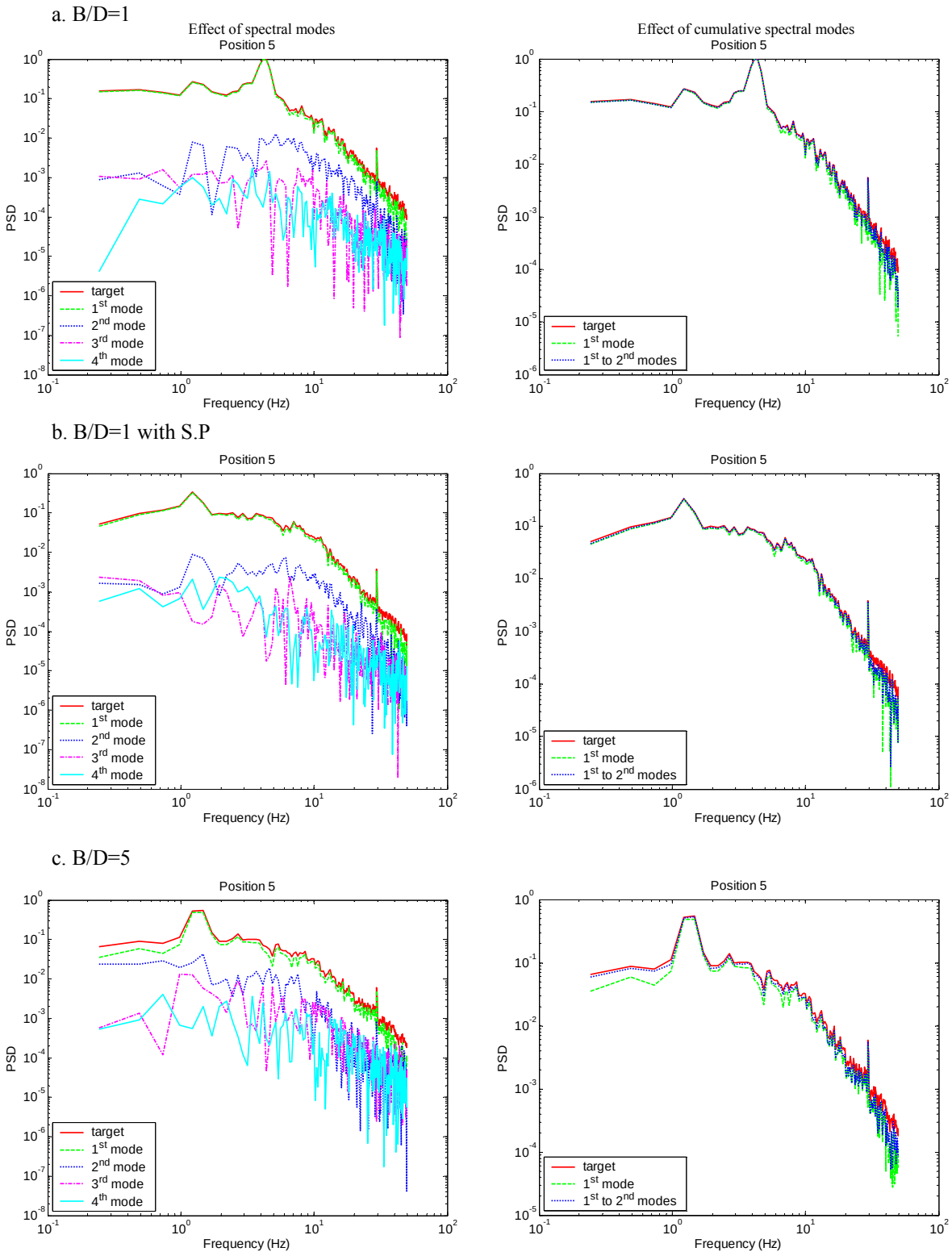

Fig. 6.14 Effects of basic and cumulative spectral modes on auto spectral reconstruction of pressure at turbulent flow U=3m/s

As can be seen from Figure 6.14, the first spectral modes also play very important role in the pressure reconstruction. Only the first spectral modes are enough for reconstruction and identification of the pressure fields. However, the first spectral modes exhibit the better than the first covariance ones in reconstructing the original pressure, because the good agreement at all frequency range can be observed with the first spectral modes whereas the good fit at the low frequency range with the first covariance one. This is very important to the first spectral mode rather than the first covariance one.

This agrees with the high energy contribution of the first spectral modes on the total energy of the pressure field at all experimental models and all turbulent flows.

6.12 Conclusion

Analysis and identification of the fluctuating pressure field around some typical rectangular sections using both the covariance matrix-based and spectral matrix-based proper orthogonal decompositions have been presented in this paper. Some points are concluded as follows:

(1) Significant role of the first covariance mode and the first spectral mode has been verified. The first mode contains certain frequency peaks of hidden physical phenomena, moreover, it contributes dominantly on the field energy. Thus the first mode is significant and accuracy enough to reconstruct and identify the pressure field for many cases.

(2) In cases of the high frequency range and of complicated pressure distributions and flows, it is suggested that more cumulative modes should be needed to reconstruct the pressure field. The more complicated the pressure field distributes and the bluff body flow behaviors, the less important the first mode contributes and the more cumulative modes are needed to reconstruct the pressure field.

(3) In the comparison, the first spectral mode expresses the better than the first covariance mode in reconstructing the pressure field.

(4) The linkage between the POD modes and physical events is valid only in the concrete cases when the pressure field behaviors simply and steadily as well as the physical events occur apparently. Because the POD modes, eigenvalues, principal coordinates modify sensitively with respect to pressure positions, pressure tap arrangements, measured region and area, so on, therefore it is supposed such linkage only can be obtained in some limited cases.

References

Berkooz, G., Holmes, P., Lumley, J.L. (1993), "The proper orthogonal decomposition in the analysis of turbulent flows", *Annu. Rev. Fluid Mech.*, **25**, 539-575.

Bienkiewicz, B., Tamura,Y., Ham, H.J., Ueda, H., Hibi, K. (1995), "Proper orthogonal decomposition and construction of multi-channel roof pressure", *J. of Wind Eng. Ind. Aerodyn.*, **54-55**, 369-381.

De Grenet, E.T., Ricciardelli, F., (2004), "Spectral proper transformation of wind pressure fluctuation: application to a square cylinder and a bridge deck", *J. of Wind Eng. Ind. Aerodyn.*, **92**, 1281-1297.

Holmes, J.D., Sankaran, R., Kwok, K.C.S., Syme, M.J. (1997), "Eigenvector modes of fluctuating pressures on low-rise building models", *J. of Wind Eng Ind. Aerodyn.*, **69-71**, 697-707.

Jeong, S.H., Bienkiewicz, B., Ham, H.J. (2000), "Proper orthogonal decomposition of building wind pressure specified at non-uniform distributed pressure taps", *J. of Wind Eng.Ind. Aerodyn.*, **87**, 1-14.

Kikuchi, H., Tamura, Y., Ueda, H., Hibi, K. (1997), "Dynamic wind pressure acting on a tall building model - Proper orthogonal decomposition", *J. of Wind Eng. Ind. Aerodyn.*, **69-71**, 631-646.

Lumley, J. L. (1970), *Stochastic tools in turbulence*, Academic Press.

Matsumoto, M., Yagi, T., Tsuboda, T., Lee, J.H., Hori, K., Kawashima, Y. (2006), "Study on unsteady pressure field around oscillatory rectangular cylinder B/D=4 using proper orthogonal decomposition", *Proc. the 4th Int'l Conference on Computational Wind Engineering (CWE4)*, Yokohama Japan, July 17-19.

Ruan, D., He, H., Castanon, D.A., Mehta, K.C. (2006), "Normalized proper orthogonal decomposition for building pressure data compression", *J. of Wind Eng. Ind. Aerodyn.*, Article in press.

Tamura, Y., Ueda, H., Kikuchi, H., Hibi, K., Suganuma, S., Bienkiewicz, B. (1997), "Proper orthogonal decomposition study of approach wind-building pressure correlation", *J. of Wind Eng. Ind. Aerodyn.*, **72**, 421-431.

Tamura, Y., Suganuma, S., Kikuchi, H., Hibi, K. (1999), "Proper orthogonal decomposition of random wind pressure field", *J. of Fluids and Structures*, **13**, 1069-1095.

Chapter 7

Representation and Simulation of Spatially-correlated Random Turbulent Field using Proper Transformations

7.1 Introduction

It is agreed that the analysis and experiment of the wind-induced vibration and response of structures always require a carefully modeling and representation of the wind turbulent field. The velocity field of the atmospheric wind is usually considered as unsteady one which comprise a time-independent mean velocity and three time-dependant fluctuating components, called as atmospheric turbulence, which are longitudinal, lateral and vertical turbulent components, respectively. It is the atmospheric turbulence to reason for generating aerodynamic phenomena, vibration and response of structures. So far, the atmospheric turbulence is defined as a zero-mean random Gaussian process. The spatial turbulent field is known as the typically coherent one in which turbulent time series at different spatial points are multi-variate and spatially-correlated in field space, moreover, the spatial correlation of the turbulent field can be characterized by either correlation coefficients in the time domain or coherence functions in the frequency one. Although each turbulent component is correlated itself, but the cross correlation between two turbulent components is usually omitted due to its small effect. In the other words, the longitudinal turbulence is uncorrelated with the lateral turbulence and the vertical one. Representation and modeling of the turbulent fields play very important role for both the analytical and experimental methods.

Because the turbulent wind fields are considered as the nature of randomness and spatial coherence, thus representation and modeling of these fields are usually expressed via the statistical functions. In the time domain, first-order statistical moments such as mean or expectation value; second-order statistical moments such as variance, mean square, correlation functions, correlation coefficients have been widely used. In the frequency domain, the second-order Fourier transform-based functions such as power spectral density functions and coherence function have been commonly applied. Furthermore, the multi-variate

spatially-correlated turbulent fields can be described comprehensively under matrix forms of either the zero-time-lag covariance matrix in the time domain or the cross spectral density matrix in the frequency domain in which cross correlation between two spatial points is accounted via either correlation coefficient function or coherence function.

Simulation of the turbulent fields is usually required for the wind-excited response analysis of structures in the time domain. It is generally agreed that the turbulent wind fields are usually considered as the multi-variate spatial-correlated stationary Gaussian random processes/ fields with zero mean. The Monte Carlo technique for generating random variables is the most widely employed to simulate the random processes/ fields in the scientific and engineering topics. Digital simulation of the random processes/ fields can be categorized by either spectral representation methods or time parametric methods.

Proper orthogonal decomposition, or the Karhunen-Loeve decomposition (Lumley 1970), has been applied widely in many scientific and engineering fields including random processes/fields, stochastic methods, numerical methods, image processing, data compression, system identification and control and so on. In the wind engineering, the proper orthogonal decomposition can be used to decompose and reconstruct the turbulent wind fields with new concept of order-reduced modeling. The advantage of the proper orthogonal decomposition is that the multi-variate correlated random processes/ fields can be described and represented by such simplified way as a combination of limited number of low-order orthogonal eigenvectors (or modes), which are determined as the modal decomposition (the eigen problem) from comprehensive matrix forms of the random field such as the zero-time-lag covariance matrix and the cross spectral matrix.

In this chapter, the representation, modeling and simulation of the multi-variate spatially-correlated turbulent field are going to be presented with emphasis on spectral representation methods using the proper orthogonal decomposition and its spectral proper transformation. Simulation of the multi-variate turbulent field along a bridge girder will be carried out as a numerical example.

7.2 Literature review on turbulent simulation

Simulation of the multi-variate spatially-correlated random turbulent field surrounding structures is usually required for evaluating the turbulent-induced forces and estimating the gust response in the time-domain analysis. Digital simulation of the random processes/ fields can be commonly branched in either the spectral representation methods or the time series parametric methods. In the both branches, the cross spectral density matrix of the random field has been usually used,

because it is the convenient way to build up this cross spectral matrix from available auto power spectral densities of single-variate turbulent processes and spatial coherence function which characterize for cross spatial correlation of the turbulent processes between two spatial points.

In the branch of the time series parametric representation methods, there are favorable techniques such as the auto-regressive technique (AR), moving-average technique (MA) and auto-regressive and moving average technique (ARMA). Auto-regressive and moving-average method has presented and developed recently by some authors as Samaras et al. 1985, Migolet et al. 1987, Li et al. 1990, Kareem et al. 1992, Meada et al. 1992.

The spectral representation methods have been widely applied so far due to direct approach of decomposition techniques of the cross spectral matrix of the random field. All spectral representation methods, moreover, depend on two decomposition techniques of the cross spectral density matrix through either the Cholesky decomposition (eg., Shinozuka and Jan 1972; Cao et al. 2000) or modal decomposition (eg., Shinozuka et al. 1990; Di Paola and Gullo 2001; Chen and Kareem 2005; Tubino and Solari 2005). In the former, the cross spectral matrix is decomposed by product of two lower triangle and upper triangular matrices, whereas the modal decomposition uses spectral eigenvectors (spectral modes) and spectral eigenvalues obtained from the spectral matrix-branched proper orthogonal decomposition in the later.

Shinozuka 1971 firstly introduced the simulation technique of the multi-variate Gaussian random processes which was developed from that of single-variate random process and based on the Cholesky decomposition of the cross spectral matrix of the random field. Simulation technique of the multi-variate Gaussian random processes was enhanced by using Fast Fourier Transform (FFT) discussed by Schuller and Shinozuka 1986, Shinozuka and Deodatis 1996. Simulation procedures of the multi-variate turbulent field around bridge girder were modified by Yang et al. 1997, Nguyen et al. 1999, Cao et al. 2000, however, they were based on the Cholesky decomposition of the cross spectral matrix. Shinozuka et al. 1990 proposed new approach of decomposition technique of the cross spectral matrix using some dominant eigenvectors determined from eigen problem of the cross spectral matrix. This technique was called as modal decomposition or modal factorization. This simulation method followed and developed by some authors such as Di Paola and Gullo 2001, Chen and Kareem 2005; Tubino and Solari 2005. Main advantage of using the spectral proper transformation in simulating the multi-variate random turbulent field is that only few number of the low-order dominant spectral modes and associated spectral eigenvalues is accuracy enough, moreover, the spectral modes and spectral eigenvalues contain their physical significance.

7.3 Representation and modeling of spatially-correlated turbulent field

7.3.1 *Mechanism of turbulent generation*

Mechanism of the turbulent generation is convincing to study the unsteady turbulent-induced forces (or buffeting forces), that relates to the oncoming flow characteristics, the wind-structure interaction of stationary or motioned structures in the atmospheric wind flows. The turbulent generation mechanism can explain spatial distribution of buffeting forces, correction functions such as the aerodynamic admittance function and coherence one. It is generally said that the uncertainties in the turbulent generation can induce limitations of the strip theory and quasi-steady theory and inaccuracy in the buffeting response as well. The turbulent flows can be generated from such following sources:

(1) *Due to oncoming turbulent flow*: Turbulence is as the nature of atmospheric wind. Atmospheric turbulence is generated by such main reasons as friction, terrain and topography, meteorological impacts such as atmospheric pressure, temperature and oceanic flows. Effect of the atmospheric wind on civil engineering structures usually behaviors under the law of the atmospheric boundary layer.

(2) *Due to wind-structure interaction*: Interaction phenomena due to separated and reattached flow and vortex shedding formation usually occur on structural surface of bluff bodies to modify around-structure flow (or bluff body flow). These interaction phenomena can generate turbulence in even ongoing smooth flow and modify turbulent conditions in the ongoing turbulent flow. Due to the movement of flexible structures such as long-span cable-supported bridges in the wind flows, furthermore, the wind-structure interaction relating to self-excited forces and aerodynamic damping can be generated structure-surrounding turbulence.

(3) *Due to wake response*: By effect of upstream structures, the oncoming flow creates and modifies wake turbulent flows to downstream structures. It is also known as the wake phenomena or signature, proximity.

Among above-mentioned sources of the turbulent generation, the turbulent flow generated by the wind-structure interaction is the most concern to the bluff sections. According to the Matsumoto (2000), moreover, in the bluff-body flow behaviors such as separation bubble, reattachment and vortex-shedding still occur whether or not oncoming flow is turbulence or smoothness due to the wind-structure interaction. This confirms that the wind-structure interaction and the bluff-body aerodynamics are convincing to explain the aerodynamic phenomena as well as to study the unsteady turbulent-induced forces.

7.3.2 *Turbulent wind field modeling*

The total wind velocity in the atmospheric wind fields at reference point M(x,y,z) due to approaching turbulent wind flow can be expressed by comprehensive manner as sum of mean velocity component and turbulent ones as follows (Tubino and Solari 2005):

$$U(x,y,z,t) = \overline{U}(x,y,z) + U^{'}(x,y,z,t) \tag{7.1}$$

where $\overline{U}(x,y,z), U^{'}(x,y,z,t)$: mean wind velocity and turbulent vectors corresponding to three directions: longitudinal (x), lateral (y) and vertical (z), which are represented as $\overline{U}(x,y,x) = \left\{\overline{U}(x,y,z),0,0\right\}^T$ and $U^{'}(x,y,z,t) = \left\{u(x,y,z,t), v(x,y,z,t), w(x,y,z,t)\right\}^T$

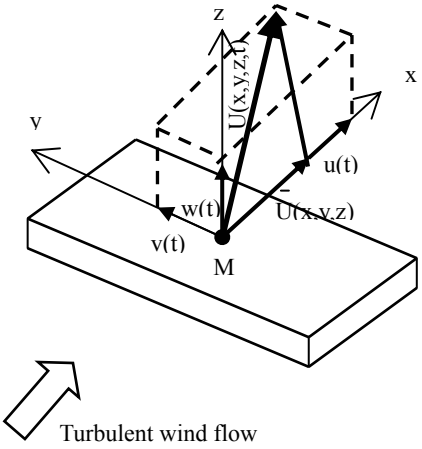

Fig. 7.1 Atmospheric wind field

Mean wind velocity is obtained due to the logarithmic law or power law in the atmospheric boundary layer theory as following formulae (Simiu and Scanlan 1976):

$$U(z) = \frac{1}{k} u_* \ln(\frac{z}{z_0}) \text{ (Logarithmic Law)} \tag{7.2-a}$$

$$U(z) = U_R(z_0)(\frac{z}{z_0})^{\alpha} \text{ (Power Law)} \tag{7.2-b}$$

where k: scale factor (k=0.4); z_0: roughness length depending on ground terrain condition (open terrain z_0=0.3m); u_*: shear or friction wind velocity: $u^{*2} = \sigma_u^2 / \beta_u$, $\beta_u = 4.4 \div 8.4$; $U_R(z_0)$: wind velocity recorded at reference altitude z_0, (in practical codes z_0=10m); α : terrain coefficient. Eq.(7.2-b) can be expressed an influence of terrain coefficient in the simplified exponential

formula:

$$U(z) = U_R(z_0)\ln(\frac{z}{z_0}) \tag{7.3}$$

The longitudinal and vertical turbulent components u(t), w(t) (lateral turbulent component v(t) is omitted due to very small effect to structure) are considered as two multi-variate spatially-correlated Gaussian random turbulent processes with zero mean. These turbulent fields at N discrete nodes are expressed as follows:

$$u(t) = \{u_1(t), u_2(t), \ldots, u_N(t)\}^T \tag{7.4}$$

$$w(t) = \{w_1(t), w_2(t), \ldots, w_N(t)\}^T \tag{7.5}$$

Because the turbulent field has its nature of random and coherent field, thus this field can be represented and modeled under conventionally statistical functions: first-order statistical moments such as mean or expectation value; second-order statistical moments such as variance, mean square, correlation functions, correlation coefficients in the time domain; or power spectral density functions, coherence function in the frequency domain.

7.3.3 *Power spectral density function of turbulence*

Energy contribution of any time series corresponding to spectral components in the frequency range is characterized by the power spectral density function as second-order Fourier transformation. Many empirical formulae can be applied for the auto power spectral densities of the longitudinal turbulence u(t) and the vertical one w(t). Von Karman 1948 firstly introduced a practical empirical formula of the auto power spectral density based on ongoing turbulent flow conditions such as mean velocity, intensities of turbulence, length scale of turbulence and so on. So far, methodology of von Karman has been exploited by some authors to develop their empirical formulae. Some empirical formulae are widely used for the auto power spectral densities of u-, w-turbulence $S_u(n)$, $S_w(n)$ in the practical application introduced hereafter (Simiu and Scanlan 1976, Matsumoto 2000):

Kaimal's, Bush and Panofsky' spectra:

$$S_u(n) = \frac{200 f u_*^2}{n(1+50f)^{5/3}};\quad S_w(n) = \frac{3.36 f u_*^2}{n(1+10f^{5/3})} \tag{7.6}$$

where f: non-dimensional Monin coordinates, $f = nz/U$; n: frequency variable (Hz); U, z: mean velocity (m/s) and altitude z (m), respectively; u*: friction or shear velocity (m/s), $u_* = kU/\ln(z/z_0)$, k, z_0: scale factor and roughness length (m).

Von Karman's spectra:

$$S_u(n)=\frac{4\sigma_u^2 L_{ux}/U}{\left[1+70.78\left(nL_{ux}/U\right)^2\right]^{5/6}};\quad S_w(n)=\frac{\left(2\sigma_w^2 L_{wx}/U\right)\left[1+188.8\left(nL_{wx}/U\right)^2\right]}{\left[1+70.78\left(nL_{wx}/U\right)^2\right]^{11/6}} \tag{7.7}$$

where σ_u, σ_w: standard derivatives; L_{ux}, L_{wx}: chordwise length scales of u-,w-turbulences.

It is supposed that von Karman's spectra express the better approach because of their dependence on basic configuration of the ongoing turbulent flow such as mean velocity (U), variances σ_u^2, σ_w^2, length scales L_{ux}, L_{wx}, but not on height z, whereas the Kaimal's, Bush-Panofsky's spectra only depend on mean velocity and height, but not on dimension of turbulence.

7.3.4 *Coherence function of turbulence*

The cross correlation in the space between two time series in the frequency domain is characterized by the spatial coherence function. The spatial coherence function between two processes $\upsilon_1(t)$ and $\upsilon_2(t)$ is defined as their cross spectral density normalized by their auto spectral ones as follows:

$$COH^2_{\upsilon_1\upsilon_2}(n,\Delta)=\frac{S^2_{\upsilon_1\upsilon_2}(n,\Delta)}{S_{\upsilon_1}(n)S_{\upsilon_2}(n)}=\frac{[S^{Co}_{\upsilon_1\upsilon_2}(n,\Delta)]^2+[S^{Qu}_{\upsilon_1\upsilon_2}(n,\Delta)]^2}{S_{\upsilon_1}(n)S_{\upsilon_2}(n)} \tag{7.8}$$

where $S^{Co}_{\upsilon_1\upsilon_2}(n,\Delta), S^{Qu}_{\upsilon_1\upsilon_2}(n,\Delta)$: co-spectrum and quadrature spectrum as real and imaginary parts of complex cross spectral density. In the homogenous turbulent flow, however, the quadrature spectrum is usually eliminated due to its less effect, we have:

$$COH^2_{\upsilon_1\upsilon_2}(n,\Delta)=\frac{[S^{Co}_{\upsilon_1\upsilon_2}(n,\Delta)]^2}{S_{\upsilon_1}(n)S_{\upsilon_2}(n)}\approx\frac{|S^2_{\upsilon_1\upsilon_2}(n,\Delta)|}{S_{\upsilon_1}(n)S_{\upsilon_2}(n)} \tag{7.9}$$

Spatial coherence functions are usually expressed under empirical formula as follows:

$$COH(n)=\exp(-nf) \tag{7.10}$$

where f: decay factor depending on spatial parameters, obtained as:

$$f=\frac{[c_x^2(x_1-x_2)^2+c_y^2(y_1-y_2)^2+c_z^2(z_1-z_2)^2]^{1/2}}{0.5[U(z_1)+U(z_2)]}=\frac{[c_x^2\Delta x^2+c_y^2\Delta y^2+c_z^2\Delta z^2]^{1/2}}{0.5[U(z_1)+U(z_2)]} \tag{7.11}$$

c_z, c_y: Exponent decay coefficients are experimentally determined; x_1, x_2, y_1, y_2, z_1, z_2: spatial coordinates of two points in the turbulent field corresponding to lateral (chordwise), longitudinal (spanwise), vertical directions in the structural axes $\Delta x=|x_1-x_2|, \Delta y=|y_1-y_2|, \Delta z=|z_1-z_2|$.

It is noted in almost practical cases, however, the length scale of turbulence in the chordwise

direction (L_{ux}, L_{wx}) is higher than structural width (B) and height (D), thus the buffeting forces are considered as fully-correlated coherence in the chordwise and vertical directions of structure, and only the cross correlation and the coherence of turbulence and buffeting forces in the spanwise direction is significant to be accounted for. It also assumed that the spanwise coherence of the longitudinal turbulence is similar to that of vertical one in many applications.

Some empirical coherence functions have been widely used for coherence of turbulence and introduced as follows (Davenport 1962, Irwin 1974, Simiu and Scanlan 1976, Matsumoto 2000, Larose 2001):

Davenport's empirical coherence:

$$COH_{\upsilon_1\upsilon_2}(n,\Delta y) = \exp\left(-c_y \frac{n\Delta y}{U}\right) \tag{7.12}$$

where c_y: decay factor in the spanwise direction, in which $8 \le c_y \le 16$, for example $c_{uy} = c_{wy} = 7$ (Davenport 1962), $c_{uy} = 10, c_{wy} = 6.5$ (Solari and Tubino 2005).

Von Karman's empirical coherence:

$$COH_u(n,\Delta y) = \frac{2}{\Gamma(5/6)}\left(\frac{\eta}{2}\right)^{5/6}\left\{K_{5/6}(\eta) - \frac{\eta}{2}K_{1/6}(\eta)\right\} \tag{7.13-a}$$

$$COH_w(n,\Delta y) = \frac{2}{\Gamma(5/6)}\left(\frac{\eta}{2}\right)^{5/6}\left\{K_{5/6}(\eta) + \frac{3(\Delta y k_1)^2}{3\eta^2 + 5(\Delta y k_1)^2}\eta K_{1/6}(\eta)\right\} \tag{7.13-b}$$

where $K_{1/6}, K_{5/6}$: modified Bessel function of the second kind; Γ: Gamma function; L_{uy}, L_{wy}: spanwise length scale of u-,w-turbulences; η: von Karman collapsing parameter defined as follows:

$$\eta = \left(\Delta y^2 k_1^2 + \frac{\Delta y^2}{L_{wy}^2}\right)^{1/2} = k_1 \Delta y \sqrt{1 + \frac{1}{k_1^2 L_{wy}^2}}, \quad k_1 = \frac{2\pi n}{U} \tag{7.14}$$

In the isotropic turbulent field, the modification of von Karman's coherence

$$COH_u(n,\Delta y) = 0.994\left\{\eta_u^{5/6} K_{5/6}(\eta_u) - \frac{\eta_u^{11/6}}{2}K_{1/6}(\eta_u)\right\} \tag{7.15-a}$$

$$COH_w(n,\Delta y) = 0.994\left\{\eta_w^{5/6} K_{5/6}(\eta_w) - \frac{\eta_w^{11/6}}{1+188.7(nL_{wy}/U)^2}K_{1/6}(\eta_w)\right\} \tag{7.15-b}$$

$$\eta_u = 0.747\frac{\Delta y}{4.5L_{uy}}\sqrt{1+70.8(\frac{nL_{uy}}{U})^2}, \quad \eta_w = 0.747\frac{\Delta y}{4.5L_{wy}}\sqrt{1+70.8(\frac{nL_{wy}}{U})^2} \tag{7.15-c}$$

It is also supposed that the von Karman's coherence model of turbulence seems the better expression than the Davenport's one, because this empirical formula is related to basic parameters of the ongoing turbulent flows as the length scales of turbulence

7.3.5 *Cross spectral matrix of the random turbulent fields*

As above-mentioned, the auto power spectral density function and spatial coherence one have been used to characterize for at any single point and correlation between two single points in the spatial field of turbulence in the frequency domain. Thus, one has used so-called cross spectral matrix to characterize for the spatial fields of turbulence in the frequency domain. The cross spectral density matrix of the N-variate turbulent field at N separated points is defined as:

$$S_{\upsilon}(n) = \begin{bmatrix} S_{\upsilon_1\upsilon_1}(n) & & \ldots & Sym. \\ S_{\upsilon_2\upsilon_1}(n) & S_{\upsilon_2\upsilon_2}(n) & \ldots & \\ \ldots & \ldots & \ldots & \ldots \\ S_{\upsilon_N\upsilon_1}(n) & S_{\upsilon_N\upsilon_2}(n) & \ldots & S_{\upsilon_N\upsilon_N}(n) \end{bmatrix} \tag{7.16}$$

where $S_{\upsilon}(n)$: cross spectral density matrix, known as positive-definite symmetrical squared one, in which elements ($S_{\upsilon_i\upsilon_i}(n), i = 1,...N$) in the main diagonal are auto spectral density functions at each point and elements ($S_{\upsilon_i\upsilon_j}(n), i \neq j,\ i, j = 1,...N$) outside the main diagonal are cross spectral ones between two points i and j; υ denotes to either longitudinal turbulence u(t) or vertical one w(t). Elements of the cross spectral matrix are determined as follows:

$$S_{\upsilon_i\upsilon_i}(n) = E\left[\hat{\upsilon}_i(n)\hat{\upsilon}_i(n)^{*T}\right],\ \ S_{\upsilon_i\upsilon_j}(n) = E\left[\hat{\upsilon}_i(n)\hat{\upsilon}_j(n)^{*T}\right] \tag{7.17}$$

where $\hat{\upsilon}_i(n), \hat{\upsilon}_j(n)$: Fourier transform functions of time series of turbulence at points i and j; E: expectation operator; *, T : complex conjugate and transpose operators.

In practical applications, however, it is difficult to obtain direct measurement of time series of turbulence at every point in the spatial field. Available empirical functions of the auto spectral density function at different points and available coherence function between two separated points are usually used to build up the cross spectral matrices of the turbulent fields. By this way, the cross spectral elements $S_{ij}(n)$ between two points i and j can be determined via the corresponding auto spectral ones and spatial coherence function as follows:

$$S_{\upsilon_i\upsilon_j}(n) = \sqrt{S_{\upsilon_i\upsilon_i}(n)S_{\upsilon_j\upsilon_j}(n)}COH_{\upsilon_i\upsilon_j}(n,\Delta) \tag{7.18}$$

where $S_{\upsilon_i\upsilon_i}(n), S_{\upsilon_j\upsilon_j}(n)$: auto spectral density functions at nodes i and j; $COH_{\upsilon_i\upsilon_j}(n)$: Coherence

function.

In many computational applications and simulation in the frequency domain, the cross spectral matrix of any field is usually used. However, it is difficult to exploit in such comprehensive form, thus decomposition techniques must be used to decouple this cross spectral matrix under form of expansion. The most applicable techniques to decouple this matrix are the Cholesky decomposition and modal one.

7.4 Proper orthogonal decomposition and spectral proper transformation

The spectral matrix-based orthogonal vectors are found as eigenvector solutions of the eigen problem from the cross spectral density matrix $S_\upsilon(n)$ of any multi-variate random field as follows:

$$S_\upsilon(n)\Psi_\upsilon(n) = \Lambda_\upsilon(n)\Psi_\upsilon(n) \tag{7.19}$$

where $S_\upsilon(n)$: cross spectral density matrix; $\Lambda_\upsilon(n), \Psi_\upsilon(n)$: spectral eigenvalue and eigenvector matrices $\Lambda_\upsilon(n) = diag(\lambda_{\upsilon 1}(n), \lambda_{\upsilon 2}(n), ...\lambda_{\upsilon N}(n))$, $\Psi_\upsilon(n) = [\psi_{\upsilon 1}(n), \psi_{\upsilon 2}(n), ...\psi_{\upsilon N}(n)]$. It is noted that spectral eigenvalues are real and positive, its spectral eigenvectors (also called as spectral modes) are generally complex, however, if cross spectral matrix is real then spectral modes are also real ones. The spectral eigenvalues and the spectral modes satisfy such orthogonal conditions as follows:

$$\Psi_\upsilon^{*T}(n)\Psi_\upsilon(n) = I;\ \Psi_\upsilon^{*T}(n)S_\upsilon(n)\Psi_\upsilon(n) = \Lambda_\upsilon(n) \tag{7.20}$$

Accordingly, the Fourier transform and the cross spectral density matrix of $\upsilon(t)$ can be represented as optimum approximation due to terms of the spectral eigenvalues and eigenvectors as follows:

$$\hat{\upsilon}(n) = \Psi_\upsilon(n)\hat{y}_\upsilon(n) \approx \sum_{j=1}^{\hat{M}} \psi_{\upsilon j}(n)\hat{y}_{\upsilon j}(n) \tag{7.21-a}$$

$$S_\upsilon(n) = \Psi_\upsilon(n)\Lambda_\upsilon(n)\Psi_\upsilon^{*T}(n) \approx \sum_{j=1}^{\hat{M}} \psi_{\upsilon j}(n)\lambda_{\upsilon j}(n)\psi_{\upsilon j}^{*T}(n) \tag{7.21-b}$$

where $\hat{\upsilon}(n)$: Fourier transform of process $\upsilon(t)$; $\hat{y}_\upsilon(n)$: spectral principal coordinates as Fourier transforms of uncorrelated random subprocesses; $\hat{M}$: number of truncated spectral modes ($\hat{M} << N$); * denotes to complex conjugate operator. Frequency-domain approximation in Eq.(7.15) is also known as spectral proper transformation (SPT).

The spectral principal coordinates have some characteristics as follows:

$$E\left[\hat{y}_{\upsilon j}(n)\hat{y}_{\upsilon i}(n)^T\right] = \delta_{ji},\ E\left[\hat{y}_{\upsilon j}^2(n)\right] = \lambda_{\upsilon j}(n) \tag{7.22}$$

Thus, when two effective random turbulent fields of the longitudinal and vertical turbulent

components u(t), w(t) are taken into account, the Fourier transform vectors or spectral density matrix of the two turbulent fields can be approximated due to the spectral proper transformation as follows:

$$\hat{u}(n) = \Psi_u(n)\hat{y}_u(n) \approx \sum_{j=1}^{\hat{M}} \psi_{uj}(n)\hat{y}_{uj}(n)\,; \quad S_u(n) = \Psi_u(n)\Lambda_u(n)\Psi_u^{*T}(n) \approx \sum_{j=1}^{\hat{M}} \psi_{uj}(n)\lambda_{uj}(n)\psi_{uj}^{*T}(n) \quad (7.23\text{-a})$$

$$\hat{w}(n) = \Psi_w(n)\hat{y}_w(n) \approx \sum_{j=1}^{\hat{M}} \psi_{wj}(n)\hat{y}_{wj}(n)\,; \quad S_w(n) = \Psi_w(n)\Lambda_w(n)\Psi_w^{*T}(n) \approx \sum_{j=1}^{\hat{M}} \psi_{wj}(n)\lambda_{wj}(n)\psi_{wj}^{*T}(n) \quad (7.23\text{-b})$$

These approximations of the spectral proper transformation will be used for simulating the turbulent fields hereafter.

7.5 Turbulent simulation procedures

7.5.1 *Turbulent simulation using Cholesky decomposition*

Here comprehensive form of the cross spectral matrix of the multi-variate turbulent field is decomposed by the Chelesky's factorization technique in which this cross spectral matrix is factorized by product between the lower triangle matrix and upper triangle one as follows:

$$S_\upsilon(n) = H_\upsilon(n)H_\upsilon(n)^{*T} \quad (7.24\text{-a})$$

$$H_\upsilon(n) = \begin{bmatrix} H_{\upsilon_1\upsilon_1}(n) & & \ldots & 0 \\ H_{\upsilon_2\upsilon_1}(n) & H_{\upsilon_2\upsilon_2}(n) & \ldots & \\ \ldots & & & \\ H_{\upsilon_N\upsilon_1}(n) & H_{\upsilon_N\upsilon_2}(n) & \ldots & H_{\upsilon_N\upsilon_N}(n) \end{bmatrix} \quad (7.24\text{-b})$$

where $H_\upsilon(n)$: complex lower triangle matrix.

The multi-variate random turbulent field can be expressed in the frequency domain using the factorized lower triangle matrix as follows:

$$\upsilon_j(t) = \sqrt{2(\Delta n)}\sum_{k=1}^{j}\sum_{l=1}^{\tilde{N}} |\, H_{\upsilon_j\upsilon_k}(n_{kl})\,| \cos(2\pi n_{kl}t - \theta_{jl}(n_{kl}) + \phi_{kl}) \quad (7.25)$$

where j: index of structural node; k: index of moving node; l: index of moving point in frequency range; $\tilde{N}$: number of frequency intervals; Δn : frequency interval $\Delta n = n_{up}/\tilde{N}$; n_{up} : upper cutoff frequency; n_{kl} : frequency point on frequency range $n_{kl} = (l-1)\Delta n + k\Delta n/N$; $H_{\upsilon_j\upsilon_k}(n_{kl})$: element of complex lower-triangle matrix; $\theta_{jl}(n_{kl})$: complex phase angle of $H_{\upsilon_j\upsilon_l}(n_{kl})$; ϕ_{kl} : random phase angles, uniformly distributed over [0,2π] as $\theta_{jl}(n_{kl}) = \tan^{-1}\dfrac{\mathrm{Im}(H_{\upsilon_j\upsilon_l}(n_{kl}))}{\mathrm{Re}(H_{\upsilon_j\upsilon_l}(n_{kl}))}$, which

are generated by Monte Carlo technique.

Elements in the complex lower triangle matrix $H_{\upsilon}(n)$ can be calculated in the practical form of the turbulent field around bridges in cases of deck nodes spaced in similar distance and similar elevation as follows (Cao et al. 2000):

$$H_{\upsilon_i\upsilon_j}(n)=\begin{cases}0 & when\ 1\le i<j\le N\\ \sqrt{S_{\upsilon_i\upsilon_j}(n)}COH^{|i-j|} & when\ \ j=1\\ \sqrt{S_{\upsilon_i\upsilon_j}(n)}COH^{|i-j|}\sqrt{1-C^2} & when\ 2\le j\le i\le N\end{cases} \tag{7.26}$$

where $S_{\upsilon_j\upsilon_j}(n)$: auto spectral density function of subprocess υ at node j; N: number of deck nodes; C: spanwise coherence function between two adjacent nodes.

In many cases, the cross spectral matrix is real (phase lags are negligible), thus the lower triangle matrix is real too, therefore phase $\theta_{jl}(n_{kl})=0$, thus spectral matrix-based simulation of single-variate turbulent subprocess in the multi-variate random turbulent field is determined as:

$$\upsilon_j(t)=\sqrt{2(\Delta n)}\sum_{k=1}^{j}\sum_{l=1}^{\tilde{N}}\left|\sqrt{S_{\upsilon_j\upsilon_j}(n)}G_{jk}(n_{kl})\cos(2\pi n_{kl}t+\phi_{kl})\right. \tag{7.27}$$

7.5.2 *Turbulent simulation using spectral proper transformation*

Simulation of the multi-variate random turbulent process using spectral representation method is widely used so far and will be presented here, in which the cross spectral matrix is decomposed by the proper spectral transformation. Accordingly, the N-variate random turbulent process $\upsilon(t)=\{\upsilon_1(t),\upsilon_2(t),...,\upsilon_N(t)\}^T$ can be represented (Di Paola and Gullo 2001; Chen and Kareem 2005; Tubino and Solari 2005):

$$\upsilon(t)=\int_{-\infty}^{\infty}\exp(i2\pi nt)dB_{\upsilon}(n) \tag{7.28}$$

where $B_{\upsilon}(n)=\{B_{\upsilon_1}(n),B_{\upsilon_2}(n),...,B_{\upsilon_N}(n)\}$: mean-zero uncorrelated orthogonal increment process satisfying as $E\lfloor dB_{\upsilon_i}(n)\rfloor=0$, $dB_{\upsilon_i}(n)=dB_{\upsilon_i}(n)^*$, $E\lfloor dB_{\upsilon_i}(n_m)dB_{\upsilon_j}(n_k)^{*T}\rfloor=\delta_{ij}\delta_{mk}S_{\upsilon}(n)dn$; $S_{\upsilon}(n)$: cross spectral matrix.

Using the spectral proper transformation Eq.(13) to decompose and approximate the cross spectral matrix $S_{\upsilon}(n)=\sum_{j=1}^{N}S_{Y_j}(n)=\Psi_{\upsilon}(n)\Lambda_{\upsilon}(n)\Psi_{\upsilon}^{*T}(n)\approx\sum_{j=1}^{\hat{N}}\psi_{\upsilon_j}(n)\lambda_{\upsilon_j}(n)\psi_{\upsilon_j}^{*T}(n)$, the multi-variate random turbulent process can be decomposed and approximated by summation of $\hat{N}$ N-variate

processes independent orthogonal:

$$\upsilon(t) = \sum_{j=1}^{\hat{N}} Y_{\upsilon_j}(t) = \sum_{j=1}^{\hat{N}} \left(\int_{-\infty}^{\infty} \psi_{\upsilon_j}(n) \sqrt{\lambda_{\upsilon_j}(n)} \exp(i2\pi nt) dn \right) \tag{7.29}$$

Subprocesses of the N-variate random turbulent process $\upsilon(t)$ can be simulated in the discrete frequency domain as:

$$\upsilon_i(t) = 2 \sum_{j=1}^{\hat{N}} \sum_{l=1}^{\overline{N}} \psi_{\upsilon_j}(n_l) \sqrt{\lambda_{\upsilon_j}(n_l) \Delta n_l} \exp(i2\pi n_l t) \tag{7.30}$$

where i: index of simulated subprocess; j: index of spectral modes; l: index of frequency points; n_l: frequency value at moving point l; $\overline{N}$: number of frequency intervals; n_l: frequency interval at moving point l.

If the frequency domain is discretized constantly at every frequency interval Δn, then the Eq.(7.29) can be expanded as follows:

$$\upsilon_i(t) = 2\sqrt{\Delta n} \sum_{j=1}^{\hat{N}} \sum_{l=1}^{\overline{N}} \psi_{\upsilon_j}(n_l) \sqrt{\lambda_{\upsilon_j}(n_l)} \cos(2\pi n_l t + \theta_{\upsilon_j}(n_l) + \phi_l) \tag{7.31}$$

where Δn_l: frequency interval at point *l;* Δn: constantly frequency interval $\Delta n = n_{up} / \overline{N}$ and $n_l = (l-1)\Delta n$, n_{up}: upper cut-off frequency; ϕ_l: phase angle considered as random variable uniformly distributed over [0,2π]; $\theta_{\upsilon_j}(n_l)$: phase angle of complex eigenvector $\psi_{\upsilon_j}(n_l) = |\psi_{\upsilon_j}(n_l)| \exp(i\theta_{\upsilon_j}(n_l))$, determined as:

$$\theta_{\upsilon_j}(n_l) = \tan^{-1} \frac{\mathrm{Im}\left(\psi_{\upsilon_j}(n_l)\right)}{\mathrm{Re}\left(\psi_{\upsilon_j}(n_l)\right)} \tag{7.32}$$

In many cases, the spectral eigenvectors are real due to auto spectral densities are real and positive, Eq.(7.30) can be simplified as follows:

$$\upsilon_i(t) = 2\sqrt{\Delta n} \sum_{j=1}^{\hat{N}} \sum_{l=1}^{\overline{N}} \psi_{\upsilon_j}(n_l) \sqrt{\lambda_{\upsilon_j}(n_l)} \cos(2\pi n_l t + \phi_l) \tag{7.33}$$

The phase angles can be randomly generated using the Monte Carlo technique. This technique also is considered as the random phase generation to defer from the random amplitude generation.

More details on recent applications of the proper orthogonal decomposition in simulating multi-variate turbulent process, including parametric time representation methods using autoregressive (AR) model can refer to Di Paola and Gullo 2002; Chen and Kareem 2005; Tubino and Solari 2005.

7.6 Numerical example

In this numerical example, the spectral proper transformation has been applied to simulate the two multi-variate turbulent fields at 30 discrete nodes along a bridge deck: $u(t) = \{u_1(t), u_2(t), ..., u_{30}(t)\}^T$, $w(t) = \{w_1(t), w_2(t), ..., w_{30}(t)\}^T$. Time series of the turbulent fields at 30 nodes have been simulated at different mean velocities U=5,10,20,30 and 40m/s. Sampling rate of simulated turbulent time series is 1000Hz for total time interval 100 seconds. Time interval is set at 0.001 second. The cross spectral density matrices of u-,w-turbulences have been formulated based on auto spectral densities and spanwise coherence function. Targeted auto power spectral density functions of u-, w-components are used the Kaimail's and Panofsky's spectral models in Eq(7.6). Coherence function between two separated nodes along bridge deck, moreover, is used by exponentially empirical model in Eq.(7.12) with decay factors $c_{uy} = 10, c_{wy} = 6.5$.

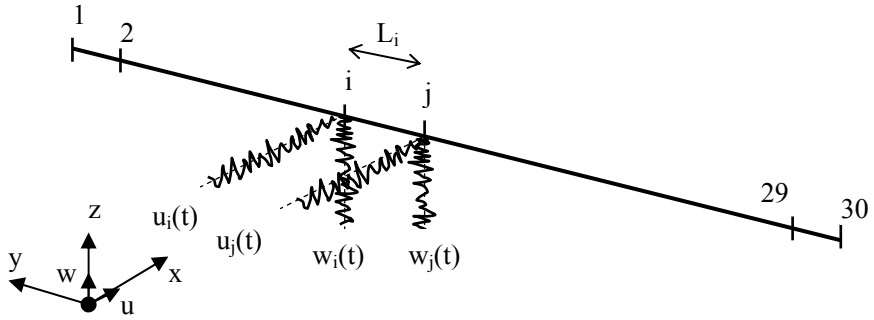

Fig. 7.2 Effective turbulent fields at bridge deck nodes

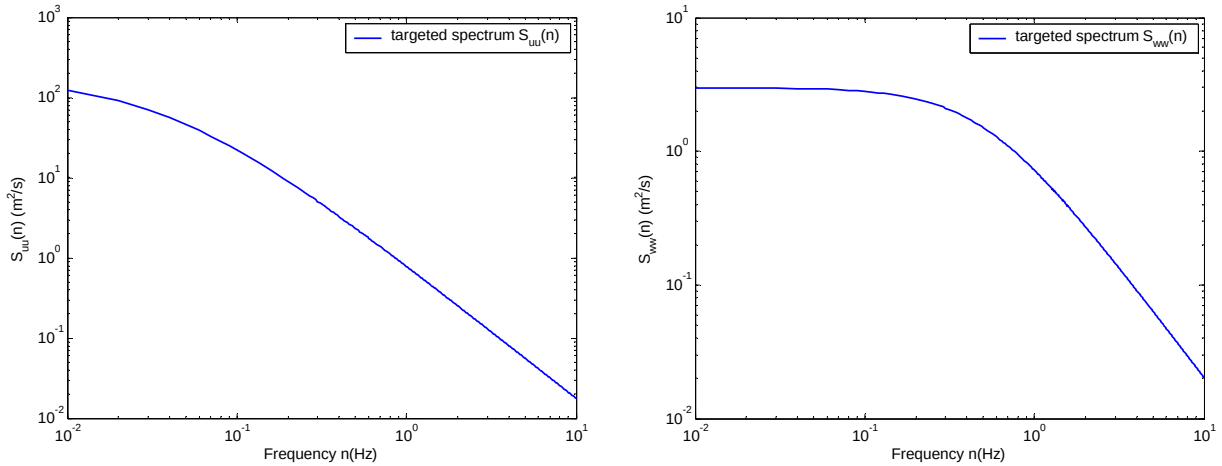

Fig. 7.3 Auto power spectral densities of u-,w-turbulences corresponding to mean velocity U=20m/s

Figure 7.3 shows targeted auto spectral density functions of u-,w-turbulences at mean velocity U=20m/s and in frequency range 0.01÷10Hz with some input parameters such as deck height z=20m, scale factor k=0.4, roughness length z_0=0.025m.

Cross spectral matrices $S_u(n)$, $S_w(n)$ of two turbulent fields u(t), w(t) at the 30 deck nodes have been formulated as 30x30 symmetrical squared matrices. It is noted that the cross spectral matrices comprise three dimensions, in which the third one represents for the frequency domain and all spectral elements at i-th row represent for auto spectral density at the node i and cross spectral ones between the node i and adjacent nodes. Figure 7.4 shows spatial distribution of the power spectral densities of w-turbulence at different nodes 3, 5, 10 and 15. As can be seen that the power spectral densities at i-th node distribute dominantly around this i-th node, and it decays fast with respect to an increases of frequencies and spatial distances.

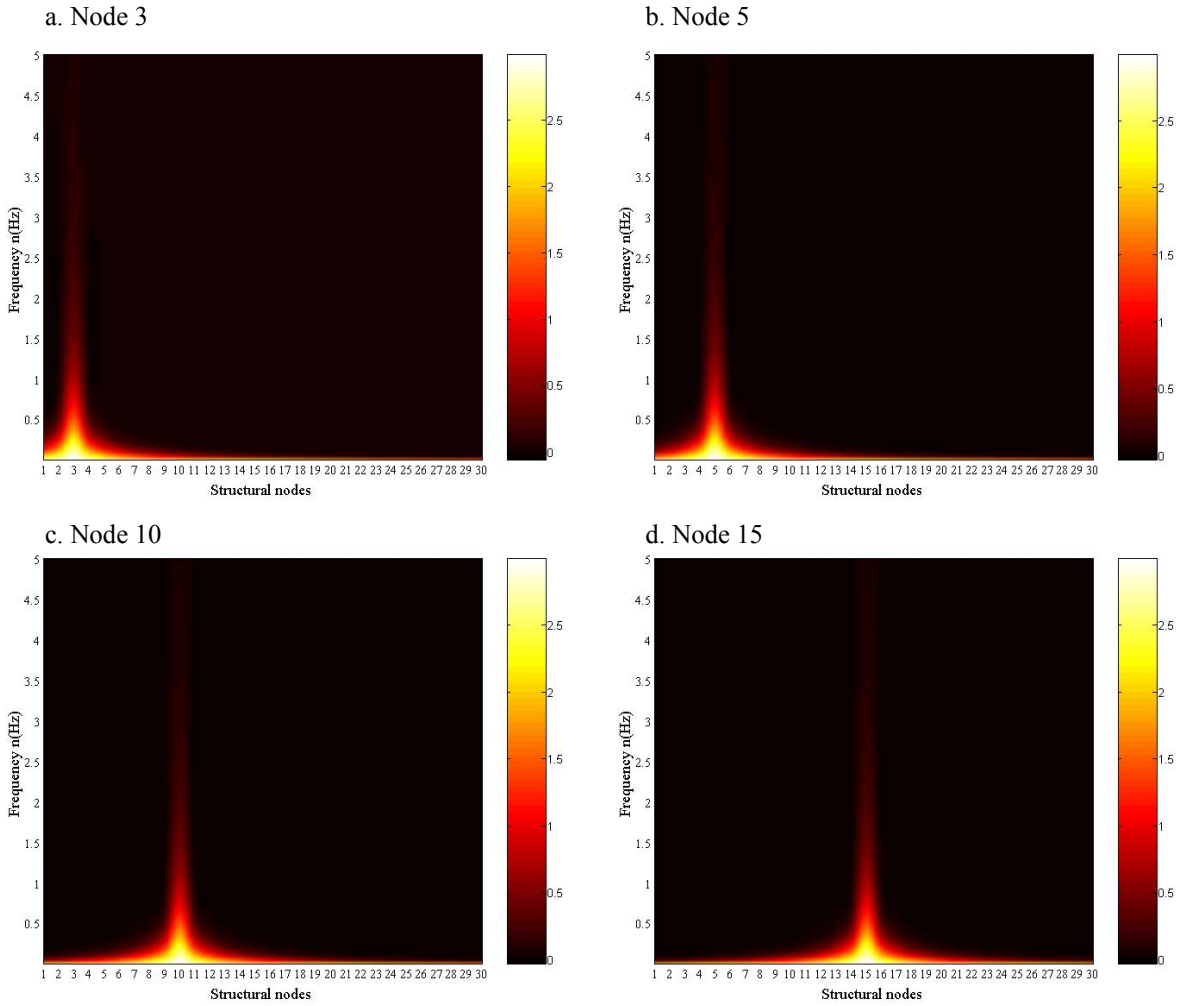

Fig. 7.4 Spatial power spectral densities of w-turbulence at some nodes 3, 5, 10 and 15

The cross spectral matrices have been decomposed using the proper orthogonal decomposition to find out pairs of the spectral eigenvectors and corresponding spectral eigenvalues. There are totally 30 pairs. Figure 7.5 shows the first five spectral eigenvalues $\lambda_1(n) \div \lambda_5(n)$ on frequency band 0.01÷10Hz at the mean velocity U=20m/s. It is observed that the first spectral eigenvalue $\lambda_1(n)$ exhibits much higher than the others on the very low frequency band 0.01÷0.2Hz with the u-turbulence, 0.01÷0.5Hz with the w-turbulence, however, all spectral eigenvalues not to differ beyond these frequency thresholds. These are considered as the effective frequency ranges.

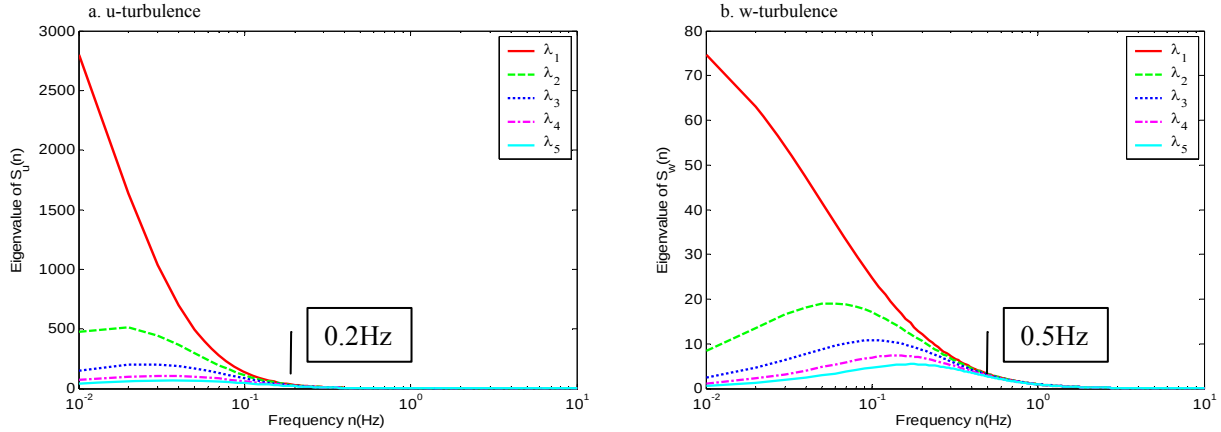

Fig. 7.5 First five spectral eigenvalues at U=20m/s: a. u-turbulence, b. w-turbulence

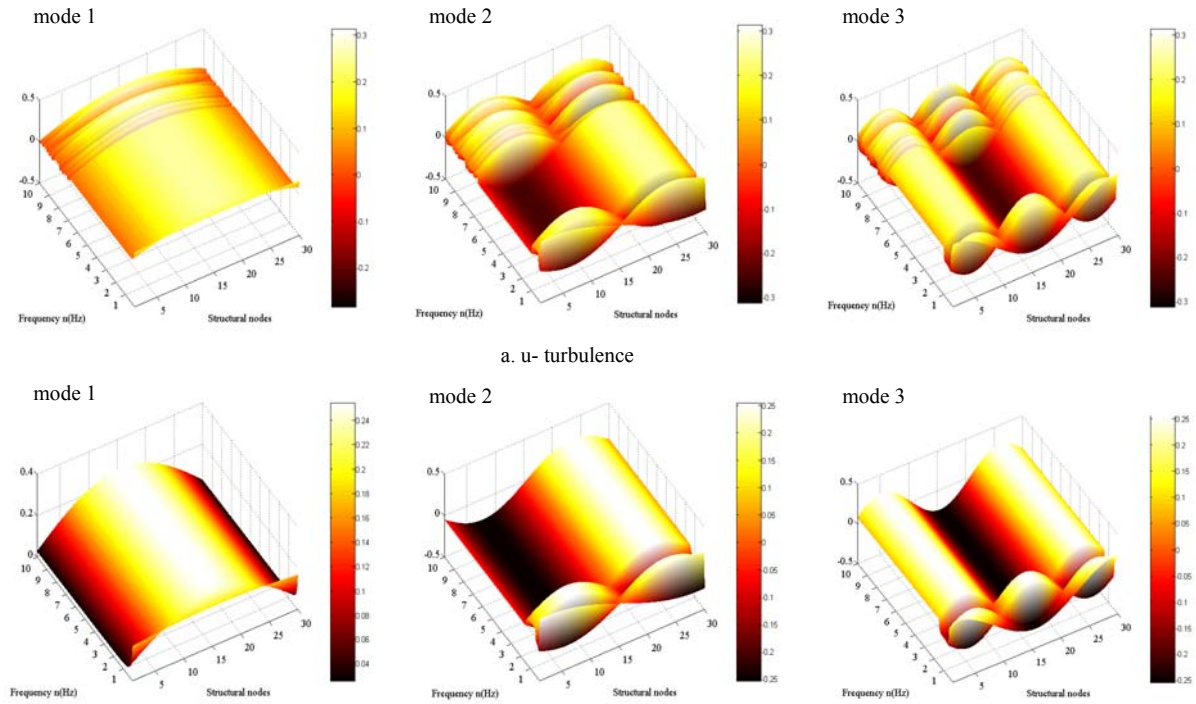

Fig. 7.6 First three spectral turbulent modes at U=20m/s: a. u-turbulence, b. w-turbulence

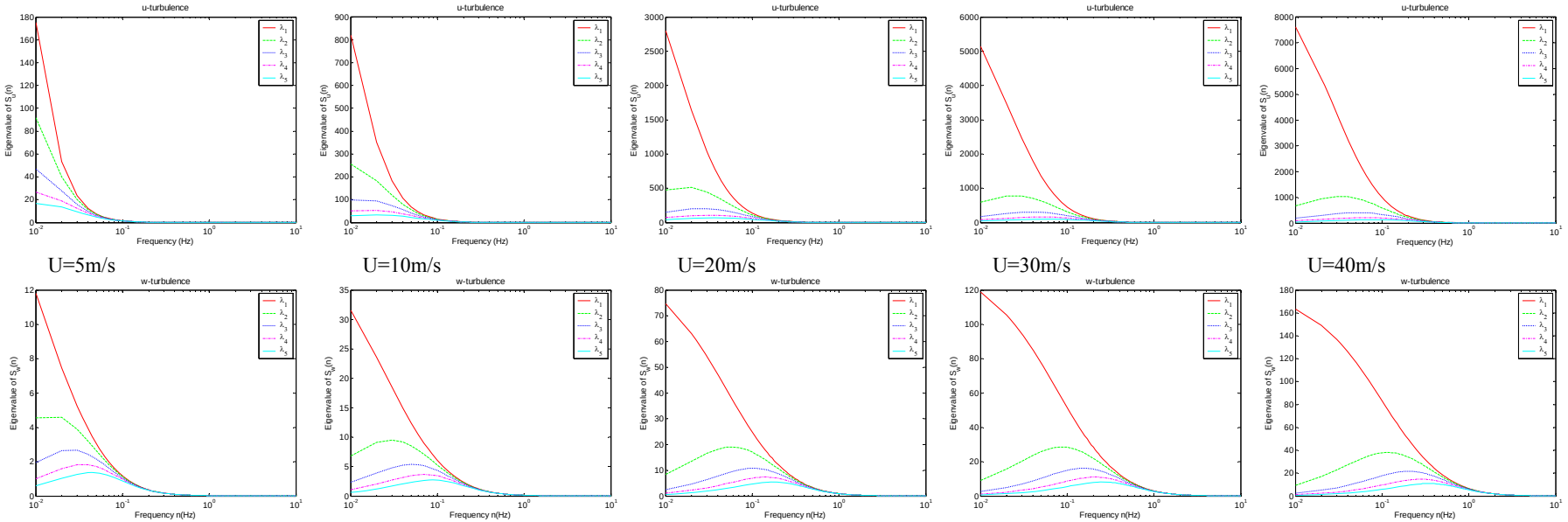

Fig. 7.7 Effect of change of wind velocities on first five spectral eigenvalues of u-,w-turbulences

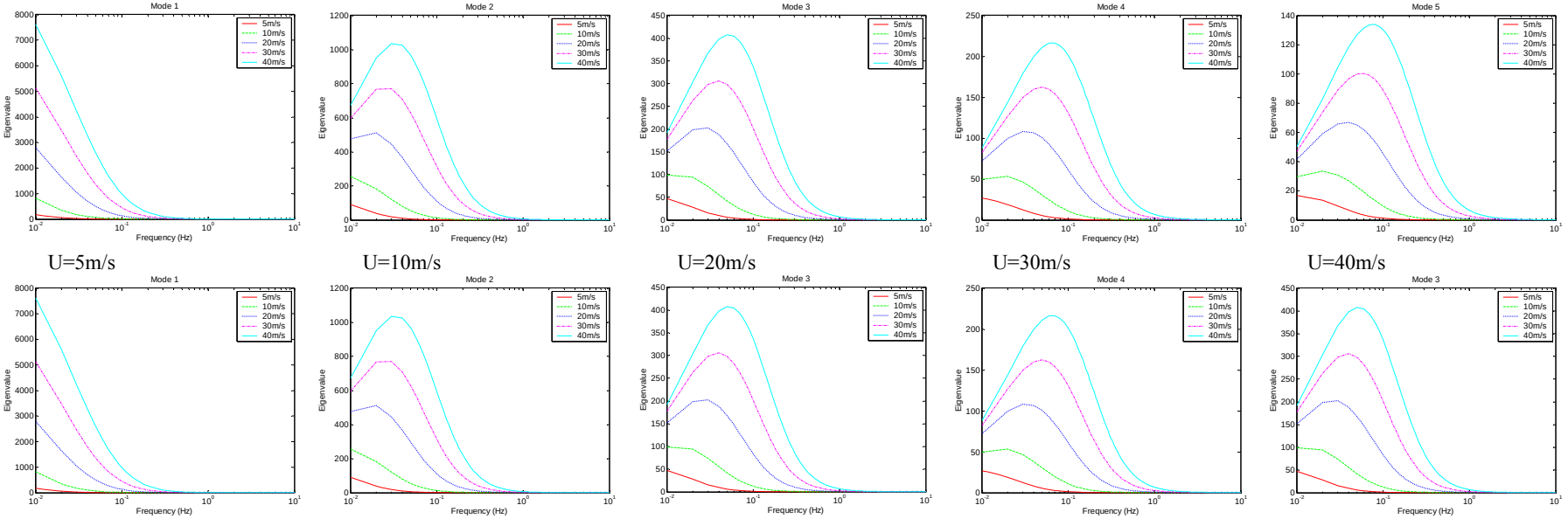

Fig. 7.8 Effect of change of wind velocities on each first five spectral eigenvalue of u-,w-turbulences

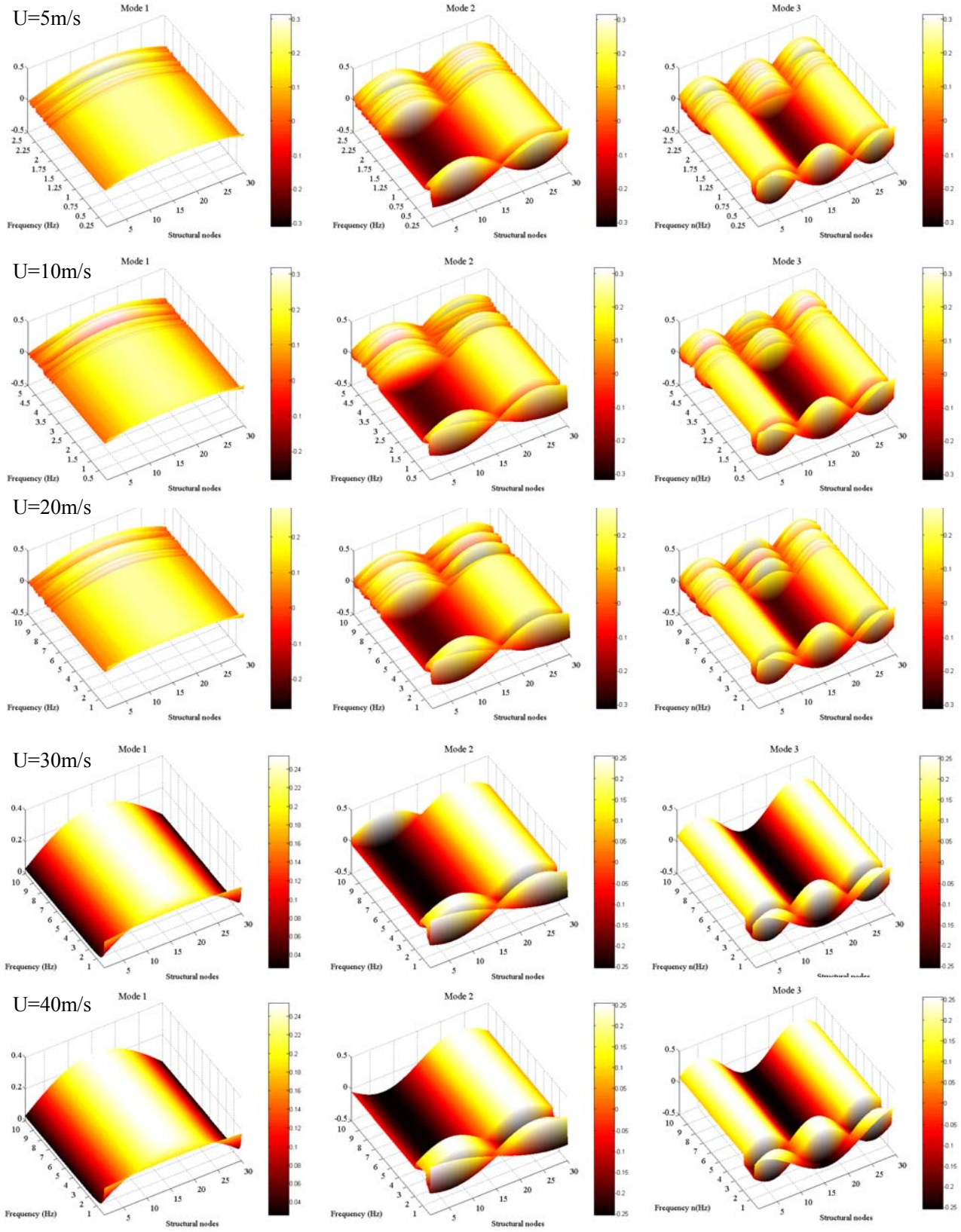

Fig. 7.9 Effect of change of wind velocities on spectral turbulent modes of u-turbulence

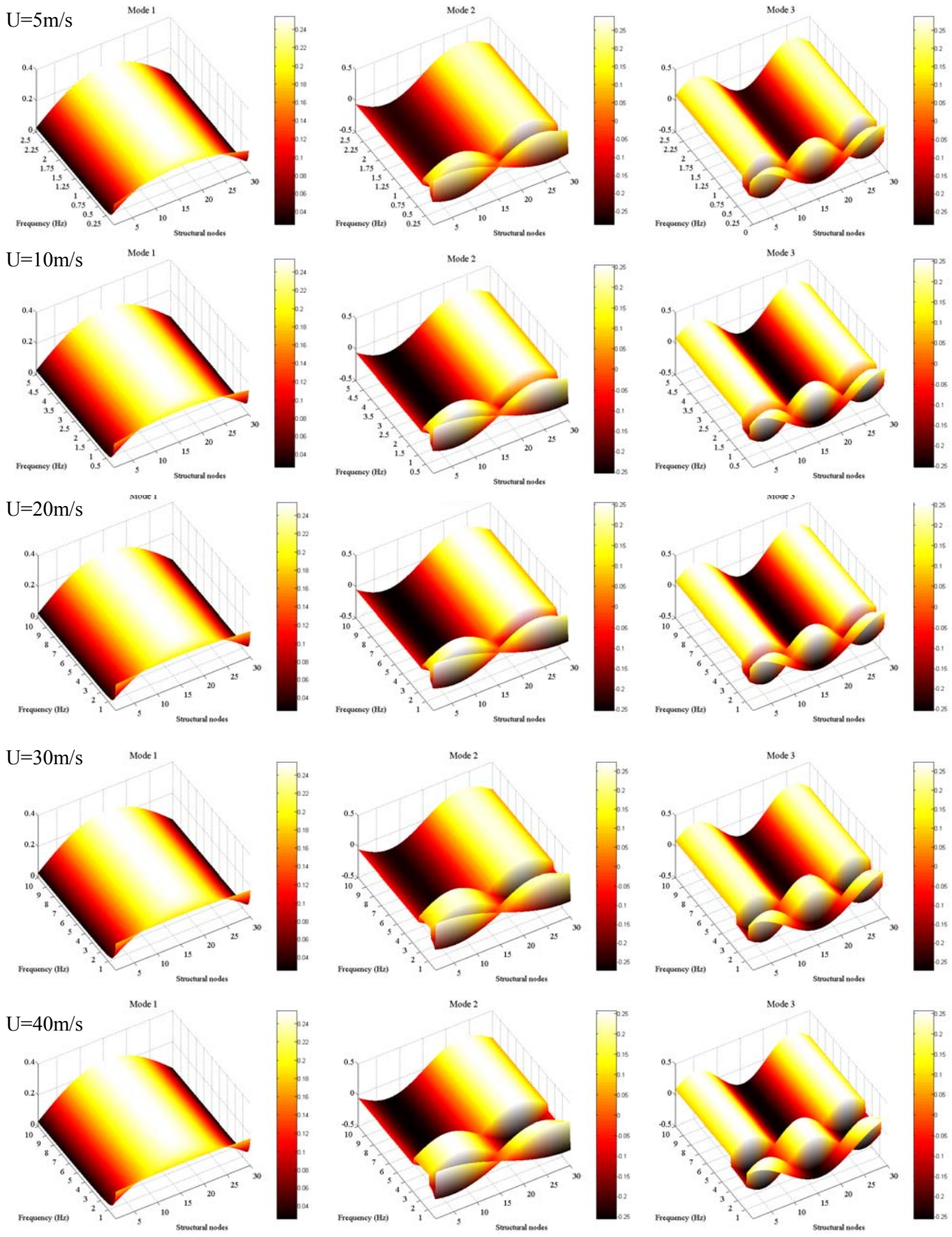

Fig. 7.10 Effect of change of wind velocities on spectral eigenvectors of w-turbulence

The first three spectral turbulent modes $\psi_{\upsilon 1}(n), \psi_{\upsilon 2}(n), \psi_{\upsilon 3}(n)$; $\upsilon = u, w$ on the same spectral band 0÷10Hz at the mean wind velocity U=20m/s is expressed in Figure 7.6. It can be seen that the turbulent modes of u-,w-components look like as symmetrically and asymmetrically sinusoidal waves, in which number of wave halves increases incrementally with the order of eigenvectors. It is also commented that because the shape of the spectral turbulent modes does not change with the frequency, thus the frequency characteristics of auto spectral densities of u-,w-turbulence depend completely on the spectral eigenvectors. It seems that the spectral eigenvalues should be considered for interpretation of physical characteristics of the ongoing turbulences.

Effect of change of mean wind velocities in turbulent flows on the spectral eigenvalues and the spectral turbulent modes is investigated herein in order to find out linkage between the spectral quantities and characteristics of the ongoing turbulent flows. Spectral eigenvalues and spectral turbulent modes are analyzed at different mean velocities U=5, 10, 20, 30 and 40m/s, and shown in Figures 7.7÷7.10. Obviously, it is observed that the shape of spectral turbulent modes exhibit constantly, not to depend on the change of the mean wind velocities. Only spectral eigenvalues strongly depend on the frequency. Therefore, the spectral eigenvalue can characterize for energy contribution of associated spectral eigenvectors to the whole system. Accordingly, the spectral eigenvalues can interpret to characteristics of the ongoing turbulent flows. It is expected the relationship between the spectral eigenvalues (associated spectral eigenvectors as well) and physical events of the ongoing turbulent flow exists.

As can be seen from Figure 7.7, in some cases the spectral eigenvalues contain frequency peaks, which these peaks increase with an increase of order of the spectral eigenvalues. In comparison at different mean velocities, it is observed that effective frequency ranges widen with increase of mean velocities. Moreover, scale of the spectral eigenvalues and their corresponding spectral peaks increase with respect to increase of the mean velocities as indicated in Figure 7.8.

The hidden events of the turbulent flows can be revealed that multi-scale eddies always exist on the turbulent flows. Large-scale eddies contain high energy, but move at low frequency, and inversely, small-scale hold small energy, but high frequency. However, the large-scale eddies tendency unstable, they break up into smaller eddies. Unstable large-scale eddies contain no energy contribution and frequency information. The scale of eddies and their corresponding frequency increase with respect to increase of the mean velocities. These characteristics of eddies in the turbulent flows can be determined via those of the spectral eigenvalues as mentioned above, therefore it is supposed that the spectral eigenvalues can interpret the scale of eddies.

Time series of two turbulent fields u(t), w(t) are simulated due to the spectral proper transformation of the cross spectral matrices of these two fields. All 30 spectral turbulent modes have been used for this turbulent simulation, therefore the simulated time series are considered as targeted time series. Figures 7.11÷7.14 show simulated time series of these turbulent processes at first ten deck nodes (from node 1 to node 10) during 100-second interval, corresponding to various mean wind velocities U=10, 20, 30 and 40m/s.

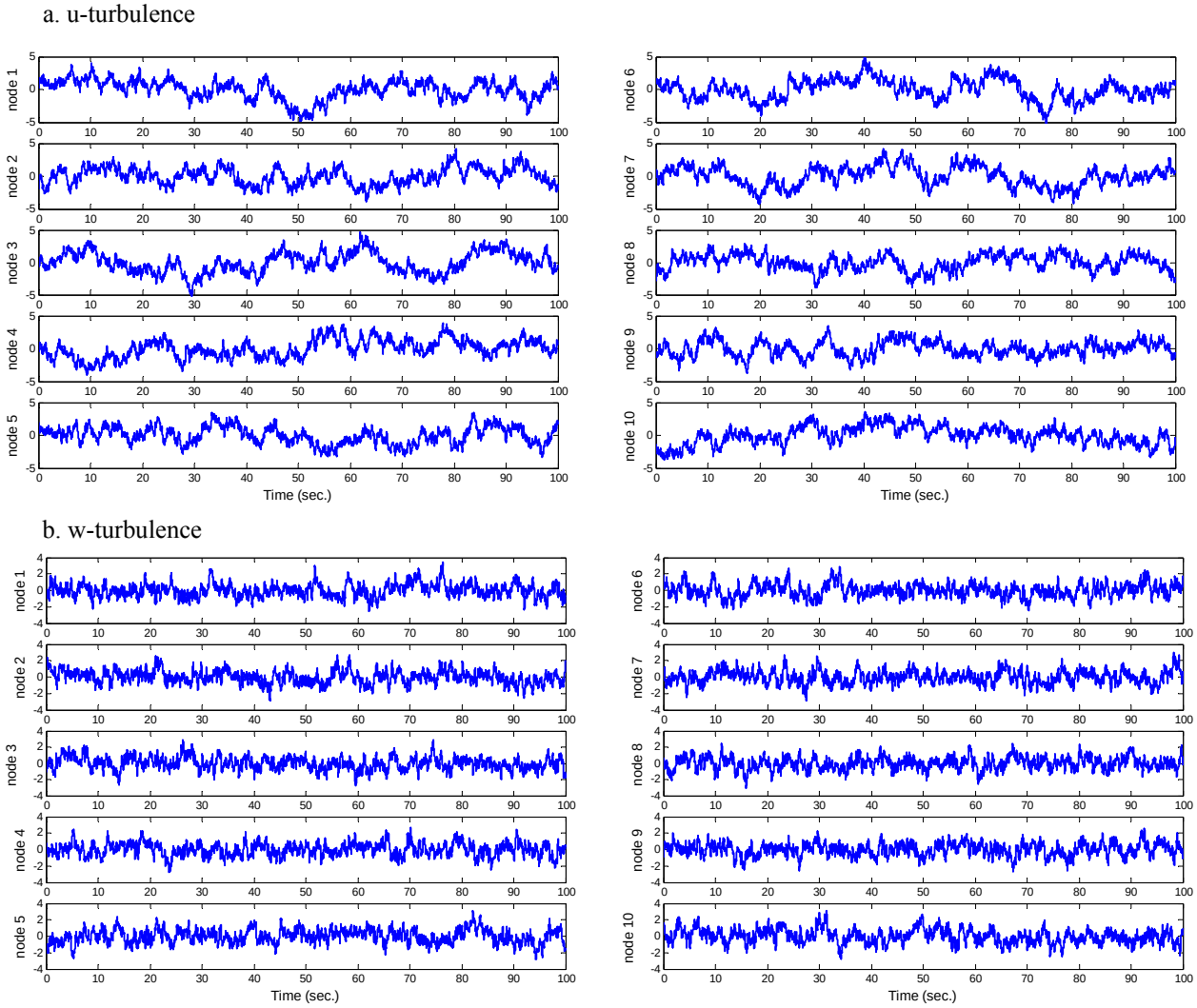

Fig. 7.11 Simulated time series at mean velocity U=10m/s: a. u-turbulence, b. w-turbulence

a. u-turbulence

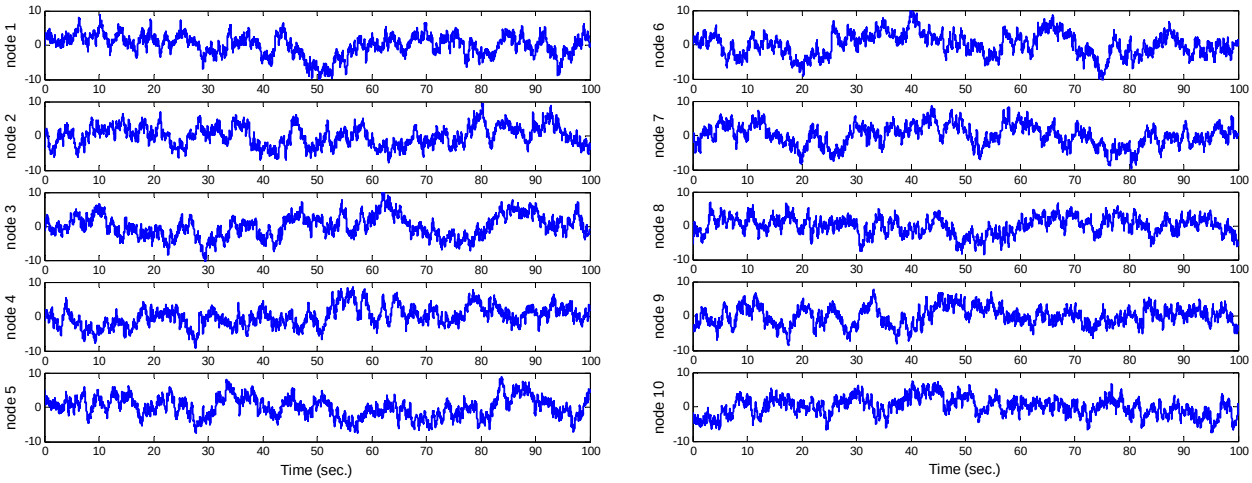

b. w-turbulence

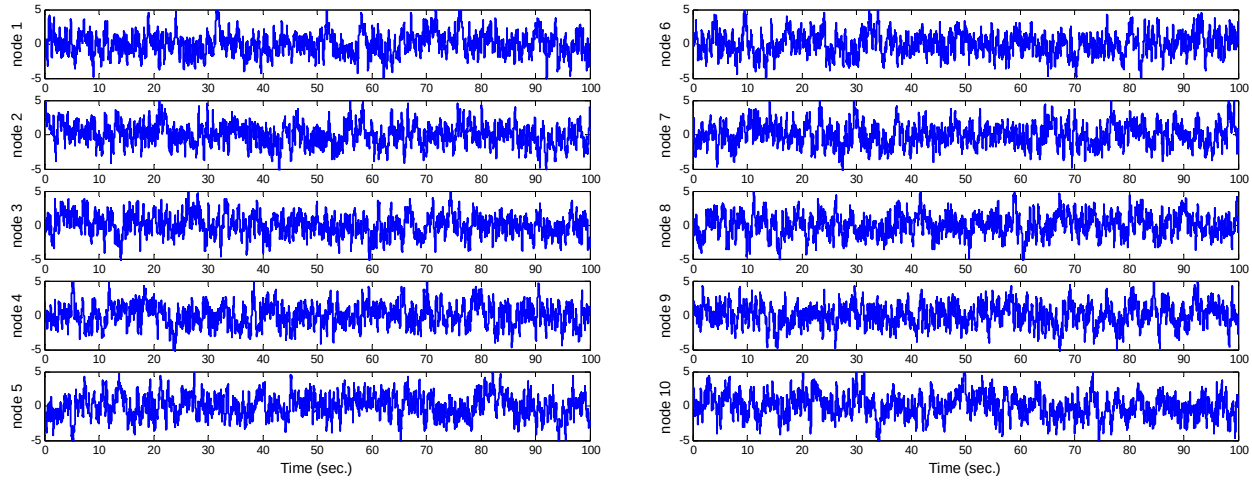

Fig. 7.12 Simulated time series at mean velocity U=20m/s: a. u-turbulence, b. w-turbulence

a. u-turbulence

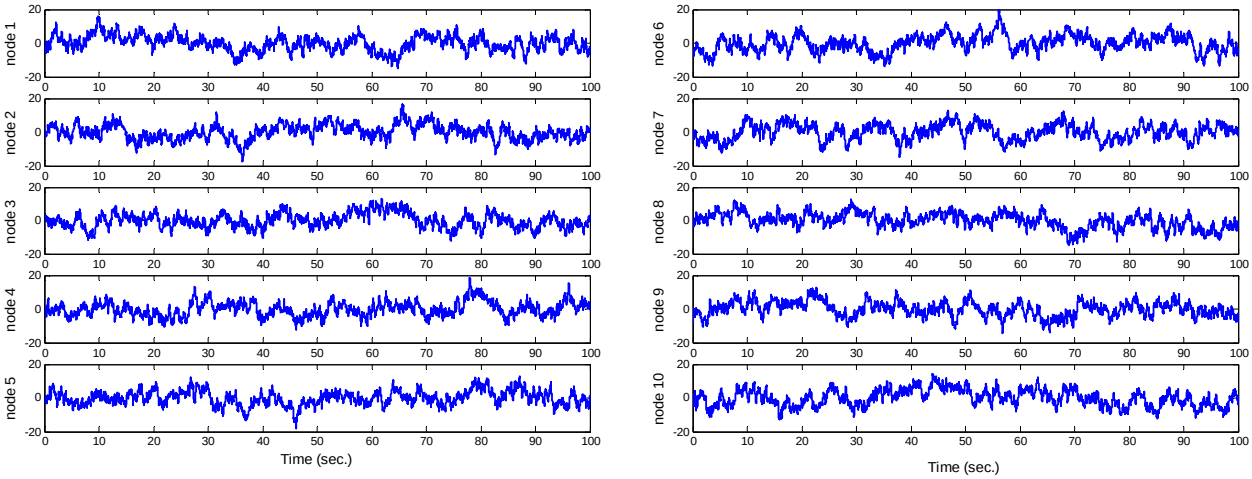

b. w-turbulence

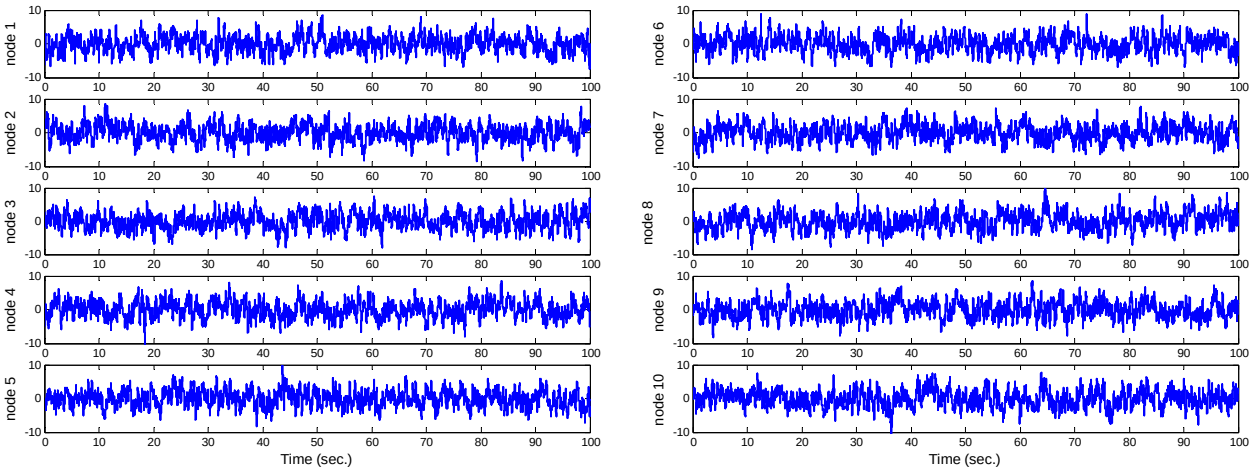

Fig. 7.13 Simulated time series at mean velocity U=30m/s: a. u-turbulence, b. w-turbulence

a. u-turbulence

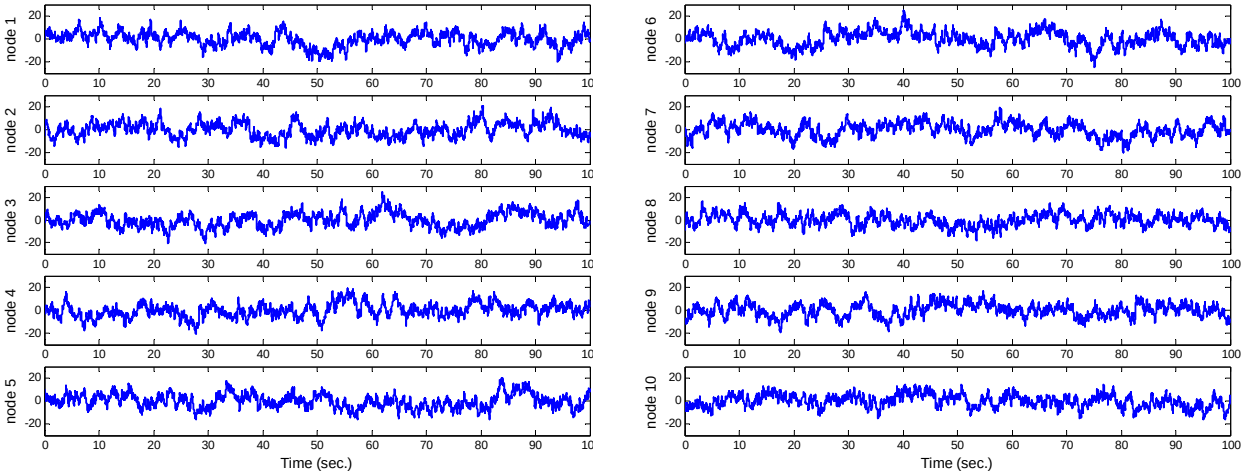

b. w-turbulence

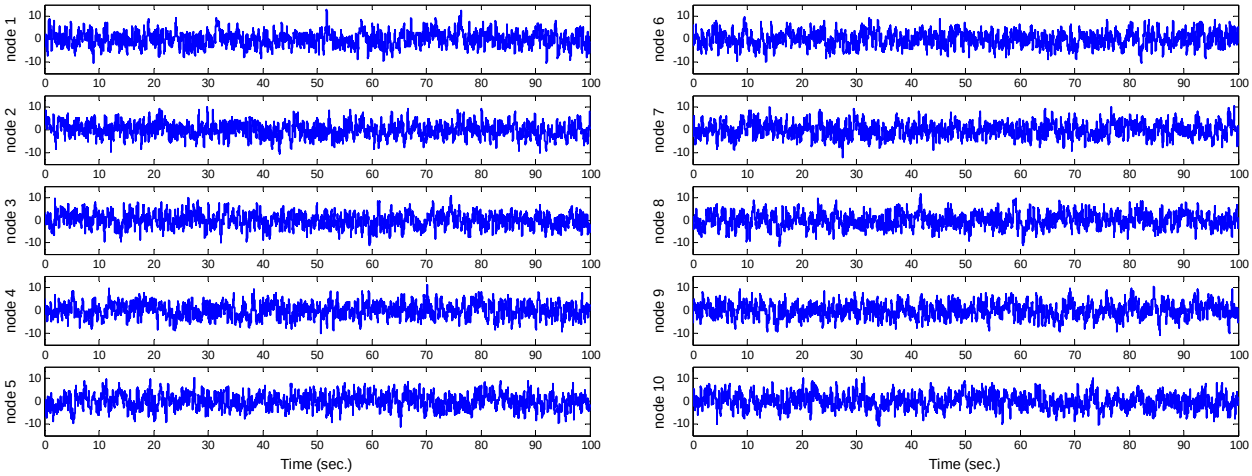

Fig. 7.14 Simulated time series at mean velocity U=40m/s: a. u-turbulence, b. w-turbulence

Simulated time series have been verified accuracy and consistence to satisfy statistical functions, power spectral densities and spatial correlation with respect to targeted conditions. It is noted that due to a sake of brevity, only verification of the simulated time series at mean velocity U=20m/s are taken into account (checking simulated time series at another turbulent conditions corresponding the mean velocities U=10, 30 and 40m/s can be carried out as the same manner, but not to present here). Characteristics of the simulated time series of u-,w-turbulences such as mean values, standard deviation and intensities of turbulence at the ten deck nodes are expressed in Table 7.1. There are good correspondence in the statistical characteristics among the simulated time series of u-,w-turbulences can be observed.

Tab. 7.1 Characteristics of simulated time series of u-,w-turbulences

	node 1	node 2	node 3	node 4	node 5	node 6	node 7	node 8	node 9	node10
	u-turbulence									
$\overline{U}$ (m/s)	3E-06	-4E-05	-9E-06	2E-05	5E-05	-9E-07	2E-06	-5E-05	-3E-05	-2E-05
σ_u (m/s)	3.0981	2.9232	3.2833	2.8647	2.9405	3.3427	3.1242	2.5777	2.7094	2.6757
I_u (%)	15.49	14.616	16.416	14.324	14.703	16.713	15.621	12.889	13.547	13.378
	w-turbulence									
$\overline{U}$ (m/s)	-1E-05	4E-05	-2E-05	1E-05	-2E-05	3E-05	-1E-07	7E-06	-2E-05	1E-05
σ_w (m/s)	1.6312	1.5704	1.5761	1.5793	1.6425	1.597	1.6078	1.617	1.5779	1.6785
I_w (%)	8.1558	7.8522	7.8805	7.8963	8.2126	7.9852	8.0389	8.0851	7.8897	8.3925

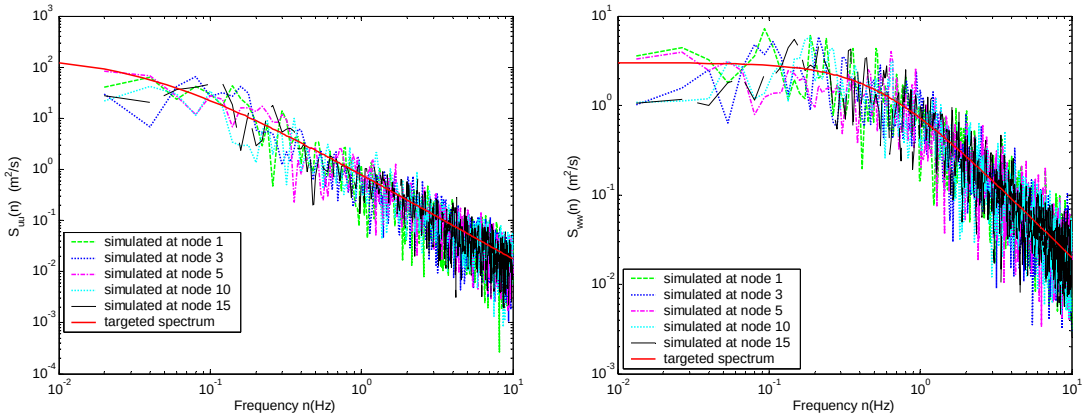

Fig.7.15 Verification between power spectral densities of simulated time series and targeted spectral densities at mean velocity U=20m/s

Figure 7.15 shows the auto power spectral densities (PSD) of simulated time series of subprocesses in the random turbulent fields u(t), w(t) at the turbulent flow U=20m/s in some representative deck nodes in verification with the targeted spectral densities. It is seen that there are good agreement between the auto spectral densities of the simulated time series and targeted ones.

Effect of number of truncated low-order spectral modes on simulation of the turbulent fields is investigated. Figure 7.16 shows the simulated time series of u-turbulence and w-turbulence at reference nodes 5 and 15 contributed by 5 modes, 10 modes, 20 modes and 30 modes as targeted time series.

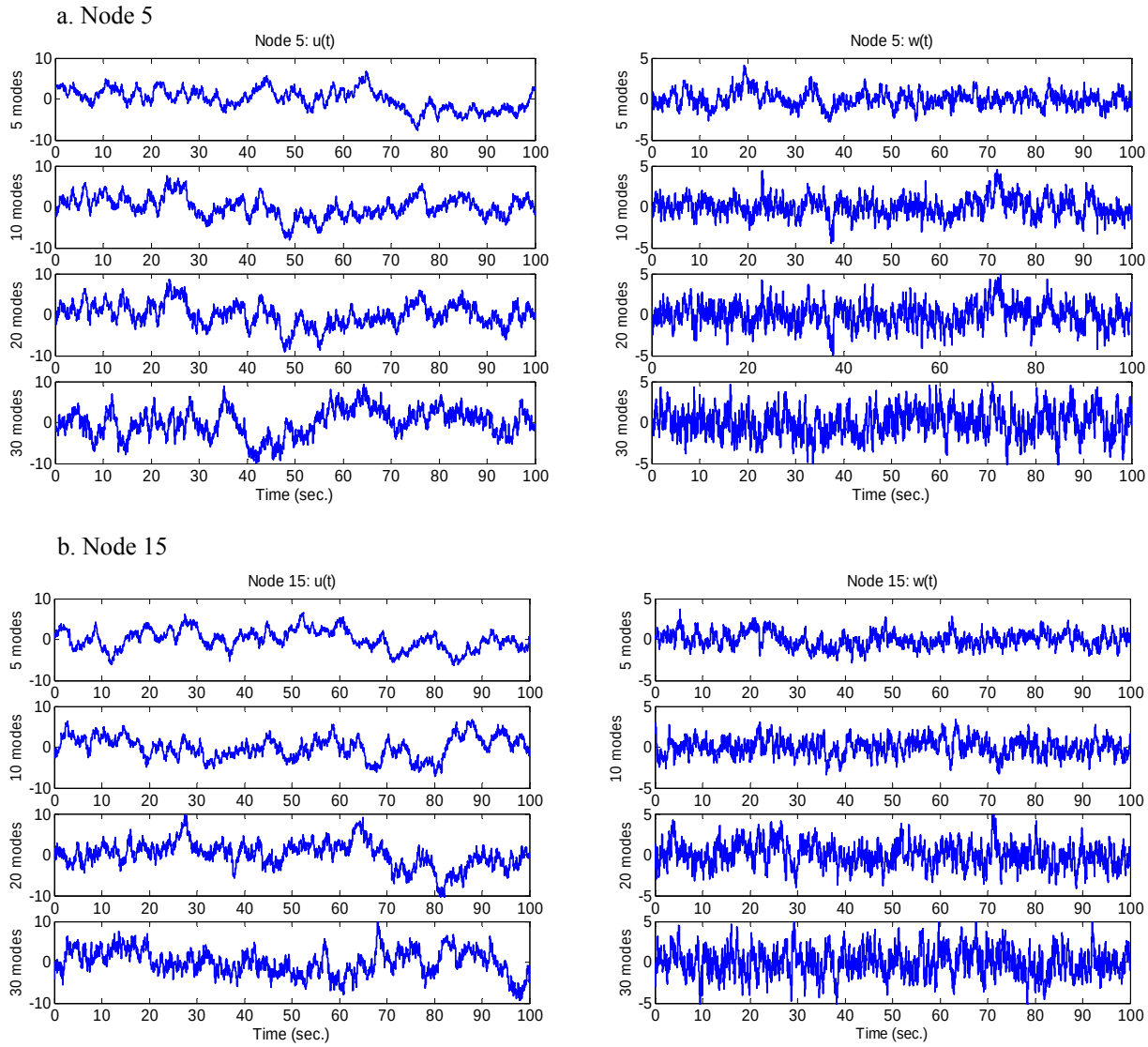

Fig. 7.16 Effect of spectral modes on simulated time series in nodes 5&15 at U=20m/s

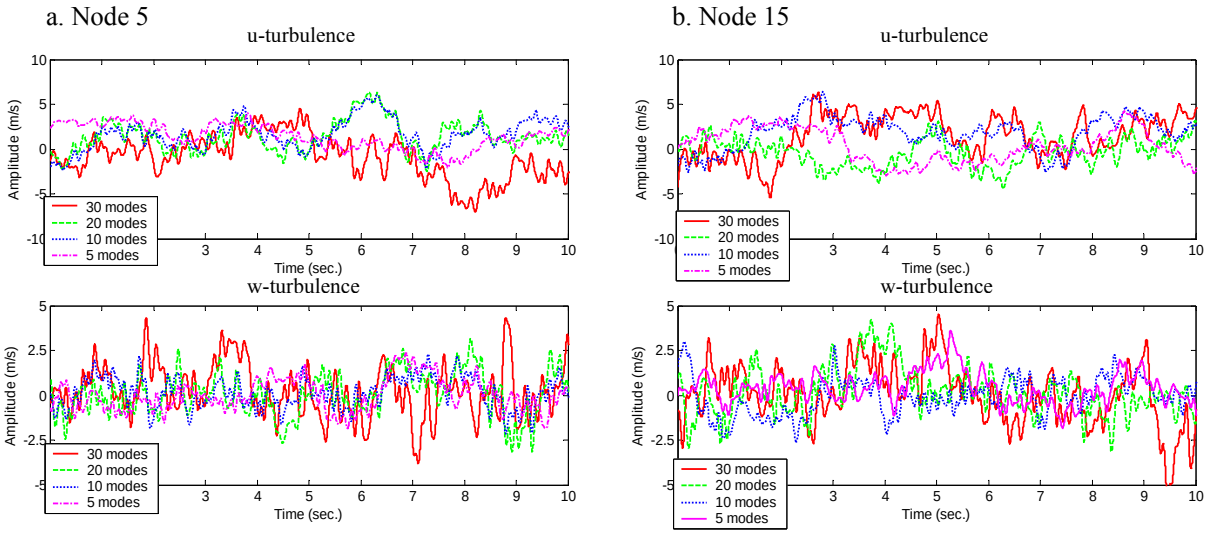

Fig. 7.17 Effect of spectral modes on simulated time series in nodes 5&15 during 10 seconds

Table 7.2 Characteristics of simulated time series of u-,w-turbulences at nodes 5&15

	u-turbulence				w-turbulence			
	5modes	10modes	20modes	30modes	5modes	10modes	20modes	30modes
	node 5							
$\overline{U}$ (m/s)	2E-05	-2E-05	-1E-06	-1E-05	-7E-06	4E-07	9E-06	-3E-06
σ_u (m/s)	2.5009	2.5704	2.8184	3.4195	0.9658	1.1766	1.3573	1.6698
I_u (%)	12.505	12.852	14.092	17.097	4.8292	5.8828	6.7867	8.3491
	node 15							
$\overline{U}$ (m/s)	2E-06	-2E-05	3E-07	-4E-05	-2E-07	2E-05	9E-06	-9E-06
σ_u (m/s)	2.4328	2.6552	3.1036	3.1368	0.9353	1.0547	1.4118	1.6403
I_u (%)	12.164	13.276	15.518	15.684	4.6765	5.2733	7.0592	8.2017

Figure 7.17 shows the time histories of simulated turbulences due to contribution of first 5 modes, 10 modes, 20 modes and 30 modes over the 10 second time interval. Furthermore, the characteristics of simulated time series at two nodes 5 and 15 corresponding to number of turbulent modes are indicated in Table 7.2. Comparison in the power spectral densities between simulated time series due to number of the turbulent modes is shown in Figure 7.18. As can be seen from Table 7.2 and Figure 7.18, there is difference in statistic characteristics and power spectral densities between simulated time series.

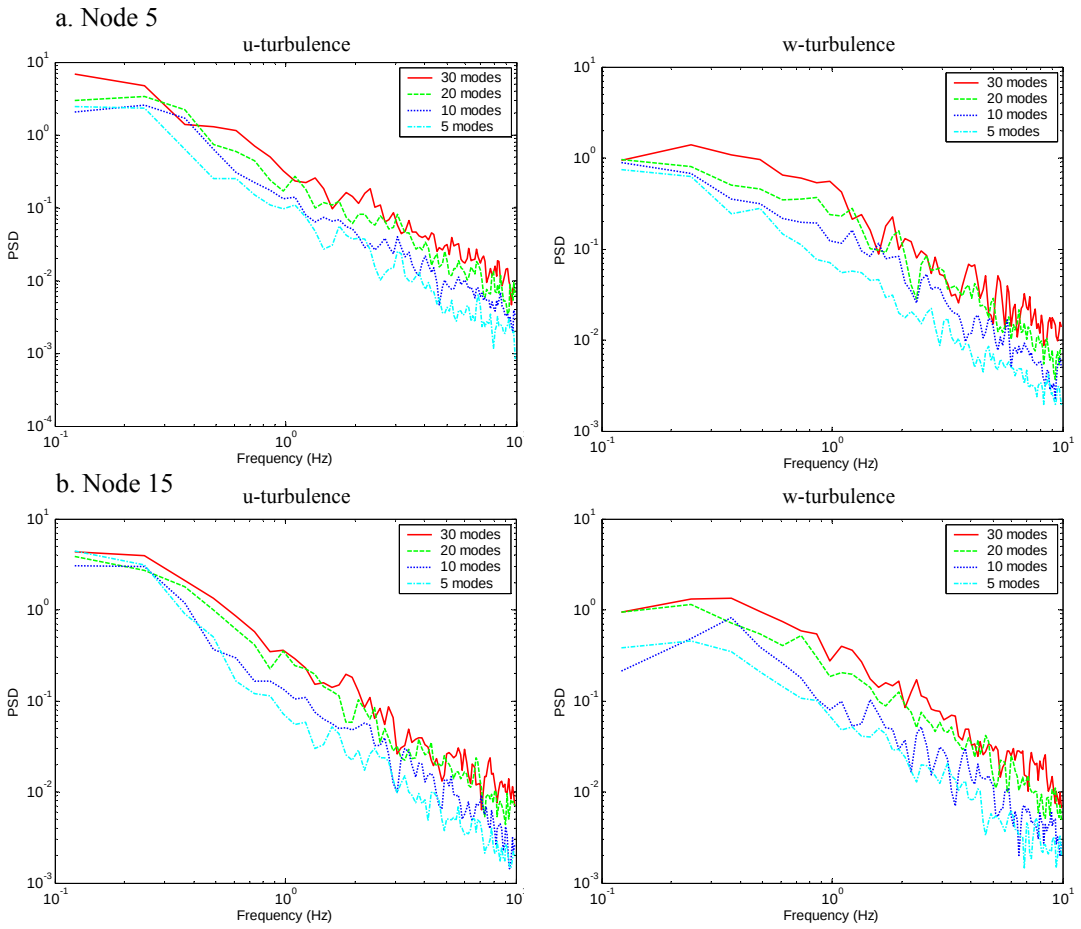

Fig. 7.18 Effect of number of spectral modes on power spectral densities of simulated time series at mean velocity U=20m/s

Simulating time series of the random turbulent fields acting on discrete deck nodes will be used as input data to predict the gust response of structure using the covariance proper transformation in the time domain.

7.7 Conclusion

Representation and simulation of the multi-variate spatially-correlated random turbulent field has been presented in this chapter with emphasis on application of the spectral proper transformation. The effect of number of spectral turbulent modes on the turbulent simulation also is discussed. Some conclusion can be given as follows:

(1) Digital simulation of multi-variate turbulent field using cross spectral matrix-based proper orthogonal decomposition and the spectral proper transformation is another approach including to conventional Cholesky decomposition in the spectral representation methods. Effect of number of the spectral turbulent modes on simulated time series has been investigated with verification for accuracy and consistence. It can be argued that it is not accurate enough for the turbulent simulation with using just few fundamental turbulent modes, many turbulent modes should be required.

(2) Physical meaning of the spectral eigenvalues and turbulent modes relating to hidden events in the ongoing turbulent flow has been tried to establish. Because the spectral eigenvectors express constantly with respect to the different mean velocities and the frequencies, and the spectral eigenvalues contain frequency information. Therefore, it is expected that the spectral eigenvalues can characterize for scale of the turbulent eddies of the ongoing turbulent flow. However, further studies on the relationship between the spectral eigenvalues, associated spectral turbulent modes and physical phenomena inside the ongoing turbulent flows will be required for more clarification of this physical linkage.

Reference

Cao, Y.H., Xiang, H.F., Zhou, Y. (2000), "Simulation of stochastic wind velocity field on long-span bridges", *J. Engrg. Mech.,* ASCE **126**(**1)**, 1-6.

Chen, X., Kareem, A. (2005), "Proper orthogonal decomposition-based modeling, analysis, and simulation of dynamic wind load effects on structures", *J.Engrg. Mech.*, ASCE **131(4)**, 325-339.

Di Paola, M. (1998), "Digital simulation of wind field velocity", *J. Wind Eng. Ind. Aerodyn.*, **74-76**, 91-109.

Di Paola, M, Gullo, I. (2001), "Digital generation of multi-variate wind field processes", *J. Prob. Engrg. Mech.*, **16**, 1-10.

Li, Y.S., Kareem, A. (1995), "Stochastic decomposition and application to probabilistic dynamics". *J. Engrg. Mech.*, ASCE **121(1)**, 162-174.

Matsumoto, M. (2000), *Aeroelasticity and bridge aerodynamics*, Textbook for Int'l Advanced Course on Wind Engineering, Genoa, Italy.

Shinozuka, M., Jan, C.M. (1972), "Digital simulation of random processes and its application, *J. Sound Vib*., **25(10)**, 111-128.

Shinozuka, M., Yun, C.M., Seya, H. (1990), "Stochastic methods in wind engineering", *J. Wind Eng. Ind. Aerodyn.*, **36**, 829-843.

Tubino, F., Solari, G. (2005), "Double proper transformation for representing and simulating turbulence field", *J. Engrg. Mech.*, ASCE **131(12)**, 1302-1312.

Yang, W.W., Chang, T.Y.P., Chang, C.C. (1997), "An efficient wind field simulation technique for bridges", *J. Wind Eng. Ind. Aerodyn.*, **67-68**, 697-708

Chapter 8

Gust Response of Bridges using Spectral Proper Transformation

8.1 Introduction

Gust response prediction of structures subjected to the turbulent-induced forces in the atmospheric turbulent flow requires as a must among wind effects and wind-induced vibrations. General formulation of gust response prediction of line-like structures has proposed by Davenport, 1962. Recent development in the buffeting response analysis of bridges in the frequency domain with emphasis on aeroelastic force coupling has been presented in some literatures (eg., Matsumoto et al. 1994, Jain et al. 1996, Katsuchi et al. 1999). As a principle, the multi-degree-of-freedom (MDOF) motion equations of structures were decomposed orthogonally in the generalized coordinates and vibrational mode shapes thanks to the structural modal transformation (SMT). However, there were inevitable difficulties to generalize external turbulent forces, which then are associated with generalized coordinates. So far, the joint acceptance function (JAF) has been applied to determine the generalized turbulent forces and gust response analysis of bridges in both the frequency and time domains (Davenport, 1992; Chen et al., 2000).

Proper orthogonal decomposition (POD), also known as Karhunen-Loeve decomposition has been applied. Basing upon a formulation of basic matrix in the proper transformation, the proper orthogonal decomposition has been divided into two branches: i. the covariance-matrix-based POD and covariance proper transformation (CPT) in the time domain and ii. the spectral-matrix-based POD and spectral proper transformation (SPT) in the frequency domain (Carassale et al. 1999; Solari et al. 2000, Chen and Kareem 2005). In the former, the basic matrix is based on the zero-time-lag covariance matrix of turbulent loading processes in the time domain, whereas cross spectral density matrix of these processes used in the frequency domain in the later. It is generally agreed that almost literatures, however, have been discussed on the covariance-based POD and CPT in the time domain. The spectral-based POD and SPT is very promising to apply for stochastic response analysis, but it burdens much in complicated computation rather than the CPT. Recently, new approach of the gust response analysis of

structures, so-called double modal transformations (DMT) has been proposed by Carassale et al., 1999, by which the structural modes decomposed by the SMT are associated with the so-called orthogonally turbulent loading modes decomposed by the SPT to determine the gust response in both the generalized and structural coordinates. Advantage of the POD applications on the gust response analysis of structures has hinged on comprehensive approach for the generalized gust force formulation in which the fully-correlated turbulent field is directed accounted. Especially, the lowest turbulent loading modes that have been decomposed from the fully-correlated turbulent field thanks to the POD analysis can contribute dominantly on the structurally generalized responses of the lowest structural modes. The DMT using the the spectral-based POD and SPT has been applied for the gust response prediction of simple frames, buildings by some authors (Carassale et al. 1999; Solari et al. 2000; Chen and Kareem 2005), and for that of bridges (Solari and Tubino 2005, Le and Nguyen 2006). Time domain gust response analysis of bridges using the covariance-based POD and CPT has firstly presented by Matsumoto et al. 2007. In previous applications of spectral-based DMT, however, the simple quasi-steady theory has been accounted for the turbulent-induced forces.

In this chapter, the spectral-matrix-based POD and its SPT will be presented and application to decoupling the multi-variate turbulent loading processes. New comprehensive approach on the gust response prediction of structures then will be formulated using the SPT with emphasis on numerical example of cable-stayed bridge. The turbulent-induced forces based on corrected quasi-steady theory with aerodynamic admittance also are used for more refinement.

8.2 Spectral Proper Transformation

The main idea of the POD is to find out a set of orthogonal vector basis which can represent a multi-variate random process into a sum of products of these basic orthogonal vectors and single-variant uncorrelated random processes. The spectral-based orthogonal vectors are found as the eigenvector solutions of the eigen problem of the cross spectral density matrix as:

$$S_\upsilon(n)\Psi_\upsilon(n) = \Lambda_\upsilon(n)\Psi_\upsilon(n) \tag{8.1}$$

where $S_\upsilon(n)$: cross spectral density matrix formed from multi-variate random process $\upsilon(t)$; $\Lambda_\upsilon(n), \Psi_\upsilon(n)$: spectral eigenvalue and eigenvector matrices $\Lambda_\upsilon(n) = diag(\lambda_{\upsilon_1}(n), \lambda_{\upsilon_2}(n), ...\lambda_{\upsilon_N}(n))$, $\Psi_\upsilon(n) = [\psi_{\upsilon_1}(n), \psi_{\upsilon_2}(n), ...\psi_{\upsilon_N}(n)]$, in which spectral eigenvector $\psi_{\upsilon_j}(n)$ associated with spectral eigenvalue $\lambda_{\upsilon_j}(n)$; n: frequency variable.

Since the cross spectral density matrix $S_\upsilon(n)$ is a Hermitian and positive definite one, thus its spectral eigenvalues are real and positive, its spectral eigenvectors are generally complex, satisfy

the orthonormal conditions as follows:

$$\Psi_{\upsilon}^{*T}(n)\Psi_{\upsilon}(n) = I;\ \Psi_{\upsilon}^{*T}(n)S_{\upsilon}(n)\Psi_{\upsilon}(n) = \Lambda_{\upsilon}(n) \tag{8.2-a}$$

$$\psi_{\upsilon_i}^{*T}(n)\psi_{\upsilon_j}(n) = \delta_{ij};\ \psi_{\upsilon_i}^{*T}(n)S_{\upsilon_i\upsilon_j}(n)\psi_{\upsilon_j}(n) = \lambda_{\upsilon_i}(n)\delta_{ij} \tag{8.2-b}$$

Thus, the Fourier transform and the cross spectral density matrix of $\upsilon(t)$ can be represented in terms of the orthogonal eigenvectors $\Psi_{\upsilon}(n)$ as follows:

$$\hat{\upsilon}(n) = \Psi_{\upsilon}(n)\hat{y}_{\upsilon}(n) \approx \sum_{j=1}^{N}\psi_{\upsilon j}(n)\hat{y}_{\upsilon j}(n) \tag{8.3-a}$$

$$S_{\upsilon}(n) = \Psi_{\upsilon}(n)\Lambda_{\upsilon}(n)\Psi_{\upsilon}^{*T}(n) \approx \sum_{j=1}^{N}\psi_{\upsilon j}(n)\lambda_{\upsilon j}(n)\psi_{\upsilon j}^{*T}(n) \tag{8.3-b}$$

where $\hat{y}_{\upsilon}(n)$: turbulent principal coordinates as Fourier transforms of uncorrelated single-variate random processes; N: dimension of cross spectral matrix $S_{\upsilon}(n)$; *,T: denote to both complex conjugate and transpose operators.

The spectral-based quantities can be approximately reconstructed by using limited number of the lowest spectral eigenvectors (assumed that the spectral eigenvectors rearranged in reduced order of their corresponding spectral eigenvalues) as follows:

$$\hat{\upsilon}(n) \approx \sum_{j=1}^{\hat{M}}\psi_{\upsilon j}(n)\hat{y}_{\upsilon j}(n) \tag{8.4-a}$$

$$S_{\upsilon}(n) \approx \sum_{j=1}^{\hat{M}}\psi_{\upsilon j}(n)\lambda_{\upsilon j}(n)\psi_{\upsilon j}^{*T}(n) \tag{8.4-b}$$

where $\hat{M}$: number of truncated spectral eigenvectors ($\hat{M} << N$).

These approximations are known as the Spectral Proper Transformation (SPT) in the frequency domain.

Two multi-variate uncorrelated turbulent processes containing longitudinally and vertically velocity fluctuations u(t), w(t) (lateral turbulent component v(t) is omitted due to very small effect) are represented at N discrete nodes along the bridge deck as two N-variate Gaussian random processes:

$$u(t) = \{u_1(t), u_2(t), \ldots, u_N(t)\}^T;\ w(t) = \{w_1(t), w_2(t), \ldots, w_N(t)\}^T \tag{8.5}$$

The cross spectral matrix $S_{\upsilon}(n)$ of the turbulent fields which comprise auto and cross spectral densities components at each node and between two nodes are given in following form:

$$S_u(n)=\begin{bmatrix} S_{u_1u_1}(n) & S_{u_1u_2}(n) & \dots & S_{u_1u_N}(n) \\ S_{u_2u_1}(n) & S_{u_2u_2}(n) & \dots & S_{u_2u_N}(n) \\ \vdots & \vdots & \vdots & \vdots \\ S_{u_Nu_1}(n) & S_{u_Nu_2}(n) & \dots & S_{u_Nu_N}(n) \end{bmatrix}; S_w(n)=\begin{bmatrix} S_{w_1w_1}(n) & S_{w_1w_2}(n) & \dots & S_{w_1w_N}(n) \\ S_{w_2w_1}(n) & S_{w_2w_2}(n) & \dots & S_{w_2w_N}(n) \\ \vdots & \vdots & \vdots & \vdots \\ S_{w_Nw_1}(n) & S_{w_Nw_2}(n) & \dots & S_{w_Nw_N}(n) \end{bmatrix} \quad (8.6)$$

where $S_{u_mu_m}(n), S_{w_mw_m}(n)$: auto spectral density elements of turbulent components u(t), w(t) at node m; $S_{u_mu_k}(n), S_{w_mw_k}(n)$: cross spectral density elements between two nodes m, k; m or k=1,2..N. The cross spectral density elements can be determined from the auto spectral density ones due to such following relationship as:

$$S_{u_mu_k}(n)=S_{u_mu_m}(n)COH_u(n,\Delta_{mk}); \quad S_{w_mw_k}(n)=S_{w_mw_m}(n)COH_w(n,\Delta_{mk}) \quad (8.7)$$

where $COH_u(n,\Delta_{mk}), COH_w(n,\Delta_{mk})$: coherence functions between two separated nodes m, k at spanwise separation $\Delta_{mk}=|y_m-y_k|$; y_m, y_k: spanwise coordinates of nodes m, k.

Two N-variate Gaussian random turbulent processes u(t), w(t) can be decomposed and transformed into the spectral principal coordinates using the spectral proper transformation:

$$\hat{u}(n)=\Psi_u(n)\hat{y}_u(n)\approx\sum_{j=1}^{\hat{M}}\psi_{uj}(n)\hat{y}_{uj}(n) \quad (8.8\text{-a})$$

$$\hat{w}(n)=\Psi_w(n)\hat{y}_w(n)\approx\sum_{j=1}^{\hat{M}}\psi_{wj}(n)\hat{y}_{wj}(n) \quad (8.8\text{-b})$$

where $\hat{u}(n), \hat{w}(n)$: Fourier transforms of u(t), v(t); $\hat{y}_u(n), \hat{y}_w(n)$: the spectral principal coordinates as Fourier transform of independent random processes; $\hat{M} << N$.

Furthermore, the cross spectral matrices are reconstructed as follows:

$$S_u(n)=\Psi_u(n)\Lambda_u(n)\Psi_u^{*T}(n)\approx\sum_{j=1}^{\hat{M}}\psi_{uj}(n)\lambda_{uj}(n)\psi_{uj}^{*T}(n) \quad (8.9\text{-a})$$

$$S_w(n)=\Psi_w(n)\Lambda_w(n)\Psi_w^{*T}(n)\approx\sum_{j=1}^{\hat{M}}\psi_{wj}(n)\lambda_{wj}(n)\psi_{wj}^{*T}(n) \quad (8.9\text{-b})$$

where $\Lambda_u(n), \Lambda_w(n), \Psi_u(n), \Psi_w(n)$: spectral eigenvalues and corresponding spectral eigenvectors: $\Lambda_u(n)=diag(\lambda_{u_1}(n),\lambda_{u_2}(n),...,\lambda_{u_N}(n))$; $\Lambda_w(n)=diag(\lambda_{w_1}(n),\lambda_{w_2}(n),...,\lambda_{w_N}(n))$

$\Psi_u(n)=\{\psi_{u_1}(n),\psi_{u_2}(n),...,\psi_{u_N}(n)\}^T$; $\Psi_w(n)=\{\psi_{w_1}(n),\psi_{w_2}(n),...,\psi_{w_N}(n)\}$ determined from spectral matrix-based proper orthogonal decomposition of the random turbulent processes u(t), w(t) following Eq.(8.1).

8.3 Frequency-domain buffeting forces

Uniform buffeting forces per unit deck length (consisting of lift, drag, moment: $L_b(t)$, $D_b(t)$, $M_b(t)$, see Figure 8.1) are determined from random turbulent field u(t), w(t) due to the corrected quasi-steady theory (Davenport 1962), in which frequency-dependant aerodynamic admittance functions are supplemented.

$$L_b(t)=\frac{1}{2}\rho U^2 B[C_L(\alpha_0)\chi_{Lu}(n)\frac{2u(t)}{U}+(C_L^{'}(\alpha_0)+C_D(\alpha_0))\chi_{Lw}(n)\frac{w(t)}{U}] \quad (8.10\text{-a})$$

$$D_b(t)=\frac{1}{2}\rho U^2 B[C_D(\alpha_0)\chi_{Du}(n)\frac{2u(t)}{U}+(C_D^{'}(\alpha_0)-C_L(\alpha_0))\chi_{Dw}(n)\frac{w(t)}{U}] \quad (8.10\text{-b})$$

$$M_b(t)=\frac{1}{2}\rho U^2 B^2[C_M(\alpha_0)\chi_{Mu}(n)\frac{2u(t)}{U}+C_M^{'}(\alpha_0)\chi_{Mw}(n)\frac{w(t)}{U}] \quad (8.10\text{-c})$$

where C_L, C_D, C_M: aerodynamic static coefficients at balanced angle of attack α_0 (usually $\alpha_0 = 0^o$); $C_L^{'}, C_D^{'}, C_M^{'}$: first derivatives with respect to angle of attack at balanced angle $C_F^{'} = dC_F(\alpha)/d\alpha\big|_{\alpha_0=0}$, $F = L, D, M$; $\chi_{F\upsilon}(n)$ $(F = L, D, M; \upsilon = u, w)$: aerodynamic transfer functions between turbulent components and turbulent-induced forces (their absolute magnitudes refer as aerodynamic admittance functions); ρ , B, U: air density, width and mean velocity, respectively.

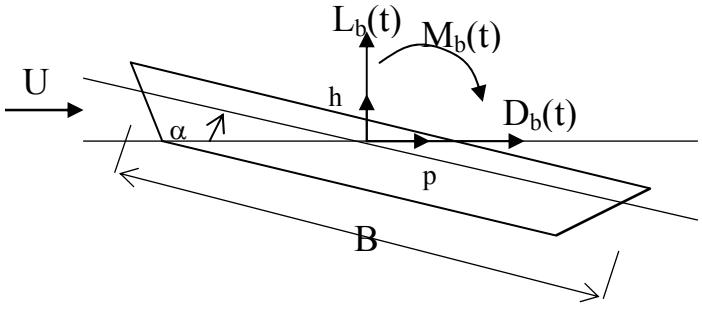

Fig. 8.1 Uniform buffeting forces on bridge deck

Then full-scale buffeting forces acting on whole structure can be formulated due to linearized lumping of the uniform buffeting forces at each deck node:

$$L_b(t)=\{L_{b1}(t),L_{b2}(t),\ldots L_{bN}(t)\}=\frac{1}{2}\rho UB[C_L\chi_{Lu}(n)\bar{L}_u 2u(t)+C_L^{'}\chi_{Lw}(n)\bar{L}_w w(t)] \quad (8.11\text{-a})$$

$$D_{bi}(t)=\{D_{b1}(t),D_{b2}(t),\ldots D_{bN}(t)\}=\frac{1}{2}\rho UB[C_D\chi_{Du}(n)\bar{L}_u 2u(t)+C_D^{'}\chi_{Dw}(n)\bar{L}_w w(t)] \quad (8.11\text{-b})$$

$$M_{bi}(t)=\{M_{b1}(t),M_{b2}(t),...,M_{bN}(t)\}=\frac{1}{2}\rho UB^2[C_M\chi_{Mu}(n)\bar{L}_u 2u(t)+C_M^{'}\chi_{Mw}(n)\bar{L}_w w(t)] \quad (8.11\text{-c})$$

or in such following form as (Solari and Tubino 2005)

$$F_b(t)=\frac{1}{2}\rho UB\left[C_u\chi_{Fu}(n)u(t)+C_w\chi_{Fw}(n)w(t)\right] \quad (8.12\text{-a})$$

$$F_b(t)=\begin{bmatrix}L_{bi}(t)\\D_{bi}(t)\\M_{bi}(t)\end{bmatrix};C_u=\frac{1}{2}\rho UB\begin{bmatrix}2C_L\bar{L}\\2C_D\bar{L}\\2BC_M\bar{L}\end{bmatrix};C_w=\begin{bmatrix}(C_L^{'}+C_D)\bar{L}\\(C_D^{'}-C_L)\bar{L}\\BC_M^{'}\bar{L}\end{bmatrix};\bar{L}=diag(L_i);L_i=\begin{cases}0.5|y_2-y_1|, & i=1\\0.5|y_{i+1}-y_{i-1}|, & 1<i<N\\0.5|y_N-y_{N-1}|, & i=N\end{cases} \quad (9.12\text{-b})$$

where C_u, C_w : full-scale force coefficient matrices; L_i: influenced distance at node i; y: longitudinal structural coordinate

In the frequency domain, transforming the uniform buffeting forces into a form of power spectral density using second-order Fourier transform, omitting cross correlation components between u(t) and w(t), the power spectral densities of the uniform buffeting forces are obtained:

$$S_L(n)=(\frac{1}{2}\rho U^2B)^2[C_L^2\chi_{Lu}^2(n)\frac{4S_{uu}(n)}{U^2}+(C_L^{'}+C_D)^2\chi_{Lw}^2(n)\frac{S_{ww}(n)}{U^2}] \quad (8.13\text{-a})$$

$$S_D(n)=(\frac{1}{2}\rho U^2B)^2[C_D^2\chi_{Du}^2(n)\frac{4S_{uu}(n)}{U^2}+(C_D^{'}-C_L)^2\chi_{Dw}^2(n)\frac{S_{ww}(n)}{U^2}] \quad (8.13\text{-b})$$

$$S_M(n)=(\frac{1}{2}\rho U^2B^2)^2[C_M^2\chi_{Mu}^2(n)\frac{4S_{uu}(n)}{U^2}+C_M^{'\,2}\chi_{Mw}^2(n)\frac{S_{ww}(n)}{U^2}] \quad (8.13\text{-c})$$

where $S_L(n), S_D(n), S_M(n)$: power spectra of lift, drag and moment, respectively; $S_{uu}(n), S_{ww}(n)$: auto power spectra of uni-variate turbulent processes u(t), w(t). Accordingly, the power spectral densities of the full-scale buffeting forces can be determined as:

$$S_{F_b}(n)=(\frac{1}{2}\rho UB)^2\left[C_u^2\chi_{Fu}^2(n)S_u(n)+C_w^2\chi_{Fw}^2(n)S_w(n)\right] \quad (8.14)$$

The buffeting forces formulated here are used for predicting the gust response of bridges.

8.4 Gust response formulation

Multi-degree-of-freedom motion equations of structures subjected to the buffeting forces can be expressed by means of the Finite Element Method (FEM):

$$M\ddot{U}+C\dot{U}+KU=F_b(t) \quad (8.15)$$

where $F_b(t)$: full-scale buffeting forces; M, C, K : structural mass, damping and stiffness matrices, respectively; $U=\{h(t)^T, p(t)^T, a(t)^T\}$: displacement vector containing three vertical, lateral and rotational displacements; $\dot{U}, \ddot{U}$: velocity and acceleration vectors.

Transforming into the mass matrix-nornalized structural generalized coordinates using the modal analysis and the Structural Modal Transformation (SMT):

$$U(t) = \Phi\xi(t) \approx \sum_{i=1}^{\overline{M}} \phi_i \xi_i \; ; \Phi^T M \Phi = I \; ; \Phi^T K \Phi = \Omega \; ; \Phi^T C \Phi = \Xi \tag{8.16}$$

where $\xi(t)$: structural generalized coordinates; Φ : modal matrix $\Phi = [\phi_1, \phi_2, ..., \phi_M]^T$; ϕ_i : i-th structural mode; I, Ω, Ξ : unit and diagonalized matrices; $\overline{M}$: number of truncated structural modes $\overline{M} << M$, M: number of dynamic degree-of-freedom of structure.

Single-degree-of-freedom motion equation in the i-th generalized coordinate is expressed

$$\ddot{\xi}_i(t) + 2\zeta_i \omega_i \dot{\xi}_i(t) + \omega_i^2 \xi_i(t) = \phi_i^T F_b(t) \tag{8.17-a}$$

$$\ddot{\xi}_i(t) + 2\zeta_i \omega_i \dot{\xi}_i(t) + \omega_i^2 \xi_i(t) = \phi_i^T \frac{1}{2} \rho U B \left[C_u \chi_{Fu_i}(n) u(t) + C_w \chi_{Fw_i}(n) w(t) \right] \tag{8.17-b}$$

where ω_i, ζ_i, m_i: circular frequency, damping ratio, mass or inertia at the i-th generalized coordinate.

Power spectral density of generalized response at the i-th generalized coordinates can be obtained in the frequency domain thanks to the first-order Fourier transform:

$$\hat{\xi}_i(n) = \frac{1}{2} \rho U B \, | H_i(n) | \, \phi_i^T \left[C_u \chi_{Fu_i}(n) \hat{u}(n) + C_w \chi_{Fw_i}(n) \hat{w}(n) \right] \tag{8.18}$$

where $\hat{\xi}_i(n)$: Fourier transform of generalized response at the i-th generalized coordinate; $\hat{u}(n), \hat{w}(n)$: Fourier transform of u-,w- random turbulent processes; $|H_i(n)|^2$: Frequency Response Function (FRF) or mechanical admittance function at natural frequency n_i.

Here the Fourier transform components of u(t), w(t) are decomposed and approximated due to the Spectral Proper Transformation (SPT) following Eqs.(8.8-a, 8.8-b), we have:

$$\hat{\xi}_i(n) = \frac{1}{2} \rho U B \, | H_i(n) | \left[\chi_{Fu_i}(n) \sum_{j=1}^{\hat{M}} \phi_i^T C_u \psi_{uj}(n) \hat{y}_{uj}(n) + \chi_{Fw_i}(n) \sum_{j=1}^{\hat{M}} \phi_i^T C_w \psi_{wj} \hat{y}_{wj}(n) \right] \tag{8.19}$$

or

$$\hat{\xi}_i(n) = \frac{1}{2} \rho U B \, | H_i(n) | \left[\chi_{Fu_i}(n) \sum_{j=1}^{\hat{M}} A_{uij}(n) \hat{y}_{uj}(n) + \chi_{Fw_i}(n) \sum_{j=1}^{\hat{M}} A_{wij}(n) \hat{y}_{wj}(n) \right] \tag{8.20-a}$$

$$A_u(n) = \sum_{j=1}^{\hat{M}} A_{uij}(n) = \sum_{j=1}^{\hat{M}} \phi_i^T C_u \psi_{uj}(n); \; A_w(n) = \sum_{j=1}^{\hat{M}} A_{wij}(n) = \sum_{j=1}^{\hat{M}} \phi_i^T C_w \psi_{wj}(n) \tag{8.20-b}$$

where $A_{uij}(n) = \phi_i^T C_u \psi_{uj}(n), A_{wij}(n) = \phi_i^T C_w \psi_{wij}(n)$: cross modal coefficients which represent the interaction between the i-th structural mode ϕ_i and the j-th turbulent one ψ_j .

Power spectral densities of the generalized responses can be obtained thanks to the

second-order Fourier transform as follows:

$$S_{\xi_i}(n) = (\frac{1}{2}\rho UB)^2 \mid H_i(n) \mid^2 (\phi_i^T)^2 \left[C_u^2 \chi_{Fu}^2(n) S_u(n) + C_w^2 \chi_{Fw}^2(n) S_w(n) \right] \tag{8.21}$$

where $S_{\xi_i}(n)$: power spectra of the generalized response of the i-th generalized coordinate; $S_u(n), S_w(n)$: cross spectral matrices.

Optimum approximations of the cross spectral matrices are used following Eqs.(8.9-a, 8.9-b), we have:

$$S_{\xi_i}(n) = (\frac{1}{2}\rho UB)^2 \mid H_i(n) \mid^2 \left[\chi_{Fu}^2(n) \sum_{j=1}^{\hat{M}} \phi_i C_u^2 \psi_{uj}(n) \lambda_{uj}(n) \psi_{uj}^{*T}(n) \phi_i^T + \chi_{Fw}^2(n) \sum_{j=1}^{\hat{M}} \phi_i C_w^2 \psi_{wj}(n) \lambda_{wj}(n) \psi_{wj}^{*T}(n) \right] \tag{8.22}$$

and

$$S_{\xi_i}(n) = (\frac{1}{2}\rho UB)^2 \left[\chi_{Fu}^2(n) \mid H_i(n) \mid^2 \sum_{j=1}^{\hat{M}} A_{uij}(n) \lambda_{uj}(n) A_{uij}^{*T}(n) + \chi_{Fw}^2(n) \mid H_i(n) \mid^2 \sum_{j=1}^{\hat{M}} A_{wij}(n) \lambda_{wj}(n) A_{wij}^{*T}(n) \right] \tag{8.23}$$

The power spectral densities of generalized response can be obtained in the comprehensive form such $S_\xi(n) = H(n) S_{F_b}(n) H(n)^{*T}$ as follows:

$$S_\xi(n) = (\frac{1}{2}\rho UB)^2 \left[H(n) \Phi C_u^2 \Psi_u(n) \Lambda_u(n) \Psi_u^{*T} \mathrm{K}(n)^2 \Phi^T H(n)^{*T} + H(n) \Phi C_w^2 \Psi_w(n) \Lambda_w(n) \Psi_w^{*T} \mathrm{K}(n)^2 \Phi^T H(n)^{*T} \right] \tag{8.24}$$

and

$$S_\xi(n) = (\frac{1}{2}\rho UB)^2 \left[H(n) A_u(n) \Lambda_u(n) K(n)^2 A_u^{*T}(n) H^T(n) + H(n) A_w(n) \Lambda_w(n) K(n)^2 A_w^{*T}(n) H(n)^T \right] \tag{8.25}$$

where $H(n)$: Frequency Response Function matrix in the structurally generalized coordinates, $H(n) = diag(\mid H_1(n) \mid, \mid H_2(n) \mid, \ldots \mid H_{\overline{M}}(n) \mid)$; $K(n)^2$: squared aerodynamic admittance function.

As the result, the power spectral densities of global response are determined:

$$S_U(n) = \Phi^T S_\xi(n) \Phi \tag{8.26}$$

where $S_U(n)$: power spectra of the global response.

Then, the mean square of the structural response is obtained

$$\sigma_U^2 = \frac{1}{2\pi} \int_0^\infty S_U(n) dn \tag{8.27}$$

where σ_U^2: Mean square of the global response

Finally, global responses with respect to vertical, longitudinal and rotational directions can be combined from single-modal responses due to the principle of the squared root of the sum of the squares (SRSS):

$$\sigma_r(n) = \sqrt{\sum_{i=1}^{\overline{M}_r} \sigma_{r,i}^2}\,;\ r = h, p, a \tag{8.28}$$

where r denotes to displacement components: vertical (h), longitudinal (p), rotational (a); $\overline{M}_r$: number of component modes in response combination;

8.5 Numerical example

A concrete cable-stayed bridge was taken for numerical example using the above-mentioned computational procedures. Bridge was spanned by 40.5+97+40.5=178m. 3D frame model was built thanks to the finite element method (FEM). There were 30 discrete nodes in the bridge deck. Total 30 nodes were on the bridge deck, while nodes 8, 23 at pylons. First ten structural modes were analyzed. Natural frequencies of the first ten structural modes vary between 0.61Hz÷1.86Hz. Damping ratios of every structural mode were assumed to be 0.005. It is also assumed that the buffeting forces act on the bridge deck only, and the forces on towers and cables are negligible. Aerodynamic static coefficients of cross section at balanced angle ($\alpha_0 = 0^0$) and their first derivatives were experimentally determined as follows: $C_L = 0.158$, $C_D = 0.041$, $C_M = 0.174$, $C_L^{'} = 3.73$, $C_D^{'} \approx 0$, $C_M^{'} = 2.06$. Two 30-variate turbulent loading processes u(t), w(t) are obtained at the deck nodes: $u(t) = \{u_1(t), u_2(t), \ldots, u_{30}(t)\}^T$ and $w(t) = \{w_1(t), w_2(t), \ldots, w_{30}(t)\}^T$.

One-sided auto spectral density functions of u-, w-turbulent components were obtained due to the Kaimail's and the Panofsky's spectral models, respectively (Simiu and Scanlan 1976). Spanwise coherence function was used the Davenport's empirical exponential function with decay factors (Davenport 1962) with decay factors $c_u = 10,\ c_w = 6.5$.

Aerodynamic admittance function was used the Liepmann's empirical function as approximation of the Sears' function as follows (Liepmann 1958):

$$\left|\chi_i(n)\right|^2 = \frac{1}{1 + \dfrac{2\pi^2 n_i B}{U}} \tag{8.29}$$

Mechanical admittance function was determined as follows:

$$\left|H_i(n)\right|^2 = \left[\left(1 - \frac{n^2}{n_i^2}\right)^2 + 4\zeta_i^2 \frac{n^2}{n_i^2}\right]^{-1} \tag{8.30}$$

Global responses of bridge is required to be predicted at referred mean velocity U=20m/s.

Tab.8.1 Modal characteristics of fundamental structural modes

Mode shape	Eigenvalue ω^2	Frequency (Hz)	Period (s)	Modal Feature
1	1.47E+01	0.609913	1.639579	S-V-1
2	2.54E+01	0.801663	1.247406	A-V-2
3	2.87E+01	0.852593	1.172893	S-T-1
4	5.64E+01	1.194920	0.836876	A-T-2
5	6.60E+01	1.293130	0.773318	S-V-3
6	8.30E+01	1.449593	0.689849	A-V-4
7	9.88E+01	1.581915	0.632145	S-T-P-3
8	1.05E+02	1.630459	0.613324	S-V-5
9	1.12E+02	1.683362	0.594049	A-V-6
10	1.36E+02	1.857597	0.53830	S-V-7

Note : S: Symmetric mode T: Torsional mode shape
A: Asymmetric mode P: Horizontal mode shape
V: Heaving mode shape

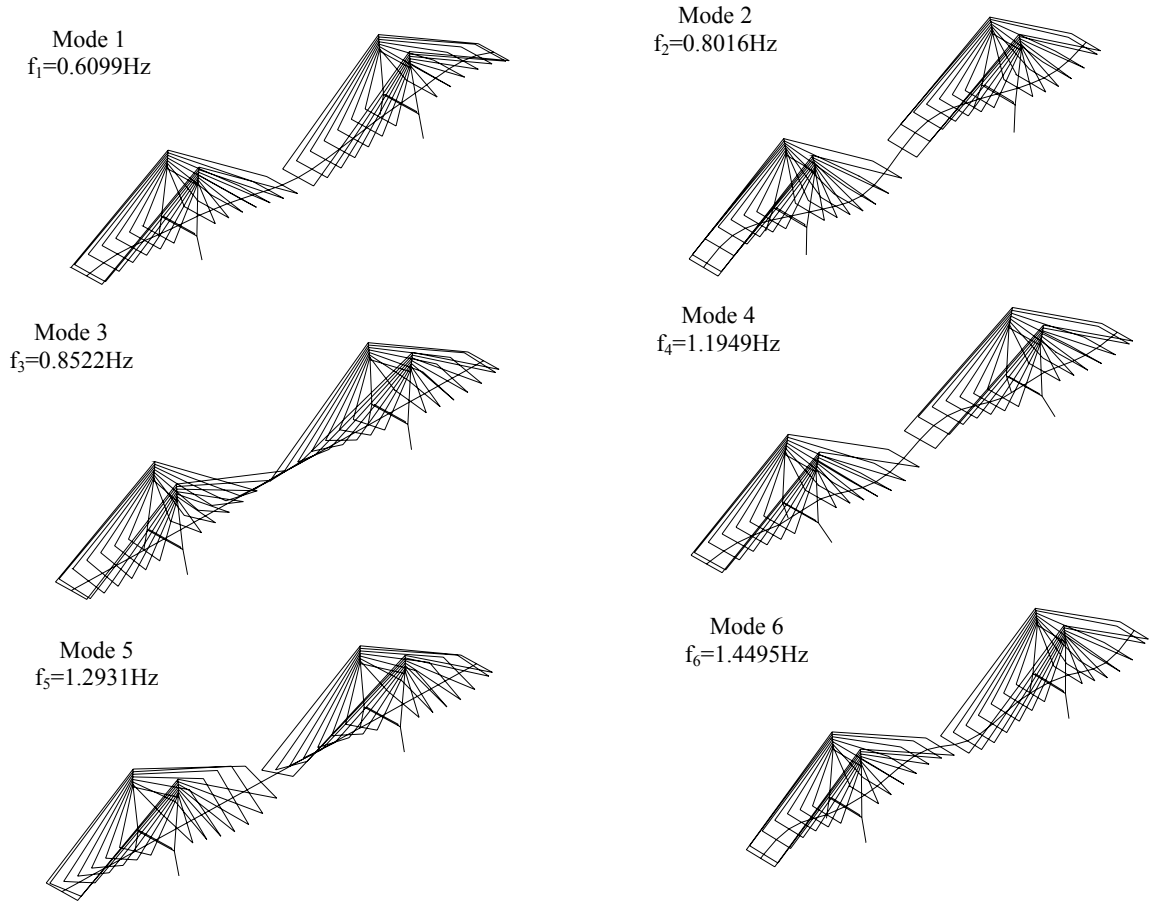

Fig. 8.2 Fundamental structural mode shapes

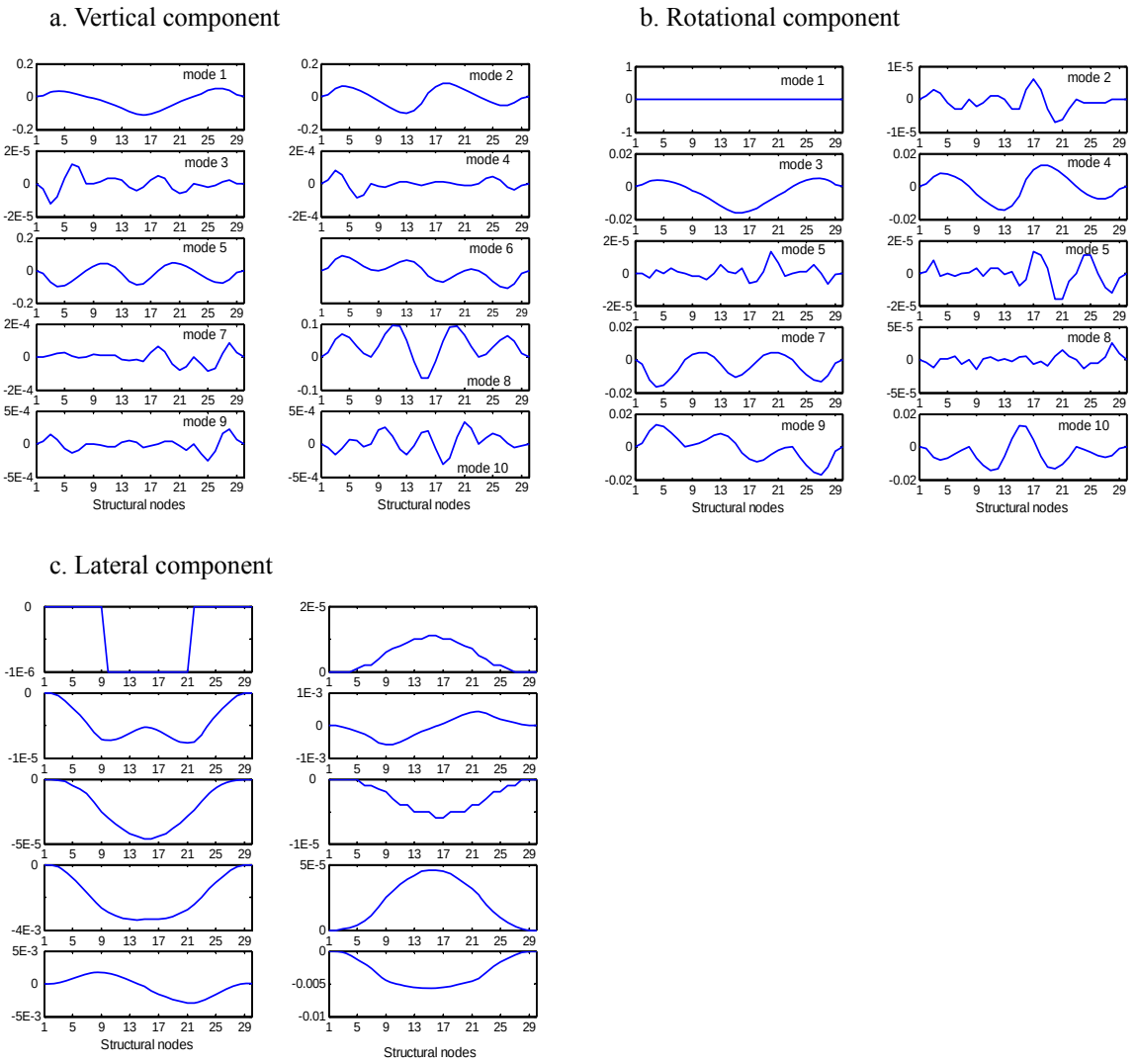

Fig. 8.3 Normalized amplitudes of structural modes: a. vertical displacement, b. rotational, c. lateral

Cross spectral matrices of the random turbulent processes u(t), w(t) acting on 30 deck nodes are constructed from available auto spectral densities $S_{uu}(n), S_{ww}(n)$ and coherence functions $COH_u(n,\Delta), COH_w(n,\Delta)$. The cross spectral matrices are determined as three-dimensional symmetrical squared matrices, in which the third dimension contains frequency information.

8.6 Results and discussions

The cross spectral matrices of the random turbulent processes are decomposed thanks to the eigen problem to find out entire 30 pairs of spectral eigenvalues and associated spectral eigenvectors depending on the frequency. Because the spectral eigenvectors create the orthogonality basis at every frequency, thus called as the spectral turbulent modes.

Figure 8.4 shows the first five spectral eigenvalues $\lambda_1(n) \div \lambda_5(n)$ on the frequency band 0.01÷10Hz. It is observed that the first spectral eigenvalue $\lambda_1(n)$ exhibits much higher than the others on the very low frequency band 0.01÷0.2Hz with the case of u-turbulence, 0.01÷0.5Hz with that of w-turbulence, however, all spectral eigenvalues seem not to differ beyond these frequency thresholds. This can imply that only first pair of spectral eigenvalue and spectral eigenvector seems to be accuracy enough for representing and simulating the random turbulent processes at the low frequency bands, however, more pairs should be required at the higher frequency bands.

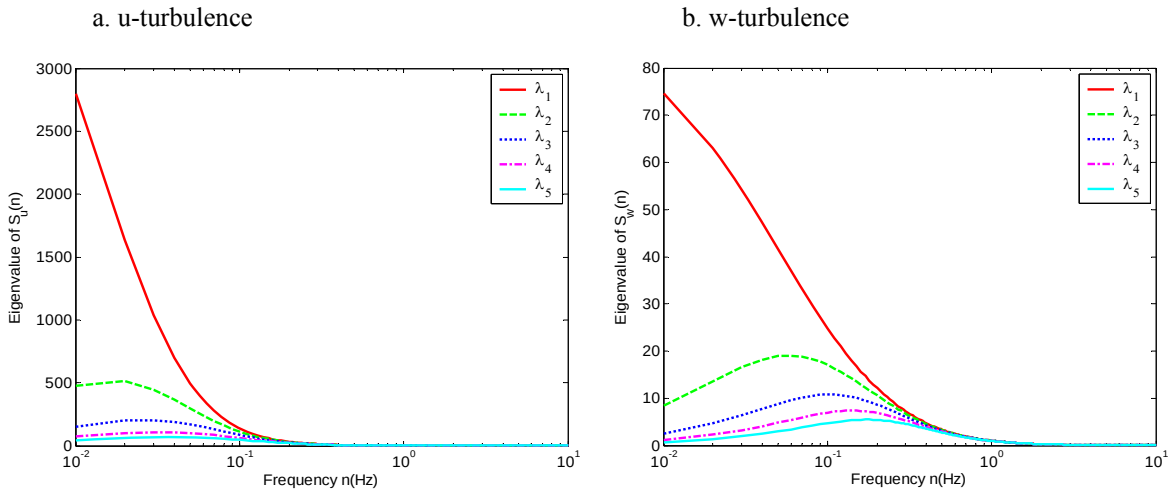

Fig. 8.4 First five spectral eigenvalues: a. u-turbulence, b. w-turbulence

The first four spectral eigenvectors $\psi_{\upsilon 1}(n), \psi_{\upsilon 2}(n), \psi_{\upsilon 3}(n);\ \upsilon = u, w$ (the spectral turbulent modes) on the same spectral band 0÷10Hz is expressed in Figure 8.5. It can be seen that the turbulent modes of u-,w-turbulences look like as symmetrically and asymmetrically waves, in which number of wave halves increases incrementally with order of the spectral turbulent modes. Shape of the turbulent modes of u-,w-turbulent components, moreover, are unchanged during structurally natural frequency band (0.61÷1.85Hz). Moreover, the spectral turbulent modes do not changed with the frequency, because the spectral modes do not change their values but sign on the frequency domain.

Figure 8.6 expresses more details the first five spectral turbulent modes at the first five structural natural frequencies, in which thick solid line, dashed one, dotted one, dot dashed one and light solid exhibit the first five turbulent modes, respectively. As can be seen from Figure 8.6, the first turbulent modes of both u-turbulence and w-one keep constant their shape and sign at structural natural frequencies, whereas the others change their sign at the natural frequencies. Spectral modes of the u-turbulence are similar to corresponding spectral modes of the w-turbulence in both their shapes and values.

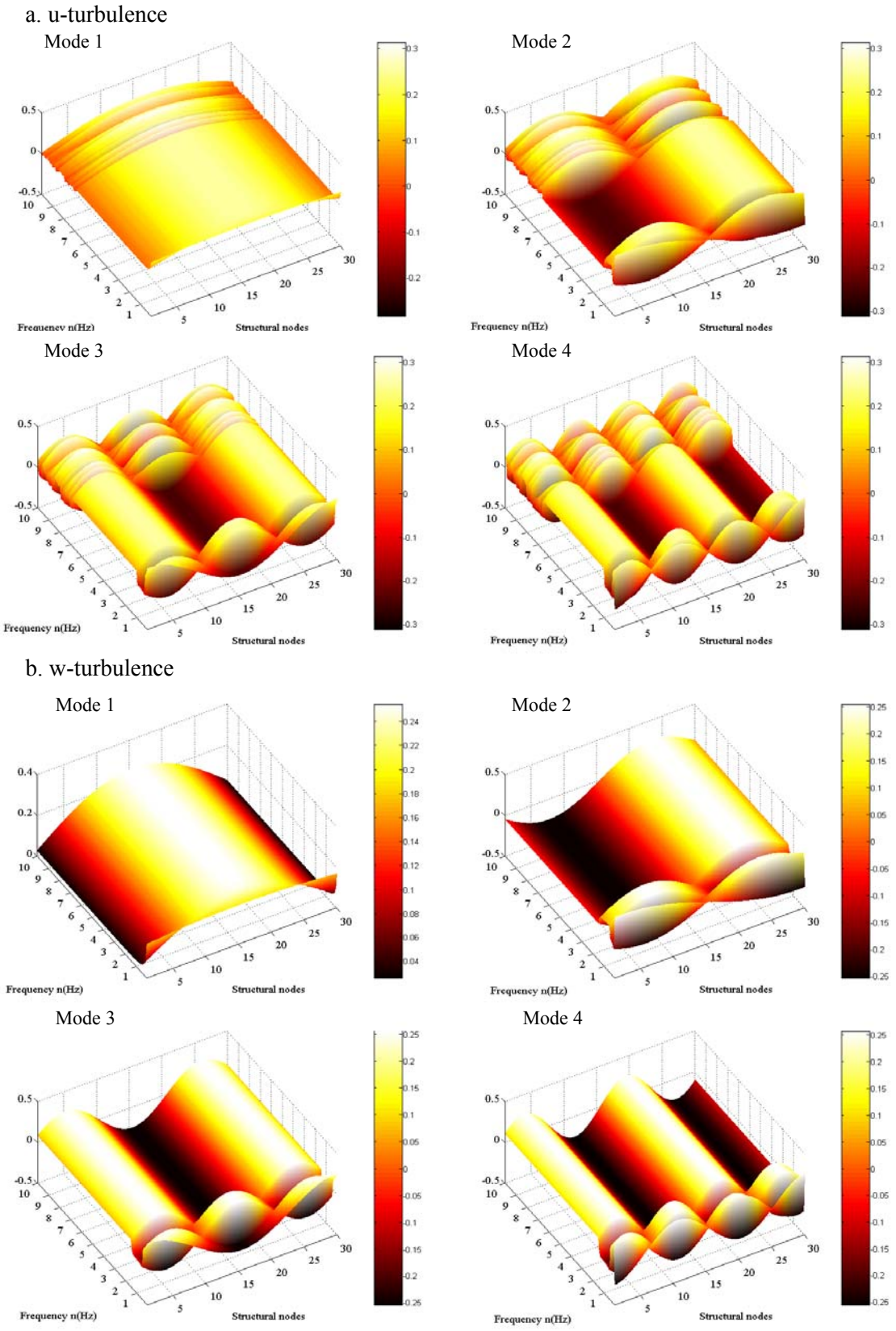

Fig. 8.5 Spectral turbulent modes: a. u-turbulence, b. w-turbulence

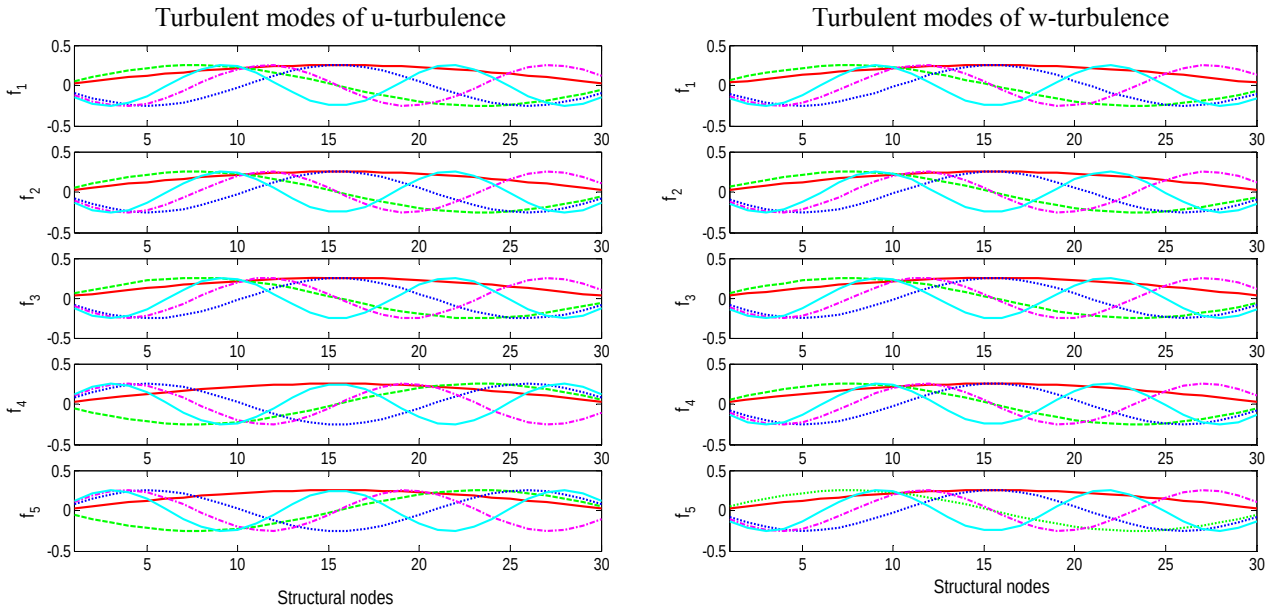

Fig. 8.6 First five spectral turbulent modes at natural frequencies: thick solid: 1st turbulent mode, dashed: 2nd mode, dotted: 3rd mode; dot dashed: 4th mode, light solid: 5th mode

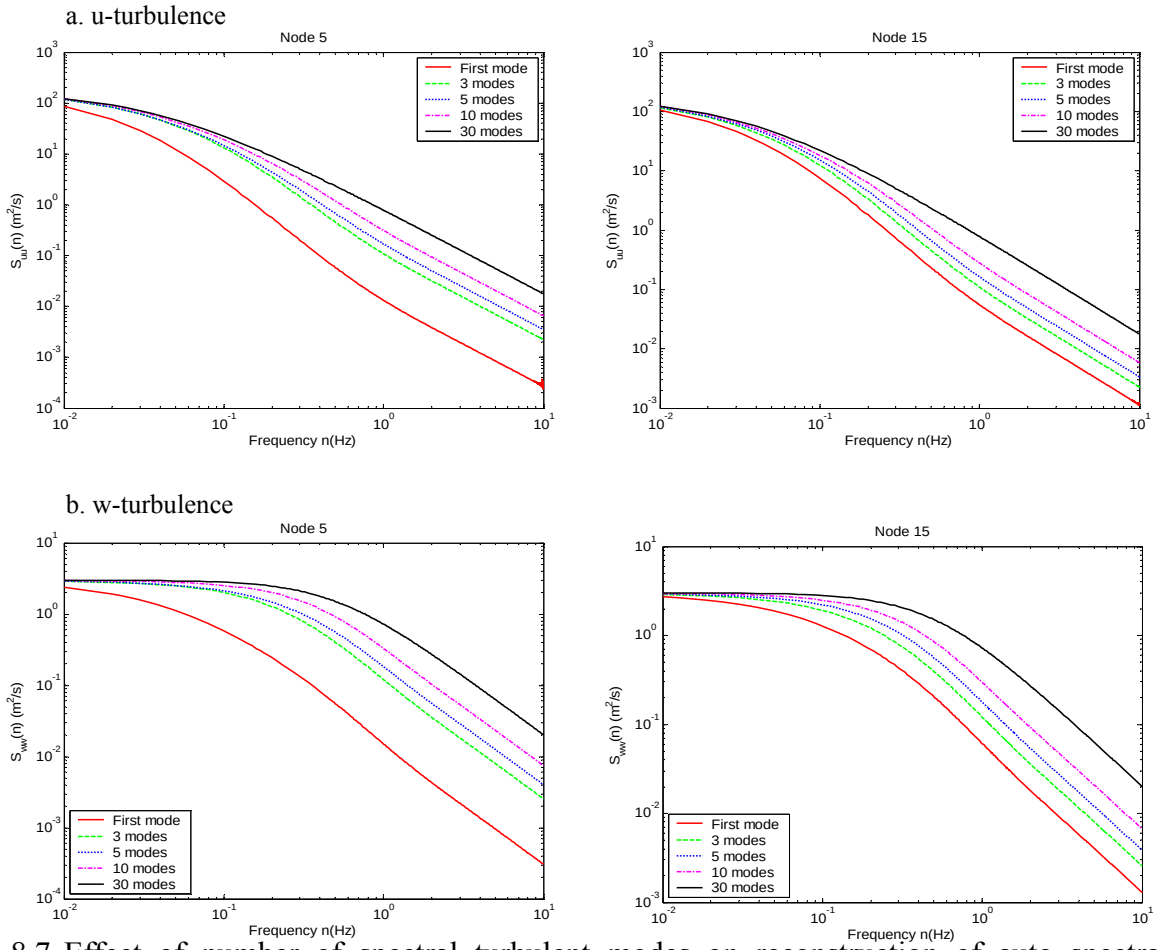

Fig. 8.7 Effect of number of spectral turbulent modes on reconstruction of auto spectral densities at nodes 5 and 15: a. u-turbulence, b. w-turbulence

Figure 8.7 shows the reconstruction of auto power spectra of u-,w-turbulences at referred mid-span node 15 using limited number of truncated spectral turbulent modes, $\hat{M} = 1;3;5;10;30$, here totally 30 turbulent modes imply for targeted value. Auto spectral values using truncated turbulent modes differ with increase of frequency band. At very low frequencies, only first or few turbulent modes are sufficient to reconstruct the auto spectral densities of turbulent field, however, many turbulent modes should be used at high frequencies. This finding is similar to that comment from Figure 8.4. Effect of number of the spectral turbulent modes on reconstruction of the auto power spectra of the u-,w-turbulences at another deck nodes also have similar results, but do not present here for the sake of brevity.

Effect of number of truncated turbulent modes on power spectral densities of the generalized responses (consisting of the vertical and rotational displacements) at referred mid-span node 15 corresponding to some structural modes is expressed in Figure 8.8. Numbers of truncated spectral modes used for computation are the first spectral turbulent mode, the first five modes, the first ten modes and total thirty modes (as targeted response).

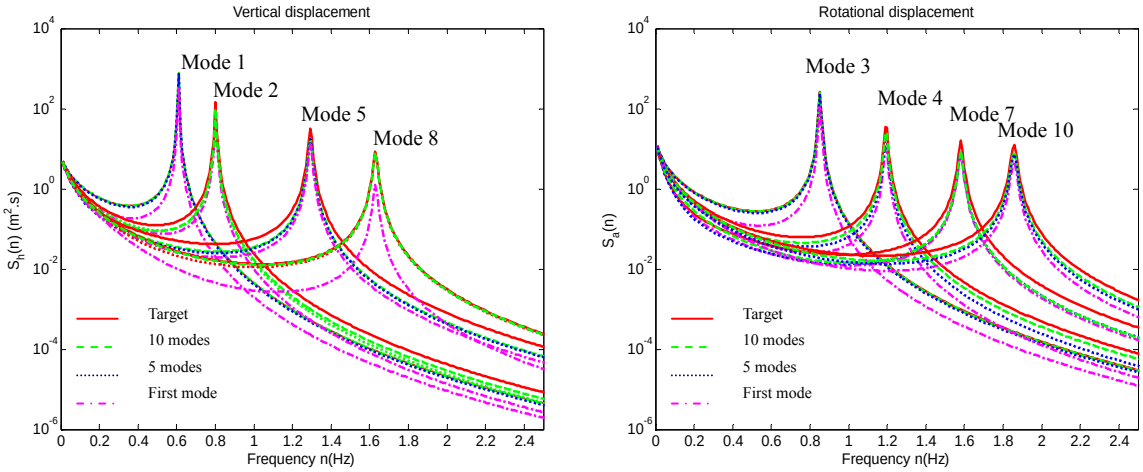

Fig.8.8 Effect of number of turbulent modes on power spectral densities of generalized vertical and rotational displacements at mid-span node 15

Figure 8.9 shows the power spectral densities of the global responses at mid-span node 15 (representative node 15 is illustrated here for a sake of brevity) and effect of number of truncated turbulent modes on the global responses. As can be seen from Figure 8.9, there is no much different among contribution of truncated turbulent modes on the global vertical and rotational displacements. It also indicates that the first turbulent mode significantly contributes on the power spectral densities of the global responses. Power spectra of resonant responses, moreover,

can be observed at the structural modal frequencies due to influence of frequency response functions at these modal frequencies.

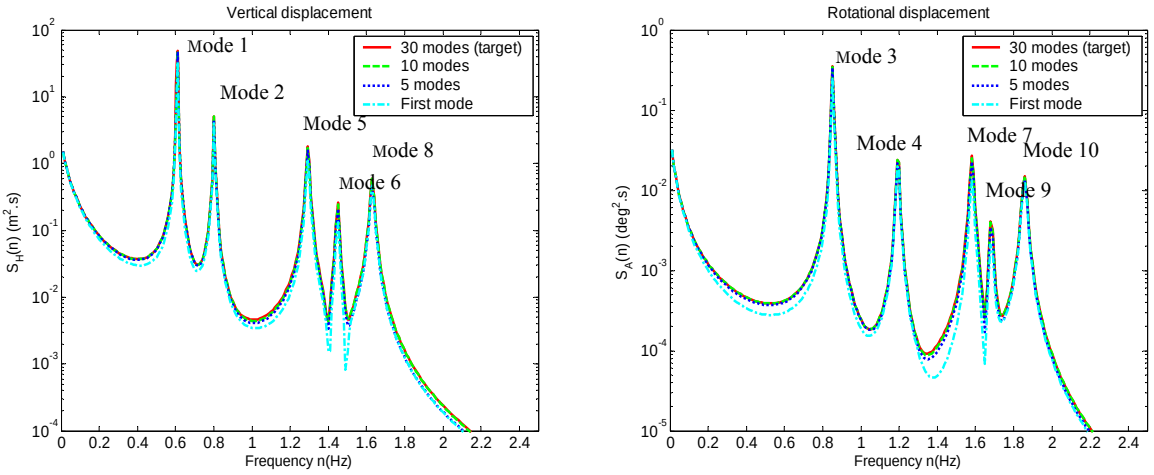

Fig.8.9 Effect of number of turbulent modes on power spectral densities of global vertical and rotational displacements at mid-span node 15

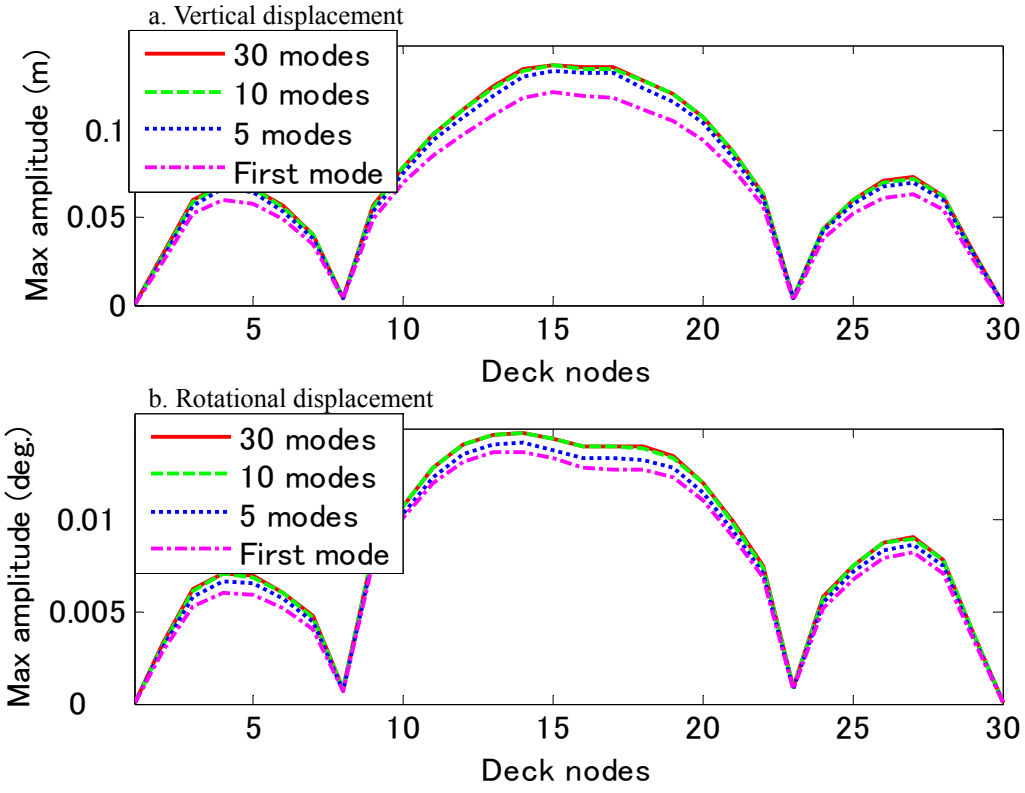

Fig.8.10 Effect of number of turbulent modes on RMS of global responses at whole deck nodes

Figure 8.10 expresses the root mean squares (RMS) of the global responses at all deck nodes with emphasis on effect of truncated turbulent modes on the global responses. The important role of the first turbulent mode on the global response can be also observed, because there is no much difference of the global response contribution between the first spectral mode and the total 30 spectral turbulent modes.

Tab. 8.2 Effect of spectral modes on maximum global amplitude

N.modes	Node 5	%	Node15	%
30	0.067	100	0.147	100
10	0.066	99	0.147	99
5	0.064	95	0.144	97
1	0.058	86	0.131	88

N.modes	Node 5	%	Node15	%
30	.0069	100	0.015	100
10	.0068	98	0.015	99
5	.0065	93	0.014	95
1	.0059	84	0.012	80

For example, the first turbulent mode, first 5 modes, first 10 modes contribute 13.1cm(88%), 14.4cm(97%), 14.7cm(99%) on 14.7cm-maximum vertical displacement (totally 30 turbulent modes) and 0.012^0(80%), 0.014^0(95%), 0.015^0(99%) on 0.015^0-maximum rotational displacement

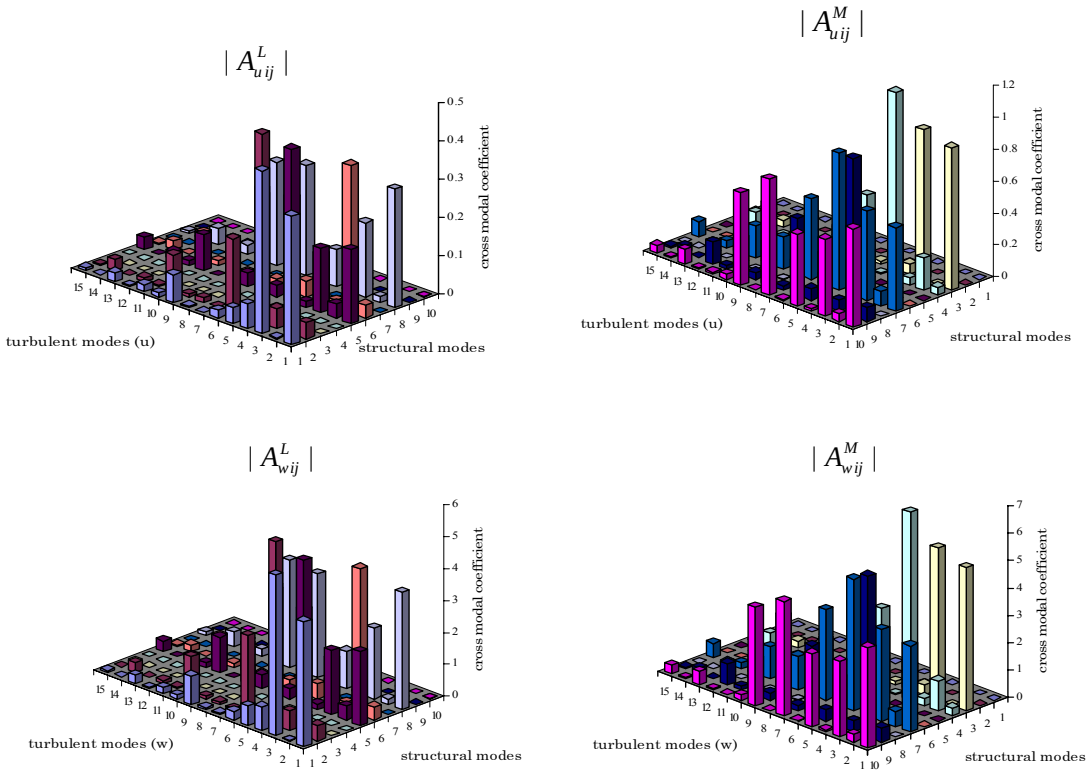

Fig.8.11 Cross modal coefficients between spectral turbulent modes and structural modes at every natural frequency

Influence of the spectral turbulent modes on structural ones has been investigated by the cross modal coefficients. Figure 8.11 shows the cross modal coefficients between first 15 spectral turbulent modes of u-,w-turbulences and first 10 structural modes for lift or vertical displacement and moment or rotational displacement. It is found out that few turbulent modes (in this case, only first 9 turbulent modes) can excite structural modes, and higher turbulent modes are orthogonal to the structural modes. For more detail, first heaving mode corresponding to the first structural mode and first torsional mode corresponding to the third structural modes are excited by the first spectral turbulent mode and the third spectral turbulent mode, respectively. Thus, the gust response can be obtained by only accounting effective cross modal coefficients. This suggests that the prediction of dominant gust response of structures can be simplified by combination between few turbulent modes and few structural ones based on effective cross modal factors. These results are also good agreements with the findings in Solari and Tubino 2005.

8.7 Conclusion

This chapter has presented the application of the proper orthogonal decomposition and its spectral proper transformation to predict the gust response of full-scale bridges due to the randomly buffeting forces. Moreover, effect of the orthogonally turbulent loading modes on the generalized and global responses of bridges also is investigated.

Some conclusions are given as follows:

(1) New and comprehensive approach on the gust response prediction of bridges in the frequency domain using the proper orthogonal decomposition-based spectral proper transformation has been presented here. The main points are that the multi-variate spatially-correlated random turbulent field acting on bridge deck has been formulated in the comprehensive form due to the cross spectral matrix of this random turbulent field, then the random turbulent field is decomposed and approximated by low-order spectral turbulent modes which are used to estimate the gust response.

(2) Only limited number of low-order spectral turbulent modes dominantly contributes on structural gust response. In many cases, the first spectral turbulent mode play very significant role and seems to be accuracy enough in predicting the gust response of bridges in the frequency domain, especially in the low frequency range.

Further development in the application of the spectral proper transformation in predicting the gust response of structures is going to be accounted the coupling effect between the buffeting forces and the aeroelastic forces (or flutter self-excited forces).

References

Carassale, L., Piccardo, G., Solari, G. (1999), "Double modal transformation and wind engineering applications", *J. Engrg. Mech.*, ASCE, **127(5)**, 432-439.

Chen, X., Matsumoto, M., Kareem, A. (2000a), "Aerodynamic coupling effects on flutter and buffeting of bridges", *J. Engrg. Mech.*, ACSE, **126(1)**, 17-26.

Chen, X., Matsumoto, M., Kareem, A. (2000b), "Time domain flutter and buffeting response analysis of bridges", *J. Engrg. Mech.*, ACSE, **126(1)**, 7-16.

Chen, X., Kareem, A. (2005), "Proper orthogonal decomposition-based modeling, analysis, and simulation of dynamic wind load effects on structures", *J. Engrg. Mech.*, ASCE, **131(4)**, 325-339.

Davenport, A.G. (1962), "Buffeting of a suspension bridge by storm winds", *J. Struct. Div.*, ASCE

Katsuchi, H., Jones, N.P., Scanlan, R.H. (1999), "Multimode coupled flutter and buffeting analysis of the Akashi-Kaikyo bridge", *J. Struct. Engrg.*, ASCE, **125(1)**, 60-70.

Le, T.H. (2004), "Experimental determination of aerodynamic coefficients of bridge sections in wind tunnel tests", *Vietnamese J. of Highways and Bridges*, **10**.

Jain, A., Jones, N.P., Scanlan, R.H. (1996), "Coupled flutter and buffeting analysis of long-span bridges", *J. Struct. Engrg.*, ASCE, **122(7)**, 716-725.

Matsumoto, M., Chen, X., Shiraishi, H. (1994), "Buffeting analysis of long-span bridges with aerodynamic coupling", *The 13th Nat. Sympo. on Wind Eng.*, JAWE, 227-232.

Matsumoto, M., Shirato, H., Le, T.H. (2006), "Gust response of bridges based on spectral proper transformation", *The 19th KKCNN Sympo. on Civ. Eng. (KKCNN19)*, Kyoto, Japan, December 10-12.

Matsumoto, M., Shirato, H., Le, T.H. (2007), "Time and frequency domain gust response of bridges using proper orthogonal decomposition", *The 12th Int'l Conf. on Wind Eng. (ICWE12)*, Cairns, Australia, July 1-6.

Li, Y.S., Kareem, A. (1995), "Stochastic decomposition and application to probabilistic dynamics", *J. Engrg. Mech.*, ASCE, **121(1)**, 162-174.

Simiu, E., Scanlan, S.H. (1997), *Wind Effects on Structures,* John Wiley&Sons.

Solari, G., Carassale, L. (2000), "Modal transformation tools in structural dynamics and wind engineering", *Wind & Structures*, **3 (4)**, 221-241.

Solari, G., Tubino, F. (2005), "Gust response of long span bridges by double modal transformation", *The 4th Euro. and Afri. Conf. on Wind Eng. (EACWE4),* Praque, Czech.

Chapter 9

Gust Response of Bridges using Covariance Proper Transformation

9.1 Introduction

Gust response prediction of long-span bridges subjected to the turbulent-induced forces (the buffeting forces) requires more concern among wind-induced vibrations and their aerodynamic responses. General formulation of gust response prediction of bridges was proposed by Davenport 1962 in the frequency domain. Recently, the state-of-the-art buffeting response analysis of bridges in coupling with the aeroelastic forces in the time domain has been carried out by some authors (eg., Matsumoto et al. 1994, Matsumoto and Chen 1996, Boonyapinyo et al. 1999, Chen at al. 2000). Computational difficulties are to decompose spatially-correlated full-scale buffeting forces into the structurally generalized coordinates which are decomposed thanks to the structural modal transformation (SMT) in order to estimate the generalized responses in the generalized coordinates and then the global responses of structures. In conventional methods in both the frequency-domain and the time-domain, the so-called joint acceptance function (JAF) has been used to decompose the full-scale buffeting forces into the structurally generalized coordinates.

Karhunen-Loeve decomposition, also known as the proper orthogonal decomposition (POD) (Lumley 1970), has been applied in many engineering fields (Liang et al. 2002). In the wind engineering topics, the proper orthogonal decomposition has been applied for analysis and order-reduced modeling of the random fields (Tamura et al. 1999, Matsumoto et al. 2006), representation and simulation of the random fields (Tubino and Solari 2005), stochastic dynamic response (Carassale et al. 1999, Solari and Carassale 2000, Chen and Kareem 2005). Basing on the basic matrix of either the zero-time-lag covariance matrix or cross spectral density matrix of the random field, the proper orthogonal decomposition has been branched by either the covariance proper transformation (CPT) or the spectral proper transformation (SPT). New approach of the gust response analysis of structures has been proposed recently by Carassale et al. 1999 in which the structural modes decomposed by the structural modal transformation are

associated with either the covariance turbulent loading modes or the spectral turbulent loading modes decomposed from proper transformations in order to determine the generalized responses and the global responses of structures. Combination manner between the structural modes and the turbulent loading modes for predicting the stochastic response of structures is named by Carassale et al. 1999 and Solari and Carassale 2000 as the double modal transformations (DMT). So far, almost literatures on the proper orthogonal decomposition application to the stochastic response of structures are formulated based on the spectral proper transformation in the frequency domain (Carassale et al. 1999, Solari and Carassale 2000, Chen and Kareem 2005). The frequency-domain gust response of structures using the spectral proper transformation has been formulated in the previous chapter. The stochastic response of structures formulated in the time domain using the covariance proper transformation is very promising because of its direct and capable solutions for nonlinear problems and unsteady aerodynamics. However, digital simulation of the time series of the random turbulent field and the direct integration methods of generalized dynamic equations are usually required that are associated with time-consumed and difficult computation.

This chapter will present the application of the covariance matrix-branched proper orthogonal decomposition and its covariance proper transformation to decompose the random turbulent loading processes, then to formulate the time-domain gust response of structures. The Newton-beta integration method is also applied to obtain the time-domain solution of the gust responses in the generalized and global coordinates. Numerical example of cable-stayed bridge will be taken into account for illustration and demonstration.

9.2 Covariance proper transformation

The main idea of the covariance matrix-based proper orthogonal decomposition and its covariance proper transformation is to find out a set of orthonormal basic vectors which can expand a multi-variate spatially-correlated random turbulent field into a sum of products of these basic orthogonal vectors (turbulent loading modes) and single-variate uncorrelated random processes (principal coordinates) based on the covariance matrix of this random field. The covariance matrix-based orthogonal vectors are found as the eigenvector solutions of the eigen problem of the zero-time lag covariance matrix $R_\upsilon(0)$ of N-variate random turbulent process $\upsilon(t)$:

$$R_\upsilon \Theta_\upsilon = \Gamma_\upsilon \Theta_\upsilon \tag{9.1}$$

where $R_\upsilon(0)$: zero-time-lag covariance matrix of $\upsilon(t)$; Γ_υ, Θ : covariance eigenvalue and eigenvector matrices $\Theta_\upsilon = [\theta_{\upsilon_1}, \theta_{\upsilon_2}, ...\theta_{\upsilon_N}]$, $\Gamma_\upsilon = diag(\gamma_{\upsilon_1}, \gamma_{\upsilon_2}, ...\gamma_{\upsilon_N})$. Because the zero-time lag

covariance matrix is positive-definite symmetrical squared one, thus its covariance eigenvalues are real and positive, and covariance eigenvectors are also real, satisfy the orthonormal conditions:

$$\Theta_\upsilon \Theta_\upsilon^T = I;\ \Theta_\upsilon C_\upsilon \Theta_\upsilon^T = \Gamma_\upsilon \tag{9.2}$$

Then, the random turbulence field and its covariance matrix can be expressed such optimum approximation as follows:

$$\upsilon(t) = \Theta_\upsilon x_\upsilon(t) \approx \sum_{j=1}^{\widetilde{N}} \theta_{\upsilon j} x_{\upsilon j}(t) \tag{9.3-a}$$

$$R_\upsilon(0) = \Theta_\upsilon \Gamma_\upsilon \Theta_\upsilon^T(n) = \sum_{j=1}^{\widetilde{N}} \theta_{\upsilon j} \gamma_{\upsilon j} \theta_{\upsilon j}^T \tag{9.3-b}$$

where $\hat{x}_\upsilon(t) = \{\hat{x}_{\upsilon_1}(t), \hat{x}_{\upsilon_2}(t), \ldots, \hat{x}_{\upsilon_N}\}^T$: covariance matrix-based principal coordinates (shortly, the covariance principal coordinates) as the N-variate uncorrelated Gaussian random subprocesses that represents as image of the random turbulent field in the covariance-based space; $\widetilde{N}$: number of truncated covariance eigenvectors ($\widetilde{N} << N$). The covariance principal coordinates can be determined from observed data under following expression:

$$x_\upsilon(t) = \Theta_\upsilon^{-1} \upsilon(t) = \upsilon(t)\Theta_\upsilon = \sum_{i=1}^{N} \upsilon_i(t)\theta_{\upsilon i} \tag{9.4}$$

These approximations are known as the Covariance Proper Transformation in the time domain. Two N-variate turbulent processes u(t), w(t) acting on the N structural nodes: $u(t) = \{u_1(t), u_2(t), \ldots, u_N(t)\}^T$ and $w(t) = \{w_1(t), w_2(t), \ldots, w_N(t)\}^T$ are represented under the zero-time lag covariance matrices in the following form:

$$R_u(0) = \begin{bmatrix} R_{u_1u_1}(0) & R_{u_1u_2}(0) & \ldots & R_{u_1u_N}(0) \\ R_{u_2u_1}(0) & R_{u_2u_2}(0) & \ldots & R_{u_2u_N}(0) \\ \vdots & \vdots & \vdots & \vdots \\ R_{u_Nu_1}(0) & R_{u_Nu_2}(0) & \ldots & R_{u_Nu_N}(0) \end{bmatrix}; R_w(0) = \begin{bmatrix} R_{w_1w_1}(0) & R_{w_1w_2}(0) & \ldots & R_{w_1w_N}(0) \\ R_{w_2w_1}(0) & R_{w_2w_2}(0) & \ldots & R_{w_2w_N}(0) \\ \vdots & \vdots & \vdots & \vdots \\ R_{w_Nw_1}(0) & R_{w_Nw_2}(0) & \ldots & R_{w_Nw_N}(0) \end{bmatrix} \tag{9.5}$$

where $R_{u_mu_m}(0), R_{w_mw_m}(0)$: mean square or variance elements of the single-variate turbulent subprocesses at structural node m; $R_{u_mu_k}(0), R_{w_mw_k}(0)$: cross correlation elements between two structural nodes m, k; m or k=1,2..N:

$$R_{u_mu_m}(0) = E\left[u_m(t)u_m(t)^T\right];\ R_{u_mu_k}(0) = E\left[u_m(t)u_k(t)^T\right] \tag{9.6-a}$$

$$R_{w_mw_m}(0) = E\left[w_m(t)w_m(t)^T\right];\ R_{w_mw_k}(0) = E\left[w_m(t)w_k(t)^T\right] \tag{9.6-b}$$

where E[] denotes to expectation operator.

Two N-variate Gaussian random turbulent processes u(t), w(t) can be transformed and approximated into the covariance principal coordinates due to the Covariance Proper Transformation:

$$u(t) = \Theta_u x_u(t) \approx \sum_{j=1}^{\tilde{N}} \theta_{u_j} x_{u_j}(t) \tag{9.7-a}$$

$$w(t) = \Theta_w x_w(t) \approx \sum_{j=1}^{\tilde{N}} \theta_{w_j} x_{w_j}(t) \tag{9.7-b}$$

where $x_u(t), x_w(t)$: the covariance principal coordinates of u-,w-turbulences, respectively.

As the same way, the covariance matrices can be approximated as follows:

$$R_u(0) = \Theta_u \Gamma_u \Theta_u^{*T} \approx \sum_{j=1}^{\tilde{N}} \theta_{u_j} \gamma_{u_j} \theta_{u_j}^{*T} \tag{9.8-a}$$

$$R_w(0) = \Theta_w \Gamma_w \Theta_w^{*T} \approx \sum_{j=1}^{\tilde{N}} \theta_{w_j} \gamma_{w_j} \theta_{w_j}^{*T} \tag{9.8-b}$$

where $\Gamma_u, \Gamma_w, \Theta_u, \Theta_w$: covariance eigenvalues and corresponding covariance eigenvectors (or covariance turbulent modes) : $\Gamma_u = diag(\gamma_{u_1}, \gamma_{u_2}, ..., \gamma_{u_N})$, $\Gamma_w = diag(\gamma_{w_1}, \gamma_{w_2}, ..., \gamma_{w_N})$, $\Theta_u = \{\theta_{u_1}, \theta_{u_2}, ..., \theta_{u_N}\}^T$; $\Theta_w = \{\theta_{w_1}, \theta_{w_2}, ..., \theta_{w_N}\}^T$ determined from the covariance matrix-based proper orthogonal decomposition of the random turbulent processes u(t), w(t) following Eq.(10.1).

9.3 Time-domain buffeting forces

Uniform quasi-steady buffeting forces per unit deck length (Lift, Drag and Moment) are determined due to the quasi-steady theory that is corrected by frequency-dependant aerodynamic admittance functions as follows:

$$L_b(t) = \frac{1}{2}\rho U^2 B[C_L \chi_{Lu}(n)\frac{2u(t)}{U} + (C_L^{'} + C_D)\chi_{Lw}(n)\frac{w(t)}{U}] \tag{9.9-a}$$

$$D_b(t) = \frac{1}{2}\rho U^2 B[C_D \chi_{Du}(n)\frac{2u(t)}{U} + (C_D^{'} - C_L)\chi_{Dw}(n)\frac{w(t)}{U}] \tag{9.9-b}$$

$$M_b(t) = \frac{1}{2}\rho U^2 B^2[C_M \chi_{Mu}(n)\frac{2u(t)}{U} + C_M^{'}\chi_{Mw}(n)\frac{w(t)}{U}] \tag{9.9.c}$$

where C_L, C_D, C_M: aerodynamic static coefficients (at balanced angle of attack); $C_L^{'}, C_D^{'}, C_M^{'}$: first-order derivatives; $\chi_{F\upsilon}(n)$ $(F = L, D, M; \upsilon = u, w)$: aerodynamic transfer functions between

turbulent components and turbulent-induced forces (their absolute magnitudes refer as aerodynamic admittance functions).

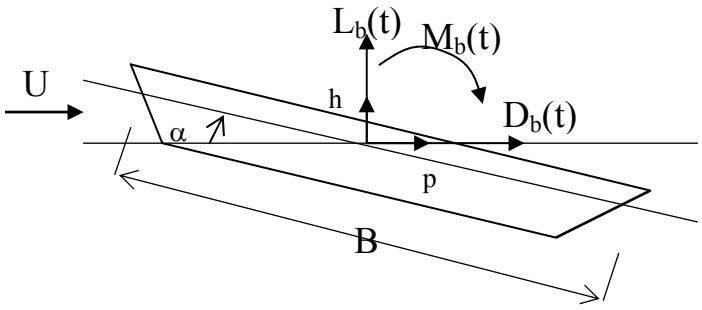

Fig. 9.1 Uniform buffeting forces on bridge deck (in time-domain formulation)

Quasi-steady buffeting forces, however, do not exactly reflect unsteady characteristics as nature of these random forces, which depend on not only geometric configuration of bridge decks, oncoming wind turbulence, but frequency-dependant parameters due to wind-structure interaction and bluff body flow. Additionally, it is indicated that unsteady fluid dynamics at low, medium flow velocity ranges must account for both past and present motion histories, thus the so-called "memory effect" of the unsteady fluid flow should be included in modeling of unsteady buffeting forces.. So far, the unsteady buffeting forces can be determined via either the indicial response functions (Scanlan 1993) or the impulse response functions (Lin 1984, Chen and Kareem 2000) thanks to convolution integration operation. Recently, the impulse response functions are usually used for modeling the unsteady buffeting forces in the time domain as follows:

$$L_b(t) = \frac{1}{2}\rho U^2 \{\int_{-\infty}^{t} I_{Lu}(t-\tau)\frac{u(\tau)}{U}d\tau + \int_{-\infty}^{t} I_{Lw}(t-\tau)\frac{w(\tau)}{U}d\tau\} \qquad (9.10\text{-a})$$

$$D_b(t) = \frac{1}{2}\rho U^2 \{\int_{-\infty}^{t} I_{Du}(t-\tau)\frac{u(\tau)}{U}d\tau + \int_{-\infty}^{t} I_{Dw}(t-\tau)\frac{w(\tau)}{U}d\tau\} \qquad (9.10\text{-b})$$

$$M_b(t) = \frac{1}{2}\rho U^2 \{\int_{-\infty}^{t} I_{Mu}(t-\tau)\frac{u(s)}{U}d\tau + \int_{-\infty}^{t} I_{Mw}(t-\tau)\frac{w(\tau)}{U}d\tau\} \qquad (9.10\text{-c})$$

where $I_{Lu}, I_{Lw}, I_{Du}, I_{Dw}, I_{Mu}, I_{Mw}$: impulse response functions which are usually obtained thanks to available admittance functions such following formulae as (Scanlan et al , Chen and Kareem 2002):

$$\bar{I}_{Lu} = 2BC_L\chi_{Lu}(n)\,;\quad \bar{I}_{Lw} = B(C_L^{'} + C_D)\chi_{Lw}(n) \qquad (9.11\text{-a})$$

$$\bar{I}_{Du} = 2BC_D\chi_{Du}(n)\,;\bar{I}_{Dw} = B(C_D^{'} - C_L)\chi_{Dw}(n) \tag{9.11-b}$$

$$\bar{I}_{Mu} = 2B^2C_M\chi_{Mu}(n)\,;\bar{I}_{Mw} = B^2C_M^{'}\chi_{Mw}(n) \tag{9.11-c}$$

where $\bar{I}_{F\upsilon}$: Fourier transform of the impulse response functions ($F = L, D, M$ $\upsilon = u, w$) : $\bar{I}_{F\upsilon} = \int_0^{\infty} I_{F\upsilon}(t)e^{-i\omega t}dt = \int_0^{\infty} I_{F\upsilon}(s)e^{-iKs}ds$.

However, the aerodynamic admittance functions determined by either empirical formula or experimental measurement are expressed at discrete values of reduced frequency. Therefore, it is essential to approximate discrete frequency-dependant function to continuous one. Rational function approximation, known as the Roger's approximation is the mostly utilized for this purpose. Aerodynamic transfer functions can be expanded using rational function approximation:

$$\chi_{F\upsilon}(n) = A_{F\upsilon,1} + (iK)\sum_{j=1}^{m_{F\upsilon}} \frac{A_{F\upsilon,j+1}}{iK + d_{F\upsilon,j}} \tag{9.12}$$

where $A_{F\upsilon,1}, A_{F\upsilon,j+1}, d_{F\upsilon,j}$ frequency-dependant coefficients ($j = 1,2,...,m_{F\upsilon}$) determined by nonlinear curve-fitting technique.

Then the impulse response functions and the unsteady buffeting forces (here only $I_{Lw}(s)$, $L_{Lw}(t)$ are expended as example) can be determined as follows:

$$I_{Lw}(s) = B(C_D + C_L^{'})\left[\left(A_{Lw,1} + \sum_{j=1}^{m_{Lw}} A_{Lw,j+1}\right)\delta(s) - \sum_{j=1}^{m_{Lw}} A_{Lw,j+1}d_{Lw,j}e^{-d_{Lw,j}s}\right] \tag{9.13-a}$$

$$I_{Lw}(s) = \frac{1}{2}\rho U^2 B(C_D + C_L^{'})\left[\left(A_{Lw,1} + \sum_{j=1}^{m_{Lw}} A_{Lw,j+1}\right)\frac{w(t)}{B} - \sum_{j=1}^{m_{Lw}} \frac{d_{Lw,j}U}{B}\phi_{Lw,j}(t)\right] \tag{9.13-b}$$

$$\dot{\phi}_{Lw,j}(t) = -\frac{d_{Lw,j}U}{B}\phi_{Lw,j}(t) + A_{Lw,j+1}\frac{w(t)}{U} \tag{9.13-c}$$

where $\phi_{Fw,j}(t)$: augmented aerodynamic state coefficient.

Then full-scale buffeting forces acting on whole structure can be formulated due to linearized lumping of the uniform buffeting forces at each deck node:

$$F_b(t) = \frac{1}{2}\rho UB\left[C_u\chi_{Fu}(n)u(t) + C_w\chi_{Fw}(n)w(t)\right] \tag{9.14-a}$$

$$F_b(t) = \begin{bmatrix} L_{bi}(t) \\ D_{bi}(t) \\ M_{bi}(t) \end{bmatrix}; C_u = \frac{1}{2}\rho UB\begin{bmatrix} 2C_L\bar{L} \\ 2C_D\bar{L} \\ 2BC_M\bar{L} \end{bmatrix}; C_w = \begin{bmatrix} (C_L^{'} + C_D)\bar{L} \\ (C_D^{'} - C_L)\bar{L} \\ BC_M^{'}\bar{L} \end{bmatrix}; \bar{L} = diag(L_i); L_i = \begin{cases} 0.5\,|\,y_2 - y_1\,|, & i = 1 \\ 0.5\,|\,y_{i+1} - y_{i-1}\,|, & 1 < i < N \\ 0.5\,|\,y_N - y_{N-1}\,|, & i = N \end{cases} \tag{9.14-b}$$

where C_u, C_w : full-scale force coefficient matrices; L_i: influenced distance at node i; y:

longitudinal structural coordinate

9.4 Gust response formulation

Multi-degree-of-freedom motion equations of structures subjected to the full-scale buffeting forces can be expressed thanks to Finite Element Method (FEM):

$$M\ddot{U} + C\dot{U} + KU = F_b(t) \tag{9.15}$$

where $U = \left\{h(t)^T, p(t)^T, a(t)^T\right\}$: displacement vector containing three vertical, lateral and rotational displacements; $\dot{U}, \ddot{U}$: velocity and acceleration vectors; $F_b(t)$: full-scale buffeting forces.

Structurally global responses can be expressed into the mass matrix-normalized generalized coordinates thanks to the Structural Modal Transformation as follows:

$$U(t) = \Phi\xi(t) = \sum_{i=1}^{\overline{M}} \phi_i \xi_i \tag{9.16}$$

where $\xi(t) = \left\{\xi_1(t), \xi_2(t), ..., \xi_M(t)\right\}$: structural generalized coordinates; $\Phi = [\phi_1, \phi_2, ..., \phi_M]^T$: modal matrix; $\overline{M}$: number of truncated structural modes ($\overline{M} << M$);

Therefore, single-degree-of-freedom motion equation of the i-th generalized coordinate is determined:

$$\ddot{\xi}_i(t) + 2\zeta_i\omega_i\dot{\xi}_i(t) + \omega_i^2\xi_i(t) = \frac{1}{2}\phi_i^T \rho UB\left[C_u u(t) + C_w w(t)\right] \tag{9.17}$$

where ω_i, ζ_i : circular frequency, damping ratio of the i-th generalized coordinate.

Using the covariance proper transformation in Eqs(10.7-a),(10.7-b), the multi-variate random turbulent processes u(t), w(t) can be approximated by uncorrelated subprocesses and covariance eigenvectors (or covariance turbulent modes). Thus, the 1DOF motion equation is expressed such following forms as:

$$\ddot{\xi}_i(t) + 2\zeta_i\omega_i\dot{\xi}_i(t) + \omega_i^2\xi_i(t) = \frac{1}{2}\rho UB\left[\phi_i^T C_u \sum_{j=1}^{\tilde{M}} \theta_{uj} y_{uj}(t) + \phi_i^T C_w \sum_{j=1}^{\tilde{M}} \theta_{wj} y_{wj}(t)\right] \tag{9.18-a}$$

$$\ddot{\xi}_i(t) + 2\zeta_i\omega_i\dot{\xi}_i(t) + \omega_i^2\xi_i(t) = \frac{1}{2}\rho UB\left[\sum_{j=1}^{\tilde{M}} A_{uij} y_{uj}(t) + \sum_{j=1}^{\tilde{M}} A_{wij} y_{wj}(t)\right] \tag{9.18-b}$$

where $A_{uij} = \phi_i C_u \theta_{uj}$; $A_{wij} = \phi_i C_w \theta_{wj}$: cross modal participation coefficients accounting for interaction between structural modes and covariance turbulent modes;

$y_u(t) = \{y_{u_1}(t), y_{u_2}(t), ..., y_{u_N}(t)\}^T$, $y_w(t) = \{y_{w_1}(t), y_{w_2}(t), ..., y_{w_N}(t)\}^T$: covariance principal

coordinates, which are determined from original turbulent fields as follows

$$y_u(t) = u(t)\Theta_u; \quad y_{u_j}(t) = u(t)\theta_{u_j} \tag{9.19-a}$$

$$y_w(t) = w(t)\Theta_w; \quad y_{w_j}(t) = w(t)\theta_{w_j} \tag{9.19-b}$$

Therefore, the 1DOF motion equations associated with vertical, horizontal and rotation structural principal coordinates can be expressed as follows:

$$\ddot{\xi}_{hi}(t) + 2\zeta_{hi}\omega_{hi}\dot{\xi}_{hi}(t) + \omega_{hi}^2\xi_{hi}(t) = \frac{1}{2}\rho UB\left[\sum_{j=1}^{\tilde{M}} A_{uij}^L y_{uj}(t) + \sum_{j=1}^{\tilde{M}} A_{wij}^L y_{wj}(t)\right] \tag{9.19-a}$$

$$\ddot{\xi}_{pi}(t) + 2\zeta_{pi}\omega_{pi}\dot{\xi}_{pi}(t) + \omega_{pi}^2\xi_{pi}(t) = \frac{1}{2}\rho UB\left[\sum_{j=1}^{\tilde{M}} A_{uij}^D y_{uj}(t) + \sum_{j=1}^{\tilde{M}} A_{wij}^D y_{wj}(t)\right] \tag{9.19-b}$$

$$\ddot{\xi}_{ai}(t) + 2\zeta_{ai}\omega_{ai}\dot{\xi}_{ai}(t) + \omega_{ai}^2\xi_{ai}(t) = \frac{1}{2}\rho UB\left[\sum_{j=1}^{\tilde{M}} A_{uij}^M y_{uj}(t) + \sum_{j=1}^{\tilde{M}} A_{wij}^M y_{wj}(t)\right] \tag{9.19-c}$$

where $A_{uij}^L, A_{wij}^L, A_{uij}^D, A_{wij}^D, A_{uij}^M, A_{wij}^M$: cross modal participation coefficients between structural modes and covariance turbulent modes which are correspondent to u-,w-turbulences and turbulent-induced lift, drag, moment.

$A_{uij}^L = \phi_{hi}C_u^L\theta_{uj}; \quad A_{wij}^L = \phi_{hi}C_w^L\theta_{wj}; A_{uij}^D = \phi_{pi}C_u^D\theta_{uj}; \quad A_{wij}^D = \phi_{hi}C_w^D\theta_{wj}; A_{uij}^M = \phi_{\alpha i}C_u^M\theta_{uj}; \quad A_{wij}^M = \phi_{\alpha i}C_w^M\theta_{wj}$

The 1DOF motion equations system is formulated in the time domain. Finding out solution of this system can be obtained based on the direct integration methods such as the Newmark-beta method, the fourth-order Runge-Kutta method and so on.

As a result, the structural global responses (vertical, lateral and rotational displacements) of structure can be determined based on the superposition principle as follows:

Vertical $$U_h = \sum_{i=1}^{\overline{M}_h} \phi_{hi}\xi_{hi}(t) \tag{9.20-a}$$

Lateral $$U_p = \sum_{i=1}^{\overline{M}_p} \phi_{pi}\xi_{pi}(t) \tag{9.20-b}$$

Rotational $$U_a = \sum_{i=1}^{\overline{M}_a} \phi_{ai}\xi_{ai}(t) \tag{9.20-c}$$

Where U_h, U_p, U_a: global vertical, lateral and rotational displacements, respectively; ϕ_h, ϕ_p, ϕ_a: structural modes corresponding to three responses; $\ulcorner$: numbers of component modes in combination of responses.

9.5 Numerical example

A concrete cable-stayed bridge was taken for numerical example using the above-mentioned computational procedures. Bridge was spanned by 40.5+97+40.5=178m. 3D frame model was built thanks to the finite element method (FEM). There were 30 discrete nodes in the bridge deck. Total 30 nodes were on the bridge deck, while nodes 8, 23 at pylons. First ten structural modes were analyzed. Natural frequencies of the first ten structural modes vary between 0.61Hz÷1.86Hz. Damping ratios of every structural mode were assumed to be 0.005. Aerodynamic static coefficients of cross section at balanced angle ($\alpha_0 = 0^0$) and their first derivatives were experimentally determined as follows: $C_L = 0.158$, $C_D = 0.041$, $C_M = 0.174$, $C_L^{'} = 3.73$, $C_D^{'} \approx 0$, $C_M^{'} = 2.06$. Some fundamental modal shapes of bridges and characteristics of free vibration modes have been presented in the Chapter 9.

One-sided auto spectral density functions of u-, w-turbulent components were obtained due to the Kaimail's and the Panofsky's spectral models, respectively (Simiu and Scanlan 1976). Coherence function was used the Davenport's empirical exponential function with decay factors with decay factors $c_u = 10,\ c_w = 6.5$ (Davenport 1962). Aerodynamic admittance function was used the Liepmann's empirical function as approximation of the Sears' function (Liepmann 1958). Mechanical admittance function was determined corresponding to structural generalized coordinates.

In this example, the global responses of bridge are required to be predicted at some different mean velocity range between 0m/s and 40m/s. It is also assumed that the buffeting forces act on the bridge deck only, and the forces on towers and cables are negligible. Therefore, 30-variate turbulent loading processes u(t), w(t) are obtained at the deck nodes: $u(t) = \{u_1(t), u_2(t), \ldots, u_{30}(t)\}^T$ and $w(t) = \{w_1(t), w_2(t), \ldots, w_{30}(t)\}^T$. In the branch of the covariance proper transformation, the covariance matrix is formulated in the time domain, thus time series of the turbulent fields u(t), w(t) must be required to be simulated at all deck nodes. The spectral representation methods using the Cholesky decomposition and the modal decomposition which were presented in the Chapter 8 are used here to simulate time series of u-,w-turbulences at 30 deck nodes based on the cross spectral matrices of the turbulent fields which are constructed thanks to available frequency-dependant auto spectral densities of single-variate turbulent processes and spatial coherence functions. Accuracy of simulated turbulent time series has been verified by comparing between power spectral densities of simulated turbulent time series and targeted ones, as well as between coherence of simulated time series and targeted coherence.

Simulated time series of u-,w-turbulences at referred ten deck nodes during 100-second interval at the mean velocity U=20m/s is expressed in Figure 9.2. Simulated time series of the turbulences at another mean velocities and deck nodes are omitted for a sake of brevity.

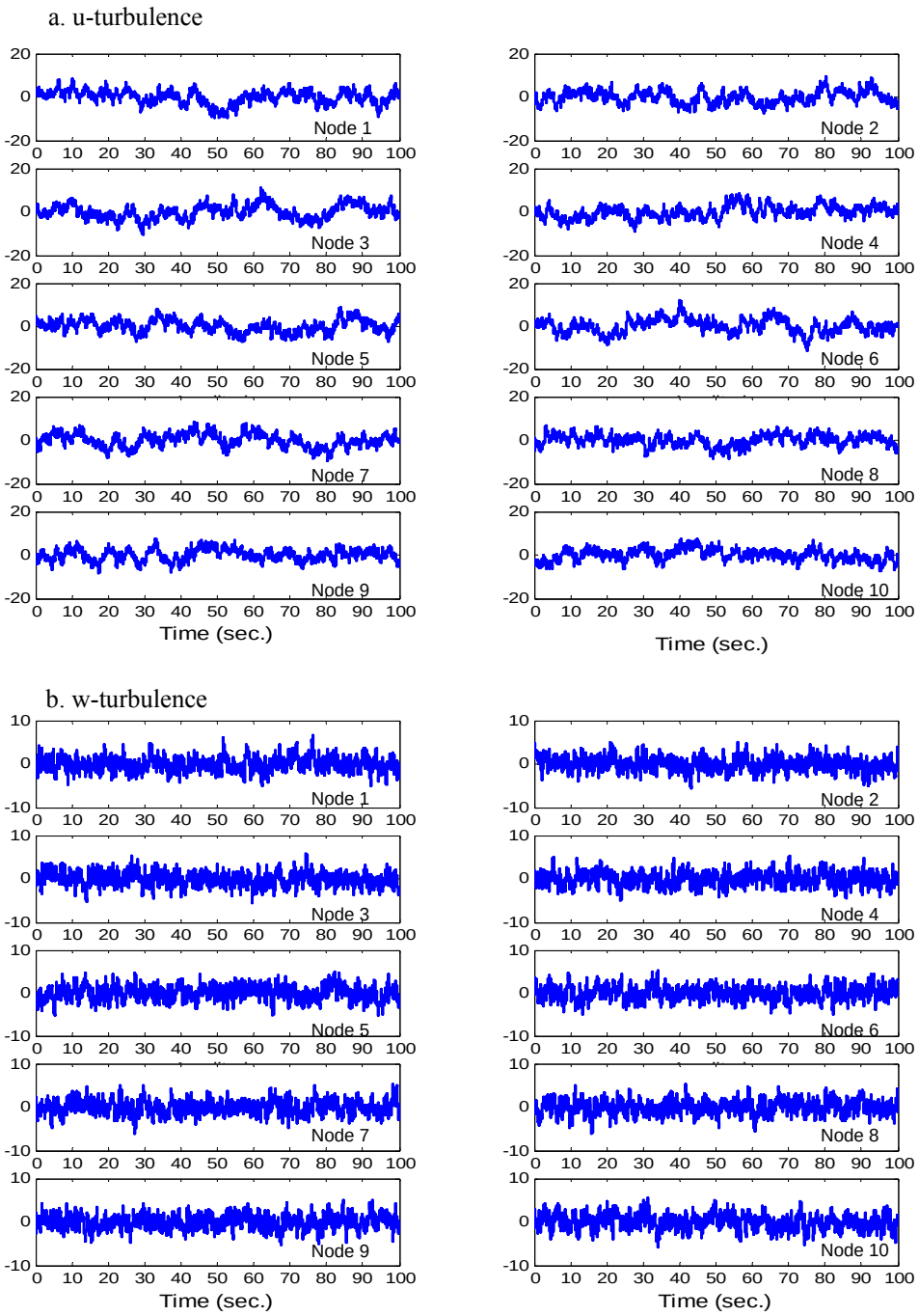

Fig. 9.2 Simulated turbulent time series at 10 deck nodes corresponding to mean wind velocity U=20m/s: a. u-turbulence, b. w-turbulence

9.6 Results and discussion

Simulated turbulent fields u(t), w(t) have been used to formulate the zero-time-lag covariance matrix. Then, the covariance eigenvectors (or covariance turbulent modes) and associated eigenvalues have been found out from the eigen solution of these covariance matrices. The covariance principal coordinates is determined based on simulated turbulent fields.

Figure 9.3 shows totally 30 covariance eigenvalues of u-,w-turbulences. Energy contribution of the covariance turbulent modes is expressed in Figure 9.4. It notes that the energy contribution of the covariance turbulent modes does not decay fast.

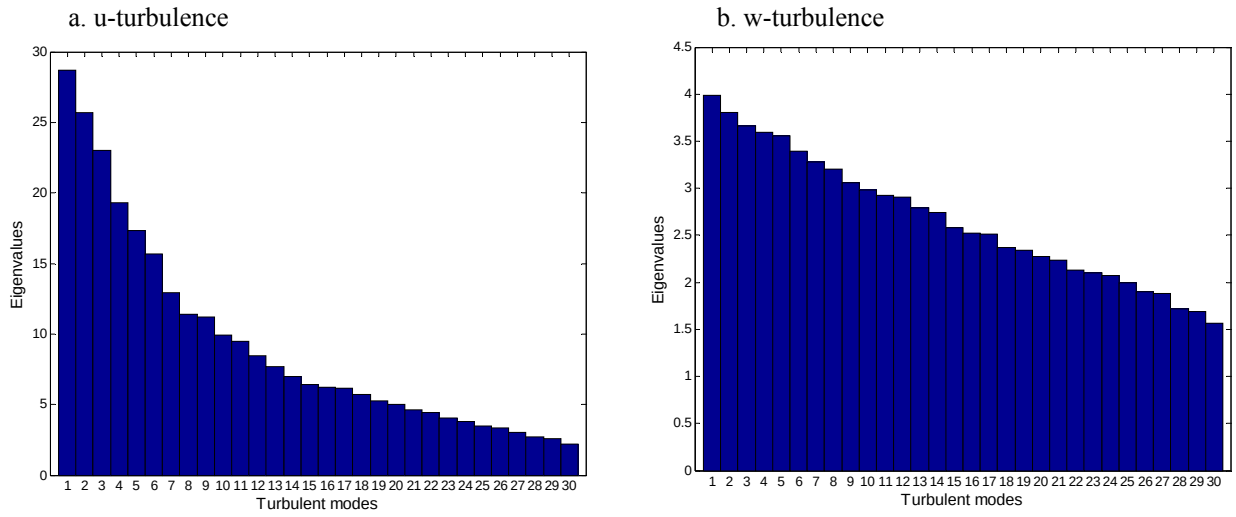

Fig. 9.3 Covariance eigenvalues: a. u-turbulence, b. w-turbulence

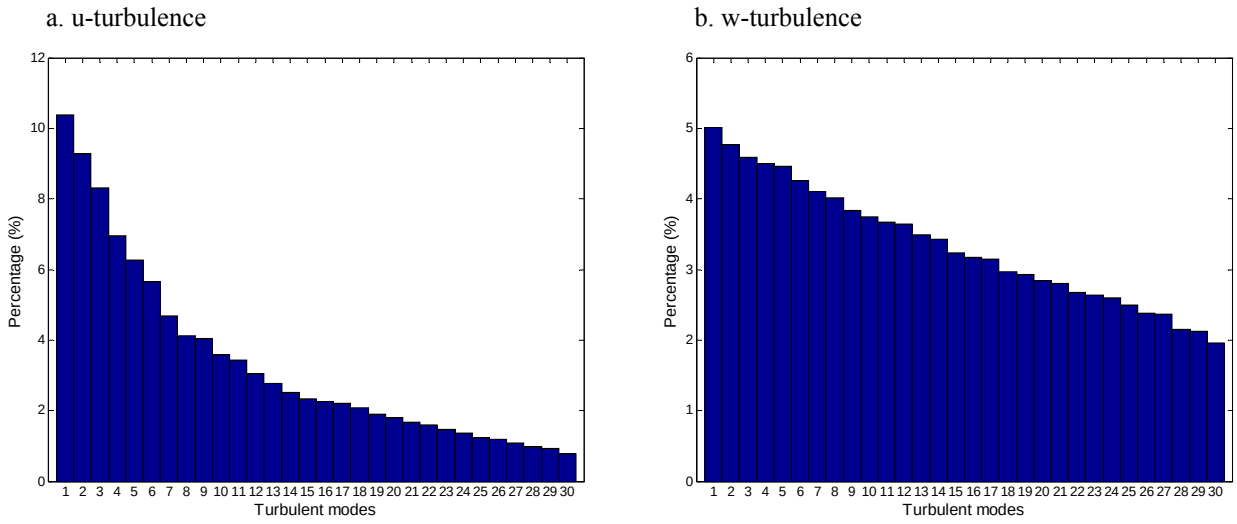

Fig. 9.4 Energy contribution of covariance eigenvectors: a. u-turbulence, b. w-turbulence

First ten covariance turbulent modes corresponding to u-turbulence and w-turbulence are indicated in Figure 9.5. Figure 10.6 shows the first ten covariance principal coordinates of the u-,w-tubulences.

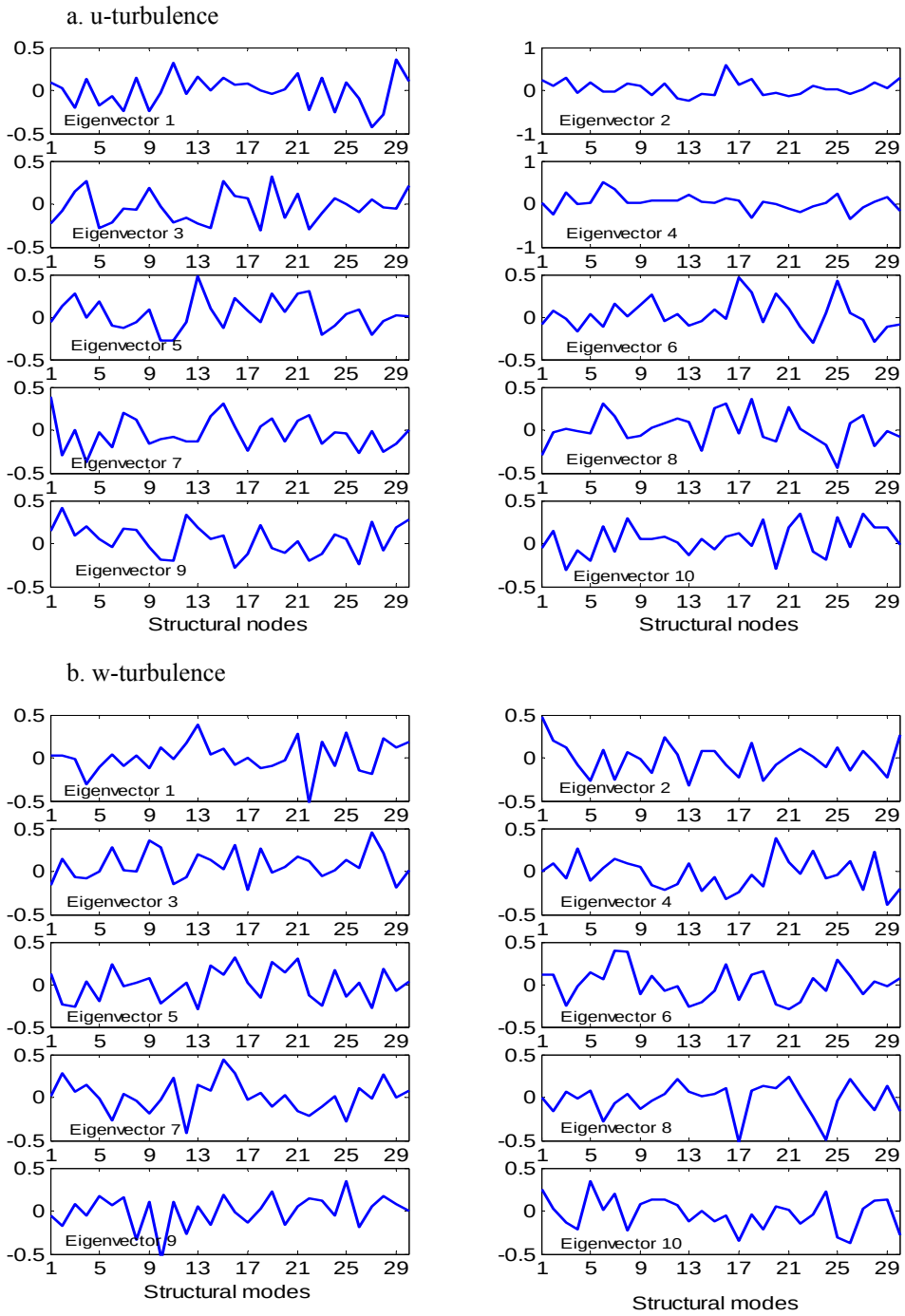

Fig. 9.5 First ten covariance turbulent modes: a. u-turbulence, b. w-turbulence

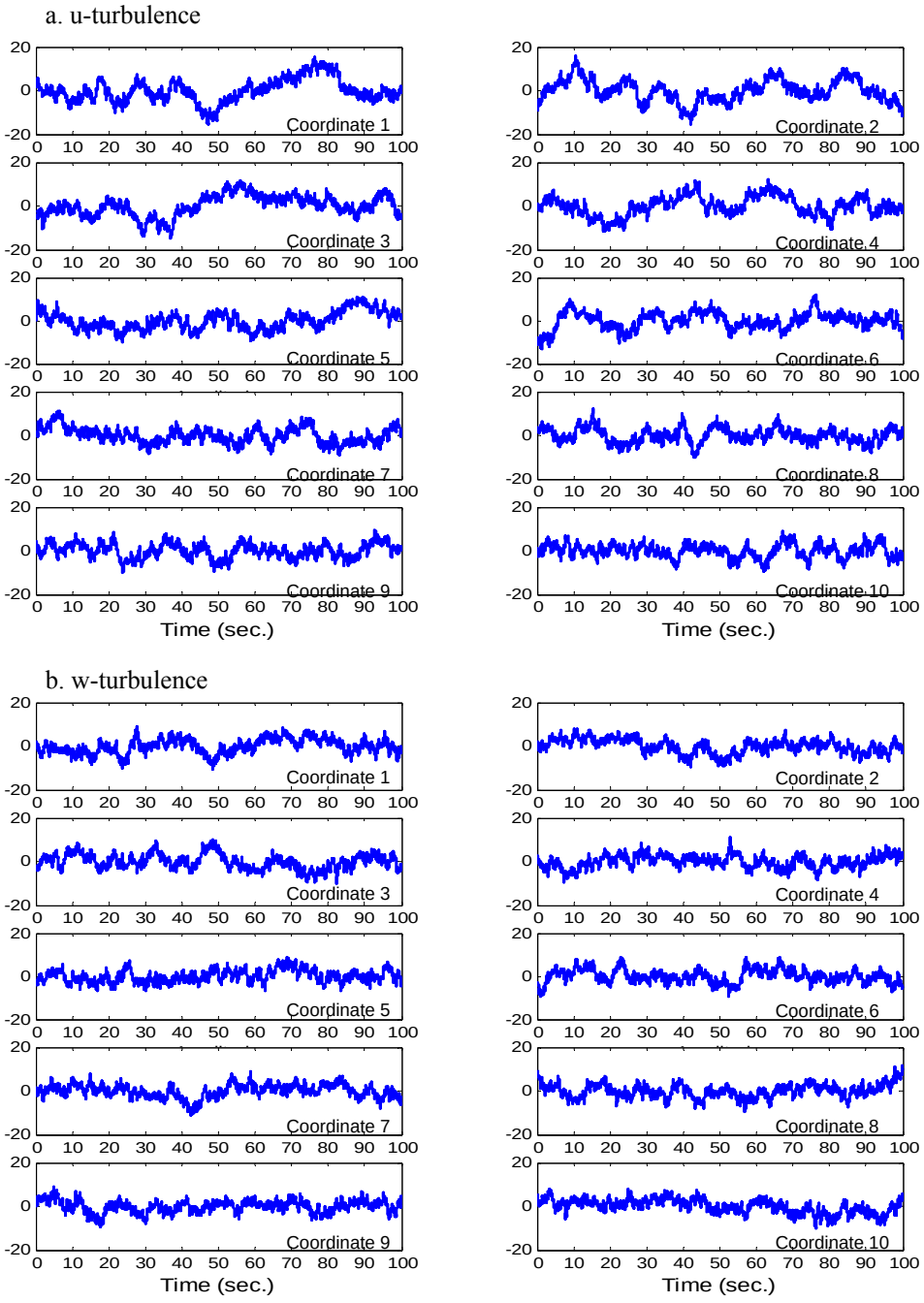

Fig. 9.6 First ten covariance turbulent coordinates: a. u-turbulence, b. w-turbulence

Time series of the global responses (vertical, rotational and lateral displacements) at deck nodes 5&15 in different mean velocities U=10, 20, 30, 40m/s have been shown from Figure 9.7 to Figure 9.10. Maximum and minimum displacements can be determined thanks to these time series of global responses.

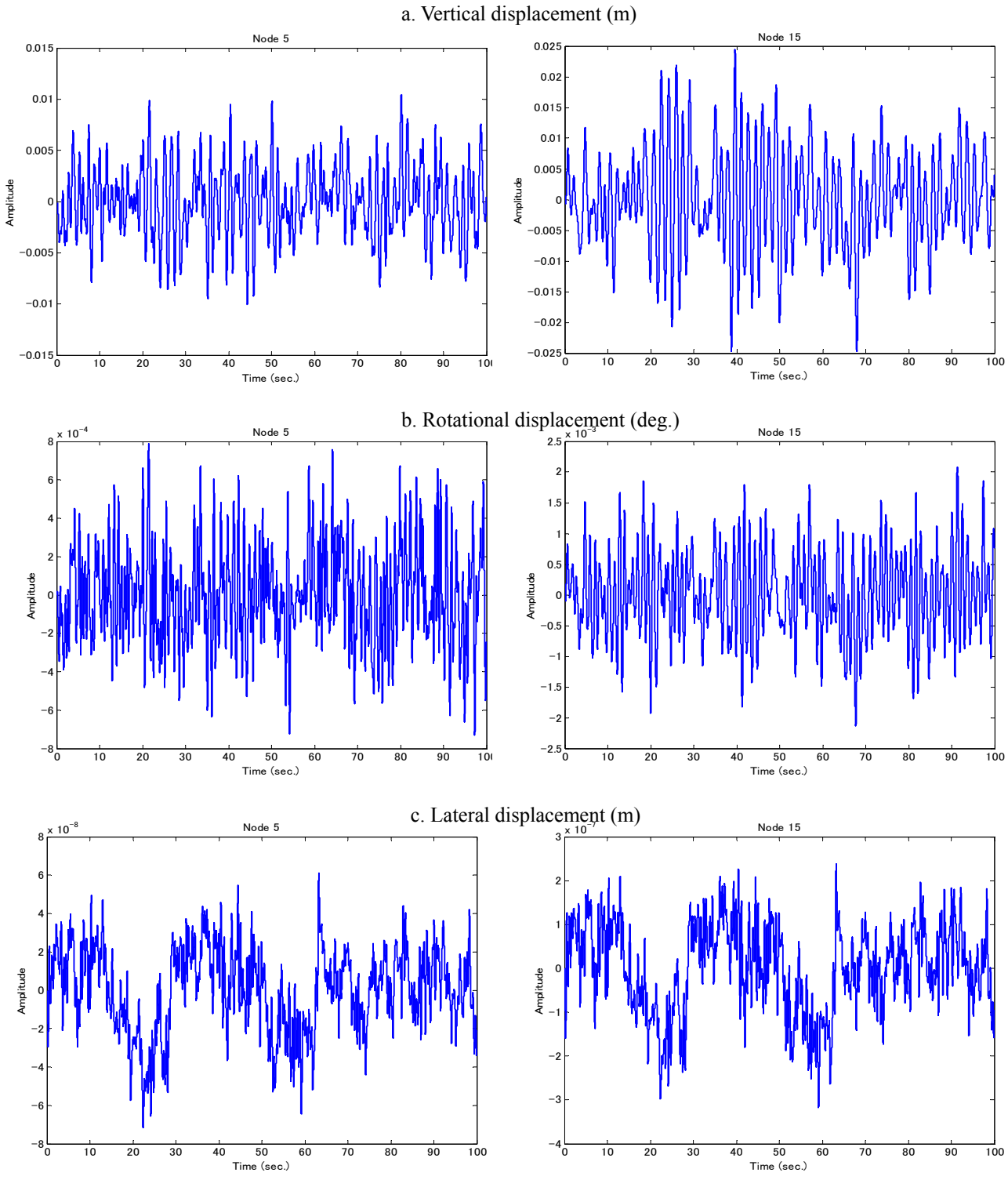

Fig. 9.7 Time histories of global responses at nodes 5&15 at mean velocity U=10m/s: a.vertical, b. rotational, c. lateral displacement

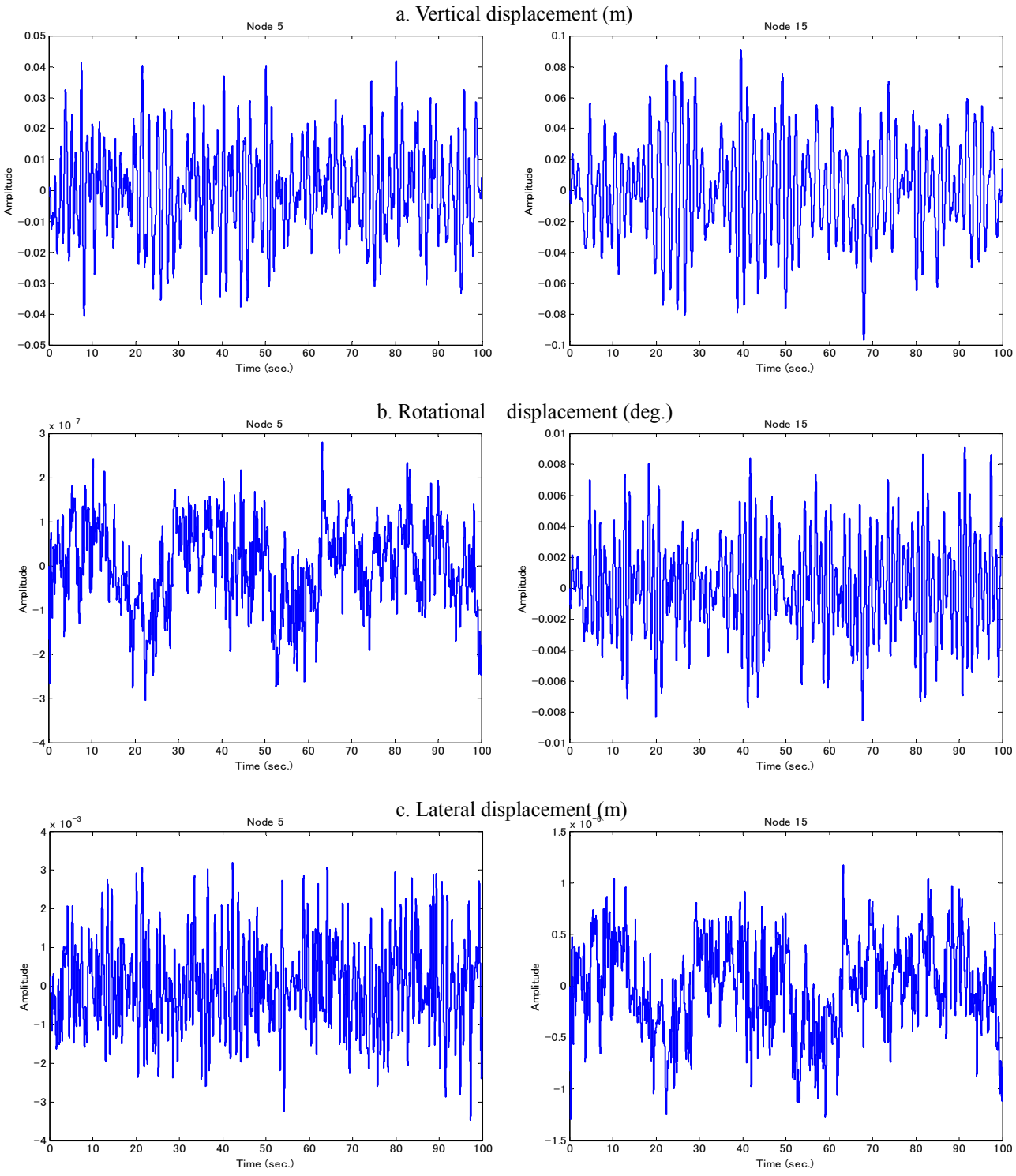

Fig. 9.8 Time histories of global responses at nodes 5&15 at mean velocity U=20m/s: a.vertical, b.rotational, c. lateral displacement

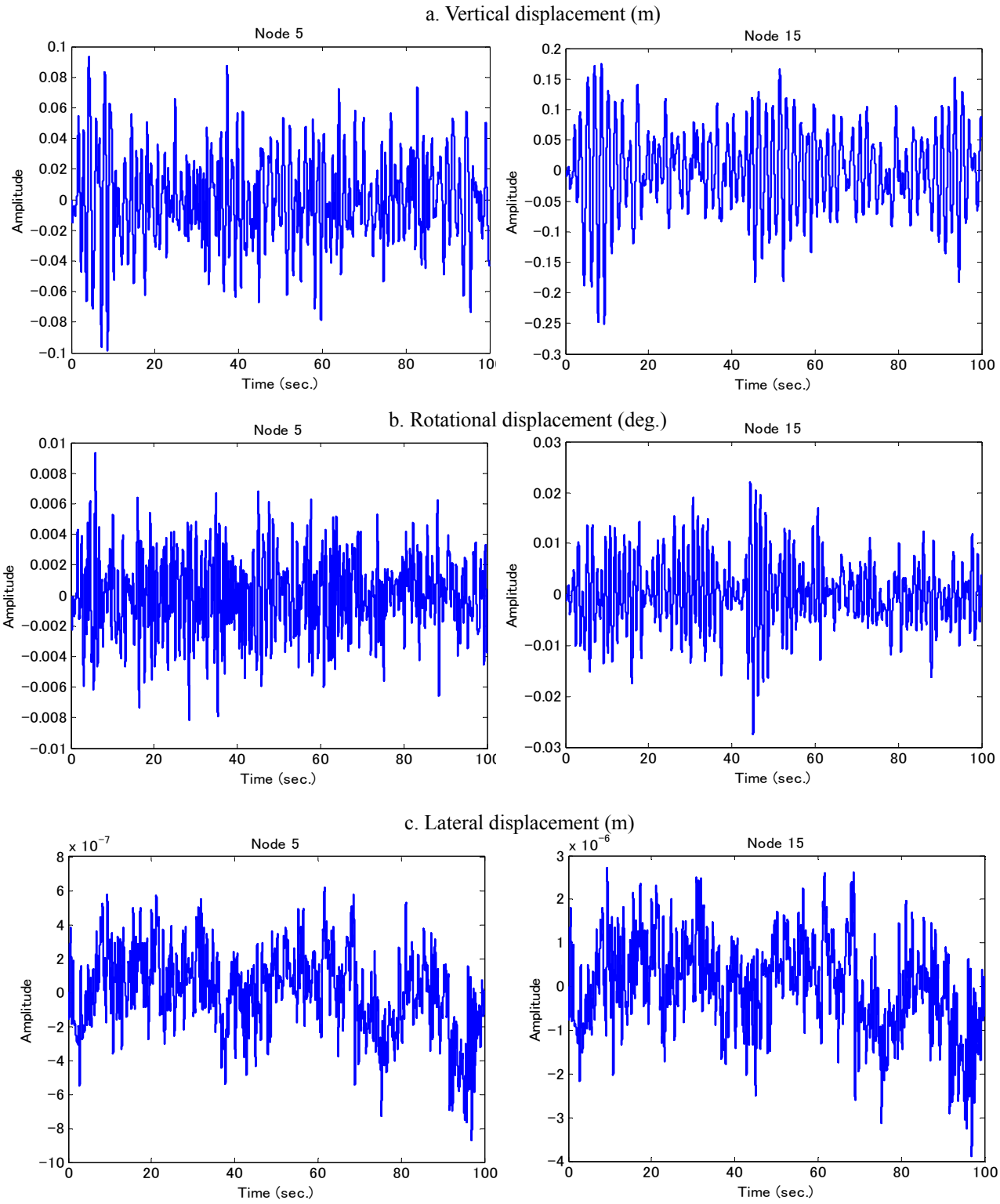

Fig. 9.9 Time histories of global responses at nodes 5&15 at mean velocity U=30m/s: a. vertical, b. rotational, c. lateral displacement

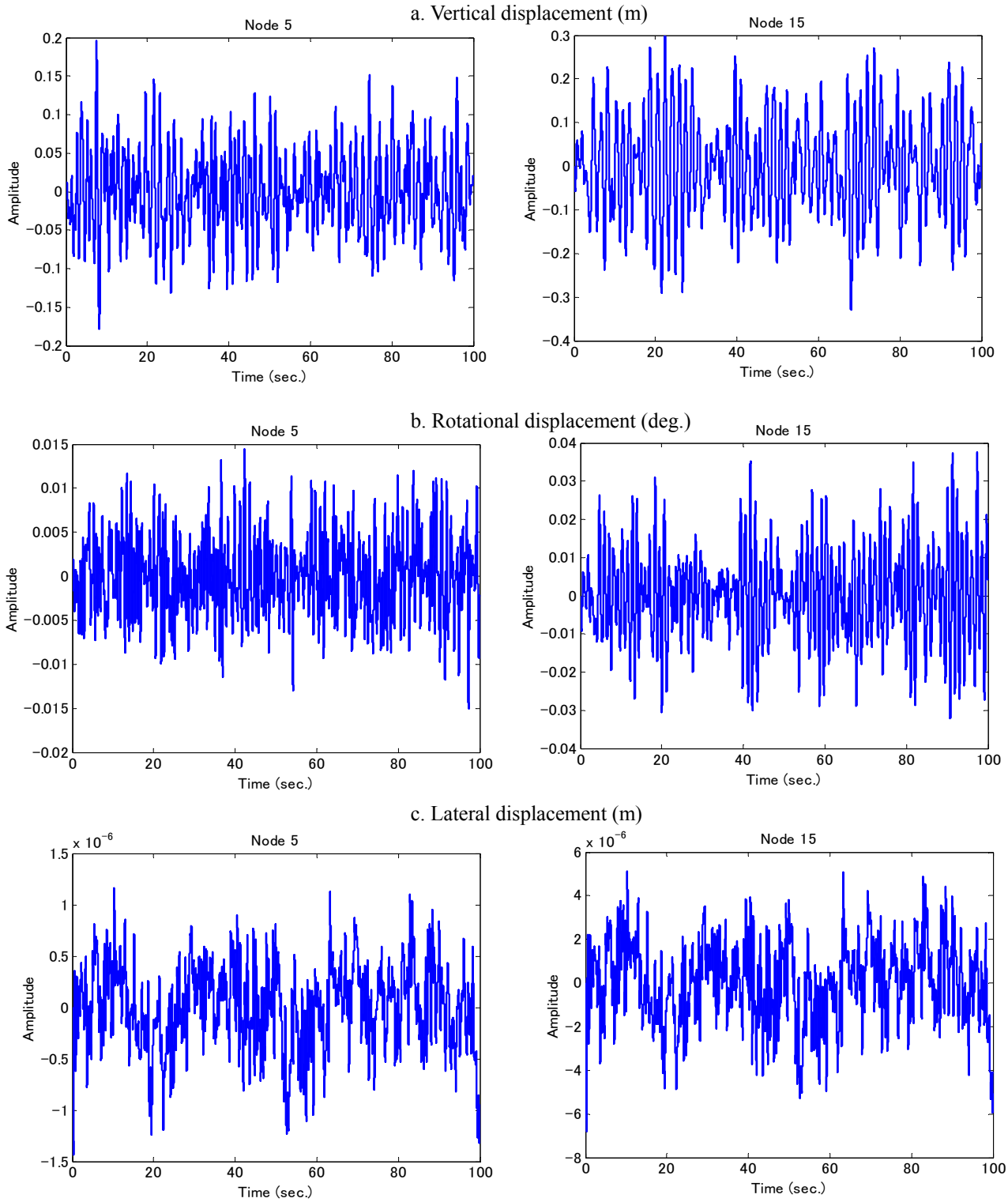

Fig. 9.10 Time histories of global responses at nodes 5&15 at mean velocity U=40m/s: a.vertical, b.rotational, c. lateral displacemen

Figure 9.11 shows the global response envelopes of the vertical and rotational displacements of bridge in referred nodes 5 and 15 in the mean velocity range between 0m/s and 40m/s.

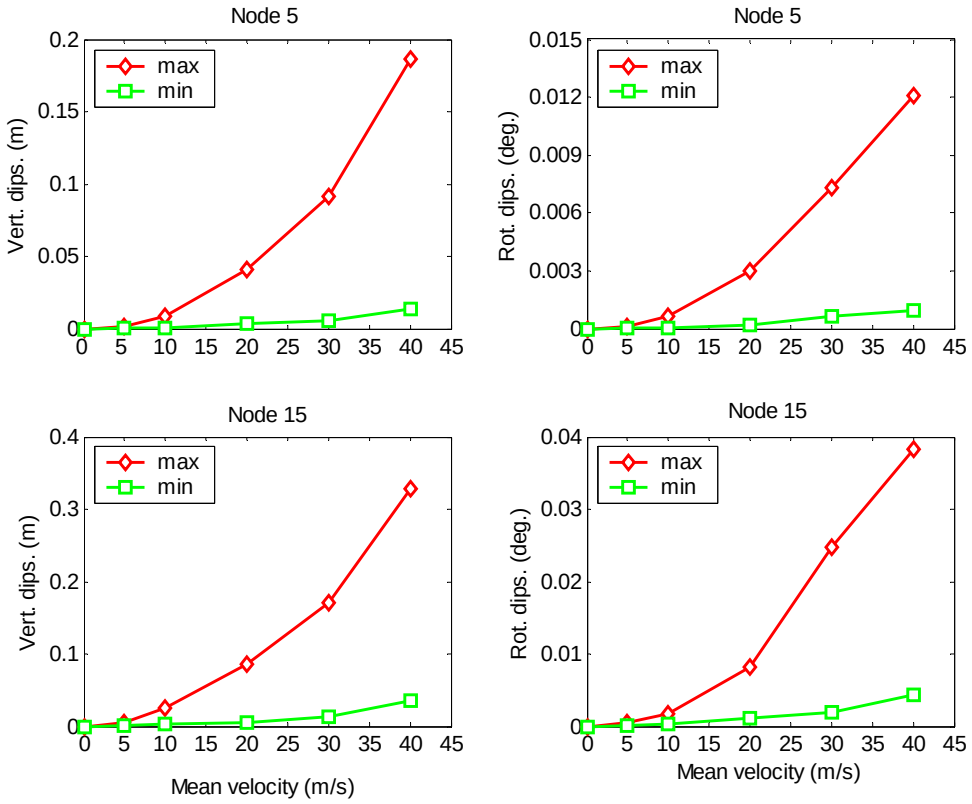

Fig. 9.11 Minimum and maximum global responses at nodes 5 & 15 corresponding to mean wind velocity range between 0÷40m/s

Tab. 9.1 Effect of covariance modes on maximum global amplitude

N.modes	Node 5	%	Node15	%
30	0.040	100	0.093	100
20	0.037	93	0.080	86
10	0.028	70	0.069	74
5	0.023	58	0.053	57

N.modes	Node 5	%	Node15	%
30	.0027	100	.0078	100
20	.0026	96	.0075	96
10	.0021	78	.0071	91
5	.0018	67	.0049	63

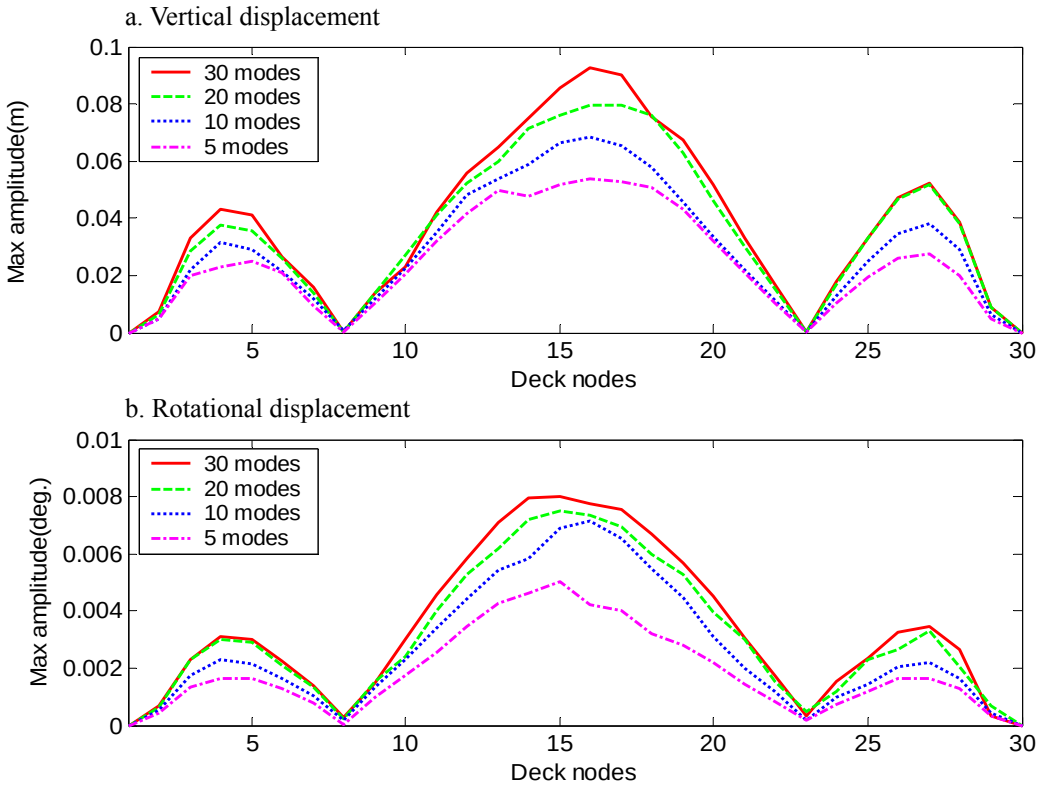

Fig. 9.12 Effect of number of truncated covariance turbulent modes on global responses at all deck nodes in case of mean velocity U=20m/s: a. vertical displacement, b. rotational displacement

Effect of truncated number of the covariance turbulent modes in the covariance proper transformation on the global responses has been investigated here. Figure 9.12 indicates the maximum structural responses on whole bridge deck at U=20m/s corresponding to number of turbulent modes ($\widetilde{M} = 30;20;10\,and\,5$, in which 30 modes imply for targeted response).

It can be seen that maximum responses reduce with respect to decrease of truncated number of turbulent modes. Number of turbulent modes to some extent does not influence considerably on global responses. For example, the maximum vertical amplitudes at midspan node 15 are 9.3cm (100%), 8.0cm (86%), 6.9cm (74%) and 5.3cm (57%) and the maximum torsional amplitudes at node 15 are 0.0078^0 (100%), 0.0075^0 (96%), 0.0071^0 (71%) and 0.0049^0 (63%) corresponding to 30, 20, 10 and 5 modes taken into account. Therefore, higher number of low-order covariance turbulent modes should be used for estimating the gust responses of bridge.

9.7 Conclusion

This chapter has presented the application of the proper orthogonal decomposition and its covariance proper transformation for the gust response prediction of full-scale bridges in the time domain. Effect of number of orthogonally turbulent loading modes on the generalized and global responses of bridges also is investigated accordingly.

Some main points can be concluded as follows:

(1) New framework on the gust response prediction of bridges has been formulated in the time domain using the covariance matrix-based proper orthogonal decomposition and its covariance proper transformation. Time series of the multi-variate random turbulent fields have been simulated via the spectral proper transformation to be used in this time-domain gust response prediction of bridges. It seems that the computational procedure presented here is very promising for the buffeting analysis and the gust response in the time domain with its advantages to treat with aerodynamic and geometrical nonlinearities.

(2) It is argued that the high number of lower-order covariance turbulent modes should be required for accuracy estimation of the gust response of bridges. In comparison with effect of number of the spectral turbulent modes, in some extent and in this investigated case, it is commented that the low-order covariance turbulent modes play less important role than spectral ones in their contributions on the gust response of bridge.

Further development in the applications of the proper orthogonal decomposition and the covariance proper transformation for the gust response prediction of bridges in the time domain is going to focus on the comprehensive model of unsteady buffeting forces model using the impulse response functions which can capture the “unsteady fluid memory effect”.

References

Boonyapinyo, V., Miyata, T., Yamada, H. (1999), "Advanced aerodynamic analysis of suspension bridges by state-space approach", *J. Struct. Engrg.*, ASCE **125(12)**, 1357-1366.

Carassale, L., Piccardo, G., Solari, G. (1999), "Double modal transformation and wind engineering applications", *J. Engrg. Mech.*, ASCE **127(5)**, 432-439.

Chen, X., Matsumoto, M., Kareem, A. (2000), "Time domain flutter and buffeting response analysis of bridges", *J. Engrg. Mech.*, ASCE **126(1)**, 7-16.

Chen, X., Kareem, A. (2002), "Advances in modeling of aerodynamic forces on bridges", *J. Engrg. Mech.*, ASCE **128(11)**, 1193-1203.

Chen, X, Kareem, A. (2005), "Proper orthogonal decomposition-based modeling, analysis, and simulation of dynamic wind load effects on structures", *J.Engrg. Mech.*, ASCE **131(4)**, 325-339.

Davenport, A.G. (1962), "Buffeting of a suspension bridge by storm winds", *J. Struct. Div.,* ASCE **88(3)**, 233-268.

Le, T.H. (2004), "Experimental determination of aerodynamic coefficients of bridge sections in wind tunnel tests", *Vietnam J. Roads and Bridges*, 10.

Liang, Y.C., Lee, P., Lim, W.Z., Lee, K., Wu, C.G. (2002), "Proper orthogonal decomposition and its applications – part I: Theory", *J. Sound Vib*. **252(3)**, 527-544.

Lumley, J.L. (1970), *Stochastic Tools in Turbulence,* Academic Press.

Matsumoto, M., Chen, X., Shiraishi, H. (1994), "Buffeting analysis of long-span bridges with aerodynamic coupling", *Proc. 13th National Symposium on Wind Engineering*, JAWE 227-232.

Matsumoto, M., Chen, X. (1996), "Time domain analytical buffeting responses for long-span bridges", *Proc. 14th National Symposium on Wind Engineering*, JAWE 515-520.

Matsumoto, M., Yagi, T., Tsuboda, T., Lee, J.H., Hori, K., Kawashima, Y. (2006), "Study on unsteady pressure field on oscillatory B/D=4 rectangular cylinder using proper orthogonal decomposition", *The 3th Int'l Conference on Computational Wind Engineering (CWE2006)*, Yokohama Japan, July 15-17.

Matsumoto, M., Shirato, H., Le, T.H. (2007), "Time and frequency domain gust response prediction using proper orthogonal decomposition", *The 12th Int'l Conference on Wind Engineering (ICWE12)*, Cairne Australia, July 1-6.

Matsumoto, M., Shirato, H., Le, T.H. (2006), "Gust response of bridges using spectral proper transformation", *The 19th Int'l Symposium on Civil Engineering (KKCN19)*, Kyoto, December

10-12.

Simiu, E., Scanlan, R.H. (1976), *Wind Effects on Structures,* John Wiley&Sons.

Solari, G.; Carassale, L. (2000), "Modal transformation tools in structural dynamics and wind engineering", *Wind & Structures*, **3(4)**, 221-241.

Tamura, Y., Suganuma, S., Kikuchi, H., Hibi, K. (1999), "Proper orthogonal decomposition of random wind pressure field, *J. Fluid Struct.,* 13, 1069-1095.

Chapter 10

Conclusions

The main aims of this dissertation are to discuss on the unsteady buffeting forces and the gust response prediction of bridges as well as to investigate on recent limitations and uncertainties in the usage of the correction functions: the aerodynamic admittance function and the spatial coherence function. Furthermore, the proper orthogonal decomposition (POD) applications are also in scope and other aim of this dissertation. The all three main applications of the POD and its proper transformations in the wind engineering fields have been revised here. Firstly, the POD is used for analysis and identification of the pressure fields around some rectangular cylinders, moreover, the linkage between the POD modes and physical causes of the bluff body flow has been established. Secondly, the digital simulation of the random turbulent fields around the bridge deck has been studied using the spectral matrix-based POD and its spectral proper transformation. Finally, new approaches on the gust response prediction of bridges in both the time domain and the frequency domain also are considered as the main core of contribution and achievement in this dissertation. Especially, both branches of the proper orthogonal decomposition based on the covariance matrix and the cross spectral matrix as well as their covariance proper transformation and the spectral proper transformation have been applied. One of the additional contents presented inside is to investigate the spatial distribution and correlation on some physical models in some unsteady flows.

Two methodological approaches including the physical measurements in the wind tunnel and the analytical method using numerical examples have been exploited in this dissertation. The physical measurements of the surface pressure fields have been carried out on three physical models with slender ratio B/D=1, B/D=1 with the splitter plate at flow wake and B/D=5 under some unsteady flows including the smooth flows, turbulent flows and the fluctuating flows in order to investigate the spatial pressure distribution, the spanwise correlation and spanwise coherence. Moreover, the three components of the buffeting forces comprising lift, drag and moment have been directly measured on experimental models B/D=5 and B/D=20 under the turbulent flows in order to study the aerodynamic admittance functions. In the numerical example

for analytical method, the full-scale three-dimensional finite-element model of the cable-stayed bridges has been exploited.

The main contributions and results of this thesis are concluded herein as follows:

Chapter 2 has reviewed on background of the buffeting forces and the gust response prediction of bridges formulated in both the time domain and the frequency domain as well as recent limitations and uncertainties produced from the quasi-steady theory and the strip theory. Although, the correction functions as the aerodynamic admittance function and the spatial coherence function have been supplemented to treat with limitations of these theories, but the correction functions themselves contain uncertainties in their measurements and the empirical models. Therefore, further studies and developments on correction functions should be required for more refinements of the buffeting forces and the response prediction, as well as new approach for the gust response prediction.

Chapter 3 has discussed on spatial distribution and correlation of the pressure fields on some rectangular models and in some unsteady flows. It is found that the normalized fluctuating pressure distributes strongly and locally in the chordwise direction on the leading edge region, moreover, distributes homogeneously in the spanwise direction in the turbulent flows. In the fluctuating flows, the spanwise convection and the spanwise distribution of the surface pressure have been strengthened with respect to decrease of the reduced frequencies (increase of reduced velocities). It is supposed that the low frequency components can play more important role on spanwise distribution of induced pressure than high frequency ones.

The spanwise correlation depends strongly on such parameters as flow conditions, investigated positions, experimental models and their slender ratios B/D in the investigated cases. High spanwise correlation has observed at some positions near the leading edge regions where the high pressure region localized. The spanwise correlation in the smooth flows is larger than that in the turbulent ones. Moreover, the effect of Karman vortex (in the case without S.P) on increases of the spanwise correlation is also found. It is discussed that the spanwise correlation reduces with increase of slender ration B/D. It is again verified that the spanwise correlation of the turbulent-induced pressure always exhibits larger than that of the turbulence. The wind-structure interaction and the bluff body flow reason for the higher mechanism of spanwise correlation of induced forces than that of the turbulence.

Chapter 4 has investigated on the aerodynamic admittance as the spectral-based transfer

functions between the turbulence and the induced forces on some physical models B/D=5 and B/D=20 in the turbulent flows. New approaches of the nonlinear admittance function and the multi-variate admittance functions, as well as relationship between the aerodynamic admittance and the aerodynamic derivatives have been discussed and compared with the conventional quasi-steady admittance function. It is found that the contribution of squared fluctuating velocities on the output forces is not considerable in investigated cases, thus these nonlinear s components can be omitted without lost of accuracy. Moreover, comprehensive form of the multi-variate aerodynamic admittance has been determined by using the system identification technique.

Chapter 5 has studied on the spanwise coherence functions of the surface pressures and wind turbulences using both the Fourier transform-based and the wavelet transform-based tools, as well as some effects on coherent structure have been investigated. Firstly, it is found obviously that the pressure coherence expresses higher than the turbulent one, this can be convinced due to the effect of the wind-structure interaction and the bluff body flow on the model surface. Empirical formulae of the turbulent coherence, moreover, used in the gust response prediction so far contain obviously a lot of uncertainties.

Secondly, coherent structures of the turbulence and the pressure depend on some parameters not only the frequency, the ongoing flow, the spatial separations as usual, but the bluff body flow and the time. It is suggested, therefore, that the empirical formulae of coherence must account for the effect of bluff body flow. The side ratio B/D is recommended as the parameter of the bluff body flow in some cases of rectangular cylinders.

Thirdly, it is observed thanks to the Fourier coherence and the wavelet coherence that the coherences of the turbulence and the pressure are significant at the low spectral band and distribute intermittently in the time domain. High coherent events, moreover, distribute on localized areas in the time-frequency plane can be observed on the temporo-spectral structures of turbulence and pressure coherences, even at large separations. Thus, existence of localized high coherent events is the nature of coherence structure.

Finally, no correspondence and simultaneous occurrence between high coherence events of turbulence and induced pressure have been observed in the time-frequency plane. This can add to uncertainties in the turbulent-induced response prediction of structures relating to the quasi-steady theory of turbulent-induced forces built from the turbulent components.

Chapter 6 has applied the POD for analysis and identification of the chordwise pressure field around the rectangular cylinders, moreover, the linkage between the POD modes and the physical

causes has been found out in these investigated cases. Two POD branches using the covariance matrix and the cross spectral matrix has been presented. It is discussed that the first covariance turbulent mode and the first spectral turbulent mode play very significant role which can characterize for whole pressure field. Concretely, the first covariance mode, the first spectral one contain certain spectral peaks of hidden physical evens, moreover, it contributes dominantly on the field energy. Therefore, only the first mode is accuracy enough to reconstruct and identify the whole pressure field.

Obviously, the POD is effective to describe the pressure field by using limited number of low-order modes and eigenvalues and associated principal coordinates. In cases of the high frequency range and of complicated pressure distributions, it is suggested that more cumulative modes should be needed to reconstruct the pressure field. In the other words, the more complicated the pressure field distributes and the bluff body flow behaviors, the less important the first mode contributes and the more cumulative modes are needed to reconstruct the pressure field. In the comparison, the first spectral mode expresses the better than the first covariance mode in reconstructing the pressure field.

It is discussed that, however, the linkage between the POD modes and physical events is valid only in the concrete cases when the pressure field behaviors simply and steadily as well as the physical events occur apparently . Because the POD modes, eigenvalues, principal coordinates modify sensitively with respect to pressure positions, pressure tap arrangements, measured region and area, so on, therefore it is supposed such linkage only can be obtained in some limited cases. The usage of the POD, moreover, for interpreting aerodynamic interference is not clear so far.

Chapter 7 has applied the spectral matrix-based POD and its spectral proper transformation for simulating the multi-variate turbulent field. Effect of number of the spectral turbulent modes on simulated time series has been investigated with verification for accuracy and consistence. Moreover, the physical meaning of the spectral eigenvalues and turbulent modes relating to hidden events in the ongoing turbulent flow has been tried to establish. It can be argued that it is not accurate enough for the turbulent simulation with using just few fundamental turbulent modes, many turbulent modes should be required.

Because the spectral eigenvectors express constantly with respect to the different mean velocities and the frequencies, and the spectral eigenvalues contain frequency information. Therefore, it is expected that the spectral eigenvalues can characterize for scale of the turbulent eddies of the ongoing turbulent flow. However, further studies on this relationship should be required for more clarification.

Chapter 8 has used the spectral matrix-based POD and the spectral proper transformation to formulate the gust response of bridges in the frequency domain. The new approach on the gust response prediction of bridges has been carried out with usage of the comprehensive form of the cross spectral matrices of the multi-variate random turbulent fields, in which the spatial correlation of the turbulent fields has been taken into account in these matrices using the spatial coherence function. Full-scale buffeting forces have been decomposed completely and projected into generalized coordinates and the structural modes without usage of the joint acceptance function as applied in the conventional methods. Moreover, the effect of the spectral turbulent modes on the generalized and global responses has been investigated. It is discussed that only limited number of low-order spectral turbulent modes dominantly contributes on structural gust response. In these cases, the first spectral turbulent mode play very significant role and seems to be accuracy enough in predicting the gust response of bridges in the frequency domain, especially in the low frequency range.

Chapter 9 has applied the covariance matrix-based POD and the covariance proper transformation to formulate the gust response prediction of bridges in the time domain. New framework on the gust response prediction of bridges in the time domain has been proposed with usage of the comprehensive form of the covariance matrices of the multi-variate random turbulent fields. The effect of the orthogonally covariance turbulent modes on the global responses of bridges also is investigated. It is concluded that the higher number of lower-order covariance turbulent modes should be required for estimating the gust response of brides. To compare with the spectral turbulent modes, it seems the covariance turbulent modes play less important role than the spectral turbulent modes on the gust response prediction.

Some further works and developments are intended in the coming time as follows:

Firstly, the applications of the POD and its proper transformations for the gust response prediction of bridges in both frequency domain and the time domain is going to focus on further works with coupling effects with the aeroelastic flutter forces, moreover, the complete unsteady buffeting forces which can capture the unsteady fluid memory effect are going to be exploited.

Secondly, the limitations and uncertainties on the usages of the correction functions on the buffeting theory are going to be studied for further clarification.